UNIVERSITAT DE BARCELONA

Geophysical evidence of the preparedness for a volcanic eruption: El Hierro 2011-2012

Carmen López Moreno

UNIVERSIDAD DE BARCELONA, FACULTAD DE GEOLOGA-UB

GEOPHYSICAL EVIDENCE OF THE PREPAREDNESS FOR A VOLCANIC ERUPTION: EL HIERRO 2011-2012

Carmen López Moreno

Programa de Doctorat de ”Ciences de la Terra”

Thesis Supervisor: Prof. Joan Martí Molist

Thesis Tutor: Prof. Joan Manuel Vilaplana Fernández

UNIVERSIDAD DE BARCELONA, FACULTAD DE GEOLOGA-UB

GEOPHYSICAL EVIDENCE OF THE PREPAREDNESS FOR A VOLCANIC ERUPTION: EL HIERRO 2011-2012

Carmen López Moreno

Programa de Doctorat de ”Ciences de la Terra”

Thesis Supervisor: Prof. Joan Martí Molist

Thesis Tutor: Prof. Joan Manuel Vilaplana Fernández

La doctoranda

Barcelona, Junio de 2017

On the cover: Sea surface evidence of El Hierro submarine eruption, occurring 2 km off the village of La Restinga. From 15 October 2011, this light-green discoloured area of sea could be observed, proving a good indication of the explosive activity occurring at the submarine vent.
Photo: Rafa Abella

Acknowledgements

Esta Tesis Doctoral es el resultado directo de la labor y esfuerzo de un gran número de profesionales, que desde hace muchos años se dedican a las labores de investigación y servicio público, en los campos de la sismología y volcanología. Quiero dar las gracias especialmente a aquellos que instalan y mantienen las estaciones de vigilancia y procesan y analizan sus señales, permitiendo la existencia de datos de observación. Esta labor es imprescindible, indispensable y a veces poco reconocida.

Quiero dar las gracias a mi Director de Tesis, Joan Martí, que creyendo en mi capacidad de aprender, infundió el interés y valor suficiente para abordar labores de investigación en el campo de la volcanología; desde entonces no ha hecho sino acrecentarse mi entusiasmo y espero que también mi conocimiento. Ha sido imprescindible su guía y dirección a lo largo de todos estos años. También le agradezco todo lo que me ha enseñado y apoyado, no solo en el campo de la investigación, sino también en situaciones de emergencia volcánica en las que ambos nos hemos visto involucrados en representación de nuestras instituciones.

Quiero dar las gracias a mi Subdirector Jesús Gómez. Además de su apoyo y confianza, me he beneficiado directamente de su visión; bajo su Dirección se creó el servicio público de vigilancia y alerta volcánica dentro del Instituto Geográfico Nacional (IGN), materializándolo con personal y presupuesto. Desde entonces, esta unidad no ha hecho sino crecer y mejorar gracias a su labor.

Quiero dar las gracias a Mª José Blanco, Directora del Centro Geofísico de Canarias del IGN, por su gran profesionalidad, por su ayuda y su colaboración. Su trabajo ha sido, y es, imprescindible para las labores que el IGN desarrolla

en materia de vigilancia volcánica. Solo una persona con sus grandes cualidades puede soportar la gran presión que supuso estar en primera línea durante todos los años en que vivimos el proceso magmático asociado a la erupción de El Hierro.

Quiero dar las gracias a todos mis compañeros, sin excepción, del IGN, que durante estos más de 25 años han compartido conmigo su trabajo y conocimiento, y especialmente a mis compañeros de volcanología, por su entusiasmo, dedicación y valía. Desde aqui os mando mi agradecimiento y mi admiración.

También quiero dar las gracias a todos aquellos que me han enseñado, y que también me han calmado, ayudado a solucionar problemas y salvado de la desazón. Por poder nombrar solo a unos pocos, muchas gracias Laura García, Rafa Abella, Carmen del Fresno, Stavros Meletlidis, Mª Ángeles Benito, Alicia Felpeto, Rubén López, Mª José García, Elena Gonzalez, María Fernández de Villalta, Pedro Torres, Víctor Villasante, Itahiza Domínguez, Sergio Sainz-Maza, Marta Calvo, Natividad Luengo, Héctor Lamolda, David Moure, Jorge Pereda, Juan Rueda, Almudena Gómis, Juan Guzmán, Benito Casas, Enrique Romero, Víctor Cabrera, Mª José Jurado, Adelina Geyer, Antonio Villaseñor.

Infinitas gracias a mi familia, en especial a Alejandro, Aurora y Martín, que me han permitido ciertas licencias. Espero que el ejemplo de esfuerzo y dedicación, compense las carencias que haya podido causar.

Por último, y no menos importante, estoy muy agradecida a la isla de El Hierro, a sus habitantes y a su erupción submarina.

Carmen López

junio 2017

Abstract

Working with observational data from an active volcano offers us the opportunity to not only deal with the physics of the recorded observables (e.g. earthquakes, surface deformation) but also with the dynamics of the volcano itself. When we undertake the geodynamic study of the volcanic phenomenon, it is necessary to extend the spatial and the temporal frame of the studied parameters, looking for the boundaries of the acting forces to obtain a comprehensive recording of its evolution.

The observational data recorded by the monitoring networks during El Hierro 2011-2012 volcanic unrest and eruption, allowed us to conduct a study of the volcanic eruptive phenomena with that wide view. The lack of previous instrumental data describing such a process in the Canaries gave us the invaluable chance of analyzing for the first time, novel geophysical signals registered before, during and after an eruptive event, allowing the study of evidence of the energy involved in the emplacement and migration of magma through the lithosphere. The aim of this PhD Thesis is to make a comprehensive revision of the physics of this eruptive process and its causes, through the analysis and processing of geophysical data which has been recorded since the time of the first instrumental record to exist in the area, to the present. Three main aspects are considered, focusing on the eruptive phenomenon of El Hierro at different temporal and spatial scales, going from the general to the specific.

The first aspect is the study of the potential relation between the regional geodynamics and the eruptive event of El Hierro 2011–2012. This potential relation, through the analysis of long-time series of geophysical observational data, has not been studied before. Highly reliable seismic and geodetic data acquired from 1996 to 2014 is analyzed, covering: from the North Atlantic Ridge to the West, to the Azores-Gibraltar boundary to the North (including

the NW African margin) and the Canary Islands. A joint regional- and local-scale analysis based on this data enabled the identification of early signs of anomalous tectonic activity from 2003 onwards, the intensity of which increased in 2007, accelerating three months before the onset of the volcanic eruption on El Hierro in October 2011.

The second aspect is the study of the precursory signals recorded during the El Hierro volcanic episode (19 July to 10 October, 2011), and their correct interpretation when only limited data is available. The seismic and deformation data corresponding to the pre-eruptive unrest is reanalyzed using novel methods, taking into account new information about the internal structure of the island. Results indicate that important changes in the medium properties and in the magmatic mechanism occurred throughout the process, identifying different phases with distinct types of fracturing. A triggered shear seismicity is observed on pre-existent faults caused by the magma pressure on the structure underneath the island, and the crossing of the Moho discontinuity.

The third aspect is the detailed study of the type and geometry of the irreversible mechanism, acting during the final phase of the unrest episode (6-10 October, 2011) and during the first days of tremor (10-15 October, 2011) recording on the seismic monitoring stations. Application of time varying fractal analysis to the seismic data and the characterization of the seismicity pattern and the strain and the stress rates, allows the identification of different stages in the source mechanism, and to infer the geometry of the path used by the magma and associated fluids to reach the Earth's surface.

Contents

List of Figures

List of Tables

You will never do anything in this world without courage. It is the greatest quality of the mind next to honor.

Aristotle

CHAPTER

1

Introduction

It is well known that magmatic and seismic activity coincide mostly at plate boundaries, where tectonic deformation also concentrates. This coincidence of earthquakes and eruptions in time, and/or space, justifies the continued questioning as to whether volcanic eruptions and earthquakes may be related. Several authors suggest that the answer is affirmative, suggesting that they could share energy (e.g. by triggering activity) (Bonali et al. 2013, Hill D P & Newhall 2002, Lupi & Miller 2014, Manga & Brodsky 2006, Marzocchi 2002, T. & Selwyn 1998, Walter & Amelung 2007) for volcanic and seismic activity. Despite being less obvious, the same question can be also addressed in intraplate volcanic areas, located far away from the active plate margins. This is the case of the Canary Islands, an oceanic island chain that lies in the Atlantic Ocean off the Northwest coast of Africa and presents active volcanism. On 2011, we had the occasion of living in real time the awakening of volcanic activity with the unrest and eruption of a submarine volcano in El Hierro, which is the smallest and western island of the Canarian Archipelago, offering a nice and valuable opportunity of understanding the ocean island volcanism and the volcanic phenomenon in the Canaries.

1.1 Motivation

During the final stages of pre-eruptive volcanic unrest, certain features are usually observed: an overall acceleration in seismicity and ground deformation (e.g. Bell & Kilburn 2012), shallower seismicity (e.g. Battaglia et al. 2005), seismic migration (e.g. (Caudron et al. 2015)) and an apparent lack of activity (hours to minutes) before the reinforcement or the onset of the eruption (e.g. Roman et al. 2016). Several well-documented eruptions show some, if not all, of these precursory features (e.g. Battaglia et al. 2005, Bell & Kilburn 2012, Caudron et al. 2015, López et al. 2012, Sigmundsson et al. 2015, Vinciguerra 2002), which suggests that similar fundamental physical processes occur within these volcanoes.

However, the physical processes preceding a new eruption are complex and poorly known, and there are still many unanswered questions regarding the requirements for an irreversible failure of the Earth's crust and non-stop magma migration from deeper levels to the surface. It is also difficult to correctly interpret the precursory signals recorded by monitoring networks and to understand the nature and extent of the physical processes that cause them. Some of the difficulties arise from the incompleteness of monitoring data and the lack of previous knowledge of the volcanic systems (e.g. type of magma, internal structure, local and regional stresses).

This PhD Thesis is the result of the multidisciplinary study of the most recent volcanic eruptive process occurred in the Spanish territory: El Hierro (Canary Islands) 2011–2012 eruption. Until this eruption, instrumental monitoring data about unrest preceding monogenetic eruptions in the Canaries, were sparse and the available information was mainly based on historical records (Albert et al. 2016), in fact, from the previous eruption occurred in the Canaries in 1971 (Teneguía eruption, in La Palma Island) there is only macroseismic information related to felt seismic activity.

Since the appearance of the first signs of anomalous seismicity in El Hierro, a comprehensive record of the activity was obtained from the high-quality network (endowed with seismic and GPS stations, gravimeters, magnetometers and geoquemical stations) deployed by the Instituto Geográfico Nacional (IGN, www.ign.es) in the Island, giving us the invaluable chance of analyzing, for the first time, the precursory signals that accompany the eruptive phenomenon from its very beginning. I collected, processed and analyzed from the global to the particular and since the time the first instrumental records exist, to date, geophysical, geochemical and petrological data in the Canaries, for a comprehensive

analysis and interpretation of the volcanic eruption precursors registered during El Hierro magmatic process.

Below, I present the scientific papers included in my PhD Thesis, which have been already published in scientific journals or accepted for revision:

López C., L. García-Cañada, J. Martí, and I. Domínguez Cerdeña (2017), Early signs of geodynamic activity before the 2011–2012 El Hierro eruption, Journal of Geodynamics, 104, 1-14, doi: http://dx.doi.org/10.1016/j.jog.2016.12.005.

López C., M.A. Benito, J. Martí, C. del Fresno, L. García-Cañada, H. Albert and H. Lamolda (2017), Driving magma to the surface: the 2011–2012 El Hierro eruption, G3, accepted by Editor.

López C., J. Martí, R. Abella and M. Tárraga (2014), Applying fractal dimensions and energy-budget analysis to characterize fracturing processes during magma migration and eruption: 2011-2012 El Hierro (Canary Islands) submarine eruption, Surveys in Geophysics, doi: 10.1007/s10712-014-9290-2.

Besides, I collaborated with different authors studying El Hierro eruption or other aspects like the eruptive mechanism in monogenetic eruptions. I used the results and retrieved knowledge from these collaborations, enriching the discussion of my papers and improving the proper interpretation of my own results. I list them below:

Martí J., C. López, S. Bartolini, L. Becerril, and A. Geyer (2017), Stress controls of monogenetic volcanism: a review, Frontiers in Earth Science, 4(106), doi:10.3389/feart.2016.00106.

Martí J., A. Villaseñor, A. Geyer, C. López, and A. Tryggvason (2017), Stress barriers controlling lateral migration of magma revealed by seismic tomography, Scientific Reports, 7, 40757, doi: 10.1038/srep40757.

Telesca L., M. Lovallo, C. López, and J. Martí (2016). Multiparametric statistical investigation of seismicity occurred at El Hierro (Canary Islands) from 2011 to 2014. Tectonophysics. http://dx.doi.org/10.1016/j.tecto.2016.01.045.

Telesca L., M. Lovallo, J. Martí, C. López and R. Abella (2015), Multifractal investigation of continuous seismic signal recorded at El Hierro volcano (Canary Islands)

during the 2011–2012 pre- and eruptive phases, Tectonophysics. Vol 642, 71-77, doi: 10.1016/j.tecto.2014.12.019.

Tárraga M., J. Martí, R. Abella, R. Carniel, C. López (2014), Volcanic tremors: good indicators of change in plumbing systems during volcanic eruptions, Journal of Volcanology and Geothermal Research, Vol. 273, 33–40.

Telesca L., M. Lovallo, J. Martì, C. López and R. Abella (2014), Using the Fisher–Shannon method to characterize continuous seismic signal during volcanic eruptions: application to 2011–2012 El Hierro (Canary Islands) eruption, Terra Nova, 0, 1-5, doi: 10.1111/ter.12114.

Martí, J.; V. Pinel; C. López; A. Geyer; R. Abella; M. Tárraga; M.J. Blanco; A. Castro and C. Rodríguez (2013), Causes and mechanisms of the 2011–2012 El Hierro (Canary Islands) submarine eruption, Journal of Geophysical Research: Solid Earth, Vol. 118, 1–17, doi:10.1002/jgrb.50087.

López C., M.J. Blanco, R. Abella, B. Brenes, V. M. Cabrera-Rodríguez, B. Casas, I. Domínguez-Cerdeña, A. Felpeto, M. Fernández de Villalta, C. del Fresno, M. J. García-Arias, L. García-Cañada, A. Gomis-Moreno, E. González-Alonso, J. Guzmán-Pérez, I. Iribarren, R. López-Díaz, N. Luengo-Oroz, S. Meletlidis, M. Moreno, D. Moure, J. Pereda de Pablo, C. Rodero, E. Romero, S. Sainz-Maza, M. A. Sentre-Domingo, P. A. Torres, P. Trigo, V. Villasante-Marcos (2012), Monitoring the volcanic unrest of El Hierro (Canary Islands) before the onset of the 2011-2012 submarine eruption, Geophysical Research Letters Vol. 39, LI3303, doi:10.1029/2012GL051846.

As an introduction, I present a revision of the recent volcanism in the Canary Islands and the review of those mathematical tools and physics used in my papers, which constitute the basis of this PhD Thesis.

1.2 Volcanism in the Canary Islands

The study of the volcanic activity that surrounds and builds oceanic islands may yield evidence of thermal and chemical anomalies within Earth's mantle. The Canary Islands are an oceanic island chain that lie in the Atlantic Ocean off the continental margin of the African plate, and offers the opportunity of understanding oceanic island volcanism. They have been the subject of numerous scientific studies, but the geological and geophysical data that have been obtained on the Canary Islands presents many open questions, giving us the opportunity for interesting research related to the island's origin and the role it plays in the regional geodynamics.

1.2.1 Geodynamic context

The Canary Archipelago consists of seven main volcanic islands and several islets lying in a chain extending for 500 km across the eastern Atlantic Ocean; its eastern edge is only 100 km from the northwest coast of Africa (see Figure 1.1). The Canaries are constructed on the passive continental margin of the African Plate in a tectonic region that is, nevertheless, bounded by very active plate boundaries.

Its borders include the Mid-Atlantic Ridge to the west, as well as the transition to the north from an oceanic (the Azores, the Gloria Fault and the Gorringe Bank) to a continental boundary where Iberia and Africa meet. This boundary to the north is only clearly defined in its oceanic part. From 11°W to 3.5°E, including the Strait of Gibraltar and the Alboran Sea southern Spain, northern Morocco, and western Algeria, is more diffuse and forms a broader area of deformation. To the northeast, the region also includes the Atlas sub-plate (Morocco), consisting of continental lithosphere and likewise subject to active deformation (Bezzeghoud et al. 2014, Mantovani et al. 2007, Serpelloni et al. 2007).

Following the classification used by several authors (e.g. Bezzeghoud et al. 2014), the whole area can be divided into different regions, each characterized by coherent seismic and kinematic properties. From west-to-east and north-to-south these regions are as follows: the Mid-Atlantic Ridge including the Azores Triple Junction (MAR-ATJ); the Azores Islands from Faial-Terceira to the islands of San Miguel (ATSM); the Gloria Fault (GF); the Gorringe Bank as far as Cadiz (GB); the Betic Mountains, the Rif Cordilleras, the Alboran Sea (BALB); the Atlas Mountains (ATL); and the Canary Islands (CAN). See schematic plot in Figure 1.2. Crustal seismicity and GPS deformation studies (Bezzeghoud

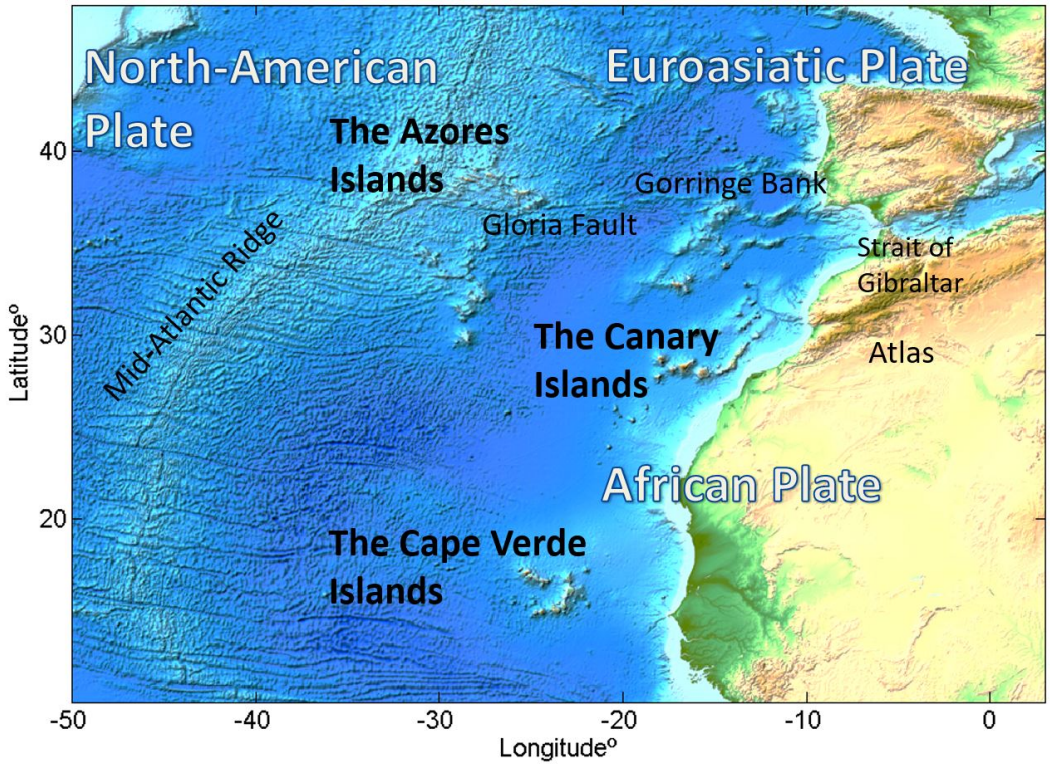

Figure 1.1: Geodynamic context and main geographical features of the studied region.

et al. 2014, Jiménez-Munt et al. 2001, Jiménez-Munt et al. 2011, Serpelloni et al. 2007) were used to identify the kinematic behavior of each region. From west-to-east, there is a quite simple deformation field characterized by an extension running perpendicular to the Mid-Atlantic and Terceira Ridges. As well, there is a right-lateral strike-slip motion along the Gloria transform faults, which becomes the dominant compressive regime running eastwards from the Gorringe Bank area to Algeria, where the continental lithosphere is involved. The other volcanic regions in this area are the Azores Archipelago, located at the intersection of the Mid-Atlantic Ridge, the North American, Eurasian, and African Plates, and the Cape Verde Archipelago, located to the south, from 450 to 600 km off the west coast of Africa, all of them with known volcanic activity in the last decades. Table 1.1 is a compilation of all known volcanic eruptive and unrest episodes that have taken place in the Azores, Canary, and Cape Verde archipelagos since 1900.

Azores Islands								
Start Date	**Stop Date**	**Eruption Certainty**	**VEI**	**Evidence**	**Location**	**Lat°N**	**Lon°W**	**Source**
1902/05/07	1902/05/08	Confirmed	0	Historical observations	Subm. vent ca. 20 km SW of Terceira	38.65	28.08	Smithsonian
1907/04/01	Unknown	Confirmed	0	Historical observations	Monaco Bank	37.6	25.88	Smithsonian
1907	Unknown	Confirmed	0	Historical observations	San Jorge	38.65	28.08	
1911/03/07	Unknown	Confirmed	1	Historical observations	Monaco Bank	37.6	25.88	Smithsonian
1957/09/27	1958/10/24	Confirmed	2	Historical Observations	West flank (Capelinhos) and summit	38.6	28.73	Smithsonian
1988/05/?	1989/01/?	-	-	Seismic unrest	Volcanic unrest Agua de Pau Volcano San Miguel	-	-	Additional Report for Azores-Gigraltar Fracture Zone
1998/11/25?	2000/03/?	Confirmed	0	Historical observations	Serreta Ridge (submarine vent W of Terceira)	38.73	27.32	Smithsonian
2003/04/26	2007/01/01	-	-	Seismic unrest	San Miguel	-	-	Wallenstein et al., 2009 Silva et al., 2012
2011/09/15	2012	-	-	Seismic and deformation unrest	San Miguel	-	-	Okada et al., 2014
Canary Islands								
Start Date	**Stop Date**	**Eruption Certainty**	**VEI**	**Evidence**	**Location**	**Lat°N**	**Lon°W**	**Source**
1909/11/18	1909/11/27	Confirmed	2	Historical observations	NW rift zone (Chinyero), Tenerife	28.27	16.64	Smithsonian
1949/06/24	1949/07/30	Confirmed	2	Historical observations	San Juan, Llano del Banco, Hoyo Negro, La Palma	28.57	17.83	Smithsonian
1971/10/26	1971/11/18	Confirmed	2	Historical observations	Teneguia, La Palma	28.57	17.83	Smithsonian
1989/05/09	-	-	-	Seismic unrest	Tenerife	-	-	Vinciguerra and Day, 2013
2004/05/12	2005/05/18	-	-	Seismic unrest	Tenerife	-	-	Domínguez-Cerdeña et al., 2011
2011/10/10	2012/03/05	Confirmed	2	Seismic and deformation unrest	Submarine S flank, El Hierro	27.73	18.03	Smithsonian
Cape Verde Islands								
Start Date	**Stop Date**	**Eruption Certainty**	**VEI**	**Evidence**	**Location**	**Lat°N**	**Lon°W**	**Source**
1909	Unknown	Confirmed	-	Historical Observations	Fogo	14.95	24.35	Smithsonian
1951/06/12	1951/08/21	Confirmed	2	Historical Observations	Northwest and south caldera floor, Fogo	14.95	24.35	Smithsonian
1995/04/02	1995/05/26	Confirmed	2	Historical Observations	WSW flank of Pico, Fogo	14.95	24.35	Smithsonian
2014/11/23	2015/02/08	Confirmed	-	-	Northwest and south caldera floor, Fogo	14.95	24.35	Smithsonian

Table 1.1: Volcanic (eruptive and unrest) activity in the Azores, Canary, and Cape Verde Islands since 1990. The descriptions of the volcanic events were taken from the Smithsonian Database (www.volcano.si.edu) and from scientific papers.

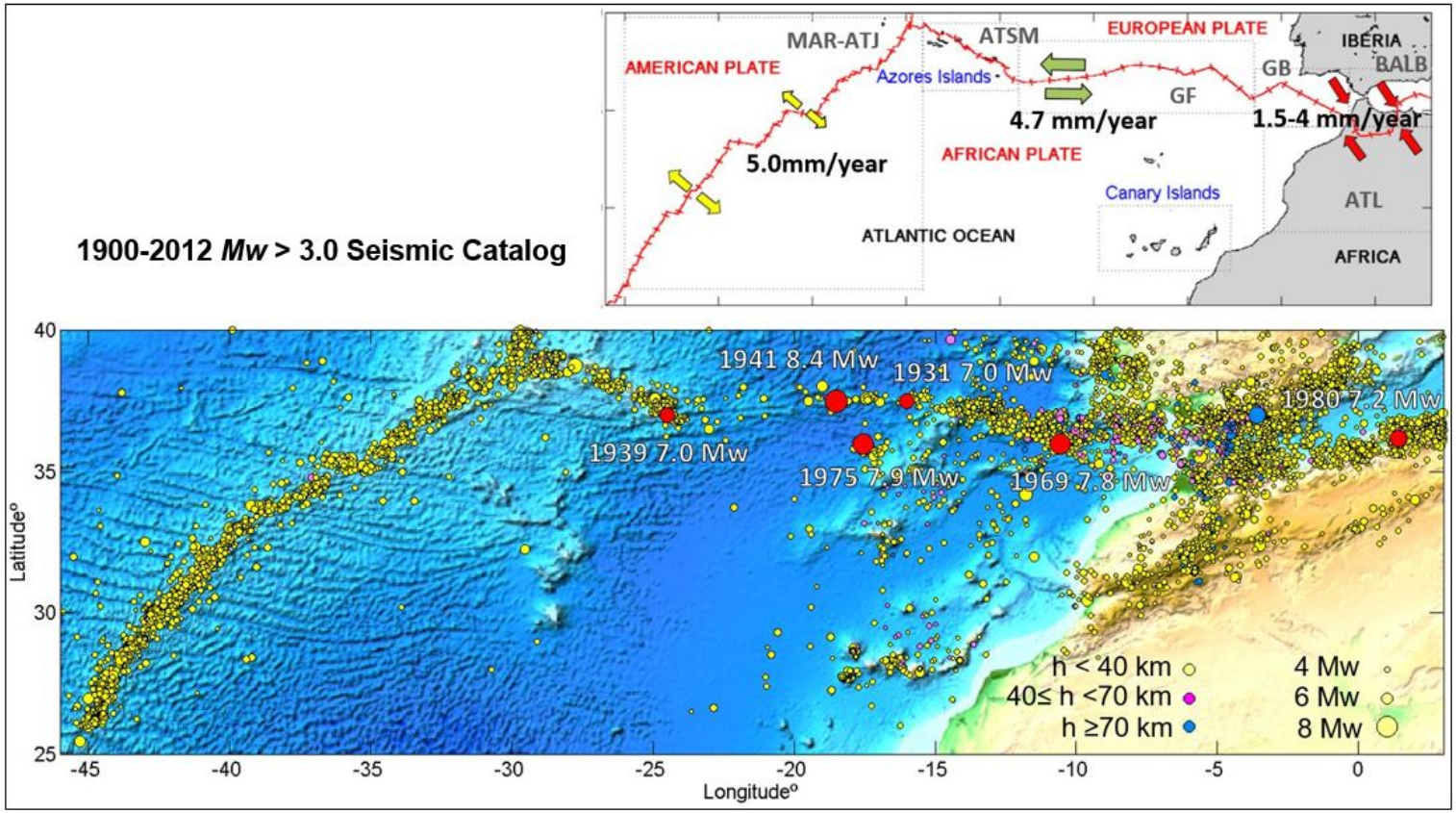

Figure 1.2: Mw>3.0 earthquake distribution during 1900-2012 (7,847 seismic events. Catalog sources: Instituto Geográfico Nacional, IGN; International Seismological Centre, ISC-GEM; The North Moroccan Earthquake Catalog of seismic hazard assessment (Cabañas et al. 2015, Peláez et al. 2007). Symbol size reflects event magnitude, with colors ranging from yellow to blue depending on the event depth. Bathymetry and topography from the National Geophysical Data Centre (NOAA). Upper figure shows the synthesis of the kinematic field in the region and the distribution of the studied areas: Mid-Atlantic Ridge including the Azores Triple Junction (MAR-ATJ); the Azores Islands from Faial-Terceira to the islands of San Miguel (ATSM); the Gloria Fault (GF); the Gorringe Bank as far as Cadiz (GB); the Betic Mountains, the Rif Cordilleras, the Alboran Sea (BALB); the Atlas Mountains (ATL); and the Canary Islands.

In this region important tectonic forces act. Deformation rates range from 5 mm/year in the Mid-Atlantic region in a E-W direction, and decrease eastward to values of 2.7-3.9 mm/year in Algeria in a NW-SE direction (Figure 1.2). This border has given rise to frequent powerful seismic events such as the 1755 Lisbon earthquake and the subsequent tsunami (8.5 Mw, felt X in southwest Portugal) (Baptista & Miranda 2009). The border running from the Azores to Algeria has been the site of recently occurring major earthquakes (Mw $>$ 7.0), including events on the Azores-Gibraltar fracture zone (1931 7.0 Mw and 1975 7.9 Mw), Santa María (1939 7.0 Mw), the Gloria Fault (1941 8.4 Mw), the Atlantic Ocean (1969 7.8 Mw), and El Asnam in North Africa (1980 7.2 Mw).

The Canarian volcanism is thought to be related with mantle dynamics, being evidence that an active mantle upwelling exists beneath the Atlantic Ocean Basin off the northwest African continental lithosphere. Duggen et al. (2009), based on geochemical data of lavas, proposed the existence of a sublithospheric mantle flow beneath the northwest African plate, through a subcontinental lithospheric corridor from the Canarian domain, crossing the Atlas Mountains and moving towards the western Mediterranean. This author relates plume push, to eastward-thinning, delamination below the Atlas and rollback of a subducting slab in the western Mediterranean, 1,500 km to the northeast from the Canaries. van den Bogaard (2013) studied the spatial and temporal distribution of the Canary Island Seamunt Province, concluding that an active and shallow mantle upwelling beneath the Atlantic Ocean basin off the NW African continental lithosphere produced recurrent melting anomalies and therefore active volcanism.

Moreover, Saki et al. (2015) interpret the existing seismic discontinuities at different sublithospheric depths in the region as a large upwelling beneath the North Atlantic not extending through the top of the transition zone as a whole, except for different plume branches which appear as a thinner upwelling in the Azores, the Canaries and also in the Cape Verde hotspots at the surface. A recent high-resolution tomography study below Morocco, Canary Islands and the Alboran sea by Bonnin et al. (2014), found the existence of a strong low velocity zone beneath the western part of Canaries down to a depth of approximately 300 km. Plume conduits beneath the three hotspots have been mapped previously by Montelli et al. (2006) and Zhao (2007). They find prominent low velocity zones beneath Azores, Cape Verde and Canaries, stretching down to at least 700 km depth. Figure 1.3 represents the slice stacks of high resolution tomographies on P-wave LLNL-G3DV3 (Simmons et al. 2012) and S-wave S2.9EA (Kustowski et al. 2008).

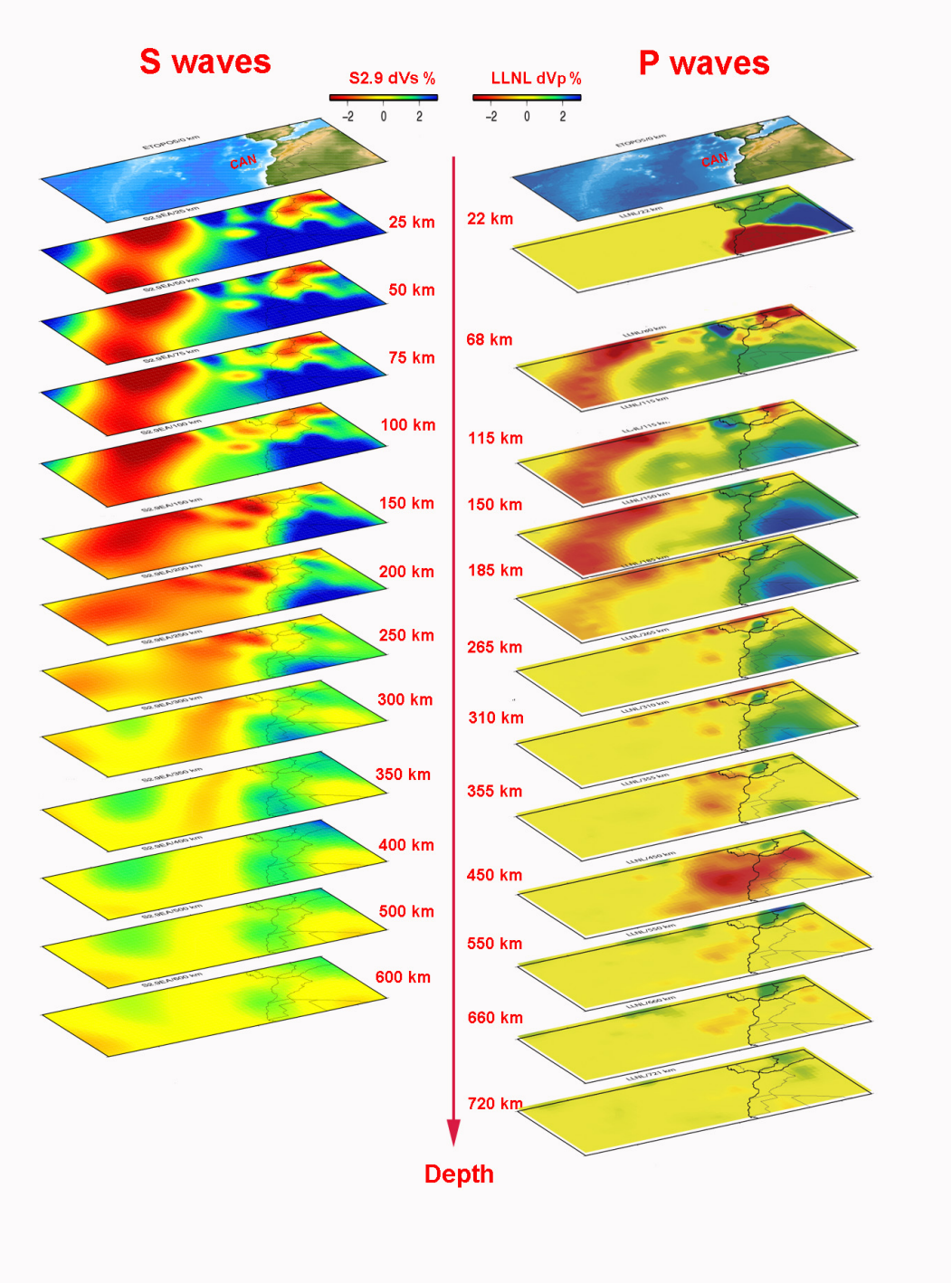

Figure 1.3: Slice stacks of shear-wave velocity perturbation, dVs% (-3:+3) of S2.9EA global tomography model (left) and compressional velocity perturbation, dVp% (-3:+3) of LLNL global tomography model (right).

These slices highlight different aspects of the lithosphere given the differing behaviors of the compressional (P) and shear (S) waves due to the variations of the state parameters with depth. However, both correspond to a broad sub-lithospheric, low velocity anomaly in the Atlantic Ocean, as well as independent lithospheric branches in contact with the surface.

At shallower depths in the Canarian lithosphere, geophysical and petrological modeling studies propose a low velocity anomaly at lithospheric (50-110 km) and sub-lithospheric (150-260 km) depths (Fullea et al. 2015, Legendre et al. 2012). The upper anomaly is modelled as a depleted and mechanically strong lithosphere showing no significant thinning with respect to the surrounding oceanic and continental domains, while the sub-lithospheric anomaly is assumed to represent a value of + 100 °C with respect to ambient mantle (mantle potential temperature of 1,435 °C) (Fullea et al. 2015).

Further towards the surface, thermobarometric and petrologic studies of basanites erupted on El Hierro and La Palma allowed to reconstruct the magma plumbing and storage beneath those islands, indicating the existence of small, intermittent magma chambers in a depth range of 15-26 km, in a similar manner to other oceanic volcanic islands fed by plumes with relatively low fluxes (Klügel et al. 2005, Martí et al. 2013, Meletlidis et al. 2015, Stroncik et al. 2009).

On El Hierro, structural studies carried out before the eruption revealed clear lithospheric anomalies below the island. Carbó et al. (2003) and Llanes et al. (2003) performed a 3D-lithospheric gravimetric inversion over a wide area around the Canary Islands (See Figure 1.4). These authors found a main regional N-S oriented Bouguer gradient to the west of the island of La Palma that passes through El Hierro, which is associated with a Bouguer wavelength of 40 km (corresponding to a depth of 48-128 km). They also identified two shallow gravity minima to the NE and SW of El Hierro, with Bouguer wavelengths of 12-40 km (corresponding to a depth of 12-48 km). In the same area that these two authors (Carbó et al. 2003, Llanes et al. 2003) found a gravity minimum to the SW of El Hierro, Montesinos et al. (2006) used a 3D gravity inversion to model a negative density anomaly at a depth of 10km.

In a field survey carried out prior to the 2011 unrest, Gorbatikov et al. (2013)studied the deep structure of El Hierro using microseismic sounding techniques. These authors found a central-eastern intrusive high velocity body in the crust that they interpreted as being related to the early stage of the formation of the island, as well as a western intrusive body below

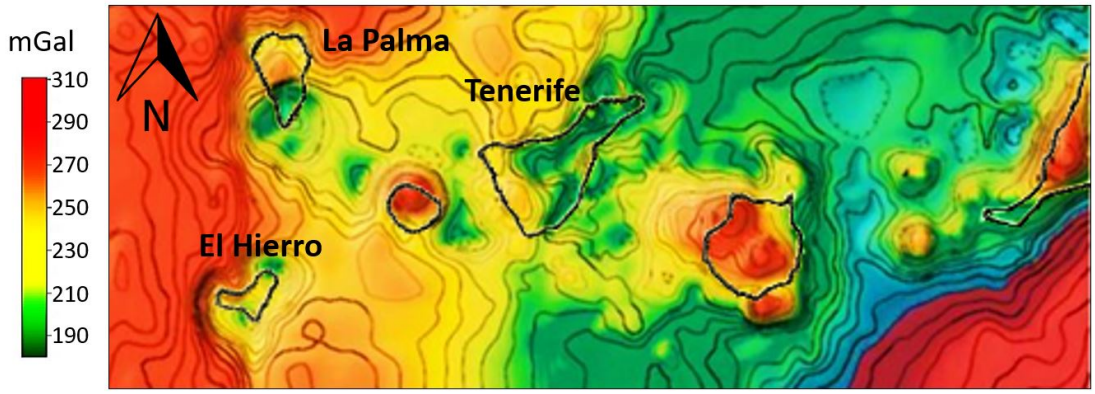

Figure 1.4: Distribution of the Bouguer anomalies in the Canaries (modified from Carbó et al. 2003, Llanes et al. 2003. Color scale in mGal.

the crust at a depth of >15 km that was interpreted as a recent magmatic reservoir. This is consistent with the depth range of 19-26 km (in the upper-mantle) reported by Stroncik et al. (2009) for the magma plumbing and storage system below El Hierro. A P- and S-wave 3D tomography performed by García-Yeguas et al. (2014) revealed on El Hierro a high-velocity crust to a depth of 10-12 km and a low-velocity anomaly below the base of the crust, interpreted as a batch of magma rising as a small plume from the mantle located beneath El Hierro.

Furthermore, recent P-wave 3D tomography (Martí et al. 2017) modeled the structural complexity of the interior of El Hierro, identifying important discontinuities. Authors interpreted these discontinuities as structural and/or rheological contrasts (i.e.: stress variations) that have conditioned magma transport inside the island and, consequently, the evolution of the location of seismicity during the different magmatic episodes, as that occurred in El Hierro since 2011.

These barriers correspond to regional tectonic structures and blocked pathways from previous eruptions, which reduces the options for fresh magma for finding a suitable pathway to the surface and for erupting (See Figure 1.5). The most important features are the upper-crustal Tanganasoga high-velocity anomaly, and the upper-mantle low velocity region, that authors interpreted as magma reservoirs.

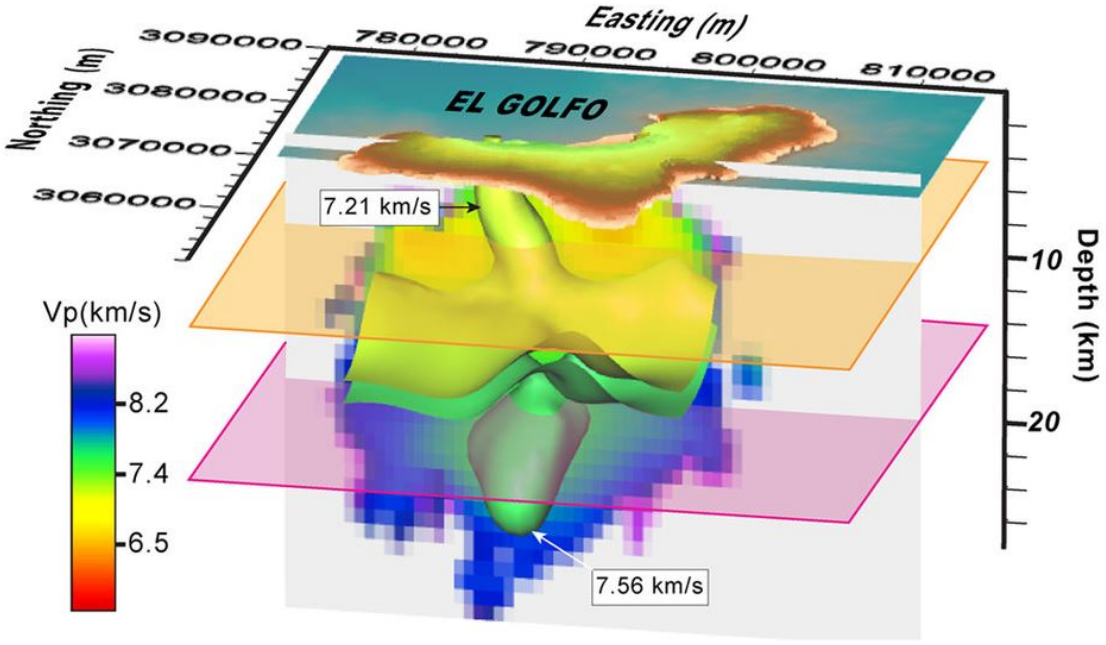

Figure 1.5: P-wave 3-D tomography model of the structure beneath El Hierro island showing the isosurfaces of 7.21 km/s and 7.56 km/s. Modified from (Martí et al. 2017).

1.2.2 Recent volcanism

The Canary Islands are one of the largest active intraplate volcanic regions of the World, beginning its volcanism about 60 Ma ago (e.g. Carracedo et al. 2002). The origin of its magmatism is still controversial and several hypotheses, including a mantle plume hot spot (Carracedo et al. 1998, Hoernle & Schmincke 1993, Holik et al. 1991), a local extensional ridge model (Fuster 1975), and an uplifted tectonic blocks model (Araña & Ortiz 1986), have been mooted to explain its geological features. Additional petrological, geophysical, and geochemical evidence of its sub-lithospheric mantle provided evidence for other possible explanations such as that stated by Anguita & Hernán (2000), who unify in a single model thermal mantle anomaly features and the role of the regional fractures and tectonic forces as sources of the magmatic activity. Its eruptive activity rate is low and only 19 eruptions have been recorded over the past 500 years of written history, all of monogenetic character on the islands of El Hierro (2011–2012), La Palma (1585, 1646, 1677, 1712, 1949, 1971), Tenerife (1704, 1706, 1798, 1909) and Lanzarote (1730–1736,1824) (Romero 2000). Figure 1.6 shows the historical eruptions occurred in the Canary Islands. In all cases, historical eruptive activity has been related to basic magmas ranging in intensity from strombolian to violent strombolian, originating scoria cones and lavas. The duration of the eruptions ranged from a few weeks to a few months, except in the case of the Timanfaya eruption in 1730 that lasted for six years.

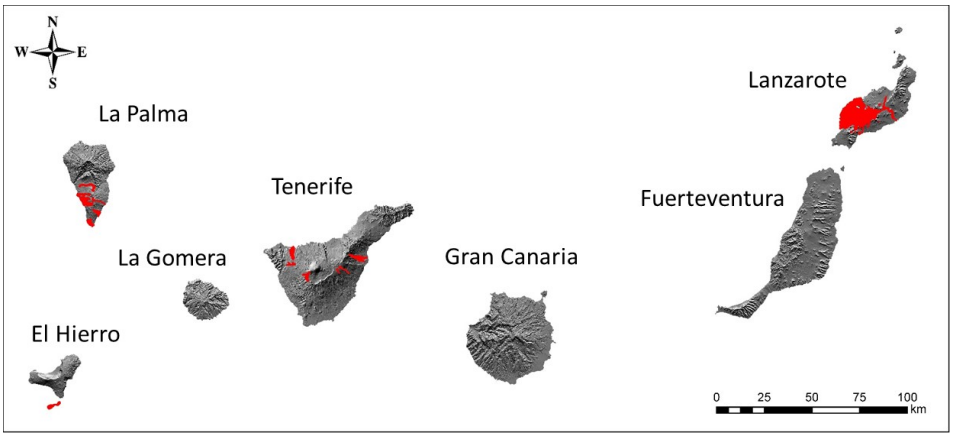

Figure 1.6: Canary Islands geographical distribution and deposits (in red) of the historical eruptions occurred in the last 500 years (Romero 2000). Modified from www.ign.es.

1.2.2.1 El Hierro 2011-2012 volcanic unrest and eruption

The 2011-2012 El Hierro eruption occurred 40 years after the eruption of Teneguia on La Palma in 1971 and represents the only such event, in the Canaries, that has ever been fully recorded from beginning to end by a local monitoring network.

On 19 July 2011, after a long period of quiescence on El Hierro, a persistent increment in seismic activity was observed. During the pre-eruptive unrest, which lasted for almost three months (19 July-10 October), a batch of deep magma accumulated at a shallow depth, migrated laterally from north to south below the crust for over 20 km before erupting (López et al. 2012, Martí et al. 2013), producing thousands of seismic events and centimetric surface deformation.

On 10 October 2011, a submarine volcanic eruption occurring 2 km south of the island culminated this process. A comprehensive record of the activity was obtained from the seismic and GPS network deployed by the IGN all over the island, and besides, by the gravimetric, geomagnetic and geochemical IGN stations. The seismic network was composed by one three components (3CC) broad-band station (CTIG) and eight short- and medium-period 3CC stations. The located seismic activity is included in the IGN seismic catalog (www.ign.es) and includes the hypocentre and size of the located events. The 3D surface deformation history was recorded by a network of four GPS stations located in the north of El Hierro, which provided daily displacements as a function of time (López et al. 2012).

Distinct pre-eruptive phases were distinguished by significant changes in the evolution of the geophysical signals:
1) a north-to-south migration of magma at a depth of 12-15 km at the Mohorovicic discontinuity in the area (Ranero et al. 1995, Watts 1994);
2) a simultaneous surface deformation pattern that also reflected a correlated migration of the pressure source towards the south;
3) a clear acceleration in the process during the final days of unrest in the form of an increment in the released seismic energy and deformation (3–5 October 2011); and, finally,
4) the occurrence on 8 October 2011 of a 4.3 $mbLg$ earthquake at a depth of 12 km in the same area where the seismicity was occurring.

On 10 October at 04:10 UTC, a clear emergent tremor signal was registered by all the seismic stations, indicating the onset of the eruptive activity. From the 8 October event, to the beginning of the eruption on 10 October, the only activity consisted of a few shallow

low magnitude earthquakes occurring offshore to the south of the island, about 5 km from the coast.

The eruption of basanitic magma constructed a submarine cone at about 2 km from the southern corner of the island at a depth of about 300 m. This cone reached a height of 220 m with a basal diameter of over 1 km (Rivera et al. 2013).

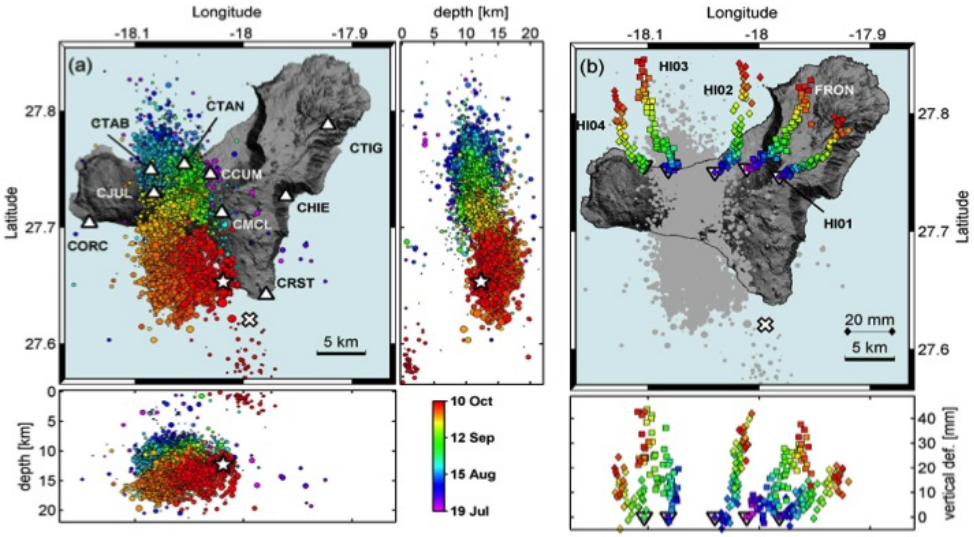

Figure 1.7: Seismic and geodetic activity registered on El Hierro during the volcanic unrest. (a) Temporal evolution of the earthquake hypocentral solutions. Seismic stations are shown as triangles. Depth of the events is shown for vertical cross-sections in N-S direction and E-W direction. White star shows the epicenter of the $mbLg$ = 4.3 event. (b) Daily horizontal deformation (colored squares and diamonds) with respect to the location of each GPS station (inversed triangles). Both panels show the position of the 2011 eruption (white cross). Figure from (López et al. 2012).

The eruption lasted until early March 2012 and was followed (2012–2014) by several further episodes of volcanic unrest. In terms of the seismic energy released and the accumulated deformation, some of these subsequent episodes were in fact more intense than the pre-eruptive unrest, although none actually culminated in further eruptions.

1.3 Methodology

A summary of the main methodology applied to the observational seismic and geodetic data is presented below; a comprehensive description of the procedures and the mathematical formulation is included in the Papers I present in this PhD Thesis (Appendix A, B and C).

1.3.1 Analysis and characterization of the located seismic activity

The information of located events included in seismic catalogs is used to study the seismicity in the region and the causal relation of its variations with El Hierro volcanic unrest and eruption. In most of the cases, it was necessary to improve the completeness of the datasets in order to make temporal and spatial evolution studies, or to re-analyzed the seismic waveform and manually picking additional earthquakes, completing the seismic catalog of events.

1.3.1.1 New regional seismic catalog

The main issue was the compilation of a new, unified (using the same magnitude scale and not including duplicated event solutions) seismic catalog, enabling the study of the seismic activity at regional scale, from the Azores to the South of the Iberia Peninsula, and from the Canary Islands to the Azores-Gibraltar fault. The compilation was performed by searching for global and regional agencies that could provide seismic locations in the region, from 1900 to date.

Consulted catalogs were the following:

1. IGN, Instituto Geográfico Nacional, Spain. On-line bulletin, http://www.ign.es. The IGN provides preliminary and final seismic locations for the whole Ibero-Maghrebian region (26°N - 45°N, 20°W - 6°E).

2. ISC, International Seismological Center. On-line bulletin, http://www.isc.ac.uk (United Kingdom, 2014). This center collates and recalculates earthquake locations from national and local agencies, and provides solutions for the region. When available, the ISC-GEM Catalog was used.

3. The North Moroccan Earthquake Catalog of seismic hazard assessment (Peláez et al. 2007) consists of records of seismicity occurring in northern Morocco (27°N - 37°N, 15°W - 1°E) in the period 1045-2006.

4. The on-line database of Earthquake Mechanism for European Area (EMMA) (Vannucci

& Gasperini 2004), a complete compilation of reliable solutions available in the literature for all events occurred before 2004.

5. GCMT, Global Centroid Moment Tensor Database (formerly, Harvard CMT), USA. This website provides moment tensors for earthquakes of a magnitude M >5 throughout the world.

6. A revision of the IGN Seismic Catalog by Cabañas et al. (2015) as part of hazard assessment in the Iberian Peninsula, which includes empirical relationships for different magnitude formulas with M_W.

Merging tasks generated a huge dataset of earthquakes, with many duplicated entries for origin time and hypocentral location, as well as several different scales for magnitude values (moment magnitude-M_W, surface wave magnitude-M_S, body wave magnitude-mb, duration magnitude-M_D, and local magnitudes M_L and $mbLg$. Final hypocentral location parameters were assigned following a prioritization rule based on the reliability and the level of revision of the seismic source, and making a special effort to homogenize magnitudes. The most reliable mb, M_S,M_W, or M_D from global agencies and M_L, $mbLg$, M_W, mb, or M_D from local observatories were selected. It was assumed that $(Mb, M_S, M_W)NEIC = (Mb, M_S, M_W)ISC$, and $(M_W)HARVARD/GCMT = (M_W)NEIC$, with only a little deviation, as shown by Scordilis (2006). It was also assumed $M_L = M_W$ ($M_L < 6.5$), following the criteria used by Heaton et al. (1986). In the case of the IGN catalog, we used the empirical relationships established by Cabañas et al. (2015) between the successive IGN magnitude ($mbLg$, mb) formulas with M_W.

1.3.1.2 Time variations of seismic rate

In order to study the temporal evolution of the seismic rate during the last days of the pre-eruptive unrest and the beginning of the El Hierro eruption (6-15 October 2011), it was addressed the task of completing the located event catalog in El Hierro with additional detected events, heretofore not included, in order to estimate the true seismic release that reflects the history of the process dynamics.

The seismic rate $R = dN/dt$, where N is the number of earthquakes, and the stress change associated with dike intrusion, can be calculated using the seismicity-rate theory of Dieterich (1994), which establishes

$$R = \frac{dN}{dt} = \frac{r}{\gamma \dot{\tau}_r}; \frac{d\gamma}{dt} = \frac{1}{a\sigma}(1 - \gamma \frac{ds}{dt}) \tag{1.1}$$

where r is the background seismicity rate at the stressing rate,$\gamma\dot{\tau}_r$, σ is the normal stress acting on the fault, a is a frictional constitutive parameter, and s is the Coulomb stress. γ can be approximated to the inverse of the stressing rate prior to dike propagation (Segall 2013).

Seismicity rate was used as an estimation of the local stress changes and the seismic energy per unit of the fault area, to calculate the minimum bound of the strain field variation. The continuous seismic waveforms were reviewed, and manually picked the arrival time and ground-motion maximum amplitude of those volcano-tectonic (VT) events registered by at least five stations, which were identified by their waveform as belonging to the same local families. This procedure increased the number of events detected on El Hierro from 677 to 6,343 (an increase of more than 800%). Each detected event magnitude was computed by correcting for attenuation and spreading for distance considering the mean location of the events located at closer time.

1.3.1.3 **Characterization**

The seismic activity was characterized based on the variations in the b value of the Gutenberg-Richter distribution, and on the variations in the travel time residuals of the seismic phases on located events. Variations in the b value can identify the different time-periods where tectonic (mainly driven by the tectonic plate activity) or volcano-tectonic (driven by the volcanic activity) seismicity predominated. In addition, the temporal variations of the $P-$ (compressional) to the S- (shear) wave velocity ratio (V_P/V_S) of local earthquakes, in volcanic areas, aid the study of the properties of the medium, the existence of fluids and/or increasing/changing crack distribution, thereby identifying the volcano state and its evolution (e.g. Hong et al. 2014, Lin & Shearer 2009.

The Gutenberg-Richter (G-R) distribution power law states that,

$$\log n(M) = a - b * M \tag{1.2}$$

where $n(M)$ is the cumulative number of earthquakes of magnitude larger than M, a represents the earthquake productivity, and b describes their size distribution (Gutenberg & Richter 1944). The unknowns, a and b, were adjusted by the maximum curvature method (Aki 1965), in overlapping moving windows of 200 earthquakes each one. The completeness magnitude (above this magnitude the catalog should include all the events recorded by

the seismic network), M_C, and the maxima magnitude, $Mwmax$, were calculated in each time period window by using the ZMAP program (Wiemer 2001).

The V_P/V_S ratio can be estimated by using a modified Wadati analysis (Wadati, 1933; Jo and Hong, 2013):

$$\frac{V_P}{V_S} - 1 = \frac{T_S - T_P}{T_P} \tag{1.3}$$

where T_P and T_S are the observer P- and S-waves phase readings. From V_P/V_S the Poisson's ratio ν (is the ratio of transverse contraction strain to longitudinal extension strain in the direction of stretching force) can be calculated by using:

$$\nu = \frac{1}{2}[1 - \frac{1}{(\frac{V_P}{V_S})^2 - 1}] \tag{1.4}$$

The V_P/V_S ratio and Poisson's ratio, ν, were calculated using the phase information (P- and S-wave arrival times) of those M_W >1.7 events included in the IGN catalog, and a robust multilinear regression in non-overlapping windows with 300 earthquakes in each.

Applying Kostrov (1974), Jackson & McKenzie (1988), Stich et al. (2006) formulations (Appendix C) it is possible to calculate the permanent seismic strain (static seismic deformation in response to stress forces) from the seismic moment (which measures the size of the earthquake and is proportional to the product of the rock strength, the fault area and the amount of slip), for different ranges of time and magnitude. This manner, the contribution to the strain of the located seismicity (included in the seismic catalogue) with magnitudes above M_C, is added to the contribution of the seismicity with magnitudes below M_C (most of them not included in the seismic catalog) inferred from the b value regression of the Gutenberg-Richter distribution. This non-catalogued seismicity is relevant when large earthquakes do not dominate the deformation ($b > 1.5$).

We used the relationship established by Hanks & Kanamori (1979) between the scalar seismic moment, Mo, and Mw, $Mo = 10^{(1.5Mw+9.05)}$, and the a, b, $Mwmax$ and M_C values obtained during the GR analysis, with $Mwmin = 1.0$, Cs = 1 and $\mu = 4 * 10^{10}$Pa (Watts 1994, Watts et al. 1997). Once an approximated value for the total moment magnitude was retrieved, it was possible to estimate the contribution of the permanent seismic deformation (static deformation) to the variations in the volume from Mo, using the approximation $\Delta V = (\Sigma Mo)/\mu$ (Aki & Richards 1980, Hill et al. 2003). With this equation, ΣMo becomes proportional to the volume of the active fractures associated with the magmatic activity.

1.3.2 Analysis and characterization of the continuous seismic activity

A summary of the main methods applied in this PhD Thesis to study the seismic activity in the continuous seismic data is included below.

1.3.2.1 Time Varying Fractal Dimension

In order to study the type (e.g. seismic noise, volcano-tectonic event, low frequency, tremor) of seismic signals as well as some other interesting parameters like the geometry of the radiated wave field, and the dynamic changes with time, time varying fractal dimension analysis is performed on the continuous seismic data. As the fractal dimension parameter reflects the spectral dependence of the seismo-volcanic source, it offers a useful tool for the characterization of the different types of seismic activity (e.g. VT and tremor) recorded during an eruptive process (see Appendix C).

Time varying fractal analysis complements the traditional Fourier analysis in the study of the complexity of waveform sample signals and shows that this technique can also be applied to observational phenomena that present self-similarity across a characteristic time-scale (Higuchi 1988).

Mandelbrot (1967) introduced the concept of fractals and the term fractal dimension to determine the length of the west coast of Great Britain. Since then, fractals and self-organized criticality have been widely used to study the level of complexity of an observable including many geological and geophysical phenomena (e.g. Turcotte 2007). Mathematically, a fractal follows the relation:

$$N_i = C/(r_i^D) \tag{1.5}$$

where N_i is the number of objects with a characteristic linear dimension r_i, C is a constant of proportionality, and D is the fractal dimension. If the fractal dimension is an integer, it is equivalent to the Euclidean dimension. The Euclidian dimension of a point is zero, of a line segment one, of a square two and of a cube three (e.g. Turcotte 2007). This author showed that a curve with a single power-law spectrum is self-similar and the index, α, of the power spectral density (PSD) has a power-law spectrum dependence on frequency:

$$P(f) = f^{-\alpha} \tag{1.6}$$

that is simply related to the fractal dimension D by the equation $D = (5 - \alpha)/2$ (for a self-affine fractal $1<D<2$). The time varying fractal dimension (FD) was estimated

applying Higuchi's algorithm on the vertical component of the continuous IGN seismic stations, for different window lengths. The seismic data was previously pre-processed in order to remove bad-quality data segments, and the ground-motion retrieved correcting by instrument response.

1.3.2.2 RSAM and seismic energy

A Real-time Seismic Amplitude Measurement (RSAM) analysis is performed to study the contribution of the continuous seismic sources (micro-seismicity, volcanic tremor or swarms of volcano-tectonic events) to the seismic data acquired during El Hierro unrest.

The RSAM (Endo & Murray 1991) is defined by:

$$RSAM = \frac{\sum_{i=1}^{3} \mid A_i - \bar{A} \mid}{n} \tag{1.7}$$

where A_i, is the signal amplitude corrected by the instrument response and the geometric and anaelastic attenuation occurred from the hypocentre to the station; $\bar{A}$ is the mean amplitude in the calculation window and n is the number of samples in the window. The RSAM was calculated on the broad-band CTIG seismic station applying different band filters (CTIG was the only station with a flat instrumental response in the whole frequency spectra that recorded the seismic activity from the beginning to the end of the unrest). The contribution of the different sources were separated by applying frequency bands filters to the continuous data: 1-3 Hz for tremor, low frequency events (LF), hybrids and medium magnitude volcano-tectonic events (VT); 3-15 Hz for small VT; and 15-30 and 30-50 Hz for very small and micro-seismic events, as per the classification in Wassermann (2012), correcting by instrument response, spreading and attenuation. P-wave RSAM was computed using the vertical component, and S-wave RSAM using the average sum of the NS and EW components. From the RSAM calculated on the S- and P-waves it was straightforward the computation of the ratio between the energy in the S- and P- radiated fields, Es/Ep, providing valuable information about the dominant fracturing type associated with the emplacement and migration of the magma.

1.3.3 Analysis and characterization of the surface deformation

1.3.3.1 GPS 3D coordinate time series

3D coordinate time series analysis is performed to study the variations of the regional stress field. Those permanent GPS stations with longest continuous dataset deployed in the stud-

ied area were used in order to retrieve slow deformation. The selected sites ranged from the Azores to the west (PDEL on San Miguel), the Iberian Peninsula (CASC in Cascaes, Portugal, VILL in Villafranca, and SFER in San Fernando, Spain) to the north, Morocco (RABT in Rabat) to the east, and the Canary Islands (LPAL on La Palma and MAS1 on Gran Canaria) to the south. GPS data was processed obtaining homogeneous coordinate time-series. 3D coordinates were computed from the first reprocessing set offered by EPN (EUREF Permanent Network, where EUREF stands for International Association of Geodesy Reference Frame Sub-Commission for Europe), that is called EPN-Repro 1 (http://epn-repro.bek.badw.de/) that covers the period from 1996 to the end of 2006. From January 2007 onwards, EPN routine solutions were used. These solutions are in two different realizations of the International Terrestrial Reference Frame (ITRF): ITRF2000 (Altamimi et al. 2002) until April 2011, when the reference frame was changed to ITRF2008 (Altamimi et al. 2011) in use up to the end of 2014. Weekly time series for the selected sites were used and removed offsets that might affect the results and their interpretation. The magnitude of these offsets in case of known origin was computed and corrected (e.g. equipment and frame changes).

The deformation time series were provided by the IGN Volcano Monitoring Service (García-Cañada et al. 2014), that computes daily 3D coordinates solutions in each one of the GPS stations. The local GPS network in El Hierro, during the unrest episode, included up to six GPS stations (IGN stations: HI01, HI02, HI03, HI04, HI05; Canarian Government station: FRON), allowing the calculation of daily solutions. The GPS data was processed using Bernese software (Dach et al., 2015) in the ITRF2008 reference frame and a network of more than 30 GPS stations located in the Canary Islands, Azores, north of Africa, and south of Spain. Precise satellite orbits and absolute antenna phase center models from IGS, along ocean-loading model FES2004, were applied (García-Cañada et al. 2014).

1.3.4 Modeling

1.3.4.1 Deformation source pressure model

Three-dimensional displacements and their associated errors were calculated for each selected time period and inverted using the dMODELS software package (Battaglia et al. 2013), which uses a nonlinear inversion algorithm to determine the best fit parameters (i.e., location, depth, and volume change) for the deformation source (Benito-Saz et al. 2017).

The spherical point source pressure model was used within an elastic, isotropic, and homogeneous half-space (Mogi 1958) with Poisson's ratio ν = 0.25 and shear modulus of 40 GPa (Watts 1994, Watts et al. 1997). To assess the uncertainty of the source model parameters, an empirical bootstrap method was applied 1,000 times to estimate 95% confidence intervals (Efron & Tibshirani 1986).

1.3.4.2 **Coulomb stress and strain changes**

The static stress changes caused by the static displacement associated with the modeled pressure sources, can be calculated in an elastic half-space approximation with uniform isotropic elastic properties, following Okada (1992) formulation and the Coulomb 3.3 software (Lin & Stein 2004, Toda et al. 2005). The shear and normal components of this Coulomb change can be computed on specific faults (receiver fault planes) or on a 3D grid (Lin & Stein 2004, Okada 1992, Toda et al. 2005). For the modeling, a Young modulus E = 100 GPa and a Poisson's ratio ν = 0.25 were used. The regional stress field (vertical component, maximum and minimum horizontal components) was modeled by using the information derived from the World Stress Map (Heidbach et al. 2008), the neotectonic modeling of the stress field proposed by Jiménez-Munt et al. (2001), and existing focal mechanism solutions ($\sigma_V = 250$ bar/km, $\sigma_H = 300$ bar (160°N) and $\sigma_h = 75$ bar (70°N)). The directions of the horizontal components are in agreement with the modeled stress field for the Canary Islands (Geyer et al. 2016).

God always geometrizes.

Plato

CHAPTER

2

Results

In the following pages, a review of the main results obtained in the papers is conducted, in accordance wih a temporal sequence of different stages. First stage includes results of the very early signs of unrest, detected from 2003 onwards through the analysis of the regional (from Atlantic Ridge to South the Iberian Peninsula, and from the Canaries to the Azores-Gibraltar fault) seismic catalog and from those permanent GPS stations located in the region with longest dataset. The second stage includes results of the pre-eruptive activity recorded by the seismic and geodetic stations located in El Hierro from 19 July to 10 October, 2011. The third stage includes results of the pre- and eruptive activity recorded during 6-15 October 2011, on El Hierro.

2.1 Temporal sequence of evidence

2.1.1 Early signs: 1996-2011

The results of regional analysis performed with the compiled new regional seismic catalog and the 3D GPS coordinates series processed for the 1996-2011 time period are presented. Figure 2.1 shows the geographical distribution of the seismicity located in the whole area ($M_W > 3.0$), which follows the known tectonic features. Shallow (depth < 40 km) seismicity is recognized in MAR-ATJ and ATSM and intermediate (40 km $\leq$ depth < 70 km) seismicity in GB, BALB and ATL. (Cunha et al. 2012) interpreted this intermediate seismicity as related to the shortening and wrenching between northern Algeria-Morocco and southern Spain, and between NW Morocco and SW Iberia. This convergence would be accommodated along NNE-SSW to NE-SW and ENE-WSW thrust faults and WNW-ESE right-lateral strike-slip faults releasing intermediate earthquakes (Cunha et al. 2012, Rosas et al. 2012, Terrinha et al. 2009). Besides, intermediate seismicity in the Canaries and in Madeira Islands is found. The temporal (in each area) and the spatial evolution (in a mesh)

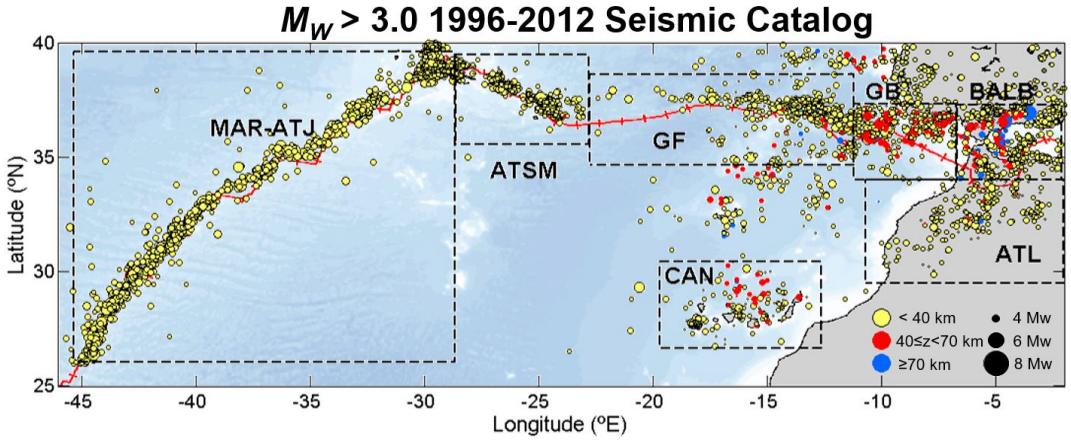

Figure 2.1: $M_W > 3.0$ earthquake distribution in 1996-2012.Bathymetry and topography from the National Geophysical Data Centre (NOAA). Dashed rectangles mark the boundaries of the different areas included in the regional study.

of the magnitude of completeness, M_C is studied to perform comparison of the seismic energy released by the activity in each one of the different regions. This study allows to establish the completeness magnitude threshold and the homogeneous calculation of the temporal variations of the seismic energy using those events with magnitude $M_W \geq M_C$ in each region. Figure 2.2 summarizes the time evolution of the released seismic energy

for all the regions. Each curve depicts the accumulated elastic energy, E_S, for those earthquakes with magnitude above the magnitude of completeness. E_S was computed using an empirical regression with the scalar seismic moment, M_0.

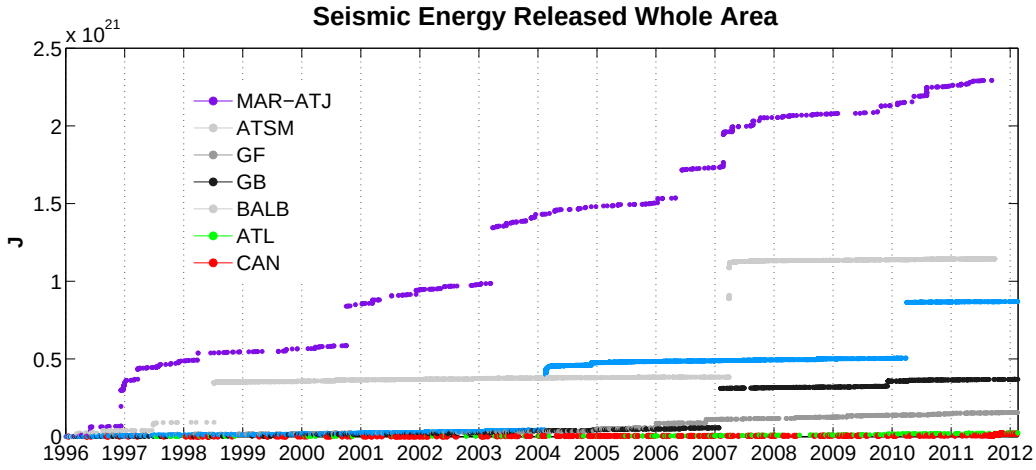

Figure 2.2: 1996-2012 comparative analysis of the accumulated seismic energy released for events with $M_W \geq M_C$ in each one of the seven areas (MAR-ATJ, $M_W \geq 4$; ATSM, $M_W \geq 2.7$; GF, $M_W \geq 3$; GB, $M_W \geq 2.9$; BALB, $M_W \geq 2.9$; ATL, $M_W \geq 2.6$; and CAN, $M_W \geq 2.7$).

A comparison between the Canaries and the surrounding areas is included in Figure 2.3, showing the evolution of the earthquake occurrence in the Canary Islands, the Atlas, the Gloria Fault and the Gorringe Bank regions.

As the global magnitude of completeness in the Canaries is rather high as consequence of the later installation of a dense seismic network, detected events are manually picked in the seismic waveform on the CHIE stations, that is the station with longer recording of continuous data in El Hierro. The lower part of Figure 2.4 consists of an histogram of the local seismicity detected by the CHIE seismic station on El Hierro (Canary Islands).

Results shows that tectonics seems to be dominated by the occurrence of the strongest events, being MAR-ATJ the area that released the maximum of seismic energy in this time period with a fairly regular pattern. Besides the known and expected seismic activity, some changes can be recognized in the trend and in the rate of the seismicity: ATSM shows an increased seismicity in 1998 associated with the Serreta (Azores) submarine eruption; a fairly general (excepting MAR-ATJ) increase in the activity can be recognized in ATSM, BALB, CAN, ATL, GF and GB series from 2003 onwards; seismic activity on the Canary

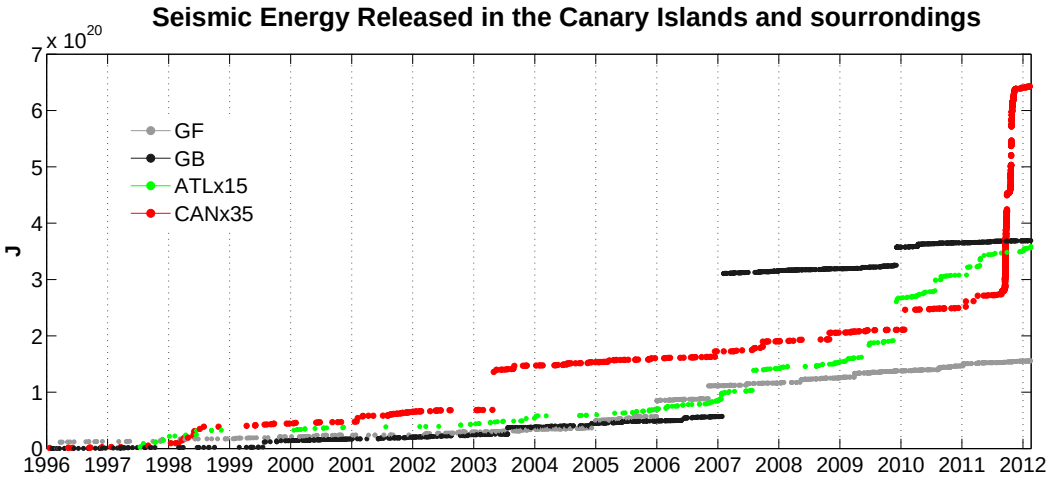

Figure 2.3: 1996-2012 comparative analysis of the accumulated seismic energy released for those events with $M_W \geq M_C$ located in in GF, $M_W \geq 3$; GB, $M_W \geq 2.9$; ATL, $M_W \geq 2.6$; and CAN, $M_W \geq 2.7$.

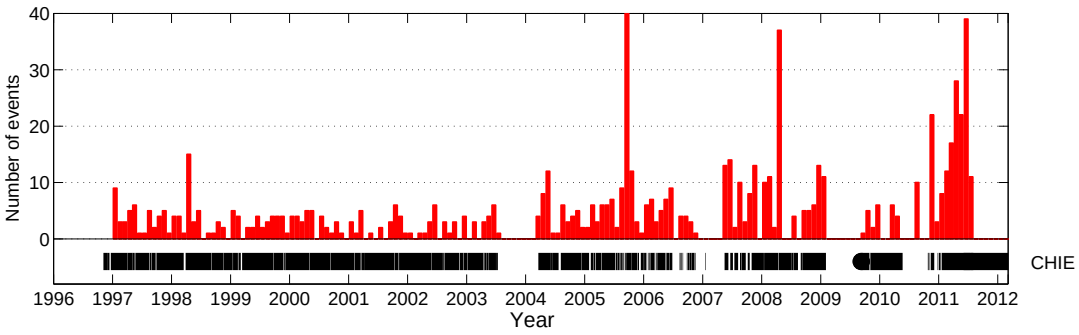

Figure 2.4: Monthly event histogram (red bars) registered at the CHIE seismic station on El Hierro. Black bars indicate the availability of the station data.

Islands and in the Atlas Mountain increased from 2003 and was followed by a further increase around 2007. Activity in the Canaries experienced a further acceleration at the beginning of 2011, which lasted until the onset of the submarine El Hierro volcanic eruption in October 2011. Most of the series (BALB, ATSM and GB) experienced increments in 2003-2004 or 2007-2008.

In relation with the surface deformation, Figure 2.5 shows the 3D (north, east, vertical) time series from the PDEL, LPAL, MAS1, CASC, RABT, and SFER GPS stations in relation to the VILL station. The errors in the time series correspond to the formal errors

computed during the data processing, which underestimated the true uncertainty given that a large number of systematic errors and mis-modeled parameters were not included. In

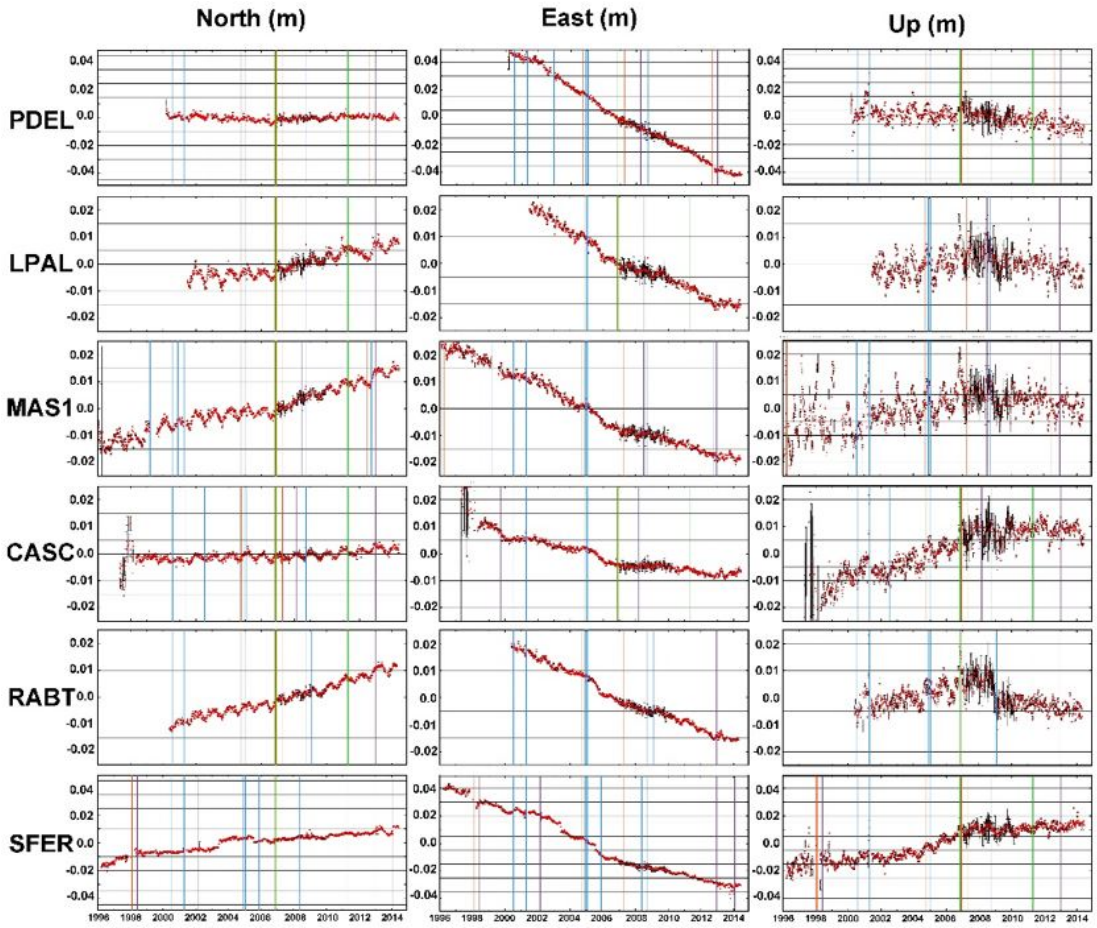

Figure 2.5: Residuals of the PDEL, LPAL, MAS1, CASC, RABT, and SFER GPS weekly coordinate series in relation to the VILL GPS station (after the removal of the offsets), marked with vertical lines (purple: both antenna and receiver changed; red: only antenna changed; blue: only receiver changed; green: reference system changed). Note that the vertical scale is double for the PDEL and SFER stations.

almost all the stations can be recognized concurrent changes in trend. In order to quantify these changes, the accumulated deformation in time periods for the horizontal and vertical components are calculated.

Figure 2.6 reflects the deformation history and the velocity evolution (horizontal and vertical vectors) calculated from the GPS series shown above, with the VILL station (European Plate) (an equivalent study respecting the RABT station (African Plate) as the reference

station is included in Annexe A). Some GPS stations are located either on the Eurasian

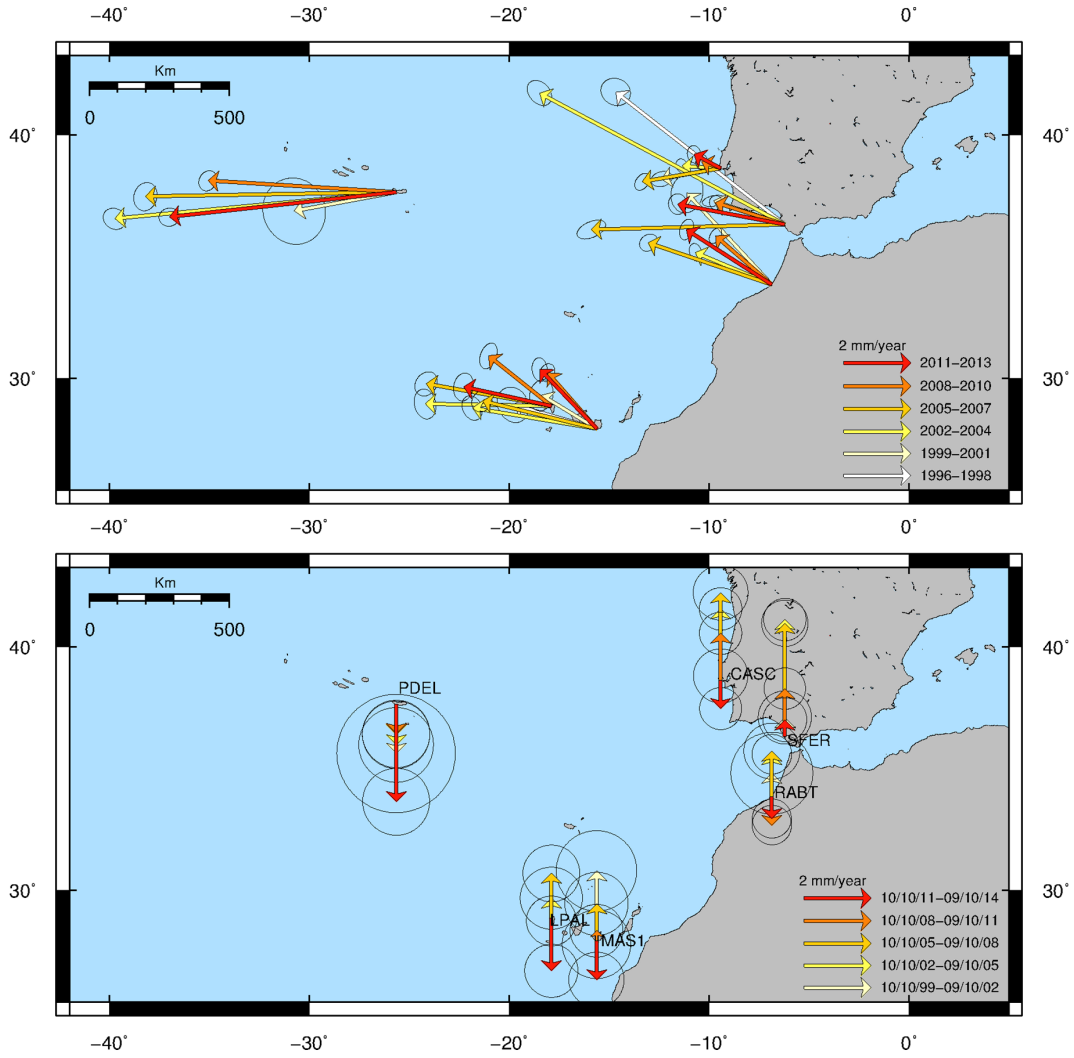

Figure 2.6: GPS velocity field (horizontal and vertical vectors) in relation to the VILL station (European Plate). For the period 10 October 1996-09 October 1999, the vertical velocity vector is excluded for the MAS1 station due to the high scattering of the vertical component.

or African Plates, but others do not belong clearly to any of the two plates but some of them are not so clearly aligned with any of them (e.g. SFER, Fernandes et al. 2007), so it is necessary to compute all the time series relative to a reference station in each one of the plates, in order to isolate the local deformations. Each vector represents the estimated velocity at each station for every three years, computed from the weekly coordinate

time-series using CATS software (Williams 2008) and taking into account annual and semi-annual periodic variations. The last vector (in red) begins on the same day as the onset of the submarine eruption on El Hierro on 10 October 2011. The data error is proportional to the size of the error ellipse and is plotted at the same scale as the deformation vector (see legend). During the period 10 October 2002-09 October 2005 the horizontal deformation showed (referenced to the VILL station) a counterclockwise rotation over a wide area (LPAL, $drift = 53^{\circ}$ SW; MAS1, $drift = 54^{\circ}$ SW; RABT, $drift = 25^{\circ}$ SW, yellow vector in Figure 2.6A), coinciding with the abrupt westwards jump recorded at the SFER station. SFER station shows several changes in the magnitude of the horizontal components but not any rotation. Thereafter, the stress field gradually reverted to steady compressive NW-SE behavior (see A and B), while the vertical deformation component continued to increase, firstly at the RABT station and subsequently at the LPAL and MAS1 stations, until the onset of the eruption (see C and D). PDEL station (Azores) did not present any change in horizontal or vertical components.

The time varying fractal dimension analysis is applied to the permanent seismic stations (CHIE on El Hierro and CCAN on Tenerife, both equipped with short-period, vertical component seismometers), and results are shown in Figure 2.7. The end time of the studied period is spammed in order to show the registered local activity associated with the post-eruption phase in El Hierro. FD evolution was estimated using the Higuchi (1988) algorithm on the vertical component. Each FD point corresponds to a 12 hour window of the ground-motion seismic signal with no window overlapping. Seismic data was pre-processed in order to remove bad-quality data segments and the ground-motion was retrieved correcting by the corresponding instrument response.

Before 2003, the FD showed cyclic variations with a mean value of $FD \geq 1.4$ for both stations and no predominant notable trends. From 2004 onwards, however, it decreased to values $DF \sim$1.1-1.2. The FD decreased more from January 2011 to the end on the unrest phase. During the eruption on El Hierro (October 2011-March 2012), reached its lowest values of $FD \sim 1$. Besides, the relative deformation between two GPS stations (LPAL on La Palma and MAS1 on Gran Canaria) is computed on the Canary Islands with the longest continuous (> 10 years) data series.

The 3D differential coordinates time series (LPAL minus MAS1) for the GPS stations are shown in Figure 2.8. The end time of the studied period is also spammed in order to show the registered local activity associated with the post-eruption phase in El Hierro. The

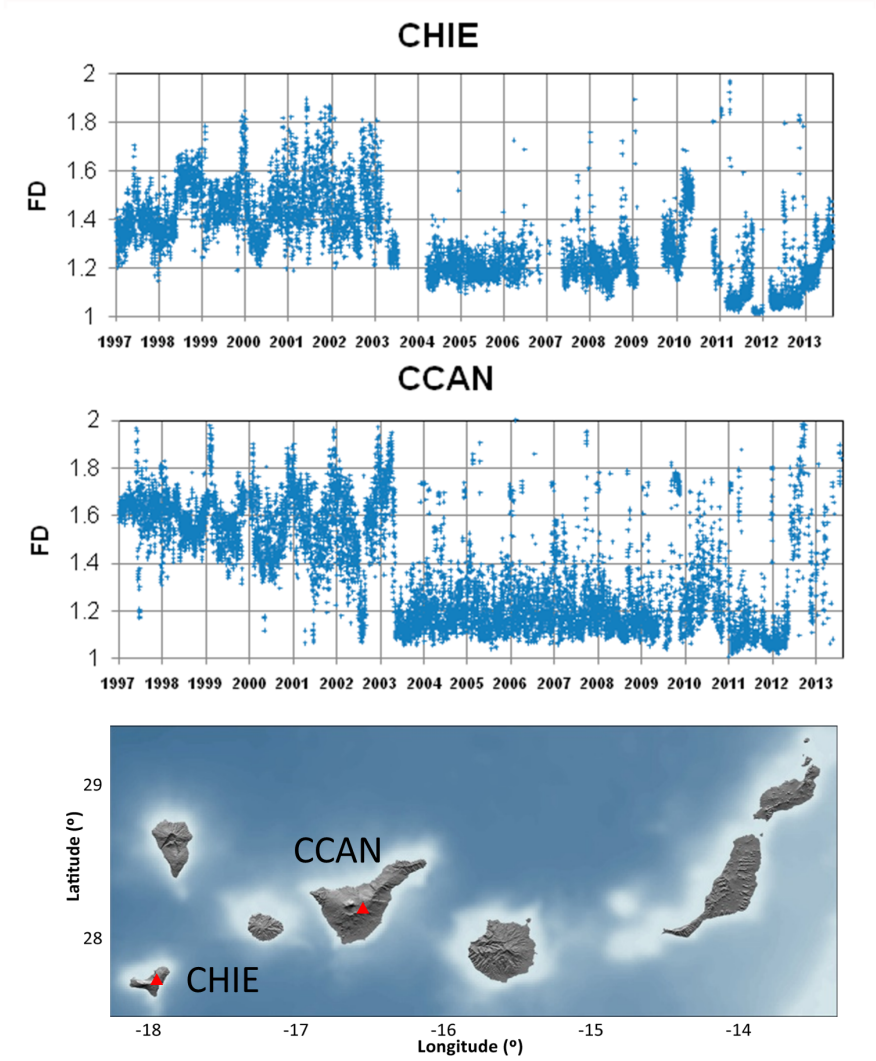

Figure 2.7: Time varying fractal dimensions FD at the stations on CHIE (El Hierro) and CCAN (Tenerife). Gaps in data are due to the lack of station availability.

deformation showed a tendency to shorten northwards and lengthen westwards, showing an extension between the stations in the E-W direction, from 2003 onwards; as well, there was a positive northward deformation episode starting in January 2011, observed more clearly from July 2011 onwards that coincided with the beginning of the pre-eruptive unrest on El Hierro. With the onset of the submarine eruption in October 2011, the northward deformation was quickly inverted.

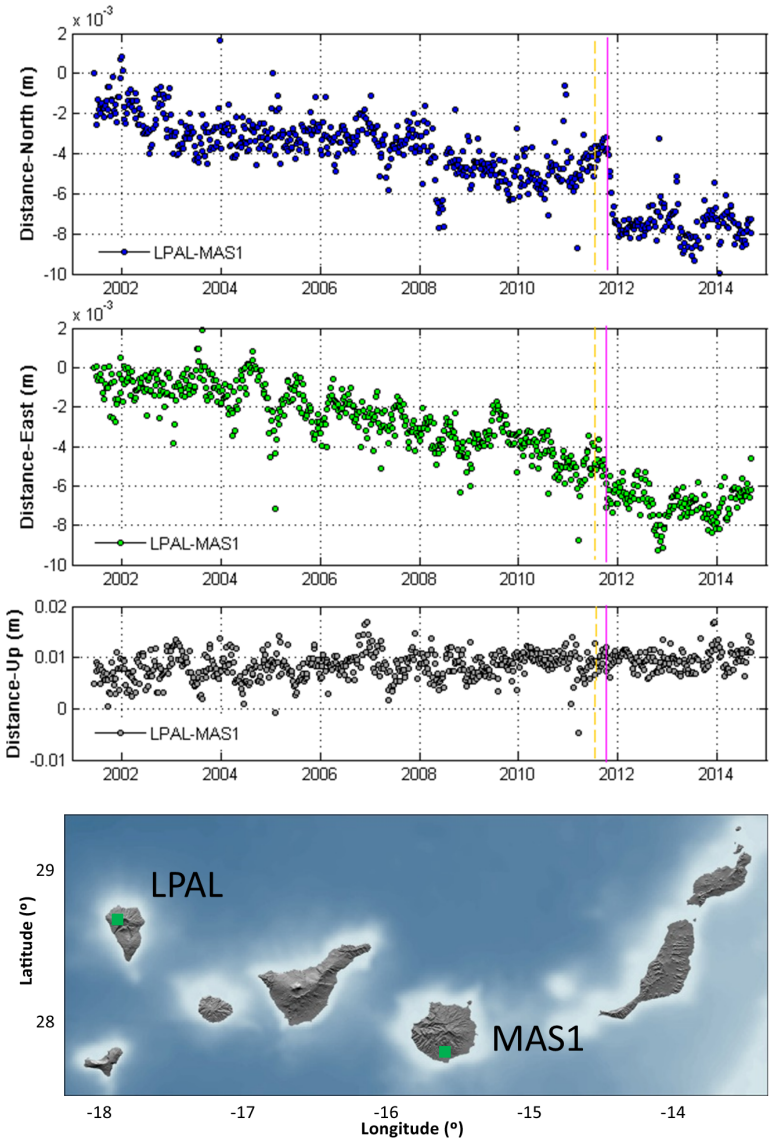

Figure 2.8: Time evolution of a three-component (north, east, upward) LPAL–MAS1 deformation.

2.1.2 Pre-eruptive unrest signs: July-October, 2011

In the following pages, the results of the analysis of the pre-eruptive activity registered by the seismic and geodetic stations located on El Hierro from 19 July to 10 October 2011, are presented. The seismic activity was registered by a total of 9 seismic stations (see Figure 2.9). Different time periods are distinguished attending to differences in rate, magnitude, depth, location and focal mechanism. The seismic activity began inland in the central-western area, and consisted of an almost-two-month period of low magnitude earthquakes, from 19 July to 8 September 2011.

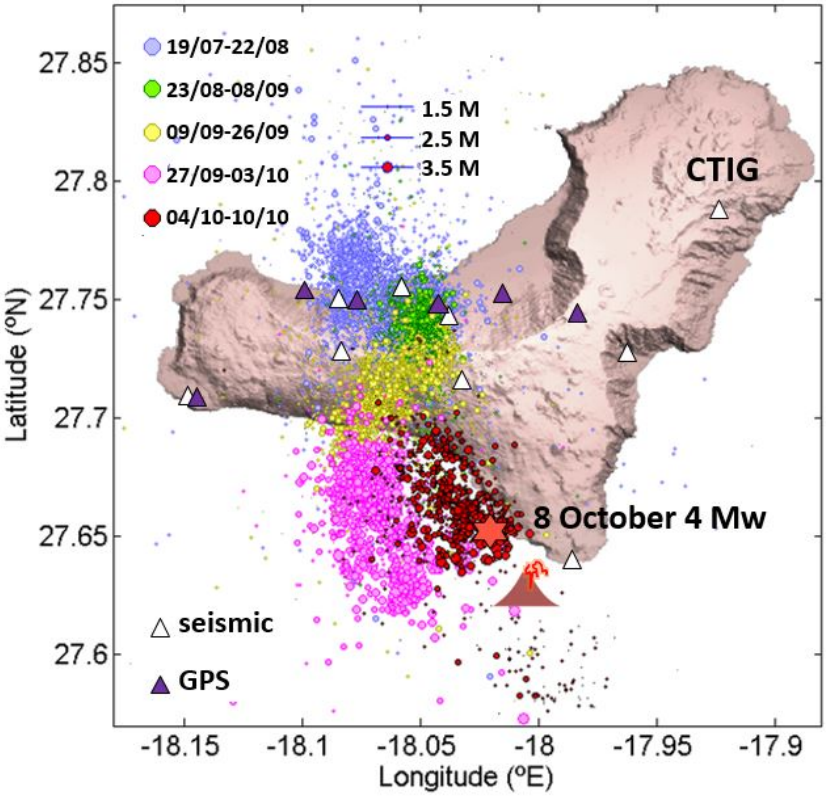

Figure 2.9: Seismicity located on El Hierro during the unrest for different time periods (purple: 19 July–22 August, green: 23 August–8 September, yellow: 9–26 September, pink: 27 September–3 October, red: 4–10 October). Seismic stations are represented by white triangles and GPS stations by black ones.

During this period, events clustered to the northwest and southeast of the first recorded activity, as highlighted by a precise double-difference relocation study that used data from 3,500 (out of a total of 10,000 events) local earthquakes registered during the unrest

(Cerdeña et al. 2014). During 9-26 September and 27 September-3 October a seismic migration is observed, being seismicity located southwards rather than the previous one with increasing magnitudes. Between 3-10 October a high magnitude sparse seismicity was located. In Figure 2.10 the evolution of the hypocentral coordinates, the magnitude values and the double-couple focal mechanism solutions of those $M_W \geq 3.5$ events located during the unrest, all registered on 27 September–9 October are shown.

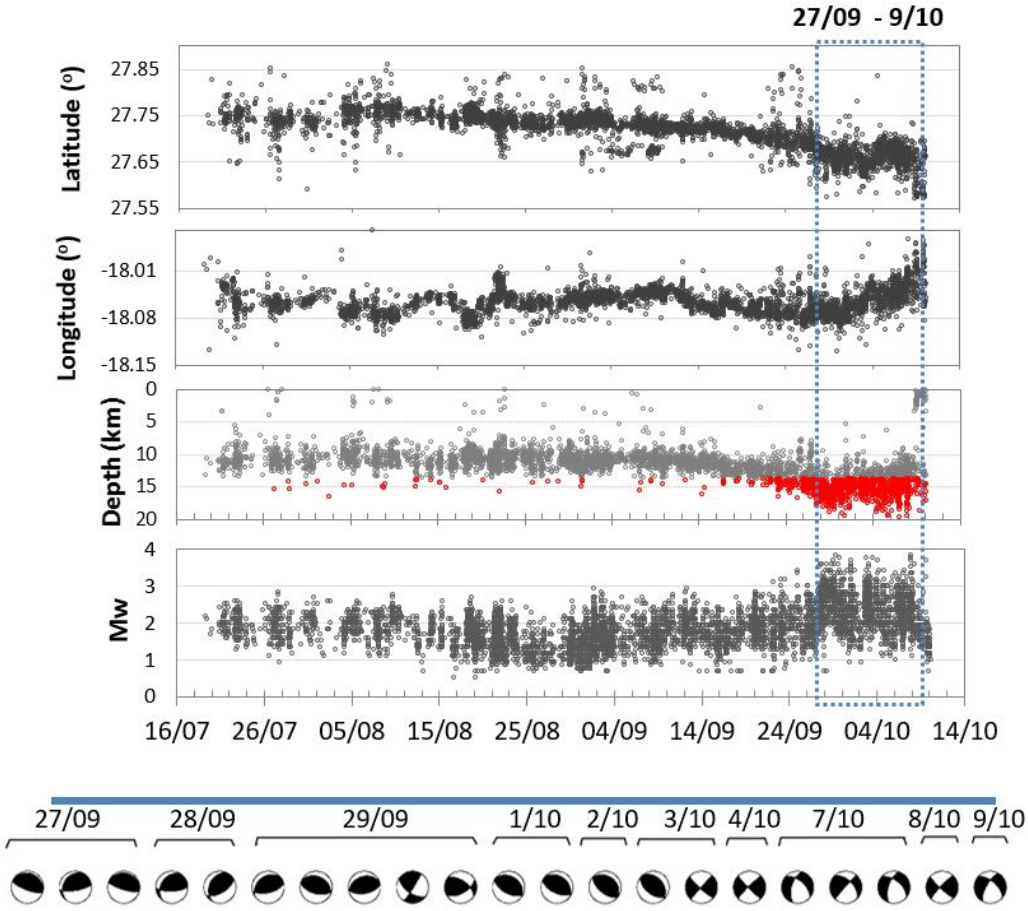

Figure 2.10: Evolution of the latitude, longitude, depth coordinates and magnitude, of the seismicity occurring from 19 July to 10 October 2011. At the bottom, double-couple focal mechanism solutions of those $M_W \geq 3.5$ events (Del Fresno 2016) are shown.

Figure 2.11 includes results of the seismic characterizations, showing the time evolution of the b, $M_W max$, M_{WC} parameters, the time evolution of the earthquake location on a N-S projection, the time fluctuations of the Vp/Vs ratio and the Poisson's ratio curve.

Variation in M_{WC} with time is readily recognized, especially during the intense seismic

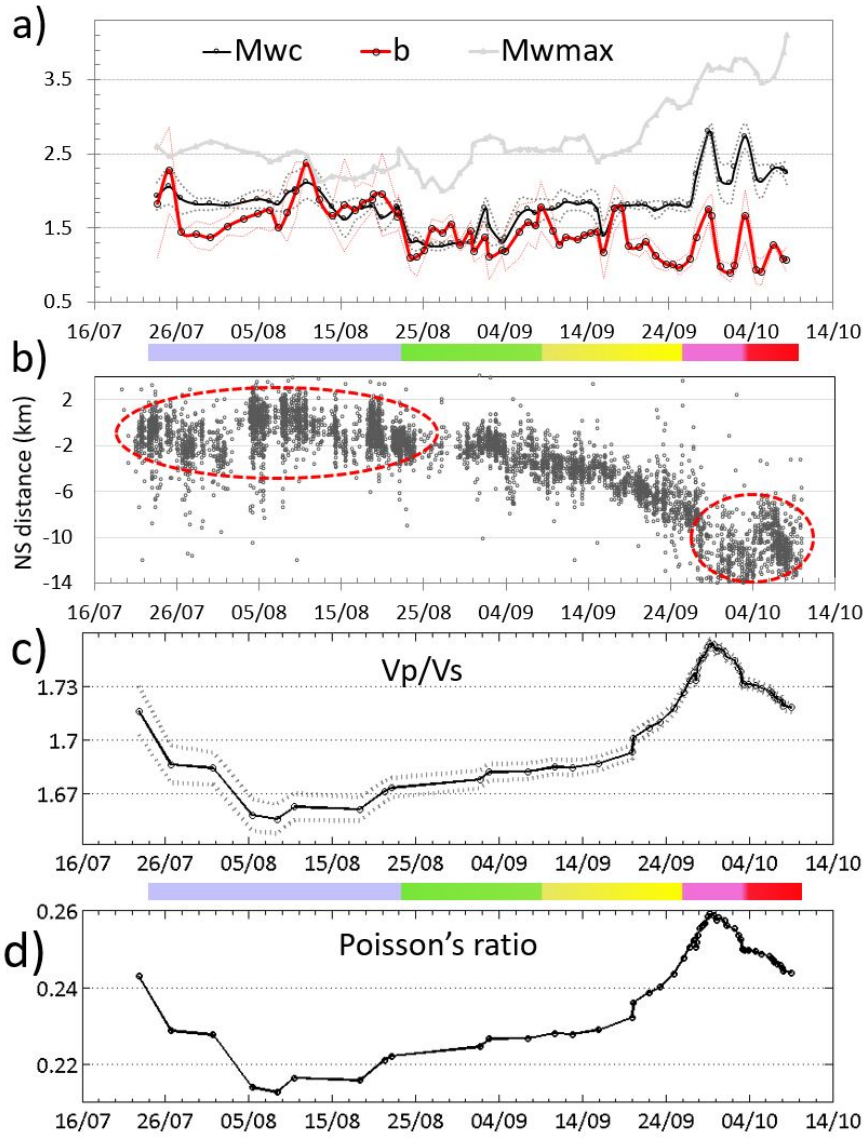

Figure 2.11: Main features of the located seismicity during the unrest, a) Time evolution of the $M_W max$, M_C and b parameters. b) N-S growth distance of the seismic events from (19/08) to the final location coordinate (10/10) after 82 days of activity. c) Vp/Vs ratio evolution and error bounds, d) Poisson's ratio evolution. Scale bar intervals: purple, 19 July–22 August; green, 23 August–8 September; yellow, 9–26 September; pink, 27 September–3 October; red, 4–10 October.

swarm episodes registered during the two weeks before the onset of the eruption.

During seismic swarms most of the seismic waveforms were partially overlapping,

thereby making the phase detection and separation of the earthquakes difficult or even impossible. The incompleteness of the IGN catalog motivated us to use an approximate method to quantify the contribution of the non-located seismicity that was not included in the seismic catalog (See Appendix C). Figure 2.12 shows results of the total seismic strain time evolution, corresponding to the located and non-located seismic events. The ground

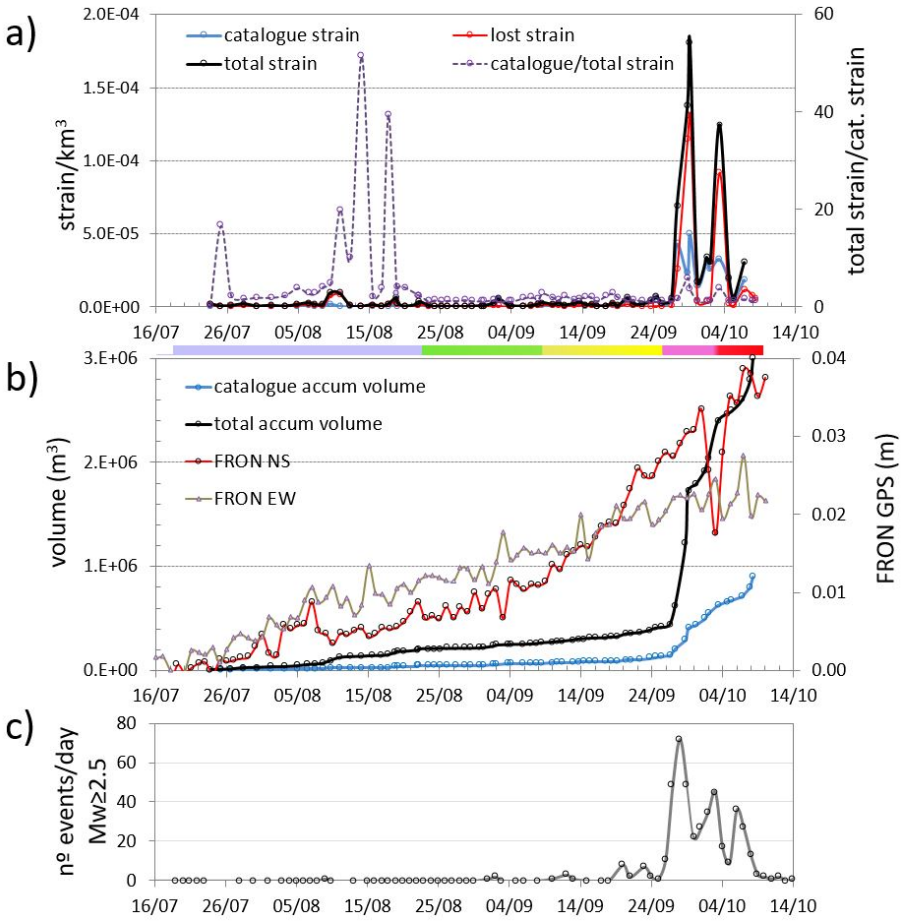

Figure 2.12: Strain analysis during the 2011 unrest. a) Seismic strain of the located events above M_{WC} (blue), below M_{WC} (red), the sum of both (black) and rate of located strain to total strain (purple). b) Contribution to the volume of the events above M_{WC} (blue), total contribution from located and no located (black) and horizontal (NS and EW) series from FRON GPS station. c) Number of $M_W \geq 2.5$ events/day. Scale bar as in previous figure.

surface deformation recorded by the GPS network is also analyzed and modeled. Figure 2.13 shows the point source pressure solutions corresponding to different time periods, selected to ensure that the resolution on the displacement measurements was sufficient, to

minimize inversion errors, and to replicate, as closely as possible, the periods used in the seismic analyses.

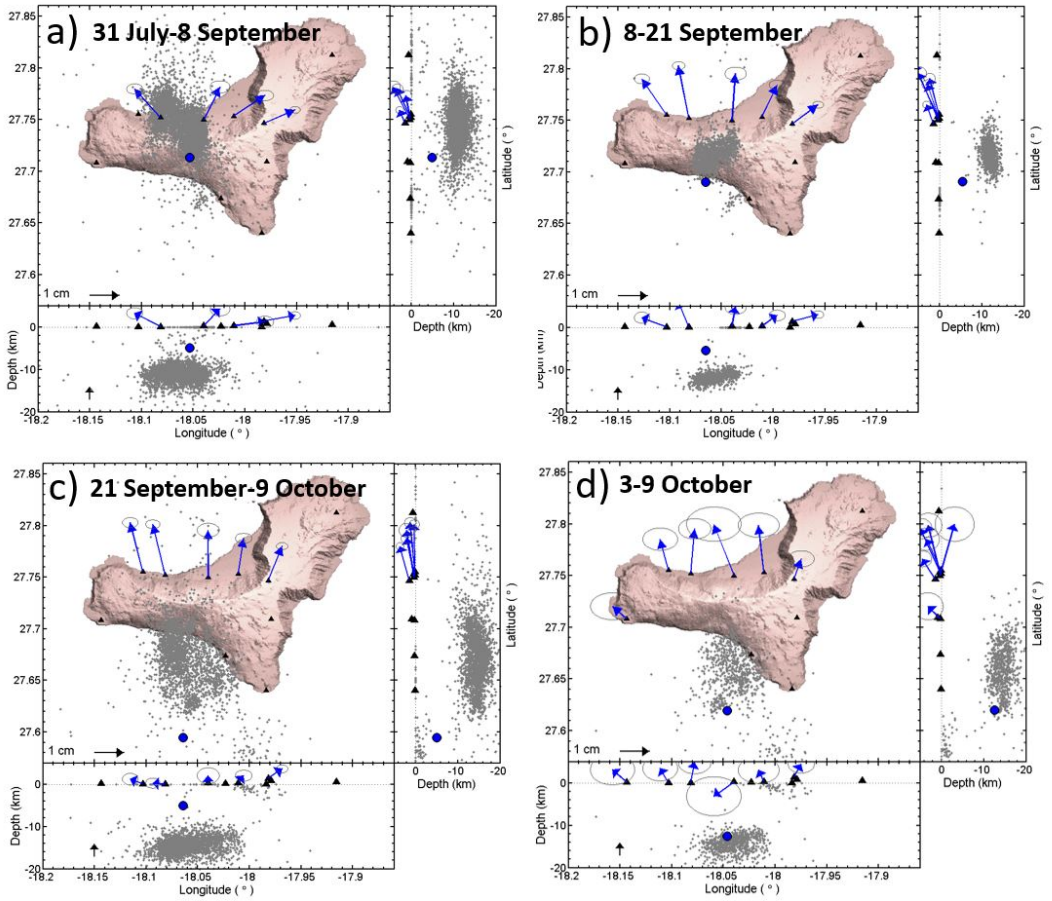

Figure 2.13: Location and depth of the sphere point pressure deformation sources for the selected time periods. GPS displacements are represented with blue arrows. a) 31 July-8 September. b) 9-21 September. c) 22 September-9 October. d) 3-9 October. GPS displacements are represented with blue arrows, and the located seismicity with grey points. Right and bottom panels show the depth of the models and the seismicity as well as the vertical GPS displacements.

As only four-to-six GPS stations were operating during these time periods, and given that most of them were located in the northern part of El Hierro, the most basic and simplest deformation source model (Mogi's point source) is performed. Therefore, we should consider the results simply as a first approximation of the deformation source, useful only to track and evaluate the evolution of the magma (volume change and position) during the

unrest. The results are summarized in Table2.1, (lower and upper limits of the 95% confidence intervals obtained by bootstrapping techniques are included in Table1, Appendix B) and includes the location, depth, volume change and chi square per degrees of freedom ($\chi^{2\nu}$) for each one of the point pressure sources.

Period	**Lat°N**	**Lon°E**	**Z km**	**Vol** km^3	$\chi^{2\nu}$
07-31/09-08	27.713	-18.053	4.9	0.004	4.7
09-08/09-21	27.690	-18.065	5.4	0.008	5.4
09-21/10-09	27.595	-18.064	5.1	0.026	6.0
10-03/10-09	27.620	-18.047	12.6	0.027	4.8

Table 2.1: Optimal point pressure source model (location, depth, volume and $\chi^{2\nu}$) for different time periods.

Using the Mogi's source corresponding to the 3-10 October, the Coulomb static stress changes are modeled (Figure 2.14) on the specific faults corresponding to the 4.0 M_W, 8 October plane solution (295°strike; 40°dip; 164°rake) (Del Fresno et al. 2015)

Seismic and geodetic analyses provided concurrent results. During 19 July-22 August, low magnitude ($< 2.5M_W$) seismic events were located in clusters in the center-north of the island at a stable range of depths (8-12 km). Seismicity showed a bi-directionally growth and $b > 1.5$ while Vp/Vs ratio decreased until reaching a value of ~ 1.66 ($\nu = 0.21$). During this first period, the contribution of the micro-seismicity was notable, as shown in RSAM at 15-30 and 30-50 Hz bands and in the high amount of non-located events reflected in the total to catalog strain ratio (See Figure 2.15).

During 23 August-8 September, seismicity continued to be located in the center-north, while b decreased slightly, fluctuating around 1.5, and Vp/Vs ratio increased to ~ 1.68 ($\nu = 0.23$). The most characteristic feature of this period is the beginning of a clear unidirectional migration of the seismicity towards the South. Modeling of the first and second periods of deformation registered by the GPS stations, that have been analyzed together, provides a source center of 0.0039 km^3.

From 9-26 September, seismicity continued its migration towards the South that lasted until 27 September, and b decreased to $b = 1$. At the end of this period (from 14-15 September to 26 September), maximum depth increased being > 15 km with the consequent Vp/Vs increasing.

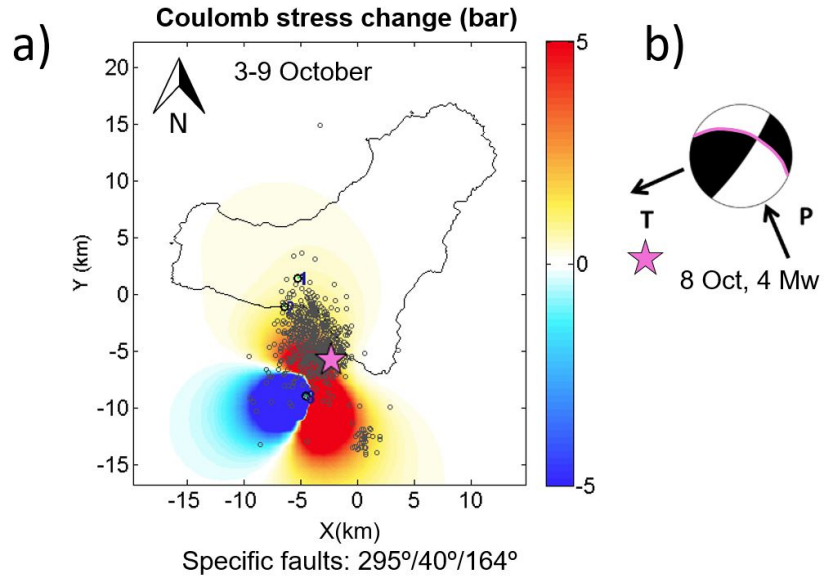

Figure 2.14: Triggered seismicity in pre-existent faults. a) Coulomb stress change (bar) distribution on (295°strike, 40°dip, 164°rake) faults at 12 km depth. We superposed the seismicity located during that time period between 10 and 20 km depth. b) Focal mechanism solution of the 4.0 M_W, 8 October event (star in pink).

Modeling of the GPS data provides a source center with a volume of 0.0079 km^3.

From 27 September to 3 October, the nature of activity varied and there were minimum $b \sim 1$, a maximum depth of the located seismic events, increased seismic rates and higher magnitudes. Although the depth range remained stable (12-16 km), Poisson's ratio changed with time (including its maximum value and a reversion in growth). The main fracturing mechanism from 27 September onwards alternated between intense wide pulses of shear fracturing and short episodes of tensile mechanism. The seismic strain registered its highest values ever.

This intense deformation occurred in two pulses (27–30 September and 2–5 October) and was registered by the seismic and the GPS network. Figure 2.16 shows the North-South time series of the GPS and the seismic strain. Of note are the coincidence between the coherent oscillation in the NS component and the seismic strain pulse (2–5 October) with maximum on 3 October, and the change in the focal mechanism from thrust fracturing to strike-slip that occurred on that date (upper panel on Figure 2.16).

From 3 to 10 October, Vp/Vs decreased continuously (beginning on 30 September), the seismic strain decreased in relation to the previous days, and the GPS stations registered

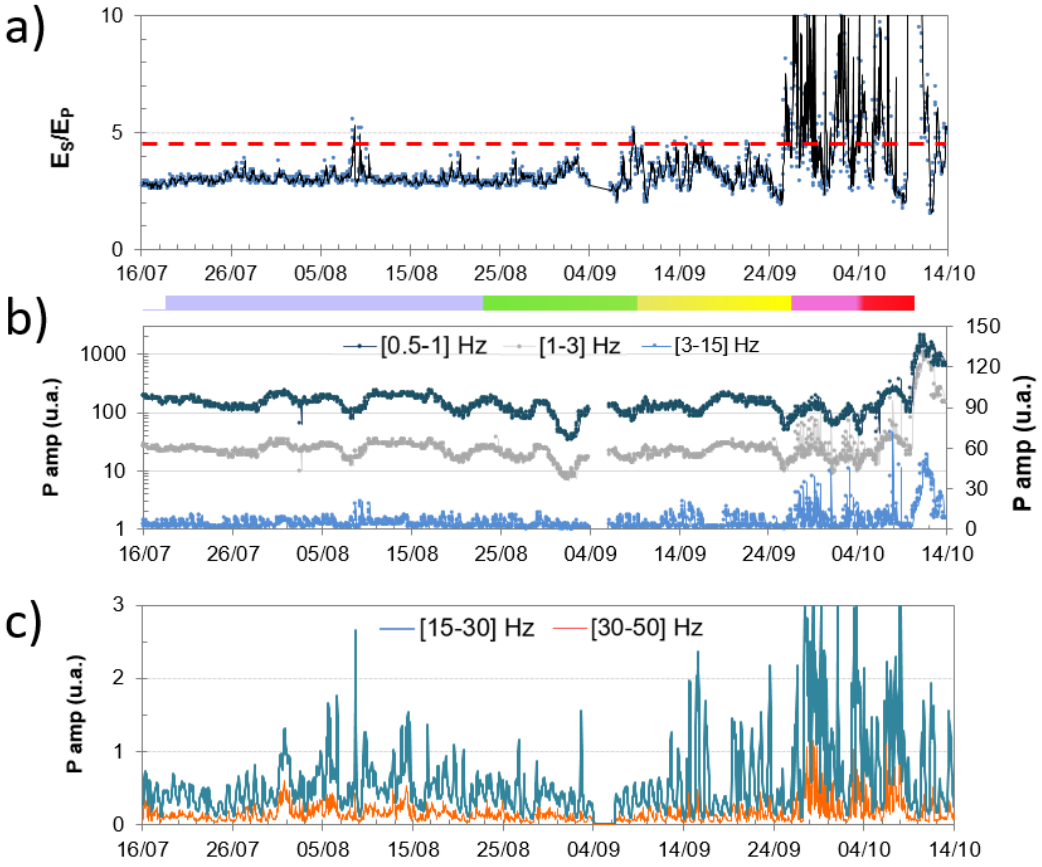

Figure 2.15: RSAM and tensile/shear type of fracturing analyses. a) ES/EP time evolution. RSAM plots in P-wave amplitude of the CTIG station for different frequency bands: b) 0.5–1, 1–3 and 3–15 Hz and c) and 15–30, 30–50 Hz. Scale bar intervals as in previous figure.

the highest deformation rate (due to the anomalous behavior of coordinates around 3 October, following the trend the rest of the days), modeling a source center of 0.027 km^3.

In all the periods, the modeled pressure centers were always shallower than the seismicity and laid slightly further to the south in the direction of the seismic migration. This bias could be partially caused by intrinsic errors due to model simplification and the sparse GPS data used for the inversion. Another possible reason for these differences (Traversa et al. 2010) is that the seismicity accompanying dyke propagation in basaltic volcanoes represents events located backwards with respect to the dyke tip position. In this case, the seismicity is not only related to the magma propagation but also to the response of the

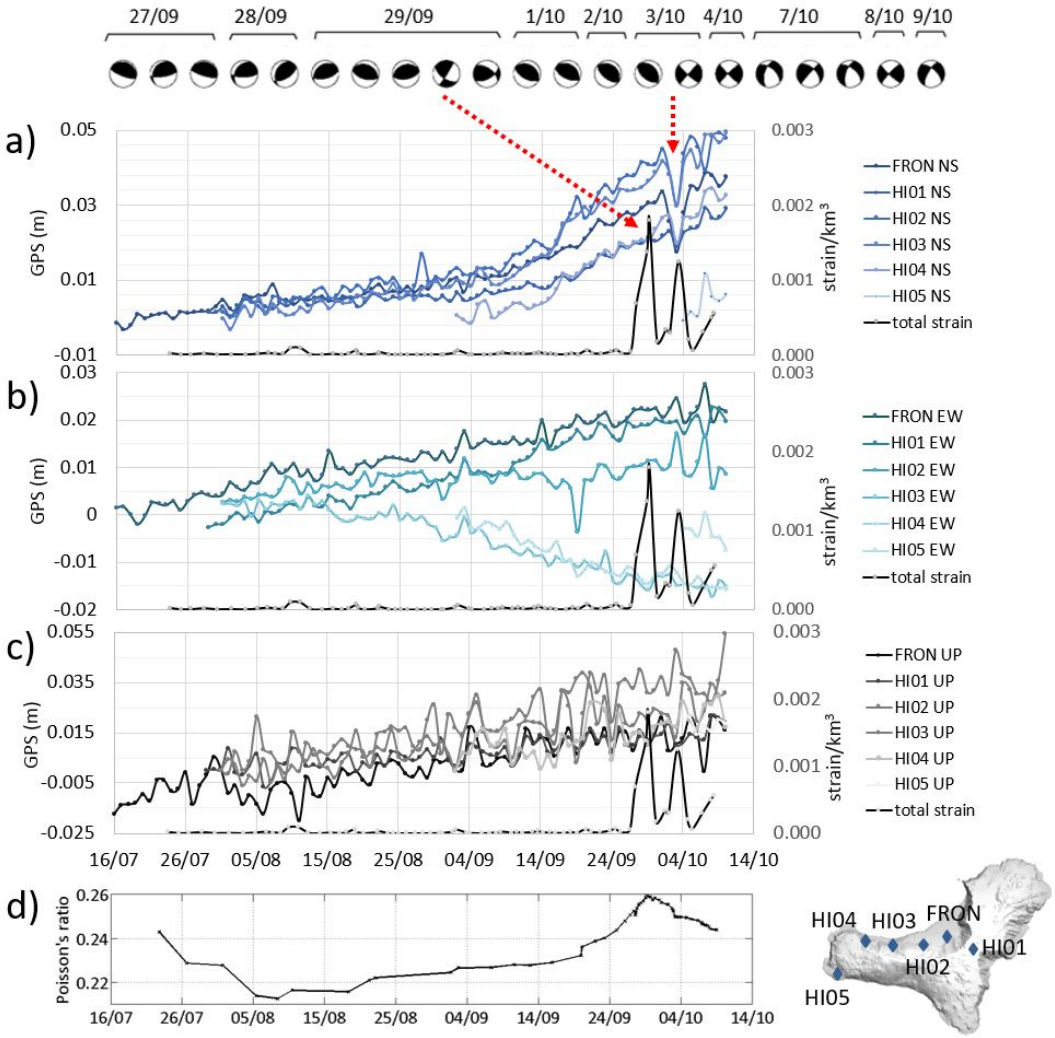

Figure 2.16: Comparison of the evolution of the seismic strain, the time series of GPS deformation and the Poisson's ratio during the 2011 El Hierro unrest. a) GPS NS component and the seismic strain, b) GPS EW components and seismic strain, c) GPS vertical components and seismic strain, d) Poisson's ratio time evolution.

edifice itself to the volumetric deformation (Traversa et al. 2010).

2.1.3 Short-term eruptive signs: 6-15 October, 2011

Hereinafter, the results of the detailed analysis performed over the data acquired during the last days of pre-eruptive unrest (6-10 October) and the first days of volcanic tremor (10-15 October) are presented. The objective of this study is to look for short-term unrest indicators and precursors of the irreversible mechanism occurring at depth below El Hierro that led the pressurized magma to the surface.

A manually review of all the seismic IGN events located during the unrest is performed, applying homogeneous criteria for phase picking and event formation. Resulting events are shown in Figure 2.17 (486 events with $rms \leq 0.3$ seconds and horizontal location error $\sigma \leq 3$ km). Seismic distribution of events suggests, from 6 October to the occurrence of the 4.3 mb event on 8 October, a slight vertical trend from a depth of 14 to 10 km. The first shallow event (at a depth of 3.5 km) occurred only 23 minutes after the main 4.3 mb event and was located to the south of the hitherto seismic source area. From then on, the hypocentral location of seismic events alternated between the deep seismic source area (75 events in total) and the shallow seismic source area (89 events in total with depths ≤ 4 km).

Some phases can be differentiated based on the evolution of the seismicity and the features that could be observed once the tremor signal started on 10 October:

1) Phase 0: considered to represent previous activity.

2) Phase I: from 6 October, 03:00 UTC (approx.) to 7 October, 21:00 UTC (approx.), which includes swarms of events whose hypocentres moved NW-SE in a lateral and almost horizontal direction.

3) Phase II: up to 8 October, 05:30 UTC (approx.), which includes the final and strongest swarm that coincided with an upwards depth trend from 13 to 10 km.

4) Phase III: up to 8 October, 20:34 UTC (duration approx. 15 hours.), which includes the relative quiescence in the seismic activity before the 4.3 mb event.

5) Phase IV: from the 4.3 mb event on 8 October to the beginning of the volcanic tremor on 10 October, which includes the double-source seismicity.

6) Phases V, VI and VII, including the different tremor signal behavior and the appearance of different surface manifestations of the eruptive activity.

The Time Varying Fractal Analysis is applied to the continuous seismic data. Figure 2.18 shows the results of the temporal variations of $FD(k = 1, ..., 5)$ for the different stations.

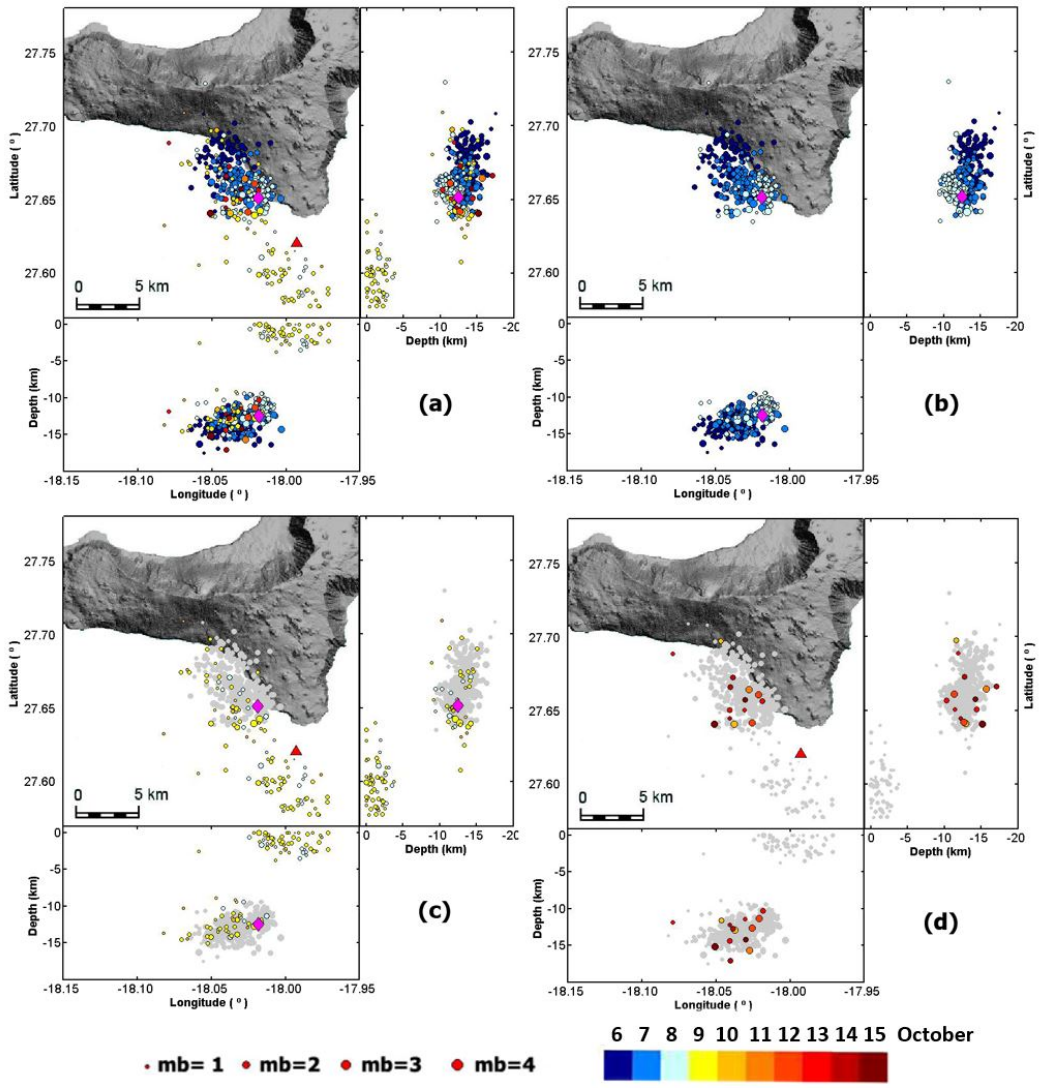

Figure 2.17: Reviewed seismic activity located during 6-15 October, 2011. (a) 498 hypocentral locations and their projections in the XZ and YZ planes. (b) The 360 events located from 6 October to the 4.3 mb event on 8 October at 20:34 UTC. (c) The 126 located events occurring from the 4.3 mb event to the beginning of the tremor signal on 10 October at 04:10 UTC. (d) The 12 events located from the tremor onset up to the end of 15 October.

Results show that up to 8 October, there were cyclic variations with a dominant value of $FD \sim 1.5$ during the most intensive seismic swarms. On 10 October a decrease to a shorter dimension began, which reached minimum values of $FD \sim 1$ in almost all stations by the end of 11 October. FD analysis reflects the effects of cyclic seismic swarms;

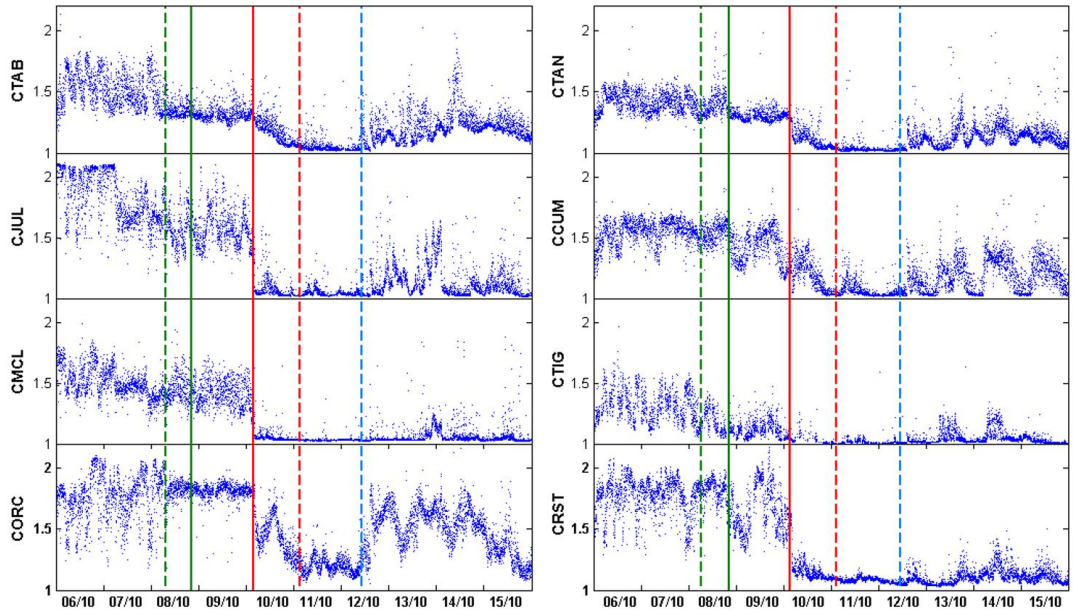

Figure 2.18: Temporal variations of $FD(k = 1, .., 5)$ at the different seismic stations. The 4.3 mb event and the onset of the seismic tremor are indicated on the graph with full green and red vertical lines, respectively. The dashed green vertical line indicates the beginning of the reduction in the seismic rate. The dashed red vertical line indicates the beginning of the fall in FD shorter values). The dashed blue vertical line indicates the onset of the appearance of light-green discolored sea-water stained by volcanic gases, which was observed about two nautical miles off the southern coast.

higher FD values would correspond to seismically quiet periods in which uncorrelated background seismic noise dominated, which agrees well with previous analyses of similar seismic patterns (see Boschetti et al. 1996, Padhy 2004, Tosi et al. 1999). Dominant seismicity approaches to the lower $FD \sim 1.5$. FD results were complemented with spectrogram analysis for source characterization. Figure 2.19 shows the ground-motion spectrogram (instrument response corrected) on the vertical component at the CTAB and CRST seismic stations, and their time traces. The successive VT swarm episodes show energy in a high-frequency band up to 25Hz, while the tremor energy is concentrated in a 0.3-5-15 Hz band.

Finally, the strain and the stress rates and their time evolution, are calculated to identify different stages in the source mechanism. These dynamic parameters reflect the state of fracturing of the crust and can be used as a potential tool for short- to medium-term forecast of the initiation of a eruption. The seismic catalog is completed, adding additional

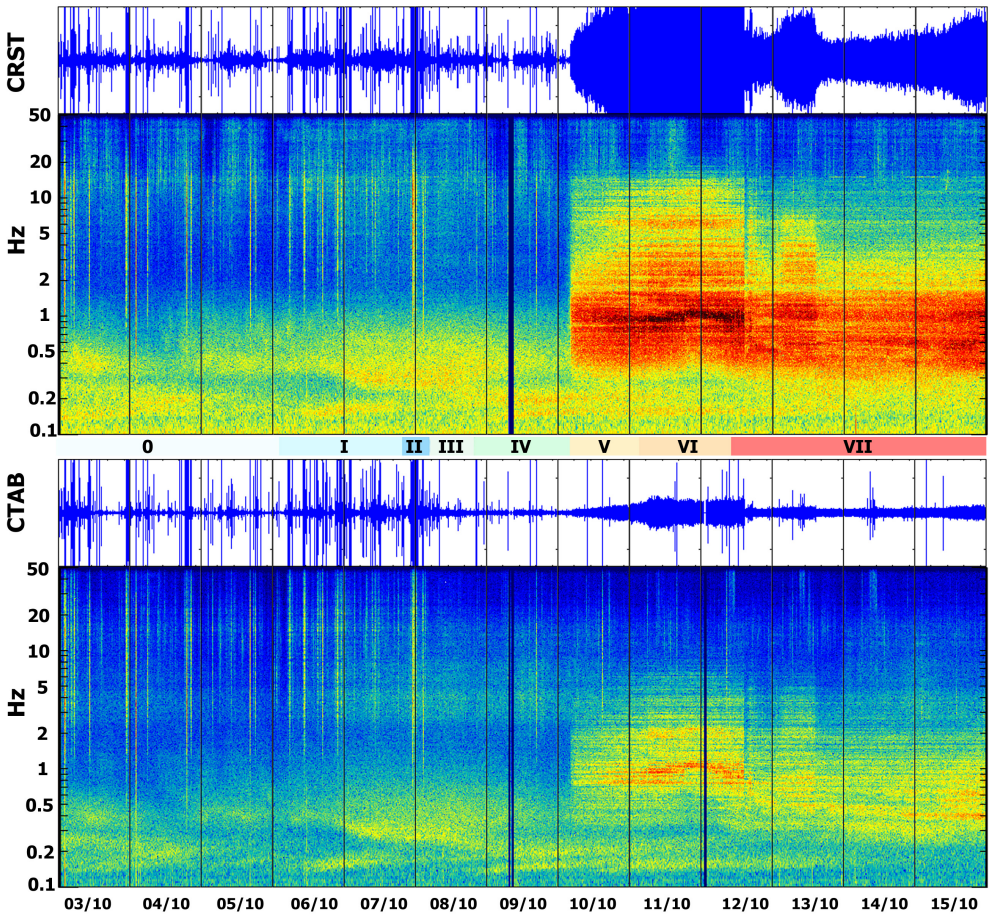

Figure 2.19: Ground-motion spectrogram of the vertical component of the CTAB and CRST stations, and their time traces (amplitude and spectrogram color scales are the same for both stations). The spectrogram is represented on a semi-logarithmic frequency axis plot from 0.1 to 50Hz. Color bands labeled 0-VII indicate different phases.

detections, incrementing the number of detected events on El Hierro from 677 to 6,343. Figure 2.20 shows the activity time evolution in terms of energy expenditure.

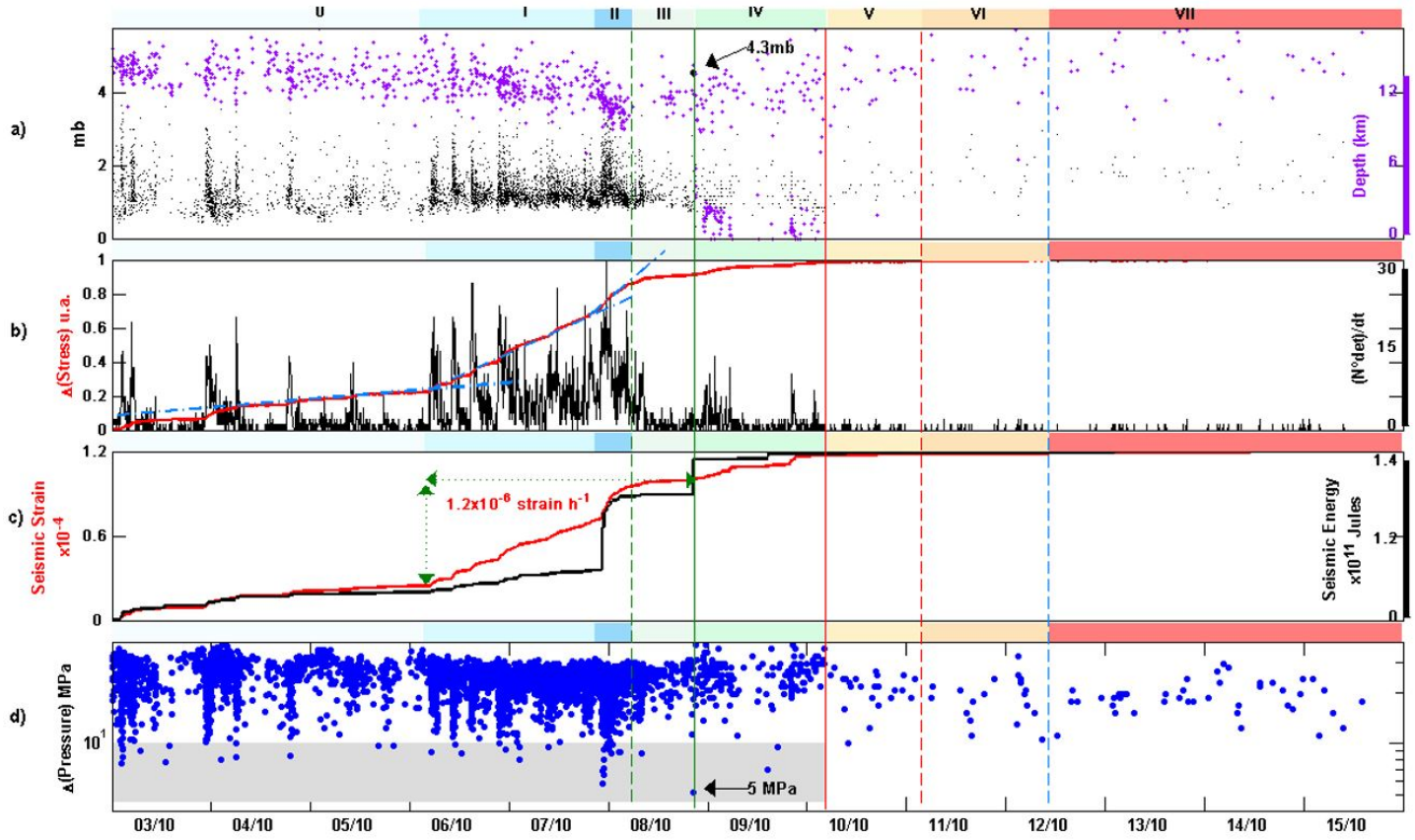

Figure 2.20: Energy, strain and stress time evolution. (a) Detection magnitude (in black) and location-depth time evolution (in purple) of seismic events. (b) Detection rate (in black) and its accumulated value (in red). (c) Seismic strain (in red) and its corresponding strain energy (in black) (or energy release under the Orowan's condition). (d) Effective pressure, at the seismic fracture surface as the minimum energy needed to initiate a catastrophic fracture through the crust towards the surface. Color bands labeled 0-VII indicate different phases.

Plots show the increase in seismic activity in the populated swarms during Phases I and II, which suggests that there was a periodic occurrence every 6-8 hours. The depth locations plot shows a slight trend for the hypocentres to move toward the surface; 15 km mean depth on 3 October, 14 km mean depth on 6 October, 14-10 km mean depth during the final strong swarm occurring in the final hours of 7 October and the first hours of 8 October. During Phase IV, the events seem to concentrate closer to the beginning and to the end of the phase, with locations alternating between the deep and the shallow seismic source areas. In the first shallow swarms, the mean depth was 2 km, while in the second and final shallow swarm, the mean depth was slightly less, around 1 km. During Phases V, VI and VII events were only observed in the deep seismic source area. The accumulated slopes of the seismic rate show different phases of the local stress field and crescent strengthening, from Phase 0 to Phase II. A higher contribution by the shallow seismicity to the local deformation is remarkable despite its lower seismic rate. The phenomenon involved in Phase II was the most energetically expensive of the whole period and produced the maximum deformation rate, even greater than the 4.3 mb event. During Phases I, II and III (65 hours approx.) 0.82x10^{11} J and 0.76 x10^{-4} strain (1.2 μstrain/hour) of deformation were released in the area. In Phase IV the corresponding values were 0.34 x10^{11} J and 0.2 x10^{-4} strain of deformation. Figure 2.20 also includes the corresponding effective pressure, σ_f, that points to the minimum energy needed to initiate a catastrophic fracture (See Appendix C). For the characteristic critical strain energy rate for the area, G, the rate used was the accumulated one during Phases I, II and III, it is highlighted from 4 to 10 MPa on a grey background. There are two critical situations where σ_f reached its lowest value, in Phase II (6 MPa) and during the 4.3 mb event (5 MPa). Crust state parameters were calculated using the standard value of Poisson's ratio for the crust $\nu = 0.25$ and $\mu = 40$ GPa (Watts 1994, Watts et al. 1997).

Nature makes nothing incomplete, and nothing in vain.

Aristotle

CHAPTER

3

Discussion

The application of classical and new approach analyses on the geophysical and geodetic data acquired in the Canaries, provided a valuable opportunity to get new results about the eruptive mechanism occurred on El Hierro. Analysis results are discussed in the following pages in relation with the emplacement and migration mechanism used by the magma to fracture and travel through the crust from its base to the Earth's surface. Thus, the most likely interpretation of the activity registered during the 2011 unrest and eruption is proposed. Throughout the discussion, it is applied knowledge about the regional Geodynamics, the El Hierro known structure and the Rock Fracture Mechanics Theory, which offers challenging interpretations of what occurs when a fluid (including magma) opens and fractures rock. Main results, and their interpretation, are chronologically presented. A conceptual model for the El Hierro magmatic mechanism is also presented.

3.1 Discusion

3.1.1 1996-2002

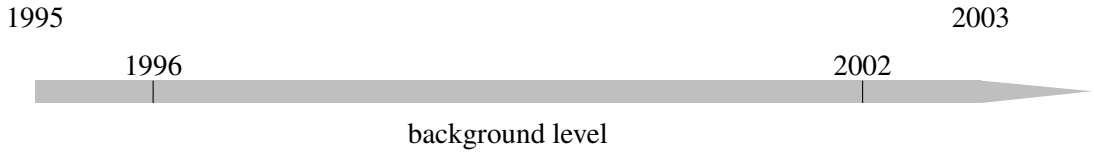

Activity. The activity registered in the Canaries during this period was rather low and steady (see Figure 2.3, Figure 2.4) and the deformations measured by the regional GPS network (horizontal components) followed the regional stress field direction in the Archipelago (Figure 2.6).

Discussion in terms of volcanic activity. Compared to the tectonic activity occurred from 2003 onwards, the activity in the Canaries may be considered in its background level.

3.1.2 2002-2011

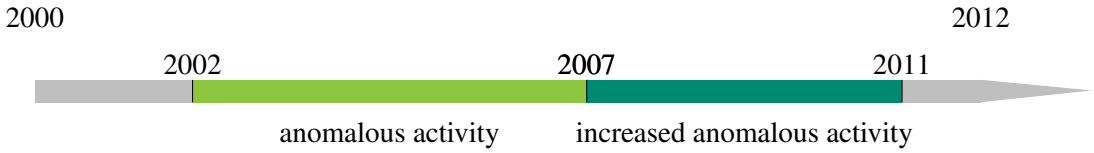

Activity. Anomalous seismic and geodetic activity were detected by a general increase in the whole region, from Azores to Strait of Gibraltar (excepting the Mid-Atlantic Ridge) with a coincident increment in the seismic energy released in 2003-2004 and/or around 2007 (see Figure 2.2, Figure 2.3, Figure 2.4) an E-W drift and uplift deformations that affected the southern Iberian Peninsula, northwest Africa, and the Canary Islands (Figure 2.6). At local scale, in the Canaries, activity affected different islands, showing common seismic patterns (similar FD evolution and an increase in seismicity) at El Hierro (more intensely) and Tenerife Islands (Figure 2.7) a concurrent stress-shift episode measured by GPS stations on La Palma and Gran Canaria Islands (Figure 2.8).

It is noteworthy that the local activity (seismicity and surface deformation) is occurring not only in El Hierro but also in Tenerife, La Palma and Gran Canaria Islands. Other authors have also reported increased activity in these periods, marked by an increase in seismicity and anomalous 222Rn and 220Rn subsurface degassing from 2003 to 2005 in Tenerife and an increased trend of diffuse CO_2 emission from Teide Volcano (Tenerife Island) in 2007 (Almendros et al. 2007, Cerdeña et al. 2011, Peréz et al. 2007). These increases in activity were interpreted as caused by the presence of new magma below the Canaries and the subsequent changes in the stress field.

Discussion in terms of volcanic activity: Anomalous tectonics, generation and emplacement of new magma in this environment may be explained either by stress changes generated at the plates boundaries or by a mantle plume upwelling (Bonnin et al. 2014, Fullea et al. 2015, Geyer et al. 2016, Legendre et al. 2012, Miller et al. 2015, Saki et al. 2015). The observed deformations (regional and local) agree with the existence of an active mantle upwelling beneath the Atlantic off the northwest African continental lithosphere (Fullea et al. 2015, Legendre et al. 2012, Saki et al. 2015). A recent study (Miller et al. 2015) has proposed the existence of a considerable amount of multiple sub-lithospheric, low-velocity material flowing sub-horizontally northeastward from the Canary hotspot to southern Spain, that is, beneath the Atlas and the Alboran Sea and from the 410-km discontinuity to the lithosphere-asthenosphere boundary.

A reactivation of this sub-lithospheric material below the lithosphere of Canaries, Morocco and southern Spain would explain the observed seismicity, the regional extension and uplift affecting the southern Iberian Peninsula, NW Africa, and the Canary Islands and could have facilitated partial melting and accumulation of magmas at different depths in the mantle below the Canary Islands. The time encompassed between the beginning of the deformation and the eruption and subsequent unrest episodes at El Hierro suggests a certain delay between mantle upwelling and melting. The fact that the Azores hotspot is different from the Canary Islands hotspot above 660 km (Saki et al. 2015) would explain the decoupled evolution of the process in the Canary Islands (eruption) and in the Azores (no eruption), despite sharing an increased seismicity.

3.1.3 **19 July-8 October, 2011**

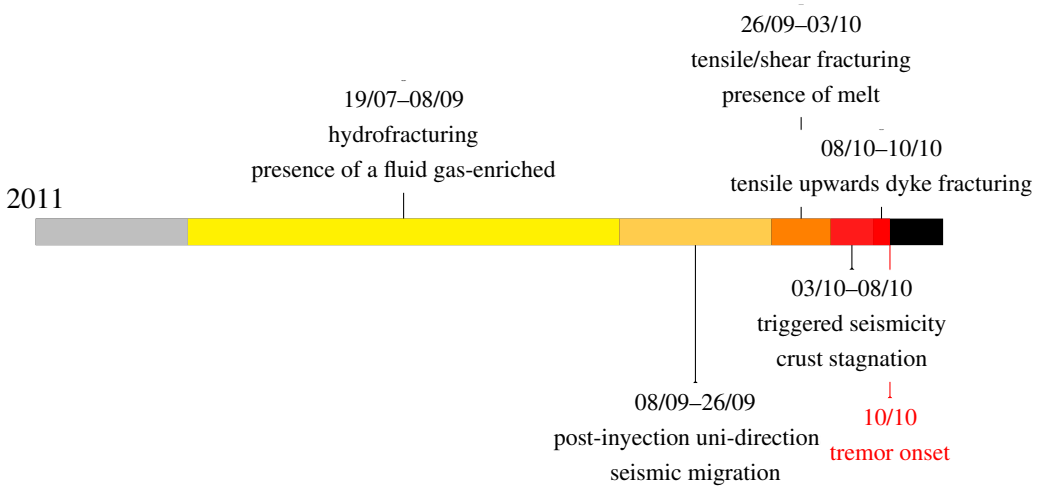

Activity. The activity registered in El Hierro from the beginning of the unrest to the date when the seismic migration at constant depth to the south started (19 July to ∼21 August) showed an hydrofracture nature (clustered swarm activity, low M_{Wmax}, $b \geq 1.5$, tensile fracturing, low Poisson's ratio and the occurrence of micro-seismicity) (see Figure 2.9, Figure 2.11, Figure 2.15, Figure 2.13). On 21, and more clearly on 27 September, the activity changed drastically, appearing deeper earthquakes from this date onwards (Figure 2.10), and very intense swarms of VT events and an alternation of shear and tensile behavior, with maximum Poisson's ratio values, maximum seismic strain release and maximum deformation as reflected by the higher modeled Mogi's source volume (see Figure 2.11, Figure 2.15, Table2.1).

The activity presented two pulses (27-30 September and 2-5 October) (Figure 2.16) registered by the seismic and the second one by the GPS network. Of note are the coincidence between the coherent oscillation in the NS component and the seismic strain pulse (2–5 October) with maximum on 3 October, and the change in focal mechanism from thrust fracturing to strike-slip that occurred on that date. During 6–8 October VT seismic activity strongly increased both in rate and in size, reflecting the seismic strain a permanent deformation accumulation, with a maximum rate of 1.4x10-6 strain h^{-1} (Figure 2.20), the greatest throughout the whole process.

Discussion in terms of volcanic activity. When an over-pressurised fluid is injected into a volume of rock, the pressure migrates through the pores (pore pressure pulses) and stress variations in the rock occur (due to the opening and fracturing of fluid-filled cracks)

(e.g. Dahm et al. 2010, Miller et al. 2004, Shapiro et al. 1997, Toda et al. 2002). In the fluid-filled crack opening and fracturing model (e.g. Dahm et al. 2010) cracks grow bi-directionally during the fluid injection process. This bidirectional growth continues for some time (post-injection) due to decompression by the remaining driving pressures, and then subsequently initiates unidirectional growth that is maintained depending on the stress gradients and the injection fluid pressure. High b values (in some cases up to 2 or even 3) in volcanoes have been interpreted as being caused by the fracturing produced by fluid/magma intrusion in the mapping areas surrounding magma bodies (e.g. Bridges & Gao 2006, Díaz-Moreno et al. 2015, McNutt 2005, Murru et al. 2007, Wiemer & Wyss 2002).

Besides, anomalous V_P/V_S ratios have also been registered in many volcanoes and low ratios are interpreted as an increase in the presence of gas in fractures (e.g. Kilauea, Johnson & Poland 2013; Mount Etna, Patanè et al. 2006; Campi Flegrei Caldera, Chiarabba & Moretti 2006; Aso Caldera, Unglert et al. 2011). These authors suggest that increasing crack density should lead to higher S-wave delay times and to lower V_P/V_S ratio values — if the cracks fill with gas.

Therefore, a fluid injection (gas-enriched) close to the crust-mantle discontinuity would explain the bi-directional seismicity growth, the high b values, the clustered seismicity and the existence of seismic back- and fore-fronts observed during 19 July to $\sim$21 August. This fluid intrusion could not go upwards through the crust due to the high velocity crust in that area, as revealed by the two P- and S-wave tomography results (Gorbatikov et al. 2013, Martí et al. 2017) but it overpressurized the entire Island promoting extension and tensile fracturing of pre-existent faults. The observation of a spatial CO_2 positive flux anomaly in a faulted area at the North of El Hierro between 22 July and 14 August (López et al. 2012) could be congruent with described state.

The seismic migration pattern observed from 21 August to $\sim$27 August (Figure 2.12), suggests a unidirectional growth of the fluid injection, driven by structural or regional stress gradients. In this regard, it is noticeable the precise coincidence of the unidirectional growth path with the lateral heterogeneity at 10-15 km depth below the Moho discontinuity (Gorbatikov et al. 2013) in El Hierro.

Previous studies in volcanic active areas, have related an increase of V_P/V_S ratio with the presence of melt (magma) and fluid-filled cracks in the media. Melt intrusions in a fractured rock result in high V_P/V_S ratios by lowering the V_S. Fracturing and increasing pore pressure also causes a relatively marked decrease of Vs but only a small decrease of

V_P, which yields an increased V_P/V_S ratio (e.g. Chiarabba & Moretti 2006, Hong et al. 2014, Koulakov et al. 2013). Moreover, a rapid migration of fluids in pre-fractured zones, leads to a high V_P/V_S ratio and to an increase of the seismicity (Chiarabba & Moretti 2006, Hong et al. 2014, Husen et al. 2004, Johnson & Poland 2013, Patanè et al. 2006, Vanorio et al. 2005).

In regard to the relationship that exists between tectonic stress field and the earthquakes triggered by magma overpressure, Roman & Heron (2007) proposed different faulting scenarios depending on the strength of the regional tectonic stress in comparison with the volcanic stress. Fault slip in the direction of the regional maximum compression if regional stresses dominated; no faulting, creating shadow zones around the inflating dyke if regional stresses balance volcanic stresses; and reverse faulting if volcanic stresses dominated (Roman & Heron 2007).

Based on these observations, we suggest that from 27 September onwards, an increase of over-pressurized melt, as suggested by the increased modeled volume of the pressure source: 0.0039 km^3 (31 July to 8 September), 0.0079 km^3 (8-21 September) (see Table2.1), reached the mantle-crust boundary, in agreement with the reverse type of the focal mechanism. This increased overpressure, affected the entire volcano edifice, promoting tectonic seismicity while increasing in volume by the tensile emplacement of additional melt material. During the reverse faulting period (27 September to 3 October) volcanic stresses likely dominated, being the source of this fracturing clearly below the crust base. Therefore, this stage could suggest a propensity for the formation of a fluid-crack and then dyke migration at the end of this process. Change in focal mechanism and the GPS oscillations pattern registered around 3 October suggest that an important change (geometry, media) occurred on that date. Fluid-crack intrusions are usually characterized by deflation-inflation sequences in the magma source and by associated subsidence-uplift cycles above, as well as by the lateral migration of earthquake swarms, as the magma moves from its source and into the dyke (Brandsdóttir & Einarsson 1979, Einarsson 1991, Moore & Krivoy 1964, Rubin et al. 1998, Toda et al. 2002), so likely on this date occurred the propagation of a dyke from the magma reservoir, allowing the decreasing of the magma pressure below the crust (change on focal mechanism from thrust to strike-slip).

The strike-slip seismicity registered during 3-8 October could be the consequence of the increased Coulomb stress transfer on pre-existent regional faults in the crust since strike-slip event planes coincided with regional NW-SE maximum compression (Geyer et al.

2016). The rapid variations in V_P/V_S recorded in this period would reflect the abrupt changes in the stress and deformation states, which cause fracturing, and the active transport of fluids (melt), these fluids driving more fracturing in a positive feedback system that ultimately leads to eruption (Koulakov et al. 2013). During the seismic gap registered after the occurrence of the 8 October 4 M_W event an intermediate scenario could have occurred, where an increasing volcanic stress balanced with the regional stress. Under this hypothesis, the aseismic area between the previous seismicity at 10-12 km deep and the surface seismicity at 3 km depth could draw the shadow around the propagating dyke.

Concerning the Coulomb static stress changes associated with the modeled Mogi's sources, both triggered seismicity and stress shadow have been observed previously associated with the evolving static stress changes during dyke propagation in active volcanoes (e.g. Green et al. 2015). The Coulomb stress change modeled with the 3-9 October source pressure in the site of the 8 October event is $\sim$5 bar. The focal mechanism of this event was modeled by Del Fresno et al. (2015), obtaining a pure double-couple mechanism with null isotropic (dilatational) component, which discards any volume changes in the source due to magma intrusion. Modeling a circular fault model (Brune 1970). Del Fresno et al. (2012) calculated 0.9 km^2 for the rupture area and 20-30 bar for the stress drop. This stress drop is higher than the 5 bar (0.5 MPa) of positive change in Coulomb stress, but in pre-existent faults similar variations promoted failure encouraging an earthquake (Chouet et al. 2013, Walter & Amelung 2007). So, a positive stress transfer by itself could have triggered the 8 October 4.0 M_W earthquake on a pre-existent fault, as well as the lower magnitude seismicity as suggested by the good fit of the 3-8 October spatial location distribution and the area covered with highest stress (Figure 2.14).

A bias in the GPS coordinates on those days due to atmospheric instabilities recorded by the meteorological stations in the island should not be ruled out. As described in Larson et al. (2010) path delays caused by the troposphere are one of the most important sources of error in GPS precision. In addition, based on Tregoning & Herring (2006), poor Zenith Hydrostatic Delay values are able to corrupt the station coordinates and the Zenith Total Delay estimates but this effect is more important in the vertical component than in the horizontal ones. Thus, although the inflation/deflation cycle coincides with days of atmospheric instabilities, it makes us think the deformation could be real, and not a bias, due to the fact that it is greater in the horizontal components than in the vertical components and, also, because there are changes in the volcanic system detected by other techniques. However,

the magnitude of the deformations these days could be influenced by tropospheric effects.

3.1.4 **8-15 October, 2011**

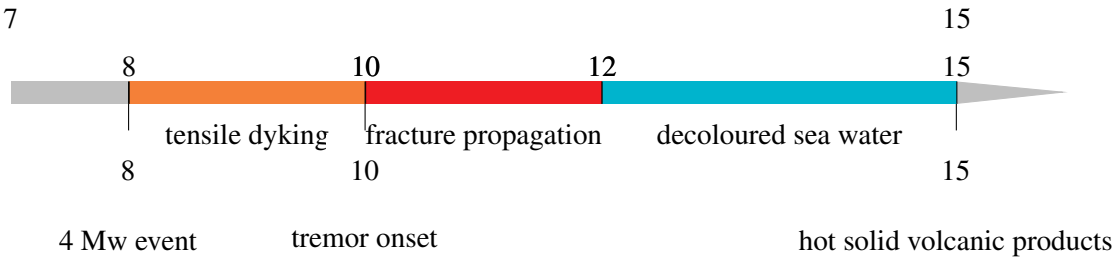

Activity. On 8 October, after the occurrence of the 4.0 M_W earthquake, the seismic rate, the seismic strain and the released seismic energy felt drastically. From this day, the seismic strain reflected a smaller but persistent permanent deformation with a maximum rate of 0.3x10^{-6} strain h^{-1}, which was maintained until the appearance of the tremor signal in all the seismic stations on 10 October (Figure 2.20). The tremor signal progressively grew from its onset until 11 October at about 6:00 UTC, with an energetic high-frequency release (0.3-15) Hz, with a maximum frequency of 0.75 Hz (Figure 2.19). FD analysis showed a continuous decrease to shorter dimensions (Figure 2.18). Up to 8 October, FD suggests that there were cyclic variations with a dominant value of $FD \sim 1.5$ during the most intensive seismic swarms suggesting the predominance of seismic activity in the signal despite the scarcity of events.

On 10 October a decrease to a shorter dimension began (Figure 2.18), which reached minimum values of $FD \sim 1$ in almost all stations by the end of 11 October. During 10 October, the only indirect evidence of the on-going eruption process was the appearance on the sea surface of many dead fish characteristic of deep zones. From 10 October (06:00)–12 October (14:30), the volcanic tremor reached its maximum energy on a broad frequency-band rich in high frequencies (Figure 2.19), with an upper spectral bound of 15Hz at the seismic station located nearest the eruption coordinates. The tremor-dominant amplitude corresponded to 0.9 Hz, higher than that of the previous phase. On 12 October 14:30h and thereafter, a sudden decrease in the tremor amplitude was recorded at all stations and a shifting of the frequency band to smaller values.

The appearance of clear eruptive signals on the sea surface (stained water and small pieces of fragmented lava) this day and time provided a good indication of the volcanic activity occurring at the submarine vent. The dominant frequency of the tremor was lower than during the previous days and reached 0.4 Hz on 15 October, the day on which abundant emission of xenopumitic fragments was observed.

Discussion in terms of volcanic activity. During the occurrence of the 4.0 M_W event, the corresponding effective pressure, σ_f, at the seismic fracture surface, reached a critical minimum of 5 MPa (Figure 2.20). We believe that this event could have surpassed the strain-rate threshold necessary to initiate such a catastrophic fracture and thus opened a path through the crust to the surface. The occurrence of the seismic event altered the shear and normal stresses and generated high local stress and local strain magnification, which increased the tendency for brittle fracturing. The 'deep' and 'shallow' seismicity registered from this event to 10 October, could represent the depths of the bottom and top edges of the strained volume. In fact FD analysis suggests the predominance of seismic activity in the signal despite the scarcity of events. The possibility exists that the persistent lower magnitude seismicity was recorded because the event signals were obscured below the background seismic noise level of the recording stations. Cornet (1992) suggested that earthquakes generated by the tensile propagation of a dyke tip are likely to be too small in magnitude to be identified by standard seismic networks.According to the observational data presented here, we conclude that at the end of this stage the over-pressurization of the system reached a critical point due to magma accumulation in the south (regardless of whether it was under or in the lower crust). This idea is also supported by the observation of high levels and a gradual increase in the H_2S flux recorded at a station located on the coastline of the Mar de Las Calmas (close to the seismic location area) prior to the onset of the eruption (Peréz et al. 2012).

When the Theory of Rock Fracture Mechanics is applied to El Hierro, results showed that the requirement for induced vertical-plane tensile faults is fulfilled at shallow depths (less than 3 km), and tensile openings are possible on fractures oriented within 22.5°from the vertical. At any other depths in the crust and at other orientations, new fractures will be shear or tensile in nature but will occur in pre-existing fractures. As the differential stress increases with depth and pore pressure, leading to smaller real differential stresses and a greater probability of a crack opening in over-pressurized formations (Fischer &

Guest 2011), we cannot rule out the possibility that tensile opening could occur near the magma reservoir or the dyke. One noticeable result is the influence of Poisson's ratio on the available faults planes that the over-pressurized magma uses to travel from depth to the surface. Whatever the case, at depths of less than 6–7 km, positive buoyant magma will open all pre-existent faults at any dip angle. Therefore, once the magma crossed the Moho south El Hierro, dyke stress would unclamp the pre-existing faults, thereby allowing the aperture of a magma path to the surface in a combined process of tensile and shear fracturing. During its migration, the geometry and orientation of the dyke changed to take advantage of new available fault planes, which gave rise to apparently aseismic migration close to the surface on 8–10 October, probably due to high-aperture tensile fracturing.

The analysis of the lava fragments collected on the sea surface near the vent area (Martí et al. 2013, Meletlidis et al. 2012, Sigmarsson et al. 2012, Troll et al. 2011) suggests that local and rapid crustal assimilation occurred at the base of the volcanic edifice when the first magma passed through that zone. Despite the different interpretations that have been proposed to explain the exact nature of these xenopumices (Meletlidis et al. 2012, Sigmarsson et al. 2012, Troll et al. 2011), all authors coincided in the fact that the assimilation of pre-existing rocks, located either at the sedimentary basement of the volcanic edifice or inside it, had occurred. The products of that crustal assimilation episode appeared after only a few hours in the form of lava fragments with a black vesicular outer crust with bulk basanite composition, surrounding a centre with a grey-white pumiceous xenolithic core (xenopumices). Even so, the decrease in the registered seismicity and in the strain rate indicate that an important change in the intrusion conditions occurred, probably reflected in this magmatic assimilation episode.

The tremor signal started on 10 October at 04:10 UTC. Right from its beginning, the tremor signal underwent important changes in its amplitude and frequency, an indication of the complexity of the phenomenon that is also reflected in the lack of identifiable persistent frequencies of source resonance. Increasing tremor amplitudes have commonly been observed on other volcanoes and are thought to occur when ascending magma massively vesiculates due to decompression or when it interacts with external water (groundwater or surface water) (McNutt 1996, Patanè et al. 2008). Based on bathymetric evidence of the deposition of juvenile material on the seafloor during the first days of the eruption, Martí et al. (2013) suggested that the eruption site migrated north for almost 3 km along a surface fracture of the southern rift, from a depth of 1000 m to 300 m. This migration was

halted by the intersection with a NE-SW-oriented normal regional fault, which facilitated the establishment of a central conduit and a vent, giving rise to the construction of a volcanic cone. During this phase, the tremor signal could be mostly caused by gas-rich fluids exsolved from the ascending magma in the final 1-4 km before the surface, which escaped massively through a complex feeding system as it changed its geometry to the smaller dimension of a central conduit. On 12 October, $FD \sim 1$ at almost all stations, suggested that the minimum dimension conduit geometry was maintained.

3.2 Conceptual Model

The results presented evidence that the renewed magmatic activity on El Hierro was preceded by years of deformation and increased seismicity. The generation and eruption of magma corresponds to a punctual geodynamic episode in which tectonism is earlier manifested than magmatism, but which would be compatible with a mantle upwelling being the cause of the observed tectonic activity. Thus, the observed anomalous tectonic activity (e.g: seismicity and deformation) can be considered as a precursor to the El Hierro eruption, being this a sequence of events that may repeat in the future. In this framework, it is also important to remark the role of tectonics in controlling magma migration. In the particular case of El Hierro it seems clear that the eruption occurred when tectonics facilitated the opening of the path that magma used to reach the surface, not being able the magma by itself to create that path.

Figure 3.1 summarizes via successive vertical cross-sections the proposed main phases that occurred in the period (15 years) before the eruption on 10 October 2011.

(a) First phase depicts the situation of background activity, considering the data registered by the seismic and GPS monitoring networks from 1996 to 2002. During this period, regional deformation followed the direction of the regional stress field, with absence of anomalous activity. A mantle upwelling beneath the Atlantic off the northwest African continental lithosphere rises from the lower mantle and spreads above 410 km in distinct sub-lithospheric upwellings beneath the Canaries, the Atlas (Morocco) and the South of Spain. Below the Canaries, a hot spot rises from the 410 km discontinuity to the LAB (lithosphere-asthenosphere boundary).

(b) During a second phase, from 2003 to 2011, mantle upwelling promoted regional seismicity, extension and uplift in the southern Iberian Peninsula, NW Africa, and the

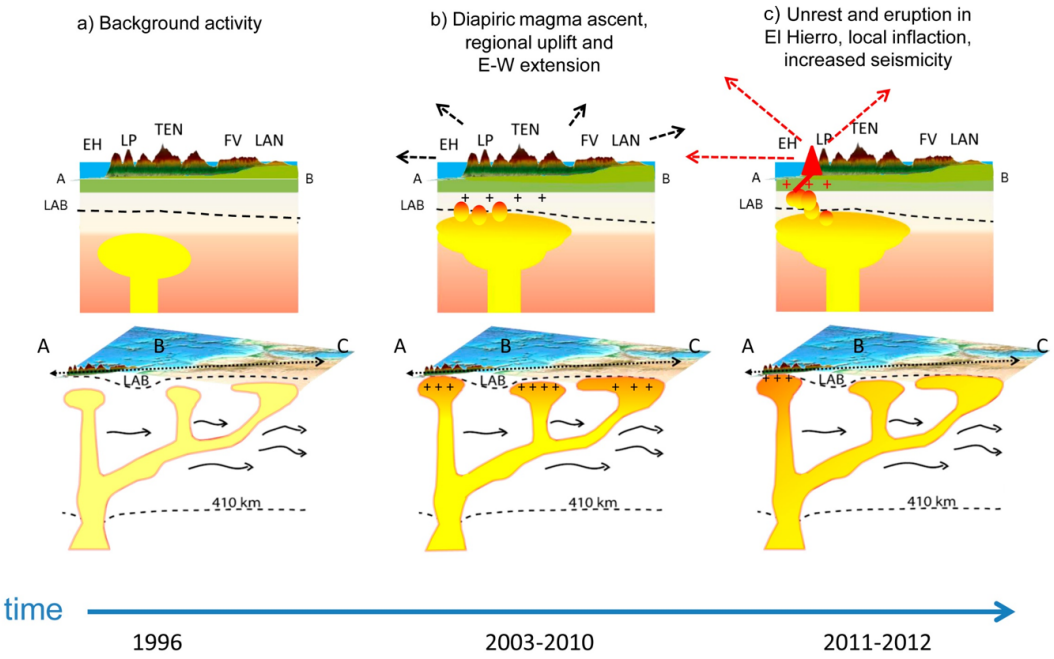

Figure 3.1: Sketch showing the vertical cross-section sequence during different phases of the process leading up to the eruption on El Hierro, on a local scale (the Canaries, upper panels) and regional scale (from the Canaries to the Alboran Sea, lower panels). The interpretative depiction of the upper mantle (lower panels) was taken from Miller et al. (2015). Black dashed line crosses from The Canaries (A) through the Atlas (B) to the Alboran Sea (C). In the upper panels, different islands from the Canaries: El Hierro (EH), La Palma (LA), Tenerife (TEN), Fuerteventura (FV) and Lanzarote (LAN)

Canary Islands and facilitated partial melting and magma ascent below the Canary Islands. This allowed that, below the LAB in the Canaries, different small pockets of magma migrated towards the base of the crust. From $\sim$ January 2011, the extensional stress regime induced by the mantle upwelling and the magma excess pressure facilitated the opening of fractures above the LAB boundary bellow the Canary Islands. The existence of a lateral strong stress gradient in the upper lithosphere close to El Hierro could have facilitated the movement of new magma in dykes and its migration from mantle to crust in this particular area.

(c) At local scale in El Hierro, ones the new magma injection reached the crust discontinuity, it start to over-pressurize the entire edifice. Magma injection overpressures the existing magma reservoir below the crust, promoting stress diffusion and hy-

draulic fracturing of pre-existing and new cracks in the lower crust with gas-enriched fluids. Increased overpressure promotes tectonic seismicity, while the reservoir increases in volume due to the tensile emplacement of additional melt material. Dyke propagation caused a fall in the magma pressure below the crust and the increase in the stress in the crust. The positive stress transfer in the crust could have triggered seismicity along a pre-existent fault on 3–8 October. An increasing volcanic stress balance with the regional stress field enabled the propagating dykes to use and maintain open the network of pre-existing faults from the crust base to the surface. In the upward migration, the magma starts by using vertical pre-existing faults and opens closer to the surface pre-existing faults of any dip angle, thereby promoting during the final kilometers horizontal (lateral E-W oriented) migration that reached the surface far from the area in which the previous seismicity had been located.

In the further magma injection episodes that occurred between 2012 and 2014 magma did no erupt, remaining stored at depths between 25 to 15 km, thus suggesting that tectonic activity did not help magma to migrate to sallower levels. This is in good agreement with the petrological imaging of the magmatic feeding systems below El Hierro and La Palma that suggest the presence of isolated magma pockets at a depth of 15–26 km, as occurs on other oceanic volcanic islands fed by plumes with relatively low fluxes (Klügel et al. 2005, Stroncik et al. 2009).

Knowledge is an unending adventure at the edge of uncertainty.

Jacob Bronowski

CHAPTER

4

Conclusion

The main goal of this Thesis is to improve knowledge about the magmatic proces involved in a volcanic eruption, including the preparatory pre-eruptive unrest phase. For that purpose, El Hierro eruption is studied, from the early signs of volcanic unrest associated with the accumulation of new magma in the region, to the evidence of magma migration towards the Earth surface. Classical and novel methods area applied to the geophysical data provided by the monitoring services (mostly from the Volcano Monitoring Department of the Instituto Geográfico Nacional, IGN). Further, knowledge about fracture mechanics and detailed information about the Geodynamics of the region and the upper-mantle and crust structure in El Hierro is included. Gain knowledge could be relevant not only to the understanding of the causes governing the initiation of the eruption on El Hierro but also to the understanding of volcanic unrest in general and the forecasting of the initiation of volcanic eruptions.

4.1 Conclusion

In relation to El Hierro eruption, and despite the fact that data used was limited, that the methods applied were merely an approximation of the physics involved in an eruptive event, and that the results include numerous uncertainties rather than simple solutions, the consistence provided by comparable results allows to hypothesize how the eruption on El Hierro took place. Following, the main conclusions about El Hierro eruption mechanism are drawn. Some general comments are also included.

(i) Even the role of regional tectonics in mantle upwelling cannot be deciphered with the results obtained, it seems evident that regional and local tectonic structures have also played a significant control on El Hierro eruption. The exact interplay between regional tectonics and mantle dynamics is a key question to understand the origin of the Canarian volcanism. As indicated before, this is a question still under debate and it is not the aim of this study to go further on this particular subject. As early signs, we consider that the increase in tectonic activity since 2003 can be consider as precursor of the magmatic and volcanic activity occurred on El Hierro, being this anomalous tectonic activity induced by the ponding of the Canarian mantle plume, which involved the drifting E-W extensional and uplift deformations observed in the Canary Islands but that also affected the south of the Iberian Peninsula and northwest Africa. We propose that the long-term monitoring of the tectonic activity (e.g: seismicity and deformation) in a broader area (from Azores to Morocco) can be considered a useful tool for the volcano hazard assessment of future eruptive events in the Canaries.

(ii) As signs of local volcanic unrest on El Hierro during 19 July-10 October, 2011, local fracturing and deformation analysis results showed evidence of magma injection below the local crust, hydraulic fracturing with gas-enriched fluids, migration of the stress perturbation to the south, crossing of the Moho discontinuity, triggering tectonic seismicity in pre-existing faults, and tensile upwards migration of melt to the earth's surface on El Hierro. Stress modeling highlights the very importance role played by the pre-existing faults in El Hierro eruption. It is also worth noting that we have reliable evidence of important changes in the crust state parameters (e.g. Poisson's ration, compressional and shear velocity) during a magmatic intrusion, therefore, all the modeling performed constant state values may bias results.

(iii) Results stressed the importance the precise knowledge of magma, structure and mechanics of the host rock has for a proper interpretation of the observational data. The characteristics of the system (magma + host rock structure) and, consequently, of the forces acting upon it may change during the course of the process and may delay, accelerate or halt the onset of the eruption. The interpretation of the observational data in isolation can be misleading and be misunderstood if the state of the crust is not previously known – or at least taken into account as an important conditioner. Stress and strain rates can be characteristic for an area and their thresholds can be considered to be a potential tool in short-term forecasts in conjunction with other forecasting methods; we believe that the implementation of real-time analysis procedures that reflect a more comprehensive stress and strain states occurring in the crust and its continuous short- and long-term changes; this will provide us with an excellent tool for the correct identification and interpretation of eruption precursors.

(iv) Even previous studies have employed some of the techniques used in this work (e.g. b-value analyses, Mogi's point source modeling), some of the methodologies used are new: e.g. the complete calculation of the whole evolution of the seismic strain and the Coulomb modeling of the stress field changes. In a similar way, no Vp/Vs temporal evolution study or Es/Ep characterization of the tensile/shear fracturing, or error analyses of the deformation Mogi's modeled sources, has been performed using the dataset from the unrest on El Hierro. Some of the evidence found is novel (e.g. occurrence of high-magnitude triggered seismicity, hydro-fracturing by gas-enriched fluids, evidence of the crossing of the mantle/crust boundary), as is the interpretation of the overall evidence in light of the detailed knowledge of the structure of El Hierro.

(v) Some of the new approaches, like the Time Varying FD analysis provided a valuable information for the characterization of different seismic volcanic sources and the geometry of a radiated seismic-wave field. This analysis could be valuable in real-time volcano monitoring activity. Likewise, knowledge of stress and strain states and their rates in the crust have proved essential for the monitoring and understanding of pre-eruptive processes during episodes of unrest.

(vi) It is also worth noting that when the seismic activity included in a seismic catalog does not include very low-magnitude seismicity (tensile fracturing), or when its performance is dependent on the seismic rate, only a very approximate (in the best of cases) path along which the magma is rising or accumulating can be drawn. High-magnitude activity can be partially related to the opening of the pre-existing network of fractures of the volcano edifice and some of the high magnitude events are caused by stress triggering.

(vii) Likewise, it is essential to have a dense GPS network for precise modeling of the magma intrusion and the changes in its geometry as it crosses the lithosphere. Otherwise, it is only possible to derive simple and probably biased models. Therefore, we stress the crucial importance of setting up a high-quality (i.e. dense, low-noise, well-distributed) network of instruments and developing new tools for comprehensive monitoring of volcanic activity and the correct interpretation of the observational data acquired.

References

Aki, K., 1965. Maximun likelihood estimate of b in the formula logN = a -bM and its confidence level. *Bull. Earthq. Res. Inst.*, 43:237–239. 19

Aki, K. & Richards, P. G., 1980. *Quantitive Seismology. Theory and Methods.* W. H. Freeman, San Francisco (EEUU). 2 volumes. 932 pages. 20

Albert, H., Costa, F. & Martí, J., 2016. Years to weeks of seismic unrest and magmatic intrusions precede monogenetic eruptions. *Geology*, 44(3):211–214. 2

Almendros, J., Ibañez, J. M., Carmona, E. & Zandomeneghi, D., 2007. Array analyses of volcanic earthquakes and tremor recorded at Las Cañadas caldera (Tenerife island, Spain) during the 2004 seismic activation of Teide volcano. *Journal of Volcanology and Geothermal Research*, 160(3-4):285–299. doi:10.1016/j.jvolgeores.2006.10.002. 51

Altamimi, Z., Collilieux, X. & Metivier, L., 2011. ITRF2008: an improved solution of the International Terrestrial Reference frame. *Journal of Geodesy*, 85(8):457–473. doi: 10.1007/s00190-011-0444-4. 23

Altamimi, Z., Sillard, P. & Boucher, C., 2002. ITRF2000: a new release of the International Terrestrial Reference frame for earth science applications. *Journal of Geophysical Research-solid Earth*, 107(B10):2214. doi:10.1029/2001JB000561. 23

Anguita, F. & Hernán, F., 2000. The Canary Islands origin: a unifying model. *Journal of Volcanology and Geothermal Research*, 103(1-4):1–26. doi:10.1016/S0377-0273(00) 00195-5. 14

Araña, V. & Ortiz, R., 1986. Marco geodinámico del volcanismo canario. *An. Fsica*, 82:202–231. 14

Baptista, M. A. & Miranda, J., 2009. Revision of the Portuguese catalog of tsunamis. *Hazards Earth Syst. Sci*, 9(1):25–42. doi:10.5194/nhess-9-25-2009. 9

Battaglia, J., Ferrazzini, V., Staudacher, T., Aki, K. & Cheminee, J. L., 2005. Pre-eruptive migration of earthquakes at the Piton de la Fournaise volcano (Reunion Island). *Geophysical Journal International*, 161(2):549–558. doi:10.1111/j.1365-246X.2005.02606.x. 2

Battaglia, M., Cervelli, P. F. & Murray, J. R., 2013. dMODELS: A MATLAB software package for modeling crustal deformation near active faults and volcanic centers. *Journal of Volcanology and Geothermal Research*, 254:1–4. doi:10.1016/j.jvolgeores.2012.12.018. 23

Bell, A. F. & Kilburn, C. R. J., 2012. Precursors to dyke-fed eruptions at basaltic volcanoes: insights from patterns of volcano-tectonic seismicity at Kilauea volcano, Hawaii. *Bulletin of Volcanology*, 74(2):325–339. ISSN 1432-0819. doi:10.1007/s00445-011-0519-3. 2

Benito-Saz, M. A., Parks, M. M., Sigmundsson, F., Hooper, A. & García-Cañada, L., 2017. Repeated magmatic intrusions at el hierro island following the 2011-2012 submarine eruption. *Journal of Volcanology and Geothermal Research*. ISSN 0377-0273. doi:10.1016/j.jvolgeores.2017.01.020. 23

Bezzeghoud, M., Adam, C., Buforn, E., Borges, J. F. & Caldeira, B., 2014. Seismicity along the Azores-Gibraltar region and global plate kinematics. *Journal of Seismology*, 18(2):205–220. doi:10.1007/s10950-013-9416-x. 5

van den Bogaard, P., 2013. The origin of the Canary Island Seamount Province - New ages of old seamounts. *Scientific Reports*, 2013(3):10–1038. doi:10.1038/srep02107. 9

Bonali, F. L., Tibaldi, A., Corazzato, C., Tormey, D. R. & Lara, L. E., 2013. Quantifying the effect of large earthquakes in promoting eruptions due to stress changes on magma pathway: The Chile case. *Tectonophysics*, 583:54–67. doi:10.1016/j.tecto.2012.10.025. 1

Bonnin, M., Nolet, G., Villaseñor, A., Gallart, J. & Thomas, C., 2014. Multiple-frequency tomography of the upper mantle beneath the African/Iberian collision zone. *Geophysical Journal International*, 198(3):1458. doi:10.1093/gji/ggu214. 9, 51

Boschetti, F., Dentith, M. D. & List, R. D., 1996. A fractal-based algorithm for detecting first arrivals on seismic traces. *Geophysics*, 61(4):1095–1102. doi:10.1190/1.1444030. 45

Brandsdóttir, B. & Einarsson, P., 1979. Seismic activity associated with the September 1977 deflation of the Krafla central volcano in northeastern Iceland. doi:10.1016/0377-0273(79)90001-5. 54

Bridges, D. L. & Gao, S., 2006. Spatial variation of seismic b-values beneath Makushin Volcano, Unalaska Island, Alaska. *Earth Planet Sci. Lett*, 245:408–415. 53

Brune, J. N., 1970. Tectonic stress and the spectra of seismic shear waves from earthquakes. *Journal of Geophysical Research*, 75(26):4997–5009. doi:10.1029/jb075i026p04997. 55

Cabañas, L., Rivas-Medina, A., Martínez-Solares, J. M., Gaspar-Escribano, J. M., Benito, B., Antón, R. & Ruiz-Barajas, S., 2015. Relationships Between M w and Other Earthquake Size Parameters in the Spanish IGN Seismic Catalog. *Pure and Applied Geophysics*, 172(9):2397–2410. doi:10.1007/s00024-014-1025-2. 8, 18

Carbó, A., Muñoz-Martín, A., Llanes, P. & Álvarez, J., 2003. Gravity analysis offshore the Canary Islands from a systematic survey. *Marine Geophysical Researches*, 24(1):113–127. ISSN 1573-0581. doi:10.1007/s11001-004-1336-2. 11, 12

Carracedo, J. C., Day, S., Guillou, H., Badiola, E. R., Canas, J. A. & Torrado, F. J. P., 1998. Hotspot volcanism close to a passive continental margin: the Canary Islands. *Geological Magazine*, 53(5):591–604. doi:10.1017/S0016756898001447. 14

Carracedo, J. C., Pérez, F. J., Ancochea, E., Meco, J., Hernán, F., Cubas, C. R., Casillas, R., Rodríguez, E., Spain, A. A., Gibbons, E., W & Moreno, T., 2002. Cenozoic volcanism II: The Canary Islands. En: *The Geology of Spain*, págs. 439–472. 14

Caudron, C., Taisne, B., Kugaenko, Y. & Saltykov, V., 2015. Magma migration at the onset of the 2012–13 Tolbachik eruption revealed by Seismic Amplitude Ratio Analysis. *J .Volcanol. Geotherm. Res*, 307(1):60–67. 2

Cerdeña, I. D., Del Fresno, C. & Moreno, A. G., 2014. Seismicity Patterns Prior to the 2011 El Hierro Eruption. *Bulletin of the Seismological Society of America*, 104(1):567–575. ISSN 0037-1106. doi:10.1785/0120130200. 35

REFERENCES

Cerdeña, I. D., Del Fresno, C. & Rivera, L., 2011. New insight on the increasing seismicity during Tenerife's 2004 volcanic reactivation. *Journal of Volcanology and Geothermal Research*, 206(1-2):15–29. doi:10.1016/j.jvolgeores.2011.06.005. 51

Chiarabba, C. & Moretti, M., 2006. An insight into the unrest phenomena at the Campi Flegrei caldera from Vp and Vp/Vs tomography. *Terra Nova*, 18(6):373–379. doi: 10.1111/j.1365-3121.2006.00701.x. 53, 54

Chouet, B. A., Matoza, R. S. & eruption, 2013. A multi-decadal view of seismic methods for detecting precursors of magma movement. *J Volcanol Geotherm Res*, 252:108–175. 55

Cornet, F. H., 1992. Fracture processes induced by forced fluid percolation. En: *IAVCEI Proceedings in Volcanology*, págs. 407–431. Springer Berlin Heidelberg. doi:10.1007/ 978-3-642-77008-1_26. 57

Cunha, T. A., Matias, L. M., Terrinha, P., Negredo, A. M., Rosas, F., Fernndes, R. M. S. & Pinheiro, L. M., 2012. Neotectonics of the SW Iberia margin, Gulf of Cadiz and Alboran Sea: a reassessment including recent structural, seismic and geodetic data. *Geophysical Journal International*, 188(3):850–872. ISSN 1365-246X. doi:10.1111/j.1365-246X. 2011.05328.x. 26

Dahm, T., Hainzl, S. & Fischer, T., 2010. Bidirectional and unidirectional fracture growth during hydrofracturing: Role of driving stress gradients. *Journal of Geophysical Research: Solid Earth*, 115(July):1–19. ISSN 21699356. doi:10.1029/2009JB006817. 53

Del Fresno, C., 2016. Determinación de la Fuente Sísmica a Distancias Regionales: Aplicación a la serie de El Hierro 2011, Universidad Complutense de Madrid, Spain, PhD Thesis. 35

Del Fresno, C., Cerdeña, I. D., Cesca, S. & Buforn, E., 2015. The 8 Octover 2011 Earthquake at El Hierro (Mw 4.0): Focal Mechanisms of the Mainshock and Its Foreshocks. *Bull Seism Soc Am*, 105(1):330–340. 39, 55

Del Fresno, C., Domínguez Cerdeã, I., Buforn, E. & Lpez, C., 2012. Función temporal (STF) del terremoto del 8 de Octubre de 2011 (Mw=4.0) en El Hierro (Islas Canarias). En: *7 Asamblea Hispano-Portuguesa de Geodesia y Geofisica*, tomo 2011. 55

Díaz-Moreno, A., Ibáñez, J., De Angelis, S., García-Yeguas, A., Prudencio, J., Morales, J., Tuvè, T. & García, L., 2015. Seismic hydraulic fracture migration originated by successive deep magma pulses: The 2011-2013 seismic series associated to the volcanic activity of El Hierro Island. *Journal of Geophysical Research: Solid Earth*. ISSN 21699313. doi:10.1002/2015JB012249. 53

Dieterich, J., 1994. A constitutive law for rate of earthquake production and its application to earthquake clustering. *Journal of Geophysical Research: Solid Earth*, 99(B2):2601–2618. ISSN 2156-2202. doi:10.1029/93JB02581. 18

Duggen, S., Hoernle, K., Hauff, F., Klügel, A., Bouabdellah, M. & Thirlwall, M., 2009. Flow of Canary mantle plume material through a subcontinental lithospheric corridor beneath Africa to the Mediterranean. *Geology*, 37(3):283–286. doi:10.1130/G25426A.1. 9

Efron, B. & Tibshirani, R., 1986. Bootstrap methods for standard errors, confidence intervals, and other. *Measures of Statistical Accuracy, Statist. Sci*, 1(1):54–75. 24

Einarsson, P., 1991. The Krafla rifting episode 1975-1989. En: *The Nature of Lake Myvatn*, págs. 97–139. Icelandic Nat. Sci. Soc., Reykjavik. 54

Endo, E. T. & Murray, T., 1991. Real-time seismic amplitude measurement (RSAM): A volcano monitoring tool. *Bulletin of Volcanology*, 53:533–545. 22

Fernandes, R. M. S., Miranda, J. M., Meijninger, B. M. L., Bos, M. S., Noomen, R., Bastos, L., Ambrosius, B. A. C. & Riva, R. E. M., 2007. Surface velocity field of the Ibero-Maghrebian segment of the Eurasia-Nubia plate boundary. *Geophysical Journal International*, 169(1):315–324. doi:10.1111/j.1365-246x.2006.03252.x. 30

Fischer, T. & Guest, A., 2011. Shear and tensile earthquakes caused by fluid injection. *Geophysical Research Letters*, 38(5). ISSN 1944-8007. doi:10.1029/2010GL045447. L05307. 57

Fullea, J., Camacho, A. G., Negredo, A. M. & Fernández, J., 2015. The Canary Islands hot spot: New insights from 3D coupled geophysical–petrological modelling of the lithosphere and uppermost mantle. *Earth and Planetary Science Letters*, 409:71–88. doi:10.1016/j.epsl.2014.10.038. 11, 51

Fuster, J. M., 1975. Las Islas Canarias: un ejemplo de evolucin temporal y espacial del vulcanismo ocenico. *Est. Geol*, 31:439–463. 14

García-Cañada, L., García-Arias, M. J., Pereda, J., Lamolda, H. & López, C., 2014. Different deformation patterns using GPS in the volcanic process of El hierro (Canary Island) 2011-2013. En: *EGU General Assembly Conference Abstracts*, tomo 16 de *EGU General Assembly Conference Abstracts*, pág. 15791. 23

García-Yeguas, A., Ibñez, J. M., Koulakov, I., Jakovlev, A., Romero-Ruiz, M. C. & Prudencio, J., 2014. Seismic tomography model reveals mantle magma sources of recent volcanic activity at El Hierro Island (Canary Islands, Spain). *Geophysical Journal International*, 199(3):1739. doi:10.1093/gji/ggu339. 12

Geyer, A., Mart, J. & Villase09or, A., 2016. First-order estimate of the Canary Islands plate-scale stress field: Implications for volcanic hazard assessment. *Tectonophysics*, 679:125 – 139. ISSN 0040-1951. doi:https://doi.org/10.1016/j.tecto.2016.04.010. 24, 51, 54

Gorbatikov, A. V., Montesinos, F. G., Arnoso, J., Stepanova, M. Y., Benavent, M. & Tsukanov, A. A., 2013. New Features in the Subsurface Structure Model of El Hierro Island (Canaries) from Low-Frequency Microseismic Sounding: An Insight into the 2011 Seismo-Volcanic Crisis. *Surveys In Geophysics*. doi:10.1007/s10712-013-9240-4. 11, 53

Green, R. G., Greenfield, T. & White, R. S., 2015. Triggered earthquakes suppressed by an evolving stress shadow from a propagating dyke. *Nat. Geosci*, 8(8):629–632. 55

Gutenberg, B. & Richter, C. F., 1944. Frequency of the earthquakes in california. *Bulletin of the Seismological Society of America*, 34(34):185–188. ISSN 0037-1106. 19

Hanks, T. C. & Kanamori, H., 1979. Moment magnitude scale. *Journal of Geophysical Research*, 84(NB5):2348–2350. doi:10.1029/JB084iB05p02348. 20

Heidbach, O., Tingay, M., Barth, A., Reinecker, J., Kurfe08, D. & Mller, B., 2008. The World Stress Map database release. doi:10.1594/GFZ.WSM.Rel2008. 24

Higuchi, T., 1988. Approach to an Irregular Time Series on the Basis of the Fractal Theory. *Phys. D*, 31(2):277–283. ISSN 0167-2789. doi:10.1016/0167-2789(88)90081-4. 21, 31

Hill, D. P., Langbein, J. O. & Prejean, S., 2003. Relations between seismicity and deformation during unrest in Long Valley. *J Volcanol Geotherm Res*, 127:175–193. 20

Hill D P, F. P. & Newhall, C., 2002. Earthquake-volcano interactions. *Phys. Today*, (55):41–47. doi:10.1063/1.1535006. 1

Hoernle, K. & Schmincke, H. U., 1993. The role of partial melting in the 15-Ma geochemical evolution of Gran Canaria: A blob model for the Canarian hotspot. *J. Pet*, 34:599–626. 14

Holik, J. S., Rabinowitz, P. D. & Austin, J. A., 1991. Effects of Canary hotspot volcanism on structure of oceanic crust off Morocco. *Journal of Geophysical Research: Solid Earth*, 96(B7):12039–12067. ISSN 2156-2202. doi:10.1029/91JB00709. 14

Hong, T.-K., Houng, S. E. & Jo, E., 2014. Temporal changes of medium properties during explosive volcanic eruption. *Geophysical Research Letters*, 41(6):1944–1950. ISSN 1944-8007. doi:10.1002/2014GL059408. 19, 54

Husen, S., Smith, R. B. & Waite, G. P., 2004. Evidence for gas and magmatic sources beneath the Yellowstone volcanic field from seismic tomographic imaging. *Journal of Volcanology and Geothermal Research*, 131(3-4):397–410. doi:10.1016/S0377-0273(03)00416-5. 54

Jackson, J. & McKenzie, D., 1988. The relationship between plate motions and seismic moment tensors, and the rates of active deformation in the Mediterranean and Middle East. *Geophys J Int*, 93:45–73. 20

Jiménez-Munt, I., Fernàndez, M., Torne, M. & Bird, P., 2001. The transition from linear to diffuse plate boundary in the Azores-Gibraltar region: results from a thin-sheet model. *Earth and Planetary Science Letters*, 192:175–189. 6, 24

Jiménez-Munt, I., Fernàndez, M., Vergés, J., Garcia-Castellanos, D., Fullea, J., Pérez-Gussinyé, M. & Afonso, J. C., 2011. Decoupled accomodation of africa-eurasia convergence in the nw-moroccan. *Journal of Geophysical Research*, 116(B8):10–1029. doi:10.1029/2010jb008105. 6

Johnson, J. H. & Poland, M. P., 2013. Seismic detection of increased degassing before Kīlaueas 2008 summit explosion. *Nature Communications*, 4:1668. doi:10.1038/ncomms2703. 53, 54

Klügel, A., Hansteen, T. H. & Galipp, K., 2005. Magma storage and underplating beneath Cumbre Vieja volcano, La Palma (Canary Islands). *Earth and Planetary Science Letters*, 236:211–226. doi:10.1016/j.epsl.2005.04.006. 11, 61

Kostrov, V., 1974. Seismic moment and energy of earthquakes, and seismic 04ow of rock. *Izv Acad Sci USSR Phys Solid Earth*, 1:23–44. 20

Koulakov, I., Gordeev, E. I., Dobretsov, N. L., Vernikovsky, V. A., Senyukov, S., Jakovlev, A. & Jaxybulatov, K., 2013. Rapid changes in magma storage beneath the klyuchevskoy group of volcanoes inferred from time-dependent seismic tomography. *Journal of Volcanology and Geothermal Research*, 263:75–91. doi:10.1016/j.jvolgeores.2012.10.014. 54, 55

Kustowski, B., Ekstr02m, G. & Dziewoński, A. M., 2008. The shear-wave velocity structure in the upper mantle beneath. *Geophysical Journal International*, 174(3):978–992. doi:10.1111/j.1365-246X.2008.03865.x. 9

Larson, K. M., Poland, M. & Miklius, A., 2010. Volcano monitoring using GPS: Developing data analysis strategies based on the June 2007 Kilauea Volcano intrusion and eruption. *Journal of Geophysical Research-solid Earth*, 115:B07406. doi:10.1029/2009JB007022. 55

Legendre, C. P., Meier, T., Lebedev, S., Friederich, W. & Viereck-G02tte, L., 2012. A shear wave velocity model of the European upper mantle from automated inversion of seismic shear and surface waveforms. *Geophysical Journal International*, 191(1):282–304. doi:10.1111/j.1365-246x.2012.05613.x. 11, 51

Lin, G. & Shearer, P. M., 2009. Evidence for water-filled cracks in earthquake source regions. *Geophysical Research Letters*, 36(17). ISSN 1944-8007. doi:10.1029/2009GL039098. L17315. 19

Lin, J. & Stein, R. S., 2004. Stress triggering in thrust and subduction earthquakes and stress interaction between the southern San Andreas and nearby thrust and strike-slip

faults. *Journal of Geophysical Research: Solid Earth*, 109(B2). ISSN 2156-2202. doi: 10.1029/2003JB002607. B02303. 24

Llanes, P., Muñoz, A., Muñoz-Martín, A., Acosta, J., Herranz, P., Carbó, A. & Palomo, C., 2003. Morphological and structural analysis in the Anaga offshore massif, Canary Islands: fractures and debris avalanches relationships. *Marine Geophysical Researches*, 24(1):91–112. ISSN 1573-0581. doi:10.1007/s11001-004-1335-3. 11, 12

López, C., Blanco, M. J., Abella, R., Brenes, B., Cabrera Rodríguez, V. M., Casas, B., Domínguez Cerdeña, I., Felpeto, A., Fernández de Villalta, M., del Fresno, C., García, O., García-Arias, M. J., García-Canada, L., Gomis Moreno, A., González-Alonso, E., Guzmán Pérez, J., Iribarren, I., López-Díaz, R., Luengo-Oroz, N., Meletlidis, S., Moreno, M., Moure, D., Pereda de Pablo, J., Rodero, C., Romero, E., Sainz-Maza, S., Sentre Domingo, M. A., Torres, P. A., Trigo, P. & Villasante-Marcos, V., 2012. Monitoring the volcanic unrest of El Hierro (Canary Islands) before the onset of the 2011-2012 submarine eruption. *Geophysical Research Letters*, 39:L13303. doi: 10.1029/2012GL051846. 2, 15, 16, 53

Lupi, M. & Miller, S. A., 2014. Short-lived tectonic switch mechanism for long-term pulses of volcanic activity after mega-thrust earthquakes. *Solid Earth*, 5:13–24. doi: 10.5194/se-5-13-2014. 1

Mandelbrot, B., 1967. How Long Is the Coast of Britain? Statistical Self-Similarity and Fractional Dimension. *Science*, 156(3775):636–638. ISSN 0036-8075. doi:10.1126/science.156.3775.636. 21

Manga, M. & Brodsky, E., 2006. Seismic triggering of eruptions in the far field: Volcanoes and geysers. *Annual Review of Earth and Planetary Sciences*, 34:263–291. doi:10.1146/annurev.earth.34.031405.125125. 1

Mantovani, E., Viti, M., Babbucci, D. & Albarello, D., 2007. Nubia-Eurasia kinematics: an alternative interpretation from Mediterranean and North Atlantic evidence. *Annals of Geophysics*, 50(3):341–366. 5

Martí, J., Castro, a., Rodriguez, C., Costa, F., Carrasquilla, S., Pedreira, R. & Bolos, X., 2013. Correlation of Magma Evolution and Geophysical Monitoring during the 2011-

2012 El Hierro (Canary Islands) Submarine Eruption. *Journal of Petrology*, 54(7):1349–1373. ISSN 0022-3530. doi:10.1093/petrology/egt014. 58

Martí, J., Pinel, V., López, C., Geyer, A., Abella, R., Tárraga, M., Blanco, M. J., Castro, A. & Rodríguez, C., 2013. Causes and mechanisms of the 2011C2012 El Hierro (Canary Islands) submarine eruption. *Journal of Geophysical Research: Solid Earth*, 118(3):823–839. doi:10.1002/jgrb.50087. 11, 15, 58

Martí, J., Villaseñor, A., Geyer, A., López, C. & Tryggvason, A., 2017. Stress barriers controlling lateral migration of magma revealed by seismic tomography. *Scientific Reports*, 7(40757):40757. doi:10.1038/srep40757. 12, 13, 53

Marzocchi, W., 2002. Remote seismic influence on large explosive eruptions. *Journal of Geophysical Research: Solid Earth*, 107(B1):EPM 6–1–EPM 6–7. ISSN 2156-2202. doi:10.1029/2001JB000307. 1

McNutt, S., 2005. Volcanic seismilogy. *Annu Rev Earth Planet Sci*, 32:461–491. 53

McNutt, S. R., 1996. Seismic monitoring of volcanoes: A review of the state-of-the-art and recent trends. En: Scarpa, R. & Tilling, R., eds., *Monitoring and Mitigation of Volcanic Hazards*, págs. 99–146. Springer-Verlag, Berlin. 58

Meletlidis, S., Roberto, A. D., Cerdeña, I. D., Pompilio, M., García-Cañada, L., Bertagnini, A., Benito-Saz, M. A., Carlo, P. D. & Sainz-Maza, S., 2015. New insight into the 2011-2012 unrest and eruption of El Hierro Island (Canary Islands) based on integrated geophysical, geodetical and petrological data. *Annals of Geophysics*, 58(5):S0546. doi:10.4401/ag-6754. 11

Meletlidis, S., Roberto, A. D., Pompilio, M., Bertagnini, A., Iribarren, I., Felpeto, A., Torres, P. A. & Oriano, C. D., 2012. Xenopumices from the 2011-2012 submarine eruption of El Hierro (Canary Islands, Spain): Constraints on the plumbing system and magma ascent. *Geophysical Research Letters*, 39:1–6. doi:10.1029/2012GL052675. 58

Miller, M. S., O'Driscoll, L. J., Butcher, A. J. & Thomas, C., 2015. Imaging Canary Island hotspot material beneath the lithosphere of Morocco and southern Spain. *Earth and Planetary Science Letters*, 431:186–194. ISSN 0012821X. doi:10.1016/j.epsl.2015.09.026. 51, 60

Miller, S. A., Collettini, C., Chiaraluce, L., Cocco, M., Barchi, M. R. & Kaus, B., 2004. Aftershocks driven by a high pressure CO2 source at depth. *Nature*, 427:724–727. 53

Mogi, K., 1958. Relations between the eruptions of various volcanoes and the deformations of the ground surface around. *Bull Earthquake Res Inst Univ Tokyo*, 36:99–134. 24

Montelli, R., Nolet, G., Dahlen, F. A. & Masters, G., 2006. A catalogue of deep mantle plumes: New results from finite-frequency tomography. *Geochemistry, Geophysics, Geosystems*, 7(11). ISSN 1525-2027. doi:10.1029/2006GC001248. Q11007. 9

Montesinos, F. G., Arnoso, J., Benavent, M. & Vieira, R., 2006. The crustal structure of El Hierro (Canary Islands) from 3-d gravity inversion. *Journal of Volcanology and Geothermal Research*, 150(1-3):283–299. doi:10.1016/j.jvolgeores.2005.07.018. 11

Moore, J. G. & Krivoy, H. L., 1964. The 1962 flank eruption of Kilauea volcano and structure of the east rift zone. *Journal of Geophysical Research*, 69(10):2033–2045. ISSN 2156-2202. doi:10.1029/JZ069i010p02033. 54

Murru, M., Console, R., Falcone, G., Montuori, C. & Sgroi, T., 2007. Spatial mapping of the b value at Mount Etna, Italy, using earthquake data recorded from 1999 to 2005. *Journal of Geophysical Research: Solid Earth*, 112(B12). ISSN 2156-2202. doi:10.1029/2006JB004791. B12303. 53

Okada, Y., 1992. Internal deformation due to shear and tensile faults in a half-space. *Bull Seismol Soc Am*, 82(2):1018–1040. 24

Padhy, 2004. Rescaled range fractal analysis of a seismogram for identification of signals from an earthquake. *S Curr Sci Asoc*, 87(5):637–641. 45

Patanè, D., Grazia, G. D., Cannata, A., Montalto, P. & Boschi, E., 2008. Shallow magma pathway geometry at Mt. Etna volcano. *Geochemistry, Geophysics, Geosystems*, 9(12). ISSN 1525-2027. doi:10.1029/2008GC002131. Q12021. 58

Patanè, G., La Delfa, S. & Tanguy, J. C., 2006. Volcanism and mantle-crust evolution: The Etna case. *Earth and Planetary Science Letters*, 241(3-4):831–843. doi:10.1016/j.epsl.2005.10.039. 53, 54

Peláez, J. A., Chourak, M., Tadili, B. A., Brahim, L. A., Hamdache, M., Casado, C. L. & Solares, J. M. M., 2007. A Catalog of Main Moroccan Earthquakes from 1045 to 2005. *Seismological Research Letters*, 78(6):614–621. doi:http://doi.org/10.1785/gssrl.78.6.614. 8, 17

Peréz, N. M., Hernández, P. A., Padron, E., Melian, G., Marrero, R., Padilla, G., Barrancos, J. & Nolasco, D., 2007. Precursory subsurface Rn-222 and Rn-220 degassing signatures of the 2004 seismic crisis at Tenerife, Canary Islands. *Pure and Applied Geophysics*, 164(12):2431–2448. doi:10.1007/s00024-007-0280-x. 51

Peréz, N. M., Padilla, G. D., Padron, E., Hernández, P. A., Melian, G. V., Barrancos, J., Dionis, S., Nolasco, D., Rodríguez, F., Calvo, D. & Hernández, I., 2012. Precursory diffuse CO2 and H2S emission signatures of the 2011-2012 El Hierro submarine eruption, Canary Islands. *Geophysical Research Letters*, 39:L16311. doi:10.1029/2012GL052410. 57

Ranero, C. R., Torne, M. & Banda, E., 1995. Gravity and multichannel seismic reflection constraints on the lithospheric structure of the Canary Swell. *Marine Geophysical Researches*, 17(6):519–534. ISSN 0025-3235. doi:10.1007/BF01204342. 15

Rivera, J., Lastras, G., Canals, M., Acosta, J., Arrese, B., Hermida, N., Micallef, a., Tello, O. & Amblas, D., 2013. Construction of an oceanic island: Insights from the El Hierro (Canary Islands) 2011-2012 submarine volcanic eruption. *Geology*, 41(January):355–358. ISSN 00917613. doi:10.1130/G33863.1. 16

Roman, D. C. & Heron, P., 2007. Effect of regional tectonic setting on local fault response to episodes of volcanic activity. *Geophysical Research Letters*, 34(13). doi:10.1029/2007gl030222. 54

Roman, D. C., Rodgers, M., Geirsson, H., LaFemina, P. C. & Tenorio, V., 2016. Assessing the likelihood and magnitude of volcanic explosions based on seismic quiescence. *Earth and Planetary Science Letters*, 450:20–28. 2

Romero, R., 2000. Actividad volcanica historica en Las Islas Canarias. En: Astiz, M. & García, A., eds., *Curso Internacional de Volcanologia y Geofisica volcanica*, págs. 115–128. 14

Rosas, F., Duarte, J., Neves, M., Terrinha, P., Silva, S., Matias, L., Gràcia, E. & Bartolome, R., 2012. Thrust–wrench interference between major active faults in the Gulf of Cadiz (Africa–Eurasia plate boundary, offshore SW Iberia): Tectonic implications from coupled analog and numerical modeling. *Tectonophysics*, 548-549(549):1–21. doi: 10.1016/j.tecto.2012.04.013. 26

Rubin, A. M., Gillard, D. & Got, J.-L., 1998. A reinterpretation of seismicity associated with the January 1983 dike intrusion at Kilauea Volcano, Hawaii. *Journal of Geophysical Research: Solid Earth*, 103(B5):10003–10015. ISSN 2156-2202. doi: 10.1029/97JB03513. 54

Saki, M., Thomas, C., Nippress, S. E. J. & Lessing, S., 2015. Topography of upper mantle seismic discontinuities beneath the North Atlantic: The Azores, Canary and Cape Verde plumes. *Earth and Planetary Science Letters*, 409:193–202. doi:10.1016/j.epsl.2014.10.052. 9, 51

Scordilis, E. M., 2006. Empirical Global Relations Converting M_S and mb to Moment Magnitude. *Journal of Seismology*, 10(2):225–236. ISSN 1573-157X. doi:10.1007/s10950-006-9012-4. 18

Segall, P., 2013. Volcano deformation and eruption forecasting. *Geological Society, London, Special Publications*, 380(1):85–106. ISSN 0305-8719. doi:10.1144/SP380.4. 19

Serpelloni, E., Vannucci, G., Pondrelli, S., Argnani, a., Casula, G., Anzidei, M., Baldi, P. & Gasperini, P., 2007. Kinematics of the Western Africa-Eurasia plate boundary from focal mechanisms and GPS data. *Geophysical Journal International*, 169(3):1180–1200. ISSN 0956540X. doi:10.1111/j.1365-246X.2007.03367.x. 5, 6

Shapiro, S. A., Huenges, E. & Borm, G., 1997. Estimating the crust permeability from fluid-injection-induced seismic emission at the KTB site. *Geophysical Journal International*, 131(2):F15–F18. ISSN 1365-246X. doi:10.1111/j.1365-246X.1997.tb01215.x. 53

Sigmarsson, O., Laporte, D., Carpentier, M., Devouard, B., Devidal, J.-L. & Marti, J., 2012. Formation of U-depleted rhyolite from a basanite at El Hierro, Canary Islands. *Contributions to Mineralogy and Petrology*, 165(3):601–622. ISSN 0010-7999. doi: 10.1007/s00410-012-0826-5. 58

Sigmundsson, F., Hooper, A., Hreinsdóttir, S., Vogfjörd, K. S., Ófeigsson, B. G., Heimisson, E. R., Dumont, S., Parks, M., Spaans, K., Gudmundsson, G. B., Drouin, V., Árnadóttir, T., Jónsdóttir, K., Gudmundsson, M. T., Högnadóttir, T., Fridriksdóttir, H. M., Hensch, M., Einarsson, P., Magnússon, E., Samsonov, S., Brandsdóttir, B., White, R. S., Ágústsdóttir, T., Greenfield, T., Green, R. G., Hjartardóttir, Á. R., Pedersen, R., Bennett, R. A., Geirsson, H., Femina, P. C. L., Björnsson, H., Pálsson, F., Sturkell, E., Bean, C. J., Möllhoff, M., Braiden, A. K. & Eibl, E. P. S., 2015. Segmented lateral dyke growth in a rifting event at Bárarbunga volcanic system, Iceland. *Nature*, 517(7533):191–195. doi:10.1038/nature14111. 2

Simmons, N. A., Myers, S. C., Johannesson, G. & Matzel, E., 2012. Llnl-g3dv3: Global p-wave tomography model for improved regional and teleseismic travel time prediction. *Journal of Geophysical Research: Solid Earth*, 117(B10). doi:10.1029/2012JB009525. 9

Stich, D., Serpelloni, E., Mancilla, F. d. L. & Morales, J., 2006. Kinematics of the iberia-maghreb plate contact from seismic moment tensors and gps observations. *Tectonophysics*, 426(3-4):295–317. doi:10.1016/j.tecto.2006.08.004. 20

Stroncik, N. A., Klügel, A. & Hansteen, T. H., 2009. The magmatic plumbing system beneath El Hierro (Canary Islands): constraints from phenocrysts and naturally quenched basaltic glasses in submarine rocks. *Contributions to Mineralogy and Petrology*, 157:593–607. doi:10.1007/s00410-008-0354-5. 11, 12, 61

T., L. A. & Selwyn, S. I., 1998. Triggering of volcanic eruptions. *Nature*, 398. 1

Terrinha, P., Matias, L., Vicente, J., Duarte, J., Luís, J., Pinheiro, L., Lourenço, N., Diez, S., Rosas, F., Magalhães, V., Valadares, V., Zitellini, N., Roque, C. & Víctor, L. M., 2009. Morphotectonics and strain partitioning at the Iberia–Africa plate boundary from multibeam and seismic reflection data. *Marine Geology*, 267(3-4):156–174. doi:10.1016/j.margeo.2009.09.012. 26

Toda, S., Stein, R. S., Richards-Dinger, K. & Bozkurt, S. B., 2005. Forecasting the evolution of seismicity in southern California: Animations built on earthquake stress transfer. *Journal of Geophysical Research: Solid Earth*, 110(B5). ISSN 2156-2202. doi:10.1029/2004JB003415. B05S16. 24

Toda, S., Stein, R. S. & Sagiya, T., 2002. Evidence from the AD 2000 Izu islands earthquake swarm that stressing rate governs seismicity. *Nature*, 419(September):58–61. 53, 54

Tosi, P., Barba, S., Rubeis, V. D. & Luccio, F. D., 1999. Seismic signal detection by fractal dimension analysis. En: *Bull Seismol Soc Am*, tomo 89, págs. 970–977. 45

Traversa, P., Pinel, V. & Grasso, J. R., 2010. A constant influx model for dike propagation: Implications for magma reservoir dynamics. *Journal of Geophysical Research: Solid Earth*, 115:1–19. ISSN 21699356. doi:10.1029/2009JB006559. 41, 42

Tregoning, P. & Herring, T. A., 2006. Impact of a priori zenith hydrostatic delay errors on GPS estimates of station heights and zenith total delays. *Geophysical Research Letters*, 33(23). ISSN 1944-8007. doi:10.1029/2006GL027706. L23303. 55

Troll, V. R., Klgel, A., Longpré, M.-A., Burchardt, S., Deegan, F. M., Carracedo, J. C., Wiesmaier, S., Kueppers, U., Dahren, B., Blythe, L. S., Hansteen, T., Freda, C., Budd, D. A., Jolis, E. M., Jonsson, E., Meade, F., Berg, S., Mancini, L. & Polacci, M., 2011. Floating sandstones off El Hierro (Canary Islands, Spain): the peculiar case of the October 2011 eruption. *Solid Earth Discussions*, 3(2):975–999. doi: 10.5194/sed-3-975-2011. 58

Turcotte, D. L., 2007. *Fractals and Chaos in Geology and Geophysics: Second Edition*. Cambridge Univ Pr. ISBN 0521567335. 2nd edition. 21

Unglert, K., Savage, M. K., Fournier, N., Ohkura, T. & Abe, Y., 2011. Shear wave splitting, v_P/v_S, and GPS during a time of enhanced activity at Aso caldera, Kyushu. *Journal of Geophysical Research: Solid Earth*, 116(B11):n/a–n/a. ISSN 2156-2202. doi:10.1029/2011JB008520. B11203. 53

Vannucci, G. & Gasperini, P., 2004. The new release of the database of Earthquake Mechanisms of the Mediterranean Area (EMMA Version 2). *Annals of Geophysics*, 47(1 Sup.). ISSN 2037-416X. doi:10.4401/ag-3277. 17

Vanorio, T., Virieux, J., Capuano, P. & Russo, G., 2005. Three-dimensional seismic tomography from P wave and S wave microearthquake travel times and rock physics characterization of the Campi Flegrei Caldera. *Journal of Geophysical Research: Solid Earth*, 110(B3). ISSN 2156-2202. doi:10.1029/2004JB003102. B03201. 54

Vinciguerra, S., 2002. Damage mechanics preceding the September-October 1989 flank eruption at Mount Etna volcano inferred by seismic scaling exponents. *Journal of Volcanology and Geothermal Research*, 113(3-4):391–397. 2

Walter, T. R. & Amelung, F., 2007. Volcanic eruptions following M $\geq$ 9 megathrust earthquakes: Implications for the Sumatra-Andaman volcanoes. *Geology*, 35:539–542. 1, 55

Wassermann, J., 2012. Volcano seismology. En: *Manual of Seismological Observatory Practice 2 (NMSOP-2*. Editor:In: Bormann, P. (Ed. 22

Watts, A. B., 1994. Crustal Structure, Gravity Anomalies and Flexure of the Lithosphere in the vicinity of the Canary Islands. *Geophysical Journal International*, 119(2):648–666. doi:10.1111/j.1365-246X.1994.tb00147.x. 15, 20, 24, 48

Watts, A. B., Peirce, C., Collier, J., Dalwood, R., Canales, J. P. & Henstock, T. J., 1997. A seismic study of lithospheric flexure in the vicinity of Tenerife, Canary Islands. *Earth and Planetary Science Letters*, 146(3-4):431–447. 20, 24, 48

Wiemer, S., 2001. A software package to analyze seismicity: ZMAP. *Seismological Research Letters*, 72(3):373–382. doi:10.1785/gssrl.72.3.373. 20

Wiemer, S. & Wyss, M., 2002. Mapping spatial variability of the frequency-magnitude distribution of earthquakes. *Advances in Geophysics*, 45:259–302. 53

Williams, S. D. P., 2008. CATS: GPS coordinate time series analysis software. *Gps Solutions*, 12(2):147–153. doi:10.1007/s10291-007-0086-4. 31

Zhao, D., 2007. Seismic images under 60 hotspots: Search for mantle plumes. *Gondwana Research*, 12(4):335 – 355. ISSN 1342-937X. doi:https://doi.org/10.1016/j.gr.2007.03.001. 9

APPENDIX

A

Early signs of Unrest

López C., L. García-Cañada, J. Martí, and I. Domínguez Cerdeña (2017), Early signs of geodynamic activity before the 2011–2012 El Hierro eruption, Journal of Geodynamics, 104, 1-14, doi: http://dx.doi.org/10.1016/j.jog.2016.12.005.

Journal of Geodynamics 104 (2017) 1–14

Contents lists available at ScienceDirect

Journal of Geodynamics

journal homepage: http://www.elsevier.com/locate/jog

Early signs of geodynamic activity before the 2011–2012 El Hierro eruption

Carmen López [a,*], Laura García-Cañada [a], Joan Martí [b], Itahiza Domínguez Cerdeña [c]

[a] Instituto Geográfico Nacional (IGN), C/Alfonso XII, 3, 28014 Madrid, Spain
[b] Group of Volcanology (GVB-CSIC), SIMGEO (UB-CSIC), Institute of Earth Sciences Jaume Almera, Lluis Solé Sabaris s/n, 08020, Barcelona, Spain
[c] Instituto Geográfico Nacional (IGN), C/La Marina 20, 2ª, 38001 Santa Cruz de Tenerife, Spain

ARTICLE INFO

Article history:
Received 28 July 2016
Received in revised form 5 December 2016
Accepted 5 December 2016
Available online 15 December 2016

Keywords:
Volcanic unrest
Tectonic activity
Mantle plume dynamics
El Hierro eruption
Canary Islands

ABSTRACT

The potential relation between mantle plume dynamics, regional tectonics and eruptive activity in the Canary Islands has not been studied yet through the analysis of long-time series of geophysical observational data. The existence of highly reliable seismic and geodetic data has enabled us to study from 1996 to 2014 the geodynamic evolution of the North Atlantic Azores-Gibraltar region (including the NW African margin) and its relationship with recent volcanic activity in El Hierro (Canary Islands). We compiled a new and unified regional seismic catalog and used long time-series of digital 3D surface displacements recorded by permanent GPS stations in the region. A joint regional- and local-scale analysis based on these data enabled us to identify signs of anomalous tectonic activity from 2003 onwards, whose intensity increased in 2007 and finally accelerated three months before the onset of the volcanic eruption on El Hierro in October 2011. Activity included the occurrence of regional extension and an uplift process affecting the southern Iberian Peninsula, NW Africa, and the Canary Islands. We interpret these observations as early signs of the geodynamic activity, which led to El Hierro eruption and the subsequent episodes of magma intrusion. Results point to the significant contribution of the mantle plume dynamics (i.e. external forces) in this renewed volcanic activity in the Canary Islands and emphasize the role of mantle dynamics in controlling regional tectonics.

1. Introduction

The relationship between tectonism and magmatism has been proven on many occasions and, in terms of global geodynamics, are clearly associated at plate boundary sites (McKenzie and Bickle, 1988; White and McKenzie, 1989; Thomson and Connolly, 1995; Foulger, 2010). Less obvious but still concurrent is the relationship between these processes in intraplate volcanic areas located far from active plate margins. In such environments, magmatism and tectonism seem to be associated with mantle plumes. Some geodynamic models propose that intraplate tectonics is driven by these asthenospheric upwellings, since mantle plumes potentially exert an important control on mantle dynamics and magmatic pulses (e.g. Zhao et al., 2006). By contrast, some authors claim that mantle dynamics in these areas respond to plate boundary processes or lithospheric thinning that create lithospheric instabilities and favor asthenospheric upwelling (e.g. Fourel et al., 2013); in these cases, the mantle reacts 'passively' to the pulses of regional tectonics

Nevertheless, a closer look at the relationship between tectonics and volcanism reveals increasing evidence in intraplate volcanic systems of the fundamental role played by stress variations in initiating volcanic unrest (i.e. a deviation from the background or baseline behavior of a volcano, Phillipson et al., 2013) and eruption (Linde and Sacks, 1998; Hill et al., 2002; Marzocchi et al., 2002; Manga and Brodsky, 2006; Walter and Amelung, 2007; Bebbington and Marzocchi, 2011; Lara et al., 2004; Eggert and Walter, 2009; Bonali et al., 2013; Lupi and Miller, 2014). Despite a number of examples (e.g. Cembrano and Lara, 2009; Legrand et al., 2011), it is much less clear how this potential relationship works in monogenetic volcanic systems.

The Canary Islands offer a good example of intraplate magmatism in which it is still a matter of controversy whether a mantle plume or regional tectonics (or a combination of both) are the main cause of magma generation and, consequently, of volcanism (Le Pichon and Fox, 1971; Anguita and Hernán, 1975, 2000; Schmincke, 1982; Araña and Ortiz, 1991; Hoernle and Schmincke,

* Corresponding author.
E-mail address: clmoreno@fomento.es (C. López).

http://dx.doi.org/10.1016/j.jog.2016.12.005
0264-3707/

1993; Carracedo et al., 1998). Evidence for the existence of a mantle plume below the Canary Islands has been provided by several authors (Hollik et al., 1991; Hoernle et al., 1995; Geldmacher et al., 2001; Duggen et al., 2009; Mériaux et al., 2015; French and Romanowicz, 2015). Likewise, signs of tectonic activity in the Canary Islands and the vicinity have clearly been identified in the geological record and in present-day seismicity (Hernández-Pacheco and Ibarrola, 1973; Emery and Uchupi, 1984; Dañobeitia and Collette, 1989; Anguita et al., 1991; Mezcua et al., 1992; Marinoni and Pasquarè, 1994; Piqué et al., 1998; Dañobeitia and Canales, 2000; Mantovani et al., 2007; Domínguez-Cerdeña et al., 2012). However, the potential relation between these two geodynamic processes has never been established, probably in part because the eruption frequency in these islands is relatively low (16 eruptions in the past 600 years) and the fact that data from instrumental monitoring data has only been available for the last years.

The 2011–2012 El Hierro eruption and subsequent episodes of magmatic intrusion occurred in that island may shed new light on this issue. This latest eruption occurred 40 years after the eruption of Teneguia on La Palma in 1971 and is the only event in the Canaries that has ever been fully recorded by a local monitoring network (López et al., 2012). During the pre-eruptive unrest (19 July–10 October, 2011), a batch of deep magma that had accumulated at a shallow depth below El Hierro Island, migrated laterally from north to south below the crust for over 20 km before erupting (Martí et al., 2013). The resulting eruption was submarine and lasted until early March 2012. It was followed (2012–2014) by several further episodes of volcanic unrest that, although in some cases more intense than the pre-eruptive unrest, did not culminate in further eruptions (Telesca et al., 2016).

The purpose of this paper is to analyze quantitatively whether the El Hierro eruption was preceded by any precursory tectonic activity and which driving forces acting in the area could have contributed in this renewed volcanism in the Canary Islands.

2. Geodynamic context

The Canary Archipelago consists of seven main volcanic islands and several islets lying in a chain extending for ~500 km across the eastern Atlantic, whose eastern edge is only 100 km from the northwest coast of Africa. The origin of its magmatism is still controversial and several hypotheses, including a mantle plume hotspot (Hollik et al., 1991; Hoernle and Schminke, 1993; Carracedo et al., 1998), a local extensional ridge model (Fuster, 1975), and an uplifted tectonic block model (Araña and Ortiz, 1991), have been mooted to explain its geological features. Additional petrological, geophysical, and geochemical evidence from its sub-lithospheric mantle have even provided evidence for other possible explanations including those reported by Anguita and Hernán (2000), who unify in a single model thermal mantle anomaly features and the critical role of regional fractures and tectonic forces at the onset of magmatic activity.

This volcanic archipelago is constructed on the passive continental margin of the African Plate on Jurassic oceanic lithosphere (e.g. Carracedo et al., 2002) in a tectonic region that is, nevertheless, bounded by very active plate boundaries (Fig. 1). Those boundaries include the oceanic Mid-Atlantic Ridge to the west and the transition to the north from an oceanic (the Azores, the Gloria Fault, and the Gorringe Bank) to a continental boundary where Iberia and Africa meet. Its boundaries are clearly defined in its oceanic part and stretch from the Azores along the Azores-Gibraltar fault to approximately 11°W (west of the Strait of Gibraltar). The boundary from 11°W to 3.5°E, including the Strait of Gibraltar, the Alboran Sea, northern Morocco, and western Algeria, is more diffuse and forms a broader area of deformation. To the southeast, the region also includes the Atlas sub-plate (Morocco) consisting of continental lithosphere that is likewise subject to active deformation (Serpelloni et al., 2007; Mantovani et al., 2007; Bezzeghoud et al., 2014; Geyer et al., 2016).

Following the classification used by several authors (e.g. Bezzeghoud et al., 2014), the whole area can be divided into seven regions (Fig. 1), each characterized by coherent seismic and kinematic properties. From west-to-east and north-to-south these regions are as follows: the Mid-Atlantic Ridge including the Azores Triple Junction (MAR-ATJ); the Azores Islands from Faial-Terceira to the island of San Miguel (ATSM); the Gloria Fault (GF); the Gorringe Bank as far as Cadiz (GB); the Betic Mountains, the Rif Cordilleras, and the Alboran Sea (BALB); the Atlas Mountains (ATL); and the Canary Islands (CAN).

Crustal seismicity and GPS deformation studies (Jiménez-Munt et al., 2001; Jiménez-Munt and Negredo, 2003; Serpelloni et al., 2007; Jiménez-Munt et al., 2011; Cunha et al., 2012; Bezzeghoud et al., 2014) have been used to identify the kinematic behavior of each region. From west-to-east, there is a quite simple deformation field characterized by an extension running perpendicular to the Mid-Atlantic and Terceira Ridges. As well, there is a right-lateral strike-slip motion along the Gloria transform faults, which becomes the dominant compressive regime running eastwards from the Gorringe Bank area to Algeria, where the continental lithosphere becomes involved. The border running from the Azores to Algeria has recently been the site of major earthquakes (moment magnitude $M_W \geq 7.0$). Major seismic activity includes events on the Azores-Gibraltar fracture zone (1931 7.0 M_W, Ribeiro et al., 1996; 1975 7.9 M_W, Lynnes and Ruff, 1985), Santa María (1939 7.0 M_W, Moreira, 1985), the Gloria Fault (1941 8.4 M_W, Moreira, 1985), the Atlantic Ocean (1969 7.8 M_W, Grimison and Chen, 1986) and El Asnam in North Africa (1980 7.2 M_W, Kanamori and Given, 1982). Deformation rates range from 5 mm/year in the Mid-Atlantic region but decrease eastward to values of 2.7–3.9 mm/year in Algeria in a NW-SE direction.

The other main active volcanic regions in this area are the Azores Archipelago, located at the intersection of the Mid-Atlantic Ridge and the North American, Eurasian, and African Plates, and the Cape Verde Archipelago, located to the south, 450–600 km off the west coast of Africa. Table 1 is a compilation of all known volcanic activity (eruptive and unrest episodes) that has taken place in the Azores, Canary, and Cape Verde archipelagos since 1900.

3. Data

The existence of highly reliable regional and global databases of recent seismic and geodetic data from the Atlantic Ridge, the Azores, and the Ibero-Maghrebian region enabled us to compile a new, unified (using the same magnitude scale and not including duplicated event solutions) seismic catalog and to analyze long GPS 3D time-series of data. Despite the progressive installation since the 1990s of many permanent seismic and GPS stations, and the subsequent improvement in data availability, until 1996 seismic and GPS networks did not contain enough stations to ensure robust and reliable medium-magnitude earthquakes location and GPS positioning. Therefore, in order to ensure the homogeneity and accuracy of the observational data we selected 1996 as the starting date for our comparative analysis, which ended after the El Hierro eruption on 2012.

3.1. Seismic data

The first step was to compile a unified seismic catalog by searching for global and regional agencies that could provide seismic

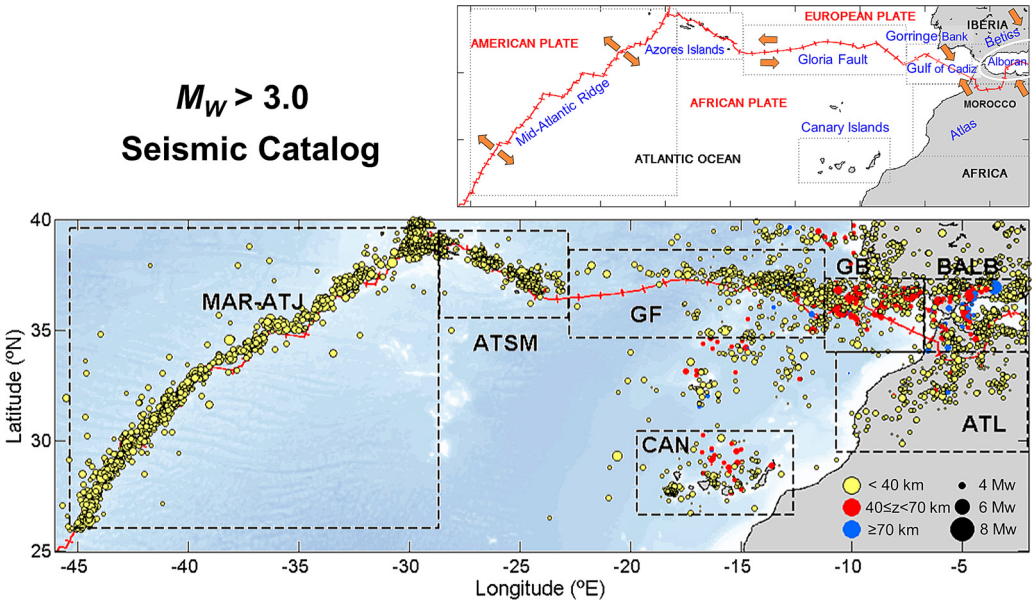

Fig. 1. M_W > 3.0 earthquake distribution in 1996–2014 (4262 events). Symbol size reflects event magnitude, with colors ranging from yellow to blue depending on the event depth. Bathymetry and topography from the National Geophysical Data Centre (NOAA). Dashed rectangles mark the boundaries of the regions considered in this study. (For interpretation of the references to colour in this figure legend, the reader is referred to the web version of this article.)

locations. We needed to compile data from different sources to cover the entire area and the full time period. We used the following six sources:

1. *IGN, Instituto Geográfico Nacional, Spain*. On-line bulletin, http://www.ign.es. The IGN provides preliminary and final seismic locations for the whole Ibero-Maghrebian region (26°N–45°N, 20°W–6°E).
2. *ISC, International Seismological Centre*. On-line bulletin, http://www.isc.ac.uk (United Kingdom, 2014). This center collates and recalculates earthquake locations from national and local agencies, and provides solutions for the region. When available, we used the ISC-GEM Catalog.
3. The *North Moroccan Earthquake Catalog* of seismic hazard assessment (Peláez et al., 2007) consists of records of seismicity occurring in northern Morocco (27°N–37°N, 15°W–1°E) in the period 1045–2006.
4. The on-line database of *Earthquake Mechanism for European Area* (EMMA) (Vannucci and Gasperini, 2004), a complete compilation of reliable solutions available in the literature for all events occurred before 2004.
5. GCMT, *Global Centroid Moment Tensor Database* (formerly, Harvard CMT), USA. This website provides moment tensors for earthquakes of a magnitude $M > 5$ from throughout the world.
6. A revision of the IGN Seismic Catalog by Cabañas et al. (2015) as part of a hazard assessment in the Iberian Peninsula, which includes empirical relationships for different magnitude formulas with M_W.

The search of these seismic catalogs generated a huge dataset of earthquakes, with many duplicated entries for origin time and hypocentral location, as well as several different scales for magnitude values (moment magnitude-M_W, surface wave magnitude-M_S, body wave magnitude-m_b, duration magnitude-M_D, and local magnitudes M_L and *mbLg*). The final solutions were selected according to a prioritization based on the reliability and the level of revision of the sources. A special effort was made to homogenize magnitudes. The most reliable m_b, M_S, M_W, or M_D from global agencies and M_L, *mbLg*, M_W, m_b, or M_D from local observatories were selected. We assumed $(M_b, M_S, M_W)_{NEIC} \approx (M_b, M_S, M_W)_{ISC}$, and $M_{W,HARVARD/GCMT} \approx M_{W,NEIC}$, with only a little deviation, as shown by Scordilis (2006). We also assumed $M_L = M_W$ ($M_L < 6.5$), following the criteria used by Heaton et al. (1986). In the case of the IGN catalog, we used the empirical relationships established by Cabañas et al. (2015) between the successive IGN magnitude (*mbLg*, m_b) formulas with M_W. For other agencies, we computed *logMo* using the relationships established by Johnston (1996) between seismic moments, *Mo*, and different magnitudes:

$$\log Mo = 24.66 - 1.883 * M_S + 0.192 * M_S^2 (3.5 < M_S < 7.5); \quad (1)$$

$$\log Mo = 18.28 + 0.679 * m_b + 0.077 * m_b^2 (3.5 < m_b < 6.5); \quad (2)$$

$$\log Mo = 17.76 + 0.360 * mbLg + 0.140 * mbLg^2 \quad (3.5 < mbLg < 6.0); \quad (3)$$

$$M_W = 2/3 * \log Mo - 10.7; \quad (4)$$

where M_D was the reported magnitude and *mbLg* the initially computed magnitude using the empirical relationship established by Mouayn et al. (2004).

$$M_D = 0.91 * mbLg + 0.32 (2.5 < mbLg < 5.5); \quad (5)$$

Fig. 1 shows the geographical distribution of the selected seismic events (M_W > 3.0, from 1996 to 2014) in the dataset. We recognized the shallow character of the seismic activity (depth < 40 km) in MAR-ATJ and ATSM and the intermediate character (40 km < depth < 70 km) of the seismicity located in GB, BALB and ATL. Cunha et al. (2012) interpreted this intermediate seismicity between Gloria Fault and North Algeria as related to the shortening and wrenching between northern Algeria–Morocco and southern Spain, and between NW Morocco and SW Iberia. This convergence would be accommodated along NNE–SSW to NE–SW and ENE–WSW thrust faults and WNW–ESE right-lateral strike-slip faults releasing intermediate earthquakes (Terrinha et al., 2009;

Table 1
Volcanic activity in the Azores, Canary, and Cape Verde Islands since 1990. Smithsonian refers to the Global Volcanism Program (http://www.volcano.si.edu/).

Start date	End date	Eruption certainty	VEI	Evidence	Azores	lat°N	lon°W	Source
1902/05/07	1902/05/08	Confirmed	0	Historical observations	Submarine vent 20 km SW of Terceira	38.65°	28.08°	Smithsonian
1907/04/01	Unknown	Confirmed	0	Historical observations	Monaco Bank	37.6°	25.88°	Smithsonian
1907	Unknown	Confirmed	0	Historical observations	San Jorge	38.65°	28.08°	Smithsonian
1911/03/07	Unknown	Confirmed	1	Historical observations	Monaco Bank	37.6°	25.88°	Smithsonian
1957/09/27	1958/10/24	Confirmed	2	Historical Observations	West flank (Capelinhos) and summit	38.6°	28.73°	Smithsonian
1988/05/?	1989/01/?			Seismic unrest	Volcanic unrest Agua de Pau Volcano, San Miguel			Additional Report for Azores-Gibraltar Fracture Zone
1998/11/25?	2000/03/?	Confirmed	0	Historical observations	Submarine vent W of Terceira, Serreta Ridge	38.73°	27.32°	Smithsonian
2003/04/26	2007/01/01			Seismic unrest	Volcanic unrest San Miguel			Wallenstein et al. (2009) Silva et al. (2015)
2011/09/15	2012			Seismic and deformation unrest	Volcanic unrest Fogo, San Miguel			Okada et al. (2015)
Start date	End date	Eruption certainty	VEI	Evidence	Canary Islands	lat°N	lon°W	Source
1909/11/18	1909/11/27	Confirmed	2	Historical observations	NW rift zone (Chinyero),Tenerife	28.27°	16.64°	Smithsonian
1949/06/24	1949/07/30	Confirmed	2	Historical observations	San Juan, Llano del Banco, Hoyo Negro, La Palma	28.57°	17.83°	Smithsonian
1971/10/26	1971/11/18	Confirmed	2	Historical observations	Teneguia La Palma	28.57°	17.83°	Smithsonian
1989/05/09				Seismic unrest	Volcanic unrest Tenerife			Vinciguerra and Day, (2013)
2004/05/12	2005/05/18			Seismic unrest	Volcanic unrest Tenerife			Domínguez-Cerdeña et al. (2012)
2011/10/10	2012/03/05	Confirmed	2	Seismic and deformation unrest	Submarine S flank El Hierro	27.73°	18.03°	Smithsonian
Start date	End date	Eruption certainty	VEI	Evidence	Cape Verde	lat°N	lon°W	Source
1909	Unknown	Confirmed		Historical Observations	Fogo	14.95°	24.35°	Smithsonian
1951/06/12	1951/08/21	Confirmed	2	Historical Observations	Northwest and south caldera floor Fogo	14.95°	24.35°	Smithsonian
1995/04/02	1995/05/26	Confirmed	2	Historical Observations	WSW flank of Pico Fogo	14.95°	24.35°	Smithsonian
2014/11/23	2015/02/08	Confirmed			Northwest and south caldera floor Fogo	14.95°	24.35°	Smithsonian

Cunha et al., 2012; Rosas et al., 2012). Besides the intermediate seismic activity at the Nubia-Eurasia Plate boundary, we found seismicity located deeper than 40 km in the Canaries. We calculated the Gutenberg-Richter *b* parameter (the relationship between the magnitude and the total number of earthquakes of at least that magnitude in a specific region and time period) corresponding to the entire catalog, and the spatial distribution of the magnitude of completeness M_C (ZMAP Analysis Tool software, Wiemer, 2001). For the period 1996–2014, the catalog gave $M_C = 2.8$ Mw, and $b = 0.9$ as a maximum likelihood solution (Fig. 2).

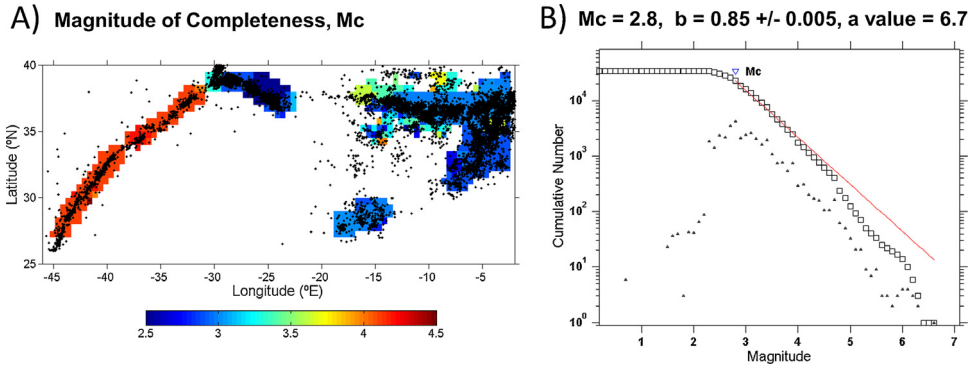

Fig. 2. Left-hand panel: completeness magnitude distribution (using ZMAP software, the maximum curvature method, a constant radius of 100 km and a minimum number of 40 events above Mc) in a $0.5^\circ \times 0.5^\circ$ grid covering the study area. Seismicity locations marked with black dots. Right-hand panel: frequency-magnitude distribution, *b-value*, and M_C for the whole seismic catalog.

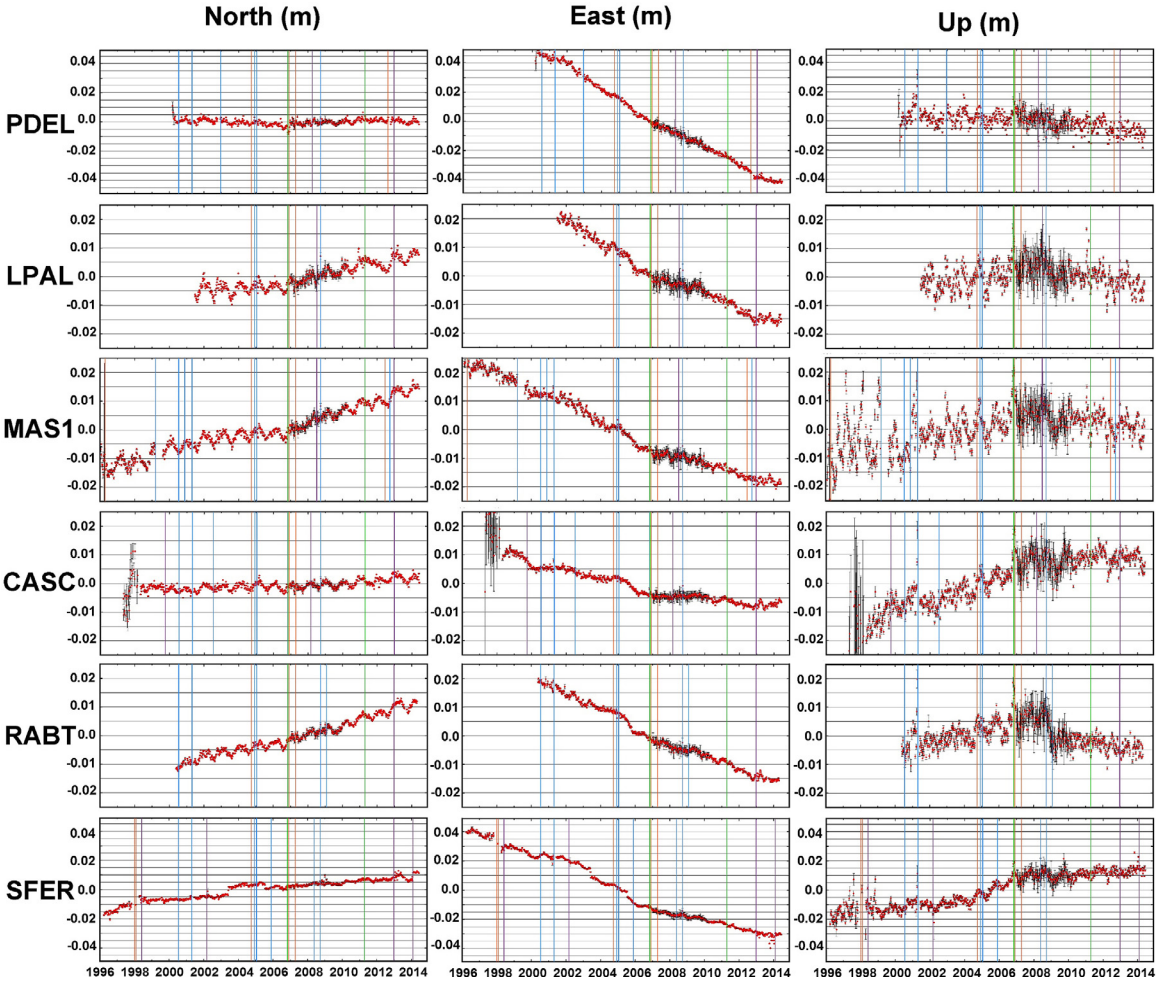

Fig. 3. Residuals of the PDEL, LPAL, MAS1, CASC, RABT, and SFER GPS weekly coordinate series in relation to the VILL station (after the removal of the offsets) marked with vertical lines (purple: both antenna and receiver changed; red: only antenna changed; blue: only receiver changed; green: reference system changed). Note that the vertical scale is double for the PDEL and SFER stations.

3.2. Deformation data

We used data from the permanent GPS stations in the region that had the longest continuous datasets. The selected sites ranged from the Azores in the west (PDEL on San Miguel), the Iberian Peninsula (CASC in Cascaes, Portugal, VILL in Villafranca, and SFER in San Fernando, Spain) in the north, Morocco (RABT in Rabat) in the east, and the Canary Islands (LPAL on La Palma and MAS1 on Gran Canaria) in the south. This network is somewhat sparse but its coverage is uniform. In order to obtain the most homogeneous coordinate time-series, we used the results obtained from the first reprocessing computed by EPN (EUREF Permanent Network, where EUREF stands for International Association of Geodesy Reference Frame Sub-Commission for Europe), that is called EPN-Repro 1 (http://epn-repro.bek.badw.de/) and covers the period from 1996 to the end of 2006. From January 2007 onwards, EPN routine solu-

tions were used. These solutions are in two different realizations of the International Terrestrial Reference Frame (ITRF): ITRF2000 (Altamimi et al., 2002) until April 2011, when the reference frame was changed to ITRF2008 (Altamimi et al., 2011) in use up to the end of 2014. We used weekly time series for the selected sites and removed offsets that might affect the results and their interpretation. We computed and corrected the magnitude of these offsets in case of known origin (e.g. equipment and frame changes). Fig. 3 shows the 3D (north, east, vertical) time series from the PDEL, LPAL, MAS1, CASC, RABT, and SFER stations in relation to the VILL station. The errors in the time series correspond to the formal errors computed during the data processing, which underestimated the true uncertainty given that a large number of systematic errors and mis-modeled parameters were not included. They have been represented as error bars; sometimes, due to their small value, bars are hidden by the coordinates. Nevertheless, errors are useful in a relative way and were used as weights in the computation of the velocities for each site.

4. Data analysis

The following is an analysis of the observed seismic and deformation data at regional (i.e. the whole area) and local (i.e. the Canary Islands) scales.

4.1. Regional analysis

We performed a comparative regional analysis of the evolution of the seismicity and the deformation. Fig. 4 summarizes through different plots the time evolution of the released seismic energy. Each curve in Fig. 4A and B depicts the accumulated elastic energy, E_S, released by earthquakes with $M_W \geq M_C$ (Appendix A). E_S was computed using an empirical regression and the scalar seismic moment, M_0 (Choy and Boatwright, 1995), of $E_S = 1.6 \times 10^{-5} M_0$ (J). Fig. 4A shows the accumulated seismic energy for the seven regions and Fig. 4C shows the time evolution of their seismicity (excepting MAR-ATJ) in a longitudinal E-W projection. Fig. 4 B shows a detailed comparison of the seismic energy released in the Canaries (CAN), Atlas (ATL), Gloria Fault (GF) and Gorringe Bank (GB) and Fig. 4D shows the evolution of the earthquake occurrence from West to East through the different islands of the Canarian Archipelago to the Atlas Mountains in Morocco. The lower panel on Fig. 4D consists of a histogram of the local seismicity detected by the CHIE seismic station on El Hierro (Canary Islands) that represents the longest record of local seismic activity from that island. Tectonics seems to be dominated by the occurrence of strongest tectonic events, being MAR-ATJ the area that released the maximum of seismic energy in this time period, and with a fairly regular pattern. Besides the known and expected seismic activity, in Fig. 4 it can be recognized some changes in the trend and in the rate of the seismicity. ATSM (drawn in clear grey dots on Fig. 4C) shows in 1998 an increased seismicity associated with the Serreta (Azores) submarine eruption (Table.1). A fairly general (excepting MAR-ATJ) increase in the activity can be recognized in ATSM, BALB, CAN, ATL, GF and GB series from 2003 onwards. Seismic activity on the Canary Islands and in the Atlas Mountain increased from 2003 (Fig. 4B and D) and was followed by a further increase around 2007. Activity in the Canaries experienced a further acceleration at the beginning of 2011, which lasted until the onset of the submarine El Hierro volcanic eruption in October 2011. Most of the series (BALB, ATSM and GB) experienced increments in 2003–2004 or 2007–2008, as result of the occurrence of tectonic earthquakes.

Fig. 5 reflects the deformation history of the area and the velocity evolution (horizontal and vertical vectors) calculated at the GPS stations, with the VILL station (European Plate) on the left and the RABT station (African Plate) on the right as the reference stations. Some GPS stations are located either on the Eurasian or African Plates, but others do not belong clearly to any of the two plates (e.g. SFER, Fernandes et al., 2007), so we computed all the time series relative to a reference station in each one of the plates, in order to isolate the local deformations. Each vector represents the estimated velocity at each station for every three years, computed from the weekly coordinate time-series using CATS software (Williams, 2008) and taking into account annual and semi-annual periodic variations. The last vector (in red) begins on the same day as the onset of the submarine eruption on El Hierro on 10 October 2011. The data error is proportional to the size of the error ellipse and is plotted at the same scale as the deformation vector (see legend). During the period 10 October 2002–09 October 2005 the horizontal deformation showed (referenced to the VILL station) a counterclockwise rotation over a wide area (LPAL, drift = 53°SW; MAS1, drift = 54°SW; RABT, drift = 25°SW, yellow vector in Fig. 5A), coinciding with the abrupt westwards jump recorded at the SFER station. SFER station shows several changes in the magnitude of the horizontal components but not any rotation. Thereafter, the stress field gradually reverted to steady compressive NW-SE behavior (see A and B), while the vertical deformation component continued to increase, firstly at the RABT station and subsequently at the LPAL and MAS1 stations, until the onset of the eruption (see C and D). PDEL station (Azores) did not present any change in horizontal or vertical components.

4.2. Local analysis

In order to study the time evolution of the seismicity and the deformations on a local scale, we selected the permanent seismic stations (CHIE on El Hierro and CCAN on Tenerife, both equipped with short-period, vertical component seismometers) and GPS stations (LPAL on La Palma and MAS1 on Gran Canaria) on the Canary Islands with the longest continuous (>10 years) data series. Then, we applied time-varying fractal dimension analysis (*FD*) to the seismic traces and calculated 3D differential coordinates time-series (LPAL minus MAS1) for the GPS stations. Time-varying FD analysis has been conducted during eruptive episodes on active volcanoes such as Mt. Etna (Vinciguerra et al., 2001; Vinciguerra, 2002), Mt. Vesuvius (Luongo et al., 1996), Mt. St. Helens (Caruso et al., 2006), the 1996 eruption on Vatnajokull (Maryanto et al., 2011), and the eruption on El Hierro in 2011–2012 (López et al., 2014) as a means of studying their fracture dynamics. Application of time varying fractal analysis to the seismic data on El Hierro allowed studying the evolution of the radiated seismic wave field, to identify the different stages in the seismic source mechanism and to infer the geometry of the path used by the magma and associated fluids to reach the Earth's surface (López et al., 2014).

Fig. 6A shows the *FD* time evolution while Fig. 6B shows the 3D time evolution of the deformations. We spammed the end time of the studied period in order to show the registered local activity associated with the post-eruption phase in El Hierro. *FD* evolution was estimated using the Higuchi (1988) algorithm (Appendix B) on the vertical component of CHIE (El Hierro) and CCAN (Tenerife) seismic stations. Each *FD* point corresponds to a 12 h window of the ground-motion seismic signal with no window overlap. Seismic data was pre-processed in order to remove bad-quality data segments and the ground-motion was retrieved correcting by the corresponding instrument response. The following input parameters, *Kmax* = 5; window size, *N = 12*60*60*sampling-rate* (being the sampling rate *sps* = 100 for CCAN station and *sps* = 50 for CHIE station) were used in Eq. (8). At the lower panel on Fig. 6B, the histogram of the local seismicity detected by the CHIE station shows the evolution of the local activity on El Hierro (Canary Islands). Before 2003, the *FD* showed cyclic variations with a mean value

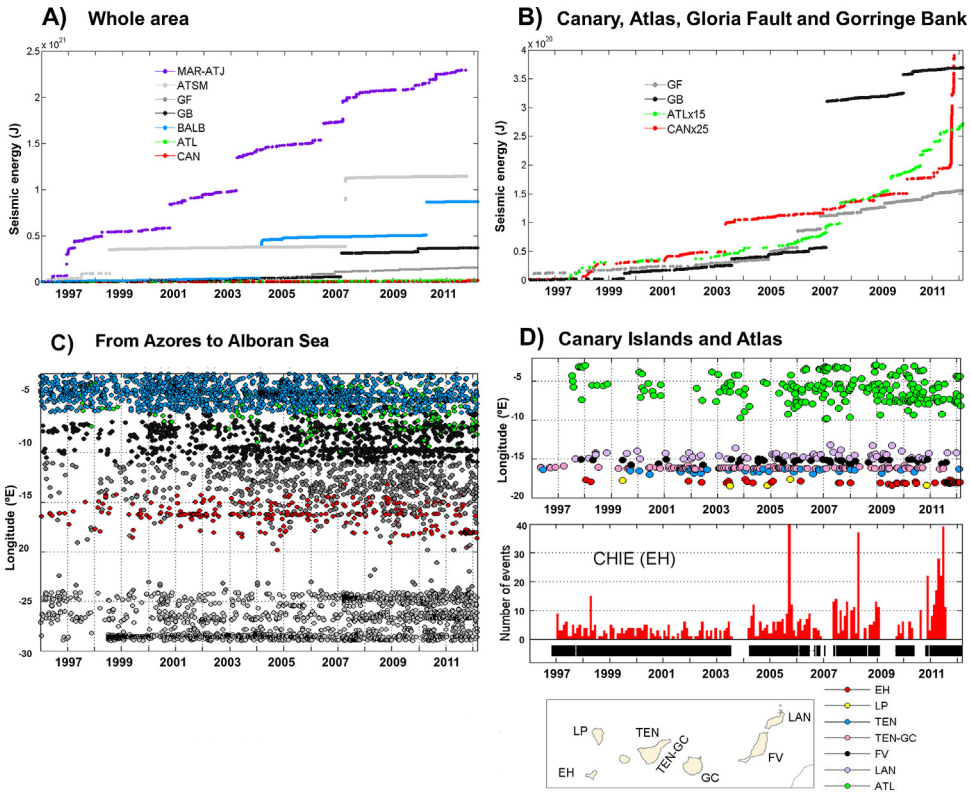

Fig. 4. Comparative analysis of the accumulated seismic energy released for events with $M_W \geq M_C$ in each area (MAR-ATJ, $M_W \geq 4$; ATSM, $M_W \geq 2.7$; GF, $M_W \geq 3$; GB, $M_W \geq 2.9$; BALB, $M_W \geq 2.9$; ATL, $M_W \geq 2.6$; and CAN, $M_W \geq 2.7$) between the seven areas (A) and the Canary Islands, Atlas, Gloria Fault and Borringe Bank areas (B). Longitudinal seismicity plots for the seismic activity located from Azores to the Alboran Sea (C) and the Canary Islands and the Atlas (D). At lower panel on D, monthly event histogram (red bars) registered at the CHIE seismic station on El Hierro (EH). Black bars indicate the availability of the station data. (For interpretation of the references to colour in this figure legend, the reader is referred to the web version of this article.)

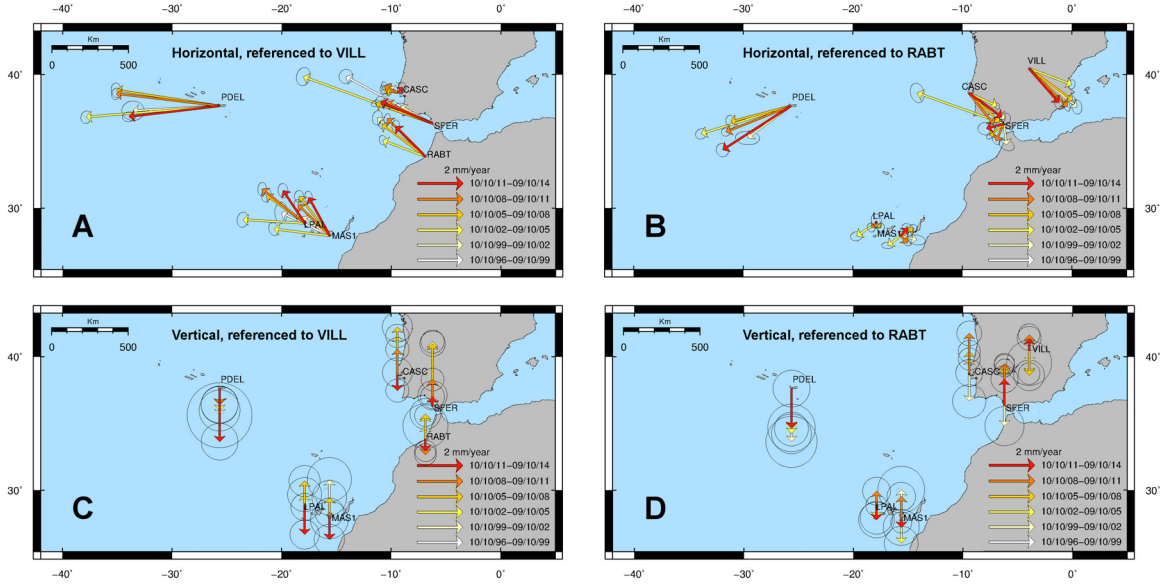

Fig. 5. Left: GPS velocity field (horizontal and vertical vectors) in relation to the VILL station (European Plate); right: GPS velocity field in relation to the RABT station (African Plate). For the period 10 October 1996–09 October 1999, the vertical velocity vector is excluded for the MAS1 station due to the high scattering of the vertical MAS1 time series (see Fig. 3).

of ≥1.4 for both stations and no predominant notable trends. From 2004 onwards, however, the *FD* decreased to values ≈1.1–1.2 and the deformation shortened in a northerly direction and lengthened westwards. The *FD* decreased more from January 2011 to the end on the unrest phase. During the eruption on El Hierro (October 2011–March 2012), the *FD* reached its lowest values of ≈1 at the CHIE station, which was interpreted as corresponding to the establishment of a minimum dimension conduit geometry used by the magma to reach the surface (López et al., 2014). It is noteworthy that the local activity (seismicity and surface deformation) is occur-

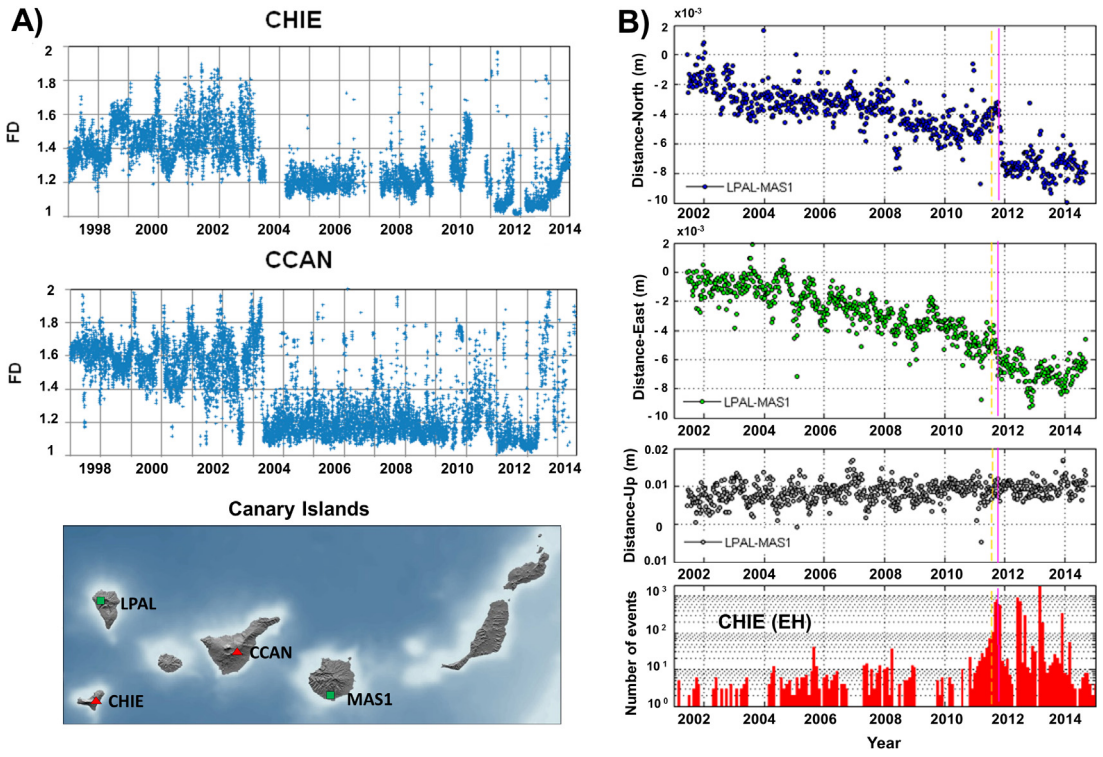

Fig. 6. (A) Time-varying evolution of fractal dimensions at the stations on CHIE (El Hierro) and CCAN (Tenerife). Each point corresponds to the *FD* of 12 h with no overlapping windows of seismic signal. (B) Time evolution of a three-component (north, east, upward) LPAL-MAS1 deformation. Lower panel: monthly event histogram (red bars) registered at the CHIE seismic station on El Hierro. Gaps in data are due to the lack of station availability. (For interpretation of the references to colour in this figure legend, the reader is referred to the web version of this article.)

ring not only in El Hierro but also in Tenerife, La Palma and Gran Canaria Islands.

The deformation showed a tendency to shorten northwards, suggesting that the stations are moving closer in the N-S direction, and lengthen westwards, showing an extension between the stations in the E-W direction, from 2003 onwards; as well, there was a positive northward deformation episode starting in January 2011, observed more clearly from July 2011 onwards that coincided with the beginning of the pre-eruptive unrest on El Hierro (Fig. 6B). With the onset of the submarine eruption in October 2011, the northward deformation was quickly inverted (see also Fig. 5A and B). From January 2012 onwards, the deformations showed no clear trends, even during the six main episodes of volcanic unrest registered on El Hierro after the end of the eruption (Fig. 6B).

5. Discussion

Despite the relatively short time series for the available data, the activity registered in the Canaries from 1996 to 2002 may be considered as the background level. During this period the seismic activity was rather low and steady (see Fig. 4D) and the deformations (horizontal components) followed the regional stress field direction. Comparing to this period, the early signs of anomalous tectonic activity occurred from 2003 onwards, including a significant increase in 2007, well before the onset of the 2011–2012 eruption on El Hierro (Fig. 6).

At regional scale this anomalous activity was characterized by a general increase in the whole area, excepting MAR-ATJ (Fig. 4A), a coincident increments in the seismic energy released in 2003–2004 and/or around 2007 in CAN, ATL, GF and GB (Fig. 4B), and an E-W drift and uplift deformations that affected the southern Iberian Peninsula, northwest Africa, and the Canary Islands (Fig. 5). At local scale, activity affected different Canarian Islands, showing common seismic patterns (similar *FD* evolution and an increase in seismicity) at El Hierro (more intensely) and Tenerife Islands and a concurrent stress-shift episode measured by GPS stations on La Palma and on Gran Canaria Islands (Figs. 5 and 6). Other authors have also reported increased activity in these periods, marked by an increase in seismicity and anomalous ^{222}Rn and ^{220}Rn subsurface degassing from 2003 to 2005 in Tenerife and an increased trend of diffuse CO_2 emission from Teide Volcano (Tenerife Island) in 2007 (Almendros et al., 2007; Pérez et al., 2007, 2010; Domínguez-Cerdeña et al., 2012). These increases in activity were interpreted as caused by the presence of new magma below the Canaries and the subsequent changes in the stress field.

Anomalous tectonics and generation and emplacement of new magma in this environment may be explained either by stress changes generated at the plates boundaries or by a mantle plume upwelling (Legendre et al., 2012; Bonnin et al., 2014; Fullea et al., 2015; Saki et al., 2015; Miller et al., 2015; Geyer et al., 2016). The observed deformations (regional and local) agreed with the existence of an active mantle upwelling beneath the Atlantic off the northwest African continental lithosphere (Legendre et al., 2012; Fullea et al., 2015; Saki et al., 2015). Saki et al. (2015) found evidences about a locally depressed 410 km discontinuity beneath the hotspots in Azores and Canaries, and a regionally elevated 660 km discontinuity in the Central Atlantic, leading to a scenario where a large hot spot may reach the transition zone but not extend through it. This mantle upwelling penetrates through the top of the transition zone (between the lower mantle and the upper mantle) as different plume branches that appear on the surface in the Azores, the Canary Islands, and in Cape Verde. One important difference between the hotspots detected in Azores and in Canary Islands is that the Canary hotspot seems to be rooted from the base of the mantle while the Azores hotspot appears only in the upper mantle (French and Romanowicz, 2015). A recent study (Miller et al., 2015)

has proposed the existence of a considerable amount of multiple sub-lithospheric, low-velocity material flowing sub-horizontally northeastward from the Canary hotspot to southern Spain, that is, beneath the Atlas and the Alboran Sea and from the 410-km discontinuity to the lithosphere-asthenosphere boundary. Miller et al. (2015) proposed a slab-plume lithosphere interaction where the Canary plume is deflected eastwards by mantle flow, giving rise to small-scale upwellings such the Atlas upwelling (Sun et al., 2014).

A reactivation of this sub-lithospheric material below the lithosphere of Canaries, Morocco and southern Spain would explain the observed seismicity, the regional extension and uplift affecting the southern Iberian Peninsula, NW Africa, and the Canary Islands and could have facilitated partial melting and accumulation of magmas at different depths in the mantle below the Canary Islands. The time encompassed between the beginning of the deformation and the eruption and subsequent unrest episodes at El Hierro suggest a certain delay between mantle upwelling and melting. The fact that the Azores hotspot is different from the Canary Islands hotspot above 660 km (Saki et al., 2015) would explain the decoupled evolution of the process in Canary Islands (eruption) and in the Azores (no eruption), despite sharing an increased seismicity.

The role of regional tectonics in mantle upwelling cannot be deciphered with the data obtained. However, it seems evident that regional and local tectonic structures have also played a significant control on El Hierro eruption. The only description of the structure of the upper lithosphere in the Canary Islands is provided by Carbó et al. (2003) and Llanes (2006), whose detailed gravimetric survey of the archipelago reports the existence of a main negative anomalies to the west with two strong linear gradients, the first trending N-S from La Palma and extending across El Hierro, and the second crossing Tenerife in a NNE-SSW direction (Carbó et al., 2003). These authors have modelled the negative anomaly as a mantle mass-deficit beneath La Palma, El Hierro, and La Gomera, which would agree with a local extension in the lithosphere. The location and direction marked by the N-S alignment on El Hierro coincides with the path defined by the location of the seismic swarm in its N-S migration under the Moho discontinuity during the pre-eruptive unrest phase (Martí et al., 2013). Pinel and Jaupart (2004) have shown that gradients in the stress field control the storage and/or the lateral/vertical propagation of magma. The existence of a lateral strong stress gradient in the upper lithosphere close to El Hierro could have facilitated the movement of magma in dykes and its migration from mantle to crust in this particular area.

The exact interplay between regional tectonics and mantle dynamics is a key question to understand the origin of Canarian volcanism. As indicated before, this is a question still under debate and it is not the aim of this study to go further on this particular subject. However, the data presented evidence that the renewed magmatic activity at El Hierro was preceded by years of deformation and increased seismicity. The generation and eruption of magma corresponds to a punctual geodynamic episode in which tectonism is earlier manifested than magmatism, but which would be compatible with a mantle upwelling being the cause of the observed tectonic activity. Thus, the observed anomalous tectonic activity (e.g: seismicity and deformation) can be considered as a precursor to the El Hierro eruption, being this a sequence of events that may repeat in the future. In this framework, it is also important to remark the role of tectonics in controlling magma migration. In the particular case of El Hierro it seems clear that the eruption occurred when tectonics facilitated the opening of the path that magma used to reach the surface (Del Fresno et al., 2015; Telesca et al., 2016), not being able the magma by itself to create that path. In the further magma injection episodes that occurred between 2012 and 2014 magma did no erupt, remaining stored at depths between 25–15 km, thus suggesting that tectonic activity did not help magma to migrate to sallower levels. This is in good agreement with the petrological imaging of the magmatic feeding systems below El Hierro and La Palma that suggest the presence of isolated magma pockets at a depth of 15–26 km, as occurs on other oceanic volcanic islands fed by plumes with relatively low fluxes (Klügel et al., 2005; Stroncik et al., 2009).

Fig. 7 summarizes via successive vertical cross-sections the proposed three main phases that occurred in the period (15 years) before the eruption. First phase (Fig. 7a) depicts the situation of background activity, considering the data registered by the seismic and GPS monitoring networks from 1996 to 2002. During this period, regional deformation followed the direction of the regional stress field, with absence of anomalous activity. A mantle upwelling beneath the Atlantic off the northwest African continental lithosphere rises from the lower mantle and spreads above 410 km in distinct sub-lithospheric upwellings beneath the Canaries, the Atlas (Morocco) and the South of Spain. Below the Canaries, a hot spot rises from the 410 km discontinuity to the LAB (lithosphere-asthenosphere boundary). During a second phase (Fig. 7b), from 2003 to 2011, mantle upwelling promoted regional seismicity, extension and uplift in the southern Iberian Peninsula, NW Africa, and the Canary Islands and facilitated partial melting and magma ascent below the Canary Islands. This allowed that, below the LAB in the Canaries, different small pockets of magma migrated towards the base of the crust. From 2011 (Fig. 7c) onwards, the extensional stress regime induced by the mantle upwelling and the magma excess pressure facilitated the opening of fractures above the LAB boundary bellow the Canary Islands. Magma injection and its migration towards the surface, triggered local seismicity and local crustal deformations that were observed during the pre-eruptive unrest (July-10 October 2011), prior to the beginning of the volcanic eruption in El Hierro Island and continued shortly afterwards with new magma injection episodes that did not end in eruption.

6. Conclusions

The Canary Islands experienced an increase in tectonic activity since 2003 that we consider as precursor of the recent magmatic and volcanic activity occurred at El Hierro Island. The analysis of the seismicity and deformation patterns occurred during this period suggest that this anomalous tectonic activity was induced by the ponding of the Canarian mantle plume, which involved the drifting E-W extensional and uplift deformations observed in the Canary Islands but that also affected the south of the Iberian Peninsula and northwest Africa. The pushing action of the ascending mantle plume and its interaction with the oceanic lithosphere gave rise to the observed seismicity, the extensional regime and the vertical transport of new magmas towards the crust. The direction of the extensive field since 2003 is compatible with the known N-S lithospheric anomalies under El Hierro, which had a significant role in controlling horizontal magma migration during the pre-eruptive unrest episode (July–October 2011).

In January 2011, a local deformation process in the Canary Islands (Fig. 6) overlapped the regional processes and then became more intense from July onwards, giving rise to three months of recorded volcanic unrest in El Hierro Island. This local deformation corresponds to the intrusion of magma through the crust in the vicinity of El Hierro, a process that culminated in a volcanic eruption in October 2011, lasting for nearly five months. The absence of additional deformation episodes in the Canary Islands since the eruption ended in March 2012 suggests that none of the unrest episodes registered on El Hierro in 2012–2014–some in fact more energetic that the actual pre-eruptive event – penetrated the island's crust and therefore did not represent any potential eruption risk.

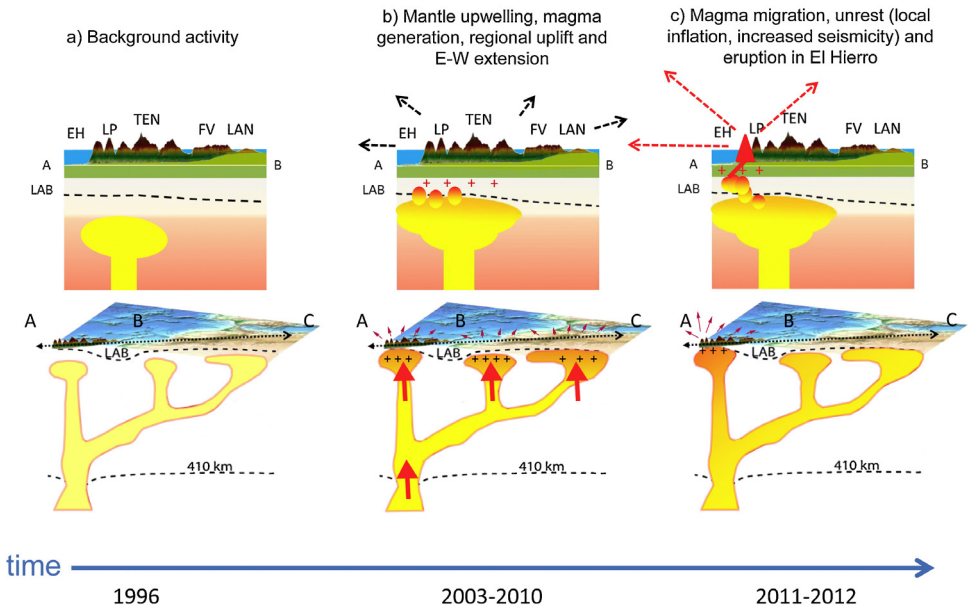

Fig. 7. Sketch showing the vertical cross-section sequence during different phases of the process leading up to the eruption on El Hierro, on a local scale (the Canaries, upper panels) and regional scale (from the Canaries to the Alboran Sea, lower panels). The interpretative depiction of the upper mantle (lower panels) was taken from Miller et al. (2015). Black dashed line crosses from The Canaries (A) through the Atlas (B) to the Alboran Sea (C). In the upper panels, different islands from the Canaries, area denoted by a code assigned in Fig. 4D (see text for more explanation).

This work presents evidence that the renewed magmatic activity at El Hierro was preceded by years of anomalous seismicity and deformation at different temporal and spatial scales. We propose that the long-term monitoring of the tectonic activity (e.g: seismicity and deformation) in a broader area (from Azores to Morocco) can be considered a useful tool for the volcano hazard assessment of future eruptive events in the Canaries.

Acknowledgements

This research was partially supported by the Instituto Geográfico Nacional (IGN), the European Commission (FP7 Theme: ENV.2011.1.3.3-1; Grant 282759: "VUELCO") and the Spanish MINECO project CGL2014-58821-C2-1-R. We would like to thank all our colleagues from the IGN and from the other Regional and Global Seismic and Geodetic monitoring networks, providers of observational data before, during, and after the volcanic eruption on El Hierro – without them this study would not have been possible. We are very grateful for the valuable suggestions made by Ana Negredo (UCM), Alicia Felpeto (IGN) and Maria Jose Blanco (IGN), which substantially improved this paper. We thank two anonymous referees for their helpful and constructive reviews. The English text was reviewed and corrected by Michael Lockwood.

Appendix A.

We computed from 1996 to 2014 the evolution of the magnitude of completeness, *Mc*, in each one of the seven studied regions (Fig. 8).

In the case of MAR-ATJ region, that includes both the Mid-Atlantic Ridge and the Triple Junction (Azores western Islands) we selected the upper bound for the *Mc* curve. The seismicity of the Mid-Atlantic Ridge is always located at tele-seismic distances, being *Mc* lower than the corresponding *Mc* parameter of the Azores (where local seismic stations at land allow the location of local seismicity). Therefore, we selected *Mc* = 4, in order to correctly monitor the Mid-Atlantic Ridge energy release evolution. The lower levels of *Mc* from 1999 onwards are the result of the increase of the Azores seismic network performance, which made the location of smaller events at local distances possible.

In the case of ATSM, we observed a jump in magnitude from 2007, in coincidence with a change in the magnitude scale type. We guess magnitude values from 2007 onwards are more reliable that the previous ones for the seismicity in this region. Therefore, we selected the mean *Mc* for that time interval (2007–2014).

In the case of the Canary Island region, selected *Mc* is over or in the range of $Mc \pm dMc$, assuring that the increase of activity in 2003 and 2007 is not an artifact due to the improvement in the network coverage.

Therefore, even it is true that the network coverage increased with time in almost all the regions, the careful data selection analysis performed in this paper allows us to suggest that the increase in seismic activity in 2003 and 2007 is well founded and not due to artefact.

Appendix B.

Higuchi (1988) shows that a curve with a single power-law spectrum is self-similar and that the index, α, of the power spectral density (*PSD*) has a power-law spectrum dependence on frequency

$$P(f) \sim f^{-\alpha}; \quad (6),$$

that is simply related to the fractal dimension, D, by the equation $D = (5-\alpha)/2$ (for a self-affine fractal, $1 < D < 2$). Higuchi (1988) presents a stable numerical computation algorithm for the estimation of D using a low number of timed sequential data. Higuchi's algorithm generates multiple time series from N equi-spaced samples (x(i), i = 1,. . .,N) that creates a new time series x_k^m as follows:

$$x_k^m : x(m), x(m+k), x(m+2k), \ldots, x\left(m + \left[\frac{N-m}{k}\right].k\right) \quad (m = 1, 2, \ldots, k); \quad (7)$$

with m and k integers and [a] denoting the integer part of a. For each time series, the absolute differences between each two successive data points are summed to calculate the vertical length

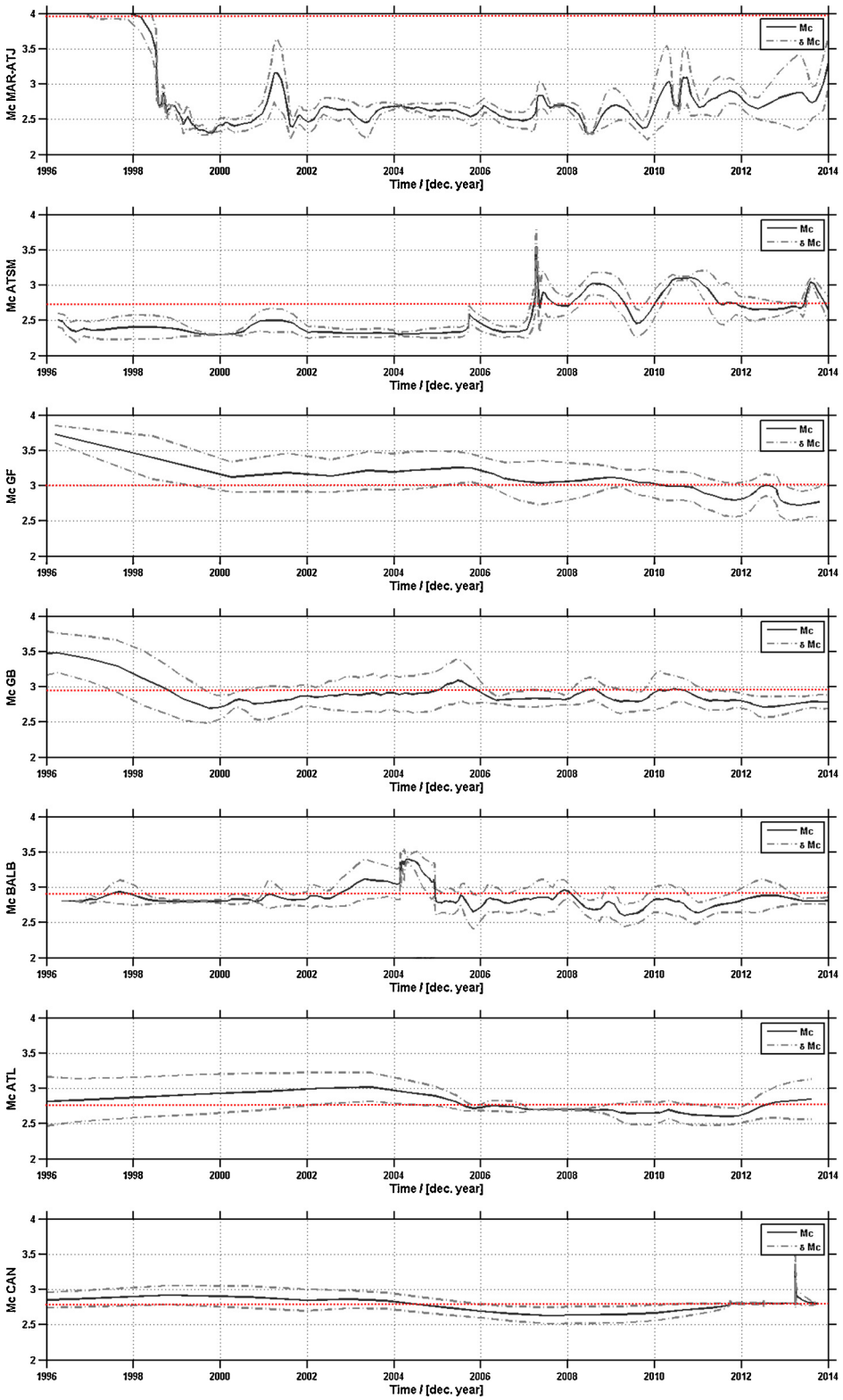

Fig. 8. Time evolution of *Mc* in each one of the seven studied regions (from top to bottom, MAR-ATJ, ATSM, GF, GB, BALB, ATL and CAN). We highlight the selected *Mc* value with a red dashed line. Each curve was computed using the ZMAP software package (Wiemer, 2001) with the following parameters: maximum curvature method, sample window of 100 events with a minimum number of 40 events. (For interpretation of the references to colour in this figure legend, the reader is referred to the web version of this article.)

of the signal with the scale size k as follows:

$$L_m(k) = \left\{ \left(\sum_{i=1}^{[(N-m)/k]} |x(m+ik) - x(m+(i-1)k)| \right) \frac{N-1}{\left[\frac{N-m}{k}\right].k} \right\}; \quad (8)$$

The length of the series segment L(k) is the mean of the Lm(k) values,

$$L(k) = \frac{\sum_{m=1}^{k} L_m(k)}{k} \text{ for m} = 1, \ldots., \text{k}; \quad (9)$$

If L(k) is proportional to k^{-D}, then the signal is fractal-like and has the FD D.

References

Almendros, J., Ibáñez, J.M., Carmona, E., Zandomeneghi, D., 2007. Array analyses of volcanic earthquakes and tremor recorded at Las Caáadas caldera (Tenerife Island, Spain) during the 2004 seismic activation of Teide volcano. J. Volcan. Geotherm. Res. 160 (3–4), 285–299, http://dx.doi.org/10.1016/j.jvolgeores.2006.10.002.

Altamimi, Z., Sillard, P., Boucher, C., 2002. ITRF2000: a new release of the international terrestrial reference frame for earth science applications. J. Geophys. Res. 107 (B10), 2214, http://dx.doi.org/10.1029/2001JB000561.

Altamimi, Z., Collilieux, X., Métivier, L., 2011. ITRF2008: an improved solution of the international terrestrial reference frame. J. Geod. 85, 457, http://dx.doi.org/10.1007/s00190-011-0444-4.

Anguita, F.A., Hernán, F., 1975. A propagating fracture model versus a hot spot origin for the Canary Islands. Earth Planet. Sci. Lett. 27 (1), 11–19 (ISSN: 0012-821X.).

Anguita, F., Hernán, F., 2000. The Canary Islands origin: a unifying model. J. Volcanol. Geotherm. Res., 10.

Anguita, F., Garcia Cacho, L., Colombo, F., Gonzalez Camacho, A., Vieira, R., 1991. Roque Nublo Caldera: a new stratocone caldera in Gran Canaria, Canary Islands. J. Volcanol. Geotherm. Res. 47 (1–2), 1–26, 45–633.

Araña, V., Ortiz, R., 1991. The Canary Islands: tectonics, magmatism and geodynamic framework. In: Kampunzu, A., Lubala, R. (Eds.), Magmatism in Extensional Structures Setting: The Phanerozoic African Plate. Springer, Verlag, pp. 209–249.

Bebbington, M.S., Marzocchi, W., 2011. Stochastic models for earthquake triggering of volcanic eruptions. J. Geophys. Res. 116, B05204, http://dx.doi.org/10.1029/2010JB008114.

Bezzeghoud, M., Adam, C., Buforn, E., Borges, J.F., Caldeira, B., 2014. Seismicity along the Azores-Gibraltar region and global plate kinematics. J. Seismol. 18 (2), 205–220, http://dx.doi.org/10.1007/s10950-013-9416-x.

Bonali, F.L., Tibaldi, A., Corazzato, C., Tormey, D.R., Lara, L.E., 2013. Quantifying the effect of large earthquakes in promoting eruptions due to stress changes on magma pathway: the Chile case. Tectonophysics 583, 54–67, http://dx.doi.org/10.1016/j.tecto.2012.10.025.

Bonnin, M., Nolet, G., Villaseñor, A., Gallart, J., Thomas, C., 2014. Multiple-frequency tomography of the upper mantle beneath the African/Iberian collision zone. Geophys. J. Int. 198, 1458–1473.

Cabañas, L., Rivas-Medina, A., Martínez-Solares, J.M., Gaspar-Escribano, J.M., Benito, B., Antón, R., Ruiz-Barajas, S., 2015. Relationships between Mw and other earthquake size parameters in the spanish IGN seismic catalog. Pure Appl. Geophys., http://dx.doi.org/10.1007/s00024-014-1025-2.

Carbó, A., Muñoz-Martín, A., Llanes, P., Alvarez, J., EEZ Working Group, 2003. Gravity analysis offshore the Canary Islands from a systematic survey. Mar. Geophys Res. 24, 113–127.

Carracedo, J.C., Day, S., Guillou, H., Rodríguez Badiola, E., Canas, J.A., Pérez Torrado, F.J., 1998. Hotspot volcanism close to a passive continental margin: the Canary Islands. Geol. Mag. 135, 591–604, http://dx.doi.org/10.1017/S0016756898001447.

Carracedo, J.C., Pérez, F.J., Ancochea, E., Meco, J., Hernán, F., Cubas, C.R., Casillas, R., Rodriguez, E., Ahijado, A., 2002. Cenozoic volcanism II: The Canary Islands. In: Gibbons, W., Moreno, T. (Eds.), The Geology of Spain. Geological Society of London, 439-472.

Caruso, F., Vinciguerra, S., Latora, V., Rapisarda, A., Malone, S., 2006. Multifractal analysis of Mount St. Helens seismicity as a tool for identifying eruptive activity. Fractals 14, 179–186.

Cembrano, J., Lara, L., 2009. The link between volcanism and tectonics in the southern volcanic zone of the Chilean Andes: a review. Tectonophysics 471, 96–113.

Choy, G.L., Boatwright, J.L., 1995. Global patterns of radiated seismic energy and apparent stress. J. Geophys. Res. 100 (B9), 18205–18228, http://dx.doi.org/10.1029/95JB01969.

Cunha, T.A., Matias, L.M., Terrinha, P., Negredo, A.M., Rosas, F., Fernandes, R.M.S., Pinheiro, L.M., 2012. Neotectonics of the SW Iberia margin, Gulf of Cadiz and Alboran Sea: a reassessment including recent structural, seismic and geodetic data. Geophys. J. Int. 188, 850–872, http://dx.doi.org/10.1111/j.1365-246X.2011.05328.x.

Dañobeitia, J.J., Canales, J.P., 2000. Magmatic underplating in the Canary Archipelago. J. Volc. Geoth. Res. 103, 27–41.

Dañobeitia, J.J., Collette, B.J., 1989. Estudio mediante sísmica de reflexión de un grupo de estructuras submarinas situadas al norte y al sur del archipiélago canario. Acta Geológica Hispánica 24, 147–163.

Del Fresno, C., Domínguez-Cerdeña, I., Buforn, E., 2015. The 8 October 2011 earthquake at El Hierro (Mw 4.0): focal mechanisms of the mainshock and its foreshocks. B. Seismol. Soc. Am. 105 (1), 330–340, http://dx.doi.org/10.1785/0120140151.

Domínguez-Cerdeña, I., del Fresno, C., Rivera, L., 2012. New insight on the increasing seismicity during Tenerife's 2004 volcanic reactivation. J. Volcanol. Geotherm. Res. 206 (2011), 15–29, http://dx.doi.org/10.1016/j.jvolgeores.2011.06.005.

Duggen, S., Hoernle, K., Hauff, F., Klügel, A., Bouabdellah, M., Thirlwall, M.F., 2009. Flow of Canary mantle plume material through a subcontinental lithospheric corridor beneath Africa to the Mediterranean. Geology 37, 283–286, http://dx.doi.org/10.1130/G25426A.

Eggert, S., Walter, T.R., 2009. Volcanic activity before and after large tectonic earthquakes: observations and statistical significance. Tectonophysics 471 (1–2), 14–26, http://dx.doi.org/10.1016/j.tecto.2008.10.003.

Emery, K.O., Uchupi, E., 1984. The Geology of the Atlantic Ocean. Springer-Verlag, New York (1050 pp.).

Fernandes, R.M.S., Miranda, J.M., Meijninger, B.M.L., Bos, M.S., Noomen, R., Bastos, L., Ambrosius, B.A.C., Riva, R.E.M., 2007. Surface velocity field of the Ibero-Maghrebian segment of the Eurasia-Nubia plate boundary. Geophys. J. Int. 169, 315–324, http://dx.doi.org/10.1111/j.1365-246X.2006.03252.x.

Foulger, G.R., 2010. Plates Vs Plumes: A Geological Controversy. Wiley-Blackwell, ISBN: 978–1-4051–6148-0, 352 pages.

Fourel, L., Milelli, L., Jaupart, C., Limare, A., 2013. Generation of continental rifts, basins, and swells by lithosphere instabilities. J. Geophys. Res. Solid Earth 118, 3080–3100, http://dx.doi.org/10.1002/jgrb.50218.

French, S.W., Romanowicz, B., 2015. Broad plumes rooted at the base of the Earth's mantle beneath major hotspots. Nature 525, 95–99, http://dx.doi.org/10.1038/nature14876.

Fullea, J., Camacho, A., Negredo, A., Fernández, J., 2015. The Canary Islands hot spot: new insights from 3D coupled geophysical-petrological modelling of the lithosphere and uppermost mantle. Earth Planet. Sci. Lett. 409, 71–88.

Fuster, J.M., 1975. Las Islas Canarias: un ejemplo de evolución temporal y espacial del vulcanismo oceánico. Est. Geol. 31, 439–463.

Geldmacher, J., Hoernle, K., van den Bogaard, P., Zankl, G., Garbe-Schönberg, D., 2001. Earlier history of the ≥70 Ma old Canary hotspot based on the temporal and geochemical evolution of the Selvagen archipelago and neighboring seamounts in the eastern North Atlantic. J. Volcanol. Geotherm. Res. 111, 55–87, http://dx.doi.org/10.1016/S0377-0273(01)00220-7.

Geyer, A., Marti, J., Villaseñor, A., 2016. First-order estimate of the Canary Islands plate-scale stress field: implications for volcanic hazard assessment. Tectonophysics 679, 125–139, http://dx.doi.org/10.1016/j.tecto.2016.04.010.

Grimison, N.L., Chen, W.P., 1986. The Azores-Gibraltar Plate Boundary: focal mechanisms, depths of earthquakes, and their tectonic implications. J. Geophys. Res. 91 (B2), 2029–2047, http://dx.doi.org/10.1029/JB091iB02p02029.

Heaton, T., Tajima, F., Mori, A.W., 1986. Estimating ground motion using recordede accelerograms. Surv. Geophys. 8, 25–83.

Hernández-Pacheco, A., Ibarrola, E., 1973. Geoquemical variation trends between the different Canary Islands in relation to their geological position. Lithos 6, 389–402.

Higuchi, T., 1988. Approach to an irregular time series on the basis of the fractal theory. Phys. D 31, 277–283.

Hill, D.P., Pollitz, F., Newhall, C., 2002. Earthquake-volcano interactions. Phys. Today 55, 41–47.

Hoernle, K., Schmincke, H.U., 1993. The role of partial melting in the 15-Ma geochemical evolution of Gran Canaria: a blob model for the Canarian hotspot. J. Pet. 34, 599–626.

Hoernle, K., Zhang, Y.S., Graham, D., 1995. Seismic and geochemical evidence for large scale mantle upwelling beneath the eastern Atlantic and western and central Europe. Nature 374, 34–39, http://dx.doi.org/10.1038/374034a0.

Hollik, J.S., Rabinowitz, P.D., Austin, J.A., 1991. Effects of Canary hot spot volcanism on structure of oceanic crust off Morocco. J. Geophys. Res. 96 (12), 067 (039-12).

Jiménez-Munt, I., Negredo, A.M., 2003. Neotectonic modelling of the western part of the Africa-Eurasia plate boundary: from the Mid-Atlantic ridge to Algeria. Earth Planet. Sci. Lett. 205 (3–4), 257–271.

Jiménez-Munt, I., Fernandez, M., Torne, M., Bird, P., 2001. The transition from linear to diffuse plate boundary in the Azores-Gibraltar region: results from a thin-sheet model. Earth Planet. Sci. Lett. 192, 175–189.

Jiménez-Munt, I., Fernández, M., Vergés, J., Garcia-Castellanos, D., Fullea, J., Pérez-Gussinyé, M., Afonso, J.C., 2011. Decoupled accomodation of Africa-Eurasia convergence in the NW-Moroccan margin. J. Geophys. Res. 116, B08403, http://dx.doi.org/10.1029/2010JB008105.

Johnston, A.C., 1996. Seismic moment assessment of earthquakes in stable continental regions. I. Instrumental seismicity. Geophys. J. Int. 124, 381–414.

Kanamori, H., Given, J.W., 1982. Use of long-period surface waves for fast determination of earthquake source parameters; 2. Preliminary determination of source mechanism of large earthquakes (Ms ≥ 6.5) in 1980. Phys. Earth

Planet. Int. 30 (2–3), 260–268, http://dx.doi.org/10.1016/0031-9201(82)90112-1.
Klügel, A., Hansteen, T.H., Galipp, K., 2005. Magma storage and underplating beneath Cumbre Vieja volcano, La Palma (Canary Islands). Earth Planet. Sci. Lett. 236, 211–226, http://dx.doi.org/10.1016/j.epsl.2005.04.006.
López, C., Blanco, M.J., Abella, R., Brenes, B., Cabrera-Rodríguez, V.M., Casas, B., Domínguez-Cerdeña, I., Felpeto, A., Fernández de Villalta, M., del Fresno, C., García-Arias, M.J., García-Cañada, L., Gomis-Moreno, A., González-Alonso, E., Guzmán-Pérez, J., Iribarren, I., López-Díaz, R., Luengo-Oroz, N., Meletlidis, S., Moreno, M., Moure, D., Pereda de Pablo, J., Rodero, C., Romero, E., Sainz-Maza, S., Sentre-Domingo, M.A., Torres, P.A., Trigo, P., Villasante-Marcos, V., 2012. Monitoring the volcanic unrest of El Hierro (Canary Islands) before the onset of the 2011–2012 submarine eruption. Geophys. Res. Lett. 39, LI3303, http://dx.doi.org/10.1029/2012GL051846.
López, C., Martí, J., Abella, R., Tarraga, M., 2014. Applying fractal dimensions and energy-budget analysis to characterize fracturing processes during magma migration and eruption: 2011–2012 El Hierro (Canary Islands) submarine eruption. Surv. Geophys. 35, 1023–1044, http://dx.doi.org/10.1007/s10712-014-9290-2.
Lara, L.E., Naranjo, J.A., Moreno, H., 2004. Rhyodacitic fissure eruption in Southern Andes (Cordón Caulle, 40.5(S) after the 1960 (Mw 9.5) Chilean earthquake: a structural interpretation. J. Volcanol. Geotherm. Res. 138, 127–138.
Le Pichon, X., Fox, P.J., 1971. Marginal offsets: fracture zones and the early opening of the North Atlantic. J. Geophys. Res. 76, 6294–6308.
Legendre, C., Meier, T., Lebedev, S., Friederich, W., Viereck-Götte, L., 2012. A shear wave velocity model of the European upper mantle from automated inver-sion of seismic shear and surface waveforms. Geophys. J. Int. 191, 282–304, http://dx.doi.org/10.1111/j.1365-246X.2012.05613.x.
Legrand, D., Barrientos, S., Bataille, K., Cembrano, J., Pavez, A., 2011. The fluid-driven tectonic swarm of Aysén Fjord: Chile (2007) associated with two earthquake s (Mw 6.1 and Mw 6.2) within the Liquiñe-Ofqui Fault Zone. Cont. Shelf Res. 31, 154–161.
Linde, A.T., Sacks, I.S., 1998. Triggering of volcanic eruptions. Nature 395, 888–890, http://dx.doi.org/10.1038/27650.
Llanes, M.P., 2006. Estructura De La Litosfera En El Entorno De Las Islas Canarias a Partir Del Análisis Gravimétrico E Isostático: Implicaciones Geodinámicas Doctoral Thesis. U. Complutense de Madrid, Spain, pp. 1–189.
Luongo, G., Mazzarella, A., Palumbo, A., 1996. A fractal approach to clustering of the 1983–1984 seismicity in the Campi Flegrei Caldera, southern Italy. Fractals 9, 29, http://dx.doi.org/10.1142/S0218348x9600005.
Lupi, M., Miller, S.A., 2014. Short-lived tectonic switch mechanism for long-term pulses of volcanic activity after mega-thrust earthquakes. Solid Earth Discuss. 5, 811–839, http://dx.doi.org/10.5194/sed-5-811-2013.
Lynnes, C.S., Ruff, L.J., 1985. Source process and tectonic implications of the great 1975 North Atlantic earthquake. Geophys. J. Roy. Astr. S. 82 (3), 497–510, http://dx.doi.org/10.1111/j.1365-246X.1985.tb0514.
Mériaux, C.A., Duarte, J.C., Duarte, S.S., Schellart, W.P., Chen, Z., Rosas, F., Mata, J., Terrinha, P., 2015. Capture of the Canary mantle plume material by the Gibraltar arc mantle wedge during slab rollback. Geophys. J. Int. 201, 1717–1721.
Manga, M., Brodsky, E.E., 2006. Seismic triggering of eruptions in the far field: volcanoes and geysers. Annu. Rev. Earth Planet. Sci. 34, 263–291, http://dx.doi.org/10.1146/annurev.earth.34.031405.125125.
Mantovani, E., Viti, M., Babbucci, D., Albarello, D., 2007. Nubia-Eurasia kinematics: an alternative interpretation from mediterranean and north atlantic evidence. Ann. Geophys. 50, 311–336, http://dx.doi.org/10.4401/ag-3073.
Marinoni, L.B., Pasquarè, G., 1994. Tectonic evolution of the emergent part of a volcanic ocean island: lanzarote, Canary Islands. Tectonophysics 239, 111–135.
Martí, J., Pinel, V., López, C., Geyer, A., Abella, R., Tárraga, M., Blanco, M.J., Castro, A., Rodríguez, C., 2013. Causes and mechanisms of the 2011–2012 El Hierro (Canary islands) submarine eruption. J. Geophys. Res. Solid Earth 118, 1–17, http://dx.doi.org/10.1002/jgrb.50087.
Maryanto, S., Santosa, R.D.R., Mulyana, I., Hendrasto, M., 2011. Fractal and chaos properties of explosion earthquakes followed by harmonic tremor at Semeru volcano, East Java, Indonesia.I nt. J. Sci. Eng. Res. 2 (7) (ISSN 2229-5518).
Marzocchi, W., Casarotti, E., Piersanti, A., 2002. Modeling the stress variations induced by great earthquakes on the largest volcanic eruptions of the 20th century. J. Geophys. Res. 107 (B11), 2320, http://dx.doi.org/10.1029/2001JB001391.
McKenzie, D., Bickle, M.J., 1988. The volume and composition of melt generated by extension of the lithosphere. J. Petrol. 29 (3), 625–679.
Mezcua, J., Buforn, E., Udías, A., Rueda, J., 1992. Seismotectonic of the Canary Islands. Tectonophysics 208 (4), 447–452, http://dx.doi.org/10.1016/0040-1951(92)90440-H.
Miller, M.S., O'Driscoll, L., Butcher, A.J., Thomas, C., 2015. Imaging Canary Island hotspot material beneath the lithosphere of Morocco and southern Spain, Earth Planet. Sci. Lett. 431, 186–194, http://dx.doi.org/10.1016/j.epsl.2015.09.026.
Moreira, V.S., 1985. Seismotectonics of Portugal and its adjacent area in the Atlantic. Tectonophysics 117 (1–2), 85–96, http://dx.doi.org/10.1016/0040-1951(85)90238-0.
Mouayn, I., Tadili, B.A., Aït Bahim, L., Ramdani, M., Limouri, M., Jabour, N., 2004. Duration magnitude scale and site residuals for Northern Morocco. Pure Appl. Geophys. 161, 1061–1080.
Okada, J., Sigmundsson, F., Ofeigsson, B.G., Ferreira, T.J.L., Rodrigues, R., 2015. Tectonic and volcanic deformation on São Miguel Island, Azores, observed by continuous GPS analysis 2008-13. In: Gaspar, J.L., Guest, J.E., Duncan, A.M., Barriga, F.J.A.S., Chester, D.K. (Eds.), Volcanic Geology of São Miguel Island (Azores Archipelago), 44. Geological Society, London, Memoirs, pp. 239–256, http://dx.doi.org/10.1144/M44.18.
Pérez, N., Hernández, A., Padrón, E., Melián, G., Marrero, R., Padilla, G., Barrancos, J., Nolasco, D., 2007. Precursory subsurface 222Rn and 220Rn degassing signatures of the 2004 seismic crisis at Tenerife Canary Islands. Pure Appl. Geophys. 164 (12), 2431–2448.
Pérez, N., Hernández, A., Melián, G., Padrón, E., Nolasco, D., Barrancos, J., Marrero, R., Padilla, G., Calvo, D., Rodríguez, F., Chiodini, G., 2010. An increasing trend of the diffuse CO2 emission from Teide volcano (Tenerife, Canary Islands): a premonitory geochemical signature of volcanic activity changes at Tenerife? In: 1.3-P-71. Cities on Volcanoes 6th, Tenerife 2010.
Peláez, J.A., Chourak, M., Tadili, B.A., Aït Brahim, L., Hamdache, M., López Casado, C., Martínez Solares, J.M., 2007. A catalog of main Moroccan earthquakes from 1045 to 2005. Seismol. Res. Lett. 78, 614–621, http://dx.doi.org/10.1785/gss rl. 78.6.614.
Phillipson, G., Sobradelo, R., Gottsmann, J., 2013. Global volcanic unrest in the 21 st century: an analysis of the first decade. J. Volcanol. Geotherm. Res. 264, 183–196, http://dx.doi.org/10.1016/j.jvolgeores.2013.08.004.
Pinel, V., Jaupart, C., 2004. Magma storage and horizontal dyke injection beneath a volcanic edifice. Earth Planet. Sci. Lett. 221 (1–4), 245–262, http://dx.doi.org/10.1016/s0012-821x(04)00076-7.
Piqué, A., Le Roy, P., Amrhar, M., 1998. Transtensive synsedimentary tectonics associated with ocean opening: the Essaouira-Agadir segment of the Moroccan Atlantic margin. J. Geol. Soc. London 155, 913–928.
Ribeiro, A., Cabral, J., Batista, R.e., Matias, L.M., 1996. Tectonic stress pattern in Portugal mainland and the adjacent Atlantic region (West Iberia). Tectonics 15, 641–659.
Rosas, F.M., Duarte, J.C., Neves, M.C., Terrinha, P., Silva, S., Matias, L., Gràcia, E., Bartolome, R., 2012. Thrust–wrench interference between major active faults in the Gulf of Cadiz (Africa–Eurasia plate boundary, offshore SW Iberia): Tectonic implications from coupled analog and numerical modeling. Tectonophysics 548–549, 1–21, http://dx.doi.org/10.1016/j.tecto.2012.04.013 (ISSN 0040-1951).
Saki, M., Thomas, C., Nippress, S.E.J., Lessing, S., 2015. Topography of upper mantle seismic discontinuities beneath the North Atlantic: the Azores, Canary and Cape Verde plumes. Earth Planet. Sci. Lett. 409, 193–202, http://dx.doi.org/10.1016/j.epsl.2014.10.052.
Schmincke, H.U., 1982. Volcanic and chemical evolution of the Canary Islands. In: yon Rad, V., Hinz, K., Shartein, M., Seibold, E. (Eds.), Geology of the Northwest African Continental Margin. Springer, New York, NY, pp. 273–306.
Scordilis, E.M., 2006. Empirical global relations converting M S and m b to moment magnitude. J. Seismol. 10, 225–236, http://dx.doi.org/10.1007/s10950-006-9012-4.
Serpelloni, E., Vannucci, G., Pondrelli, S., Argnani, A., Casula, G., Anzidei, M., Baldi, P., Gasperini, P., 2007. Kinematics of the Western Africa-Eurasia plate boundary from focal mechanisms and GPS data. Geophys. J. Int. 169, 1180–1200, http://dx.doi.org/10.1111/j.1365-246X.2007.03367.x2.
Silva, R., Ferreira, T., Medeiros, A., Carmo, R., Luis, R., Wallenstein, N., Bean, C., Sousa, R., 2015. Chapter 17 seismic activity on São Miguel Island volcano-tectonic structures (Azores archipelago). Geol. Soc. London, Memoirs 44, 227–238, http://dx.doi.org/10.1144/M44.17.
Stroncik, N.A., Klügel, A., Hansteen, T.H., 2009. The magmatic plumbing system beneath El Hierro (Canary Islands): constraints from phenocrysts and naturally quenched basaltic glasses in submarine rocks. Contrib. Mineral. Petrol. 157, 593–607, http://dx.doi.org/10.1007/s00410-008-0354-5.
Sun, D., Miller, M.S., Holt, A., Becker, T.W., 2014. Hot upwelling conduit beneath the Atlas mountains, Morocco. Geophys. Res. Lett. 41, 8037–8044.
Telesca, L., Lovallo, M., Lopez, C., Marti, J., 2016. Multiparametric statistical investigation of seismicity occurred at El Hierro (Canary Islands) from 2011 to 2014. Tectonophysics 672–673, 121–128, http://dx.doi.org/10.1016/j.tecto.2016.01.045.
Terrinha, P., Matias, L., Vicente, J., Duarte, J., Luís, J., Pinheiro, L., Lourenço, N., Diez, S., Rosas, F., Magalhães, V., Valadares, V., Zitellini, N., Roque, C., Mendes Víctor, L., 2009. Morphotectonics and strain partitioning at the Iberia-Africa plate boundary from multibeam and seismic reflection data. Mar. Geol. 267 (3–4), 156–174, http://dx.doi.org/10.1016/j.margeo.2009.09.012 (15, ISSN 0025-3227).
Thomson, A.B., Connolly, J.A.D., 1995. Melting of the continental crust: some thermal and petrological constraints on anatexis in continental cllision zones and other tectonics settings. J. Geophys. Res. 100 (15), 579, http://dx.doi.org/10.1029/95JB00191 (565-15).
Vannucci, G., Gasperini, P., 2004. The new release of the database of earthquake mechanisms of the mediterranean area (EMMA version 2). Ann. Geophys. 47 (N.1), 307–334 (Supplement to V.).
Vinciguerra, S., Day, S., 2013. Magma intrusion as a driving mechanism for the seismic clustering following the 9 may 1989 earthquake swarms at the Canary Islands. Acta Geophys. 61 (6), 626–1641, http://dx.doi.org/10.2478/s11600-013-0152-y.
Vinciguerra, S., Gresta, S., Barbano, M.S., Distefano, G., 2001. The two behaviours of Mt. Etna Volcano before and after a large intrusive episode: evidences from b value and fractal dimension of seismicity. Geophys. Res. Lett., 28, http://dx.doi.org/10.1029/2000GL012434.
Vinciguerra, S., 2002. Damage mechanics preceding the September–October 1989 flank eruption at Mt. Etna volcano inferred by seismic scaling exponents. J. Volcanol. Geotherm. Res. 113, 391–397.

Wallenstein, N., Silva, R., Riedel, C., Lopes, C., Ibáñez, J., Silveira, D., Montalvo, A., 2009. In: Bean, C.J., Braiden, A.K., Lokmer, I., Martini, F., O'Brien, G.S. (Eds.), Recent Developments in Seismic Studies in the Fogo Volcano Area, São Miguel Island (Azores). VOLUME Project Consortium, Dublin, pp. 207–216, VOLUME project, EU PF6 (No. 018471), ISBN 978–1-905254–39-2.

Walter, T.R., Amelung, F., 2007. Volcanic eruptions following M ≥ 9 megathrust earthquakes: implications for the Sumatra-Andaman volcanoes. Geology 35, 539–542, http://dx.doi.org/10.1130/G23429A.1.

White, R., McKenzie, D., 1989. Magmatism at rift zones: the generation of volcanic continental margins and flood basalts. J. Geophys. Res. 94 (B6), 7685–7729.

Wiemer, S., 2001. A software package to analyze seismicity: ZMAP. Seismol. Res. Lett. 72, 373–382.

Williams, S.D.P., 2008. CATS: GPS coordinate time series analysis software. GPS Solut. 12 (2), 147–153, http://dx.doi.org/10.1007/s10291-007-0086-4.

Zhao, D.P., Lei, J., Inoue, T., Yamada, A., Gao, S.S., 2006. Deep structure and origin of the Baikal rift zone. Earth Planet. Sci. Lett. 243, 681–691.

APPENDIX

B

Pre-eruptive unrest signs

López C., M.A. Benito, J. Martí, C. del Fresno, L. García-Cañada, H. Albert and H. Lamolda (2017), Driving magma to the surface: the 2011–2012 El Hierro eruption, G3, accepted by Editor.

AGU PUBLICATIONS

Journal Home | GEMS Desktop | Author Instructions | Reviewer Instructions | Change Journal | Contact | AGU.org | Join AGU

G³ | Geochemistry, Geophysics, Geosystems

AN AGU JOURNAL

Detailed Status Information

Manuscript #	2017GC007023
Current Revision #	0
Submission Date	2017-05-15 15:51:37
Current Stage	All Reviewers Assigned
Title	Driving Magma to the Surface: the 2011–2012 El Hierro Volcanic Eruption
Running Title	El Hierro Eruption
Manuscript Type	Research Article
Special Sections	N/A
Cover Letter	Dear Journal of Geochemistry, Geophysics and Geosystems Editor, Please find enclosed the manuscript entitled "Driving Magma to the Surface: the 2011-2012 El Hierro Volcanic Eruption" to be considered for publication in your Journal. In this paper we analyze the precursory seismic and geodetic activity that preceded the most recent eruptive experience occurred in the El Hierro Island (Canary Islands, Spain) in 2011-2012. We applied novel methods and took into account new information about the internal structure of El Hierro. This enabled us to identify new features about the process as a prolonged first phase characterized by hydraulic tensile fracturing, and induced shear seismicity on pre-existent faults within the volcano and raised the Coulomb stress over the whole crust. These results will facilitate interpretations of eruption precursors registered by monitoring networks during volcanic unrest This study is not a duplicate publication and has not been submitted elsewhere. The manuscript has been approved by all authors. The authors declare that they have no conflict of interest for the publication of this article. We would like to suggest the following potential reviewers: Maurizio Battaglia, Maurizio.battaglia@uniroma1.it Jürgen Neuberg, locko@earth.leeds.ac.uk Steve McNutt smcnutt@usf.edu Jesús Ibañez, jibanez@ugr.es Ana Negredo, anegredo@fis.ucm.es Thank you very much for taking your time to review this manuscript.

Figure B.1: Proof of delivery to G3 and acceptance by the Editor

Driving Magma to the Surface: the 2011–2012 El Hierro Volcanic Eruption

Carmen López [1,*], Maria A. Benito-Saz [1], Joan Martí [2], Carmen del-Fresno [1], Laura García-Cañada [1], Helena Albert [3], Héctor Lamolda [1,4]

[1] Instituto Geográfico Nacional (IGN), C/Alfonso XII, 3, 28014 Madrid, Spain.

[2] Group of Volcanology (GVB-CSIC), SIMGEO (UB-CSIC), Institute of Earth Sciences Jaume Almera, Lluis Solé Sabaris s/n, 08020, Barcelona, Spain.

[3] Earth Observatory of Singapore, Nanyang Technological University, 639798, Singapore, Singapore.

[4] Universidad Politécnica de Madrid (UPM), C/Ramiro de Maeztu, 7, 28040 Madrid, Spain.

*Corresponding author: Carmen López (clmoreno@fomento.es)

Key Points:

- Identification of a prolonged first unrest phase of hydraulic tensile fracturing
- Occurrence of magma-triggered shear seismicity on pre-existent faults in the volcano edifice
- Evidence of magma pulses crossing the Moho discontinuity

Abstract

In order to improve knowledge of the mechanisms operating during volcanic unrest and their quantification when only limited data is available, we reanalyzed the seismic and deformation data corresponding to the pre-eruptive unrest on El Hierro (Canary Islands) in 2011. We applied novel methods and took into account new information about the internal structure of the island. We corrected the hitherto-incomplete seismic catalogue to estimate the full evolution of the released seismic energy and demonstrate the importance of non-located earthquakes. Using seismic data and GPS displacements, we characterized the shear-tensile type of the predominant fracturing and modelled the strain and stress fields for different time periods. This enabled us to identify a prolonged first phase characterized by hydraulic tensile fracturing, which we interpret as being related to the beginning of the emplacement of new magma below the volcanic edifice on El Hierro. This was followed by post-injection unidirectional migration, probably controlled by the stress field and the distribution of the structural discontinuities. We identified the effects of energetic magmatic pulses occurring a few days before the eruption that induced shear seismicity on pre-existent faults within the volcano and raised the Coulomb stress over the whole crust. We suggest that these magmatic pulses reflect the crossing of the Moho discontinuity, as well as changes in the path geometry of the dyke migration towards the surface. The final phase involved magma ascent through a pre-fractured crust. These results will facilitate interpretations of eruption precursors registered by monitoring networks during volcanic unrest.

1 Introduction

The occurrence of seismic swarms, surface deformation and thermal and geochemical anomalies constitute the main evidence for the reactivation of a volcanic system [e.g. *Phillipson et al*., 2013], and the study of the spatial and temporal variations constitute the most robust tool for forecasting the future behaviour of volcanic unrest [*Sparks*, 2003].

During the final stages of pre-eruptive volcanic unrest, certain geophysical and geodetical features are usually observed: an overall acceleration in seismicity and ground deformation [e.g. *Bell and Kilburn*, 2011], shallower seismicity [e.g. *Battaglia et al*., 2005], seismic migration [e.g. *Caudron et al.*, 2015] and an apparent lack of activity (hours to minutes) before the reinforcement or the onset of the eruption [e.g. *Roman et al*., 2016]. Several well-documented eruptions show some, if not all, of these precursory features [e.g. *Vinciguerra*, 2002; *Battaglia et al*., 2005; *Bell and Kilburn*, 2011, *López et al*., 2012; *Sigmundsson et al*., 2015; *Caudron et al*., 2015], which suggests that similar fundamental processes occur within these volcanoes. Whether this reactivation gives rise to an eruption or only represents a departure from the normal state of activity of the volcano will depend on the type of processes that have caused the reactivation (e.g. magmatic, hydrothermal and/or tectonic). However, the processes preceding a new eruption are complex and poorly known, and there are still many unanswered questions regarding the requirements for an irreversible failure of the Earth's crust and non-stop magma migration from deeper levels to the surface. It is also difficult to correctly interpret the precursory signals recorded by monitoring networks and to understand the nature and extent of the physical processes that cause them. Some of the difficulties arise from the incompleteness of monitoring data and the lack of previous knowledge of the volcanic systems (e.g. type of magma, internal structure, local and regional stresses). In particular, instrumental monitoring data about unrest preceding monogenetic eruptions are sparse and the available information is mainly based on historical records (Albert et al., 2016).

The observational data collected during the volcanic eruption on El Hierro in 2011–2012 provides an opportunity to address this topic. During the unrest (19 July–10 October 2011), the Instituto Geográfico Nacional's (IGN, Spain) monitoring network recorded intense seismicity and surface deformation, thereby suggesting magma accumulation and migration near the base of the crust below the island [see *López et al*., 2012]. Despite all the scientific work devoted to this eruption [e.g. *López et al*., 2012, 2014; *Martí et al*., 2013, 2017; *Tárraga et al.*, 2014; *González et al*., 2013; *Klügel et al*., 2015; *Sainz-Maza* et al., 2014; *García-Yeguas et al*., 2014; *Meletlidis et al*., 2015; *Telesca et al*., 2014, 2015; *Díaz-Moreno et al*., 2015], there are still a number of unresolved questions regarding the unrest process. Did the seismicity truly define the path followed by the magma during the pre-eruptive unrest process? When was the new magma emplaced below the island? Which processes controlled the aseismic upward migration of the magma to the surface and why was it aseismic?

Magma migration through the brittle part of the lithosphere causes fracturing and dike propagation, which is driven by magma overpressure, the physical properties of the magma and crust, and the local and regional stress fields [e.g. *Pinel and Jaupart*, 2004; *Maccaferri et al*., 2011]. In light of new published information about the internal structure below El Hierro [*García-Yeguas et al*., 2014; *Martí et al*., 2017], we reanalyzed the seismic and geodetic data recorded during El Hierro volcanic unrest to gain deeper understanding of the nature of the precursory signals and how to correctly interpret them when only limited data is available. We applied novel methods for retrieving the maximum amount of information from the data and were able to obtain new details regarding the eruptive mechanism. The results will not only be useful for understanding the eruption on El Hierro and its unrest process but also for comprehending the dynamics of other volcanoes in active monogenetic fields.

1.2 El Hierro overview

El Hierro is the smallest and youngest of the group of seven volcanic islands that form the Canarian Archipelago located off the northwest coast of Africa [*Carracedo et al*., 2002] (Figure 1a). In July 2011, after more than 200 years of quiescence, a period of volcanic unrest began that culminated in a submarine eruption on 10 October 2011, less than 2 km off the island's southern coast. The eruption lasted for four months and generated serious bubbling and the emission of ash and scoriaceous fragments onto the surface of the sea [e.g. *Meletlidis et al*., 2015].

Structural studies carried out on El Hierro before the eruption reveal clear lithospheric anomalies below the island. *Carbó et al*. [2003] and *Llanes* [2006] performed a 3D-lithospheric gravimetric inversion over a wide area around the Canary Islands (Figure 1b). These authors found a main regional N-S oriented Bouguer gradient to the west of the island of La Palma that passes through El Hierro, which is associated with a Bouguer wavelength of 40 km (corresponding to a depth of 48–128 km). They also identified two shallow gravity minima to the NE and SW of El Hierro, with Bouguer wavelengths of 12-40 km (corresponding to a depth of 12–48 km) (Figure 1c). In the same area that these two authors (*Carbó et al*. [2003] and *Llanes* [2006]) found a gravity minimum to the SW of El Hierro, *Montesinos et al*. [2006] used a 3D gravity inversion to model a negative density anomaly at a depth of 10km.

In a field survey carried out prior to the 2011 unrest, *Gorbatikov et al*. [2013] studied the deep structure of El Hierro using microseismic sounding techniques. These authors found a central-eastern intrusive high velocity body in the crust that they interpreted as being related to the early stage of the formation of the island, as well as a western intrusive body below the crust at a depth of >15 km that was interpreted as a recent magmatic reservoir (Figure 1d). This is consistent

with the depth range of 19–26 km (in the upper-mantle) reported by *Stroncik et al*. [2009] for the magma plumbing and storage system below El Hierro.

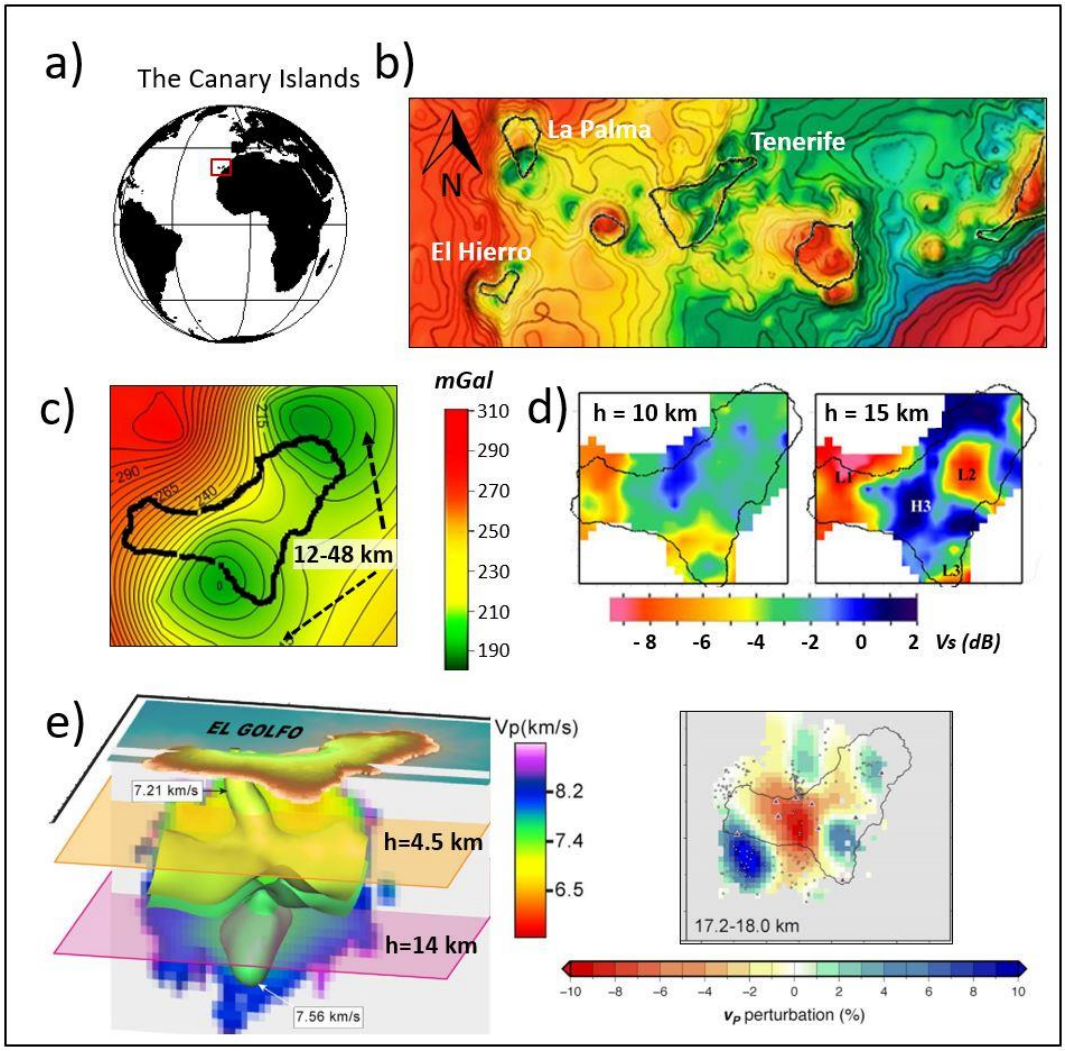

Figure 1. El Hierro location and its internal structure. a) Geographical location of the Canary Archipelago. b) Distribution of the islands over the Bouguer anomaly map [modified from *Carbó et al*., 2003; *Llanes* 2006] and c) zoom of the local structures around El Hierro (colour scale, in mGal, is the same in b)). d) S-wave velocity distribution at 10 and 15 km depth [modified from *Gorvatikov et al*., 2013]. e) P-wave 3-D tomography of the structure of El Hierro, and its horizontal projection at 17.2-18 km depth [modified from *Martí et al*., 2017].

After the 2011–2012 El Hierro eruption, P- and S-wave 3D tomography was performed with the 13,000 local earthquakes registered from July 2011 to September 2012 [*García-Yeguas et al*., 2014]. It revealed a high-velocity crust to a depth of 10–12 km and a low-velocity anomaly below the base of the crust, interpreted as a batch of magma rising as a small plume from the mantle located beneath El Hierro. Furthermore, recent P-wave 3D tomography [*Martí et al*., 2017] performed with 20,000 local earthquakes registered in September 2011–March 2014, revealed additional and valuable features. *Martí et al*. [2017] were able to model the structural complexity of the interior of El Hierro, including the identification of a number of stress barriers corresponding to regional tectonic structures and blocked pathways from previous eruptions, which reduces the

options for fresh magma for finding a suitable pathway to the surface and for erupting (Figure 1e). These authors also propose the existence of a magma reservoir in the upper-mantle, situated in the central area of the island.

The unrest on El Hierro began on 19 July 2011 with the observation of low magnitude seismicity located first in the central part of the island and subsequently migrating to the south at a depth of ~9–16 km [*López et al.*, 2012; *Domínguez Cerdeña et al*., 2014]. A simultaneous surface deformation reflected a correlated southwards migration of the source of pressure [*Meletlidis et al*., 2015]. Two weeks before the eruption a clear acceleration in this process was registered in the form of an increase in the rate of deformations and in the scale of the seismicity. Previous geophysical interpretations [e.g. *González et al.*, 2013; *Lopez et al*., 2014; *Sainz-Maza et al*., 2014; *Meletlidis et al*., 2015] suggest that the final magma migration from depth to the surface could have started some days before the beginning of the eruption; however, the mechanism involved is unknown. On 8 October 2011, a *Mw* 4.0 earthquake, occurred 1.5 km off the southwest coast of the island. From this event to the beginning of a volcanic tremor signal on 10 October 2011 (04:10 UTC), the only recorded activity consisted of a few shallow (1–3 km depth) and low magnitude (< 2 *Mw*) earthquakes occurring 5-km south of the island [*López et al.*, 2014].

Figure 2 shows the seismicity located by the IGN monitoring network (Figure 2a), the evolution of the located hypocentres (Figure 2b) and the double-couple focal mechanism solutions of the $M_W \geq 3.5$ events located during the unrest, all registered during 27 September–9 October [*del Fresno et al.*, 2016] (Figure 2c).

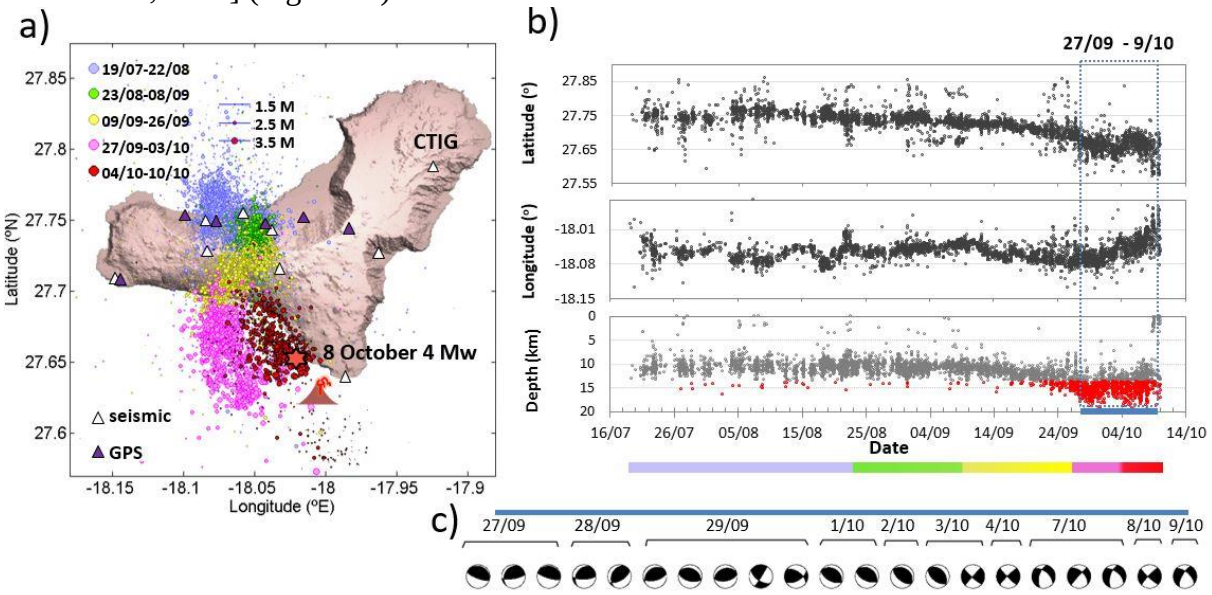

Figure 2. Seismicity located on El Hierro during the unrest. a) Distribution for different time periods; b) evolution of hypocentre coordinates. Scale bar (purple: 19 July–22 August, green: 23 August–8 September, yellow: 9–26 September, pink: 27 September–3 October, red: 4–10 October). c) Double-couple focal mechanism solutions of the $M_W \geq 3.5$ events in the period 27 September–9 October. Seismic stations are represented by white triangles and GPS stations by black ones.

From 19 July to 8 September 2011, activity consisted of low magnitude earthquakes located in clusters, as highlighted by a precise double-difference relocation study that used data

from 3,500 (out of a total of 10,000 events) local earthquakes registered during the unrest [*Domínguez Cerdeña et al*., 2014]. We distinguish two periods (9–26 September and 27 September–3 October) during which the seismicity of increasing magnitude was located to the south of the previous activity. Finally, high-magnitude sparse seismicity occurred on 3–10 October (including the 8 October 4.0 *Mw* earthquake).

2 Methodology and analyses

We performed seismic and deformation characterization based on 1) temporal variations in the *b*-value of the Gutenberg-Richter distribution and the *Vp/Vs* ratio; 2) the evolution of the accumulated seismic strain and seismic volume; 3) the characterization of the different seismo-volcanic signals and the tensile-shear type of the fracturing; and 4) the modelling of the geodetic pressure sources for different time periods.

The seismic data was provided by the IGN catalogue (www.ign.es) and includes the activity registered by the permanent seismic stations installed on El Hierro: one three-component (3CC) broad-band station and eight short- and medium-period 3CC stations (Figure 2a). Despite its low density, this network was well distributed and had a mean error of 3 km for epicentre location and 5 km for depth estimation [*López et al.*, 2012]. The local GPS network during the unrest episode had up to six stations, which allow daily coordinate solutions to be calculated. Although they registered data for almost the whole of the unrest episode, the distribution of these stations was uneven and only covered properly the north and central parts of the island (Figure 2a).

2.1 Seismic *b*-value and *Vp/Vs* ratio temporal evolution

We calculated the variations in the *b*-value of the Gutenberg-Richter law (see Annex.1) to identify different time periods in which tectonic (driven mainly by tectonic plate activity) or volcano-tectonic (driven by the volcanic activity) seismicity predominated. We adjusted the unknowns, *a* and *b*, using the maximum curvature method [*Aki*, 1965] in overlapping moving windows with 200 earthquakes. We then computed the completeness magnitude (above this magnitude the catalogue should include all the events recorded by the seismic network), Mw_C, and the maxima magnitude reached, Mw_{max}, in each time period window [ZMAP program; *Wiemer*, 2001].

In addition, we analyzed the temporal variations in the P- (compressional) and S- (shear) wave travel-time velocities (*Vp/Vs*) of the local earthquakes on El Hierro. In volcanic areas, the *Vp/Vs* ratio aids the study of the properties of the medium, the existence of fluids and/or increasing/changing crack distribution, thereby identifying the volcano state and its evolution [e.g. *Lin and Shearer*, 2009, *Hong et al*., 2014]. We calculated the *Vp/Vs* ratio and Poisson's ratio, *v*, using the phase information (P- and S-wave arrival times) of the located and a robust multilinear regression for those $Mw>1.7$ events in non-overlapping windows with 300 earthquakes (see Annex.1).

2.2 Seismic strain and volume

By applying the formulations in *Kostrov* [1974], *Jackson and McKenzie* [1988] and *Stich et al*. [2006] (see Annex.2), we calculated the permanent seismic strain (static seismic deformation in response to stress forces) from the seismic moment (which measures the size of the earthquake, and is proportional to the product of the rock strength, the fault area and the amount of slip) for different ranges of time and magnitude. We summed the contributions to the strain of the located

seismicity (included in the seismic catalogue) with magnitudes above Mw_C to the contribution of the seismicity with magnitudes below Mw_C (most of them not included in the seismic catalogue) inferred from the *b*-value regression of the Gutenberg-Richter distribution. This non-catalogued seismicity is relevant when large earthquakes do not dominate the deformation ($b > 1.5$). We used the relationship established by *Hanks and Kanamori* [1979] between the scalar seismic moment, *Mo*, and *Mw*, $M_o = 10^{1.5Mw+9.05}$, and the *a*, *b*, Mw_{max} and Mw_C values obtained in 2.1, with Mw_{min} = 1.0, the seismic consistency *Cs* = 1 and the shear modulus μ=4×10^{10}Pa [*Watts*, 1994; *Watts et al*., 1997].

We estimated the contribution of the permanent seismic deformation (static deformation) to the variations in the volume from *Mo* using the approximation $\Delta V = \frac{\sum Mo}{\mu}$ [*Aki and Richards*, 1980; *Hill et al*., 2003]. With this equation, $\sum Mo$ becomes proportional to the volume of the active fractures associated with the magmatic activity. In fact, for hydraulic fracturing or geothermal exploration projects this parameter allows operators to assess the extent of the stimulated rock volume and the efficiency of the injection activities [*Maxwell et al*., 2006; *Shapiro et al*., 2011].

2.3 Type of seismic signals and tensile-shear fracturing

The continuous raw waveform includes a wide variety of seismic signals: transient signals such as volcano-tectonic events and low frequency events and continuous signals such as micro-seismicity, volcanic tremors and swarms of volcano-tectonic events. To study the different contribution of these seismic sources to the seismic data acquired, and to discriminate weak seismic signals from noise, we performed a Real-time Seismic Amplitude Measurement (RSAM) analysis. The RSAM analysis is a robust tool for monitoring volcanic activity because it provides a simple indicator of the level of seismic energy released [*Endo and Murray*, 1991].

We calculated the RSAM (see Annex.3) on the broadband CTIG seismic station (the CTIG was the only station with a flat instrumental response in the whole frequency spectra that recorded the seismic activity from the beginning to the end of the unrest). We separated the different seismic sources by applying bands filters to the continuous data: 1–3 Hz for tremors, low frequency events (LF), hybrids and medium magnitude volcano-tectonic events (VT); 3–15 Hz small VT; and 15–30 and 30–50 Hz for very small and micro-seismic events, as per the classification in *Wassermann* [2012]. We corrected for instrument response and for attenuation, *Q*, (which is frequency-dependent). We adopted for the local S-wave attenuation (Qs = 90* f $^{0.5}$) the average of the values calculated by *Núñez* [2017] for El Hierro crust. The P-wave attenuation, Q_P, was calculated using the *Knopoff* [1971] approximation, $Q_P \approx 2.25 * Q_S$. We also corrected data for geometrical spreading using a (1/r) dependence of amplitude with the source-receiver distance, *r*. The P-wave RSAM was computed using the vertical component and the S-wave RSAM using the average sum of the NS and EW components.

After performing the RSAM on the S- and P-waves, the computation of the ratio between the energy in the S- and P- radiated fields, E_S/E_P, was straightforward, and provided valuable information about the dominant fracturing type associated with the emplacement and migration of the magma.

2.4 Modelling of the geodetic pressure sources and the strain and stress fields

The GPS data was processed using Bernese software [*Dach et al*., 2015] in the ITRF2008 reference frame and a network of more than 30 GPS stations located in the Canary Islands, Azores, North Africa and southern Spain. Precise satellite orbits and absolute antenna-phase centre models from the IGS, along with ocean-loading model FES2004, were applied [*Benito-Saz et al*., 2017].

Three-dimensional displacements and their associated errors were calculated for each selected time period and inverted using the dMODELS software package [*Battaglia et al*., 2013], which uses a nonlinear inversion algorithm to determine the best-fit parameters (i.e. location, depth and volume change) for the deformation source. We used the spherical point pressure source model within an elastic, isotropic and homogeneous half-space [*Mogi*, 1958] with ν = 0.25 and μ= 40 GPa [*Watts*, 1994; *Watts et al*., 1997]. To assess the uncertainty of the source model parameters, an empirical bootstrap method was applied 1,000 times to estimate the 95% confidence intervals [*Efron and Tibshirani*, 1986]. Despite the simplicity these models provide a first-order analysis of the deformation sources and their evolution over time. As well, we calculated the static stress changes caused by the static displacement associated with the point pressure sources, following *Okada's* [1992] formulation [Coulomb 3.3 software, by *Lin et al*., 2004; *Toda et al*., 2005]. We modelled the static stress changes (see Annex.4) using Young modulus E = 100 GPa and ν = 0.25.

3 Results

The characterization analysis of the located seismicity showed significant variations of the Catalog performance. Figure 3 shows the time evolution of the *b-value*, Mw_{max} and Mw_C parameters (Figure 3a), the time evolution of the earthquake location on a N-S projection (Figure 3b), the time fluctuations of the *Vp/Vs* ratio (Figure 3c) and the Poisson's ratio curve (Figure 3d). Variation in Mw_C with time is immediately obvious (Figure 3a), especially during the intense seismic swarm episodes registered during the two weeks before the onset of the eruption. During seismic swarms most of the seismic waveforms were partially overlapping, thereby making the phase detection and separation of the earthquakes difficult or even impossible. The incompleteness of the IGN catalogue motivated us to use an approximate method for quantifying the contribution of the non-located seismicity that was not included in the seismic catalogue (section 2.2).

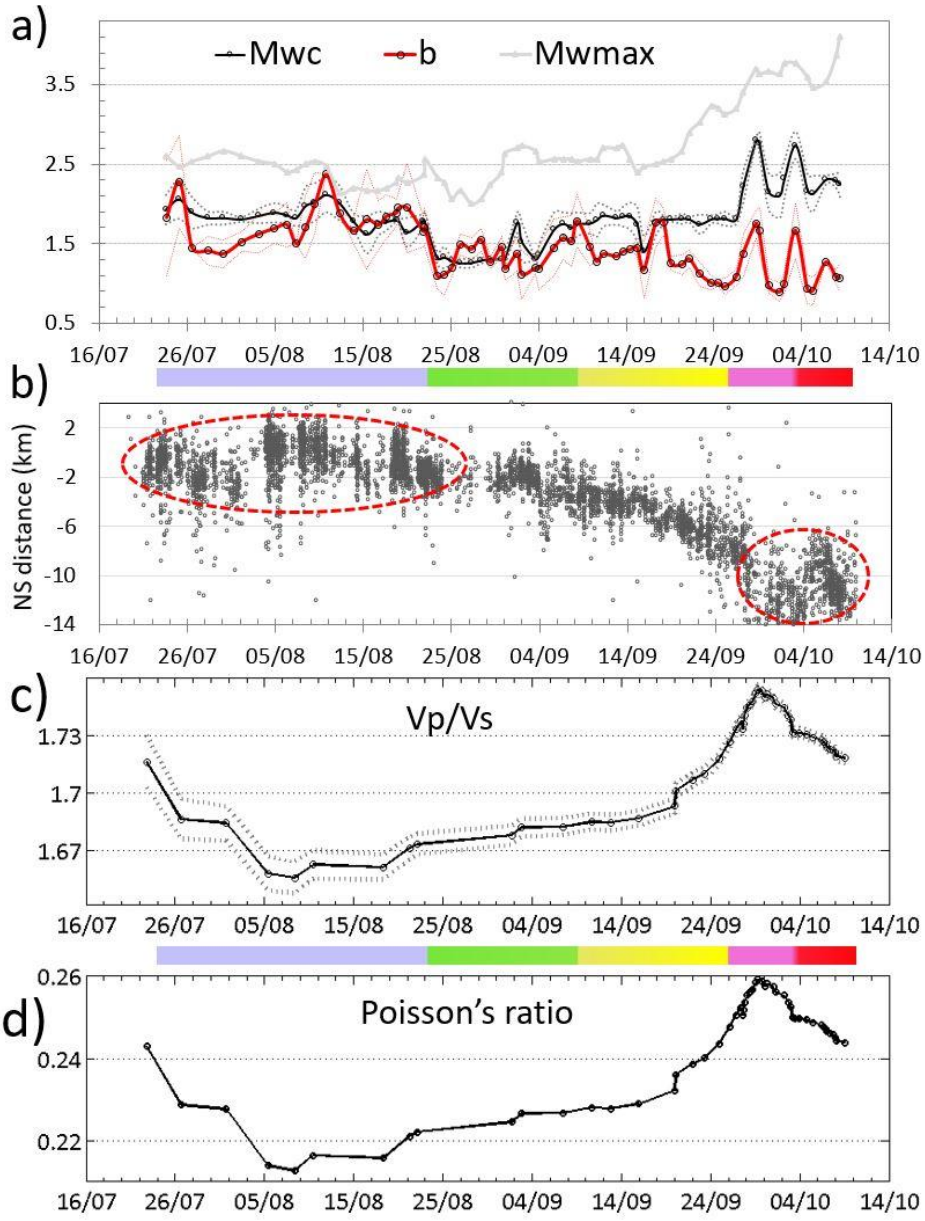

Figure 3. Main features of the located seismicity on El Hierro Island during the 2011 unrest. a) Time evolution of the Mw_{max}, Mw_C and *b*-value parameters. b) N-S growth distance from 19/08 to 10/10 (82 days), c) *Vp/Vs* ratio evolution and error bounds, d) Poisson's ratio evolution. Scale bar intervals as in previous figure.

Figure 4a shows the seismic strain time evolution corresponding to the located (above Mw_C) and non-located seismic events, the accumulated seismic volume (Figure 4b), and the daily $Mw \geq 2.5$ seismic events located by the IGN (Figure 4c).

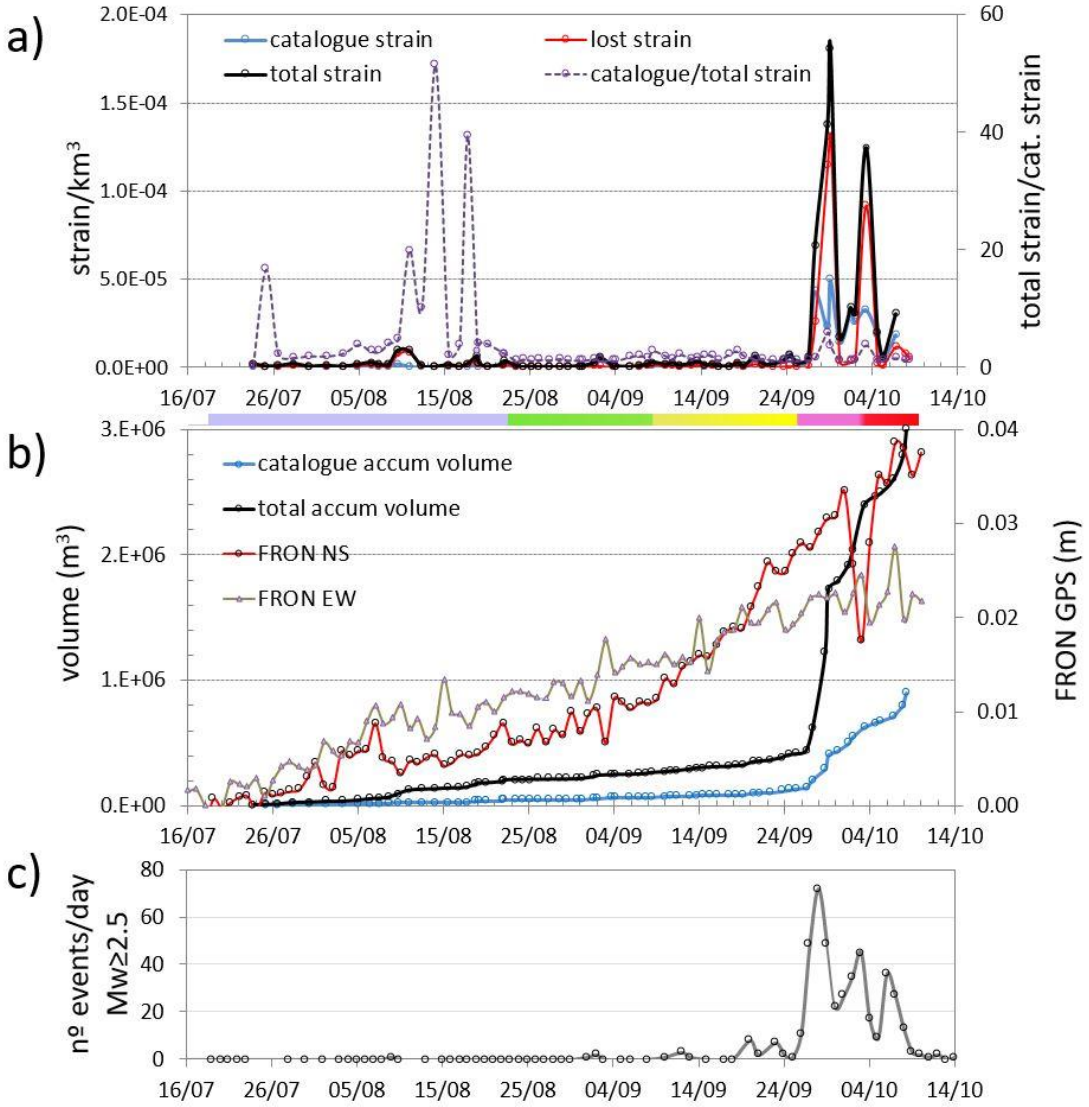

Figure 4. Strain analysis on El Hierro Island during the 2011 unrest. a) Seismic strain of the located earthquakes above Mw_C (blue curve), below Mw_C (in red), the sum of both (in black) and rate of located strain to total strain (in purple). b) Contribution to the volume of the earthquakes above Mw_C (in blue), total contribution from located and no located (in black) and horizontal (NS and EW) daily series from the FRON GPS station. c) Number of $Mw \geq 2.5$ events per day. Scale bar intervals are as in previous figure.

In addition, given that the seismic catalogue only includes volcano-tectonic seismicity above the Mw_C, we studied the continuous seismic waveform to try to extract additional information regarding the fracturing mechanism. Figure 5a shows the time evolution of E_S/E_P. P-wave RSAM curves for different frequency bands are shown in Figure 5b and 5c.

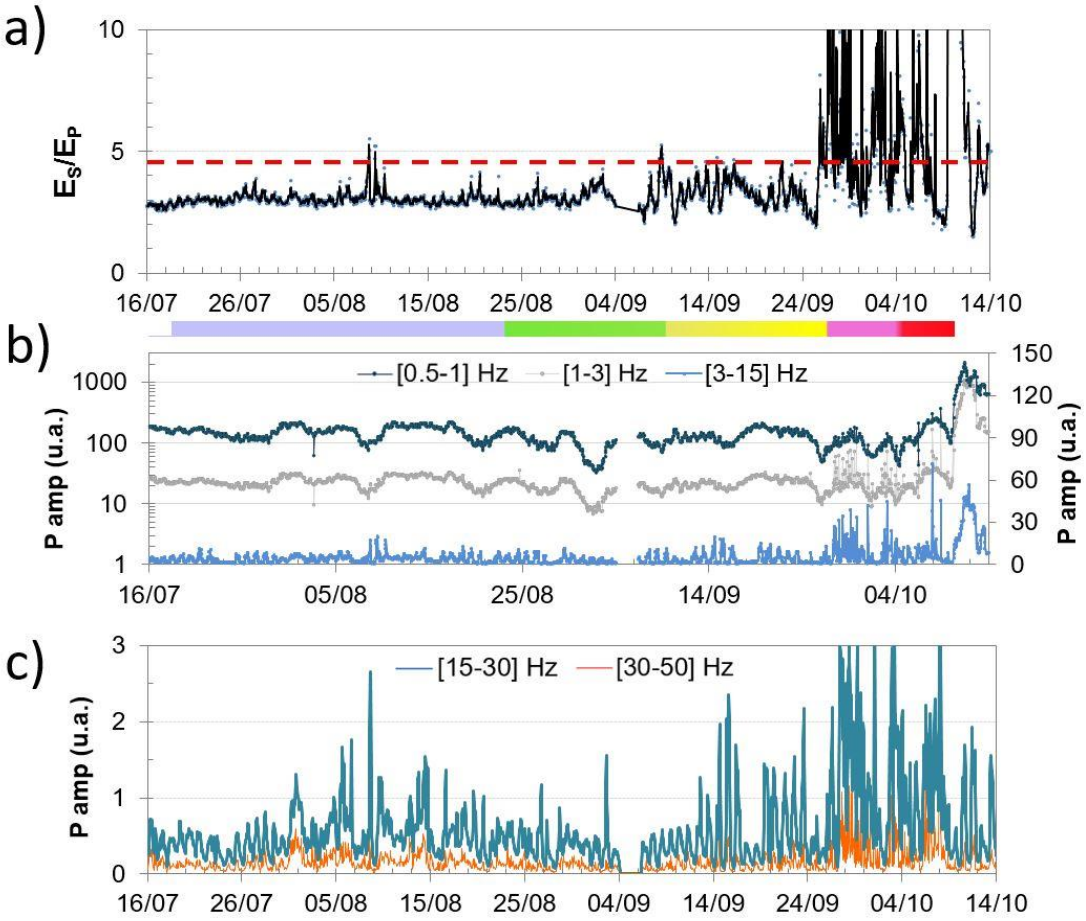

Figure 5. RSAM and tensile/shear type of fracturing analyses. a) E_S/E_P time evolution. RSAM plots in P-wave amplitude of the CTIG station for different frequency bands: b) 0.5–1, 1–3 and 3–15 Hz and c) and 15–30, 30–50 Hz. Scale bar intervals as in previous figure.

We also analyzed and modelled the ground surface deformation recorded by the GPS network. Figure 6 shows the point pressure source solutions corresponding to the following time periods: 31 July–8 September (Figure 6a), 9–21 September (Figure 6b) and 22 September–9 October (Figure 6c), with in this final period an additional inversion for 3–9 October (Figure 6d). We selected these time periods to ensure that the resolution on the displacement measurements was sufficient, to minimize inversion errors, and to replicate as closely as possible the periods used in the seismic analyses. As only four-to-six GPS stations were operating during these time periods, and given that most were located in the northern part of El Hierro, we performed the most basic and simplest deformation source model (Mogi's point source). Therefore, we should consider the results simply as a first approximation of the deformation source, useful only for tracking and evaluating the evolution of the magma (volume change and position) during the unrest. However, other source geometries, heterogeneities of the crust or topography of the island should also be taken into account if more accurate results are required [e.g. *Masterlark*, 2007]. The results are summarized in Table 1, and include the location, depth, volume change and chi square per degrees of freedom (χ^2v) for each of the point pressure sources, together with the lower and upper limits of the 95% confidence intervals obtained by bootstrapping techniques.

Time periods	Longitude (°)	Latitude (°)	Depth (km)	ΔV (km^3)	X^2v
2011-07-31 / 2011-09-08	$-18.053^{-18.012}_{-18.140}$	$27.713^{27.730}_{27.629}$	$4.9^{14.0}_{2.3}$	$0.004^{0.030}_{0.001}$	4.7
2011-09-08 / 2011-09-21	$-18.065^{-17.990}_{-18.136}$	$27.690^{27.701}_{27.518}$	$5.4^{21.6}_{4.1}$	$0.008^{0.091}_{0.004}$	5.4
2011-09-21 / 2011-10-09	$-18.064^{-18.043}_{-18.092}$	$27.595^{27.599}_{27.504}$	$5.1^{11.6}_{4.2}$	$0.026^{0.060}_{0.023}$	6.0
2011-10-03 / 2011-10-09	$-18.047^{-17.971}_{-18.139}$	$27.620^{27.668}_{27.506}$	$12.6^{22.9}_{3.0}$	$0.027^{0.085}_{0.009}$	4.8

Table 1. Optimal point pressure source model parameters with 95% confidence intervals.

Figure 6.e shows the Coulomb static stress changes (modelled with the 3–10 October Mogi's source) (Table 1) on the specific faults corresponding to the 4.0 *Mw*, 8 October plane solution (295º strike; 40º dip; 164º rake) [*del Fresno et al*., 2015].

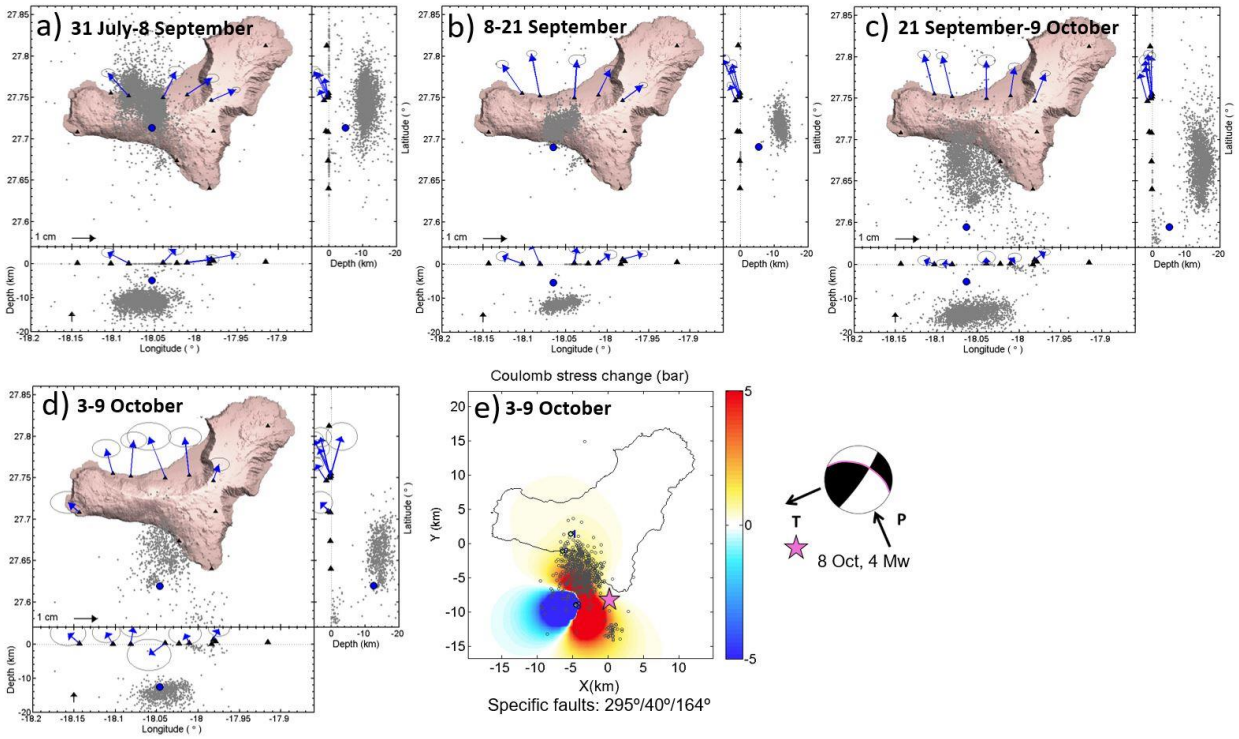

Figure 6. Location and depth of the sphere point pressure deformation sources for the selected time periods. GPS displacements are represented with blue arrows. a) 31 July–8 September. b) 9–21 September. c) 22 September–9 October. d) 3–9 October. e) 3-9 October, Coulomb stress change (bar) distribution on (295º strike, 40º dip, 164º rake) faults at a depth of 12 km, and focal mechanism solution of the 4.0 *Mw* 8 October event (pink star).

We noticed that the modelled pressure centres were always shallower than the seismicity and lay slightly further to the south in the direction of the seismic migration. This bias could be

partially caused by intrinsic errors due to model simplification and the sparse GPS data used for the inversion. Another possible reason for these differences [*Traversa et al*. 2010] is that the seismicity accompanying dyke propagation in basaltic volcanoes represents events located backwards with respect to the dyke tip position. In this case, the seismicity is not only related to the magma propagation but also to the response of the edifice itself to the volumetric deformation [*Traversa et al*., 2010].

4 Discussion

Based on the results obtained here we discuss the emplacement and migration mechanism used by the magma on El Hierro to fracture and travel through the crust from its base to the Earth's surface. Thus, we provide the most likely interpretation of the activity registered during the 2011 unrest.

4.1 Magma emplacement

To discuss this issue, we applied hydraulic fracture theory – which offers challenging interpretations of what occurs when a fluid (including magma) opens and fractures rock – to our results. When an over-pressurised fluid is injected into a volume of rock, the pressure migrates through the pores (pore pressure pulses) and stress variations in the rock occur (due to the opening and fracturing of fluid-filled cracks) [e.g. *Shapiro et al*., 1997; *Miller et al*., 2004; *Toda et al*., 2002; *Dahm et al*., 2010]. In the fluid-filled crack opening and fracturing model [e.g. *Dahm et al*., 2010] cracks grow bi-directionally during the fluid injection process. This bidirectional growth continues for some time (post-injection) due to decompression by the remaining driving pressures, and then subsequently initiates unidirectional growth that is maintained depending on the stress gradients and the injection fluid pressure.

High *b*-values (in some cases up to 2 or even 3) in volcanoes have been interpreted as being caused by the fracturing produced by fluid/magma intrusion in the mapping areas surrounding magma bodies [e.g. *Wiemer and Wyss*, 2002; *McNutt*, 2005; *Bridges and Gao*, 2006, *Murru et al*., 2007; *Díaz-Moreno et al*., 2015]. Additionally, several studies have highlighted how fluids, crack density and pore pressure influence the *Vp/Vs* ratio. Laboratory measurements [*Dvorkin et al*., 1999] have shown that crack opening in rock samples induced by increasing pressure in gas-enriched pores leads to decreasing *Vp/Vs* ratios. Anomalous *Vp/Vs* ratios have also been registered in many volcanoes and low ratios are interpreted as an increase in the presence of gas in fractures [e.g. Kilauea, *Johnson and Poland*, 2013; Mount Etna, *Patanè et al*., 2006; Campi Flegrei Caldera, *Chiarabba and Moretti*, 2006; Aso Caldera, *Unglert et al*., 2011]. These authors suggest that increasing crack density should lead to higher S-wave delay times and to lower *Vp/Vs* ratio values — if the cracks fill with gas.

The activity registered on El Hierro from the beginning of the unrest to when the seismic migration to the south at a constant depth started (19 July to ~21 August) presented clustered swarm activity, low Mw_{max}, $b \geq 1.5$, tensile fracturing (low E_S/E_P ratio), low *Vp/Vs* ratio (low Poisson's ratio) and micro-seismicity. Based on hydro-fracturing models, a fluid injection close to the crust-mantle discontinuity would explain the bi-directional seismicity growth, the *b*-values, the clustered seismicity and the existence of seismic back- and fore-fronts. The high $b > 1.5$ values and decreasing *Vp/Vs* ratio values would reflect the existence of crack opening and fluid-filled activity (gas-enriched). Nevertheless, variations in the *Vp/Vs* ratio cannot be attributed to any variation in depth in the fracturing since the seismicity depth range remained stable, thereby supporting the

hydro-fracturing (mainly tensile) origin of the seismicity registered from 19 July to ~21 August. This fluid intrusion could not ascend through the crust due to the high velocity crust in the area, as revealed by the two P- and S-wave tomography results [*Gorvatikov et al*., 2013; *Martí et al*., 2017] (Figure 1); instead, it over-pressurized the entire island and promoted extension and tensile fracturing of pre-existing faults. The injection of magma into a pre-existing mantle reservoir is supported by petrological data (Longpre et al., 2014). The observation of a spatial CO_2 positive flux anomaly in a faulted area in the north of El Hierro on 22 July–14 August [*López et al*., 2012] could be congruent with this described state.

The seismic migration pattern observed from 21 August to ~ 27 August suggests unidirectional growth in the fluid injection, with the growth being driven by structural or regional stress gradients. In this sense, the exact coincidence between the unidirectional growth path and the lateral heterogeneity at 10–15 km below the Moho discontinuity is notable [*Gorbatikov et al*., 2013] on El Hierro (Figure 1). *Díaz et al*. [2015] also suggest the existence of stress diffusion and hydraulic fracturing in the seismic activity in their analysis of the temporal and spatial distribution of the seismic activity occurring on El Hierro in 2011–2013.

4.2 Evidence of increasing magma pressurization

On 21 and, more clearly, on 27 September, the activity changed drastically and from this date onwards features appeared that had never been observed before: deeper earthquakes, very intense swarms of VT events, alternation of *b*-values minima close to 1 with maxima of *b*~1.5, alternation of shear and tensile behaviour, maximum Poisson's ratio values, maximum seismic strain release, and the greatest deformation, as reflected by the higher modelled Mogi's source volume. This activity occurred in two pulses (27–30 September and 2–5 October) and was registered by the seismic and the GPS network. Figure 7 shows the time series of the GPS, the seismic strain and the evolution of Poisson's ratio. Of note are the coincidence between the coherent oscillation in the NS component and the seismic strain pulse (2–5 October) with maximum on 3 October, and the change in the focal mechanism from thrust fracturing to strike-slip that occurred on that date (upper panel on Figure).

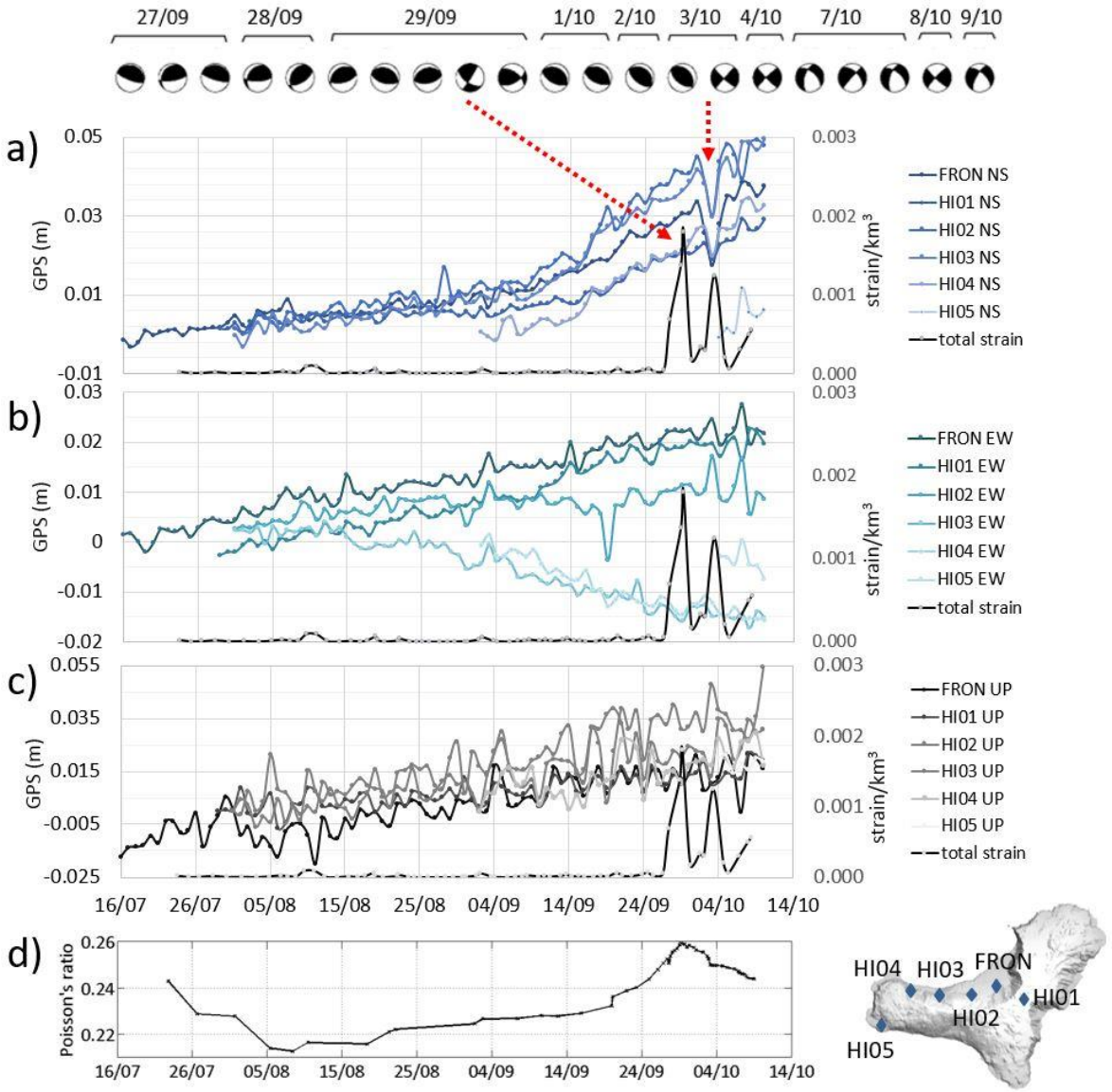

Figure 7. Comparison of the evolution of the seismic strain, the geodetic strain (time series of GPS deformation) and the Poisson's ratio during the 2011 El Hierro unrest. a) GPS NS component and the seismic strain, b) GPS EW components and seismic strain, c) GPS vertical components and seismic strain, d) Poisson's ratio time evolution.

The variations in the *Vp/Vs* ratio from 27 September onwards cannot be attributed clearly to any variation in the depth of the fracturing since the seismicity depth range remained stable (at least the seismicity located and included in the seismic catalogue). Furthermore, at the maxima of these two pulses, the E_S/E_P values show shear fracturing and *b*-values over 1.5, while at the minima, the E_S/E_P values show tensile fracturing and *b*~1. Rapid variations in the deformation (inflation/deflation cycles) have been related to dyke propagation that allows the movement of magma and temporal changes in the local stress and strain fields [e.g. *Heimisson et al*., 2015].

We cannot rule out a bias in the GPS coordinates during (3-5 September) due to atmospheric instabilities recorded by the meteorological stations on the island. As described in *Larson et al*. [2010], path delays caused by the troposphere are one of the most important sources

of error in GPS precision. In addition, based on *Tregoning and Herring* [2006], poor Zenith Hydrostatic Delay values are able to corrupt the station coordinates and the Zenith Total Delay estimates; nevertheless, this effect is more significant in the vertical component than in the horizontal ones. Thus, we believe that the deformation was real and not biased given that it was greater in its horizontal components than in its vertical ones (Figure 7) and that there were changes in the volcanic system detected by other techniques. However, the magnitude of the deformations on those days could have been influence by tropospheric effects.

When discussing the relationship that exists between tectonic stress fields and the earthquakes triggered by magma overpressure, *Roman et al*. [2007] propose different faulting scenarios that vary in terms of the strength of the regional tectonic stress compared to the volcanic stress. Faults slip in the direction of the regional maximum compression if regional stresses dominate; there is no faulting and shadow zones are created around the inflating dyke if regional stresses balance volcanic stresses; and reverse faulting occurs if volcanic stresses dominate [*Roman et al*., 2007].

In regard to the Coulomb static stress changes associated with the modelled sphere pressure sources, both triggered seismicity and stress shadow have been observed in association with evolving static stress changes during propagating dyke mechanisms in active volcanoes [e.g. *Green et al.*, 2015]. The Coulomb stress at the site of the 8 October event (Figure 6.e) was ~ 5 bar. The focal mechanism of this event was modelled by *del Fresno et al*. [2015], who obtained a pure double-couple mechanism with a null isotropic (dilatational) component, which rules out any volume changes in the source due to magma intrusion. By modelling a circular fault model [*Brune*, 1970], *del Fresno et al*. [2012] calculated a rupture area of 0.9 km^2 and 20–30 bar for the stress drop. This stress drop is higher than the 5 bar (0.5 MPa) of positive change in the Coulomb stress; in pre-existing faults similar variations provoke faulting, thereby provoking an earthquake [*Walter and Amelung*, 2006, *Chouet et al*., 2013]. Thus, a positive stress transfer by itself could have triggered the 8 October 4.0 *Mw* earthquake along a pre-existent fault, as well as other lower magnitude seismicity, as suggested by the close coincidence between the 3–8 October spatial location distribution and the area with greatest stress (in red) (Figure 6.e).

Based on these observations, we suggest that from 27 September onwards, an increase in over-pressurized melt, reached the mantle-crust boundary, in accordance with the reverse type of the focal mechanism. This increased overpressure promoted tectonic seismicity while increasing in volume due to the tensile emplacement of additional melt material. During the reverse faulting period (27 September–3 October), volcanic stresses probably dominated, the source of this fracturing being clearly located below the crust base. The change in focal mechanism and the GPS oscillation patterns registered around 3 October suggest that an important change occurred, probably due to the propagation of a dyke from the magma reservoir that caused a fall in the magma pressure below the crust. The strike-slip seismicity registered on 3–8 October could have been the consequence of increased Coulomb stress transfer on pre-existing regional faults in the crust since strike-slip event planes coincided with the maximum regional NW-SE compression [*Geyer et al*., 2016]. The rapid variations in the *Vp/Vs* recorded in this period probably reflect the abrupt changes in the stress and deformation states, which cause fracturing, and the active transport of fluids (melt) driving more fracturing in a positive feedback system that ultimately leads to the eruption [*Koulakov et al*., 2012]. During the seismic gap registered after the occurrence of the 8 October 4 *Mw* event, an intermediate scenario could have occurred, whereby increasing volcanic stress balanced out the regional stress.

4.3 Geometry of the upwards magma migration

Martí et al. [2013] proposed a mechanistic model for the eruption on El Hierro by modelling numerically the stress and the strain fields in an elastic lithosphere, and including the effects of flexure, edifice load and the water layer. Their results explain some of the aspects and features observed during the unrest, including the lateral sill propagation of the magma below the crust and the lateral ascent towards the surface away from the edifice centre. These authors suggest the presence of an intrusive complex characterized by different rheology that would explain the halt in the vertical progression of the magma when it reached the bottom of the crustal boundary.

Here, we complement the mechanism by applying the conditions for tensile and shear fracturing in monogenetic volcanism [e.g. *Martí et al*., 2016] (see Annex.5). For the crust failure, the magma pressure needs to reach values over 10-200+σ_n to create new fractures under the normal stress (σ_n) or greater than 1+σ_n bar to open a pre-existing fault. In the case of tensile faulting (σ_n<0), the pressure required will be lower [e.g. *Gudmundsson*, 2012; *Martí et al*., 2016]. Therefore, it is evident that, in the event of low-pressure conditions, the most probable scenario is the emplacement of magma into previously faulted areas of the crust as a result of tensile opening. As the stress drop after a tensile earthquake is smaller than in the case of shear failure volcanic earthquakes associated with tensile failure will have small magnitudes and the radiated seismic waves will have more energy at higher frequencies. This was probably the case of the high-frequency micro-seismicity registered during the El Hierro unrest in the periods in which tensile behaviour was dominant (Figure 5c).

Figure 8 represents the results of the bi-axial modelling [*Zang and Stephansson*, 2010] of the differential stress field and the magma pressure (ascending from a 3MPa over-pressurized source located at a depth of 20 km). The overpressure in the fracture, $P_{net} = (P - \sigma_n)$, is calculated for different dip angles (see Annex.5). We located the roof of the magma chamber at a depth of 20 km, in accordance with the modelled anomalous body found at that depth by *Marti et al*. [2017]. We used the same values for magma and crust densities as used by *Becerril et al*. [2013] in their numerical modelling of the feeder dykes on El Hierro: $\rho_m = 2.65 \times 10^3$ kg m^{-3} for the basaltic magma density and $\rho_r = 2.75 \times 10^3$ kg m^{-3} for the host crust. We used v=0.27 (Figure 8a) and v=0.24 (Figure 8b) that bound the Poisson's ratio values obtained from the seismic catalogue analysis. Our modelling shows that the requirement for induced vertical-plane tensile faults, ($\sigma_V - \sigma_H$) < 560 bar, is fulfilled at shallow depths (less than 3 km), and tensile openings are possible on fractures oriented within 22.5º from σ_V (Figure 8 a, b). At any other depths in the crust and at other orientations, new fractures will be shear or tensile in nature but will occur in pre-existing fractures. As the differential stress increases with depth and pore pressure, leading to smaller real differential stresses and a greater probability of a crack opening in over-pressurized formations [*Fischer and Guest*, 2011], we cannot rule out the possibility that tensile opening could occur near the magma reservoir or the dyke. One noticeable result is the influence of Poisson's ratio on the available faults planes that the over-pressurized magma uses to travel from depth to the surface. Whatever the case, at depths of less than 6–7 km, positive buoyant magma will open all pre-existent faults at any dip angle.

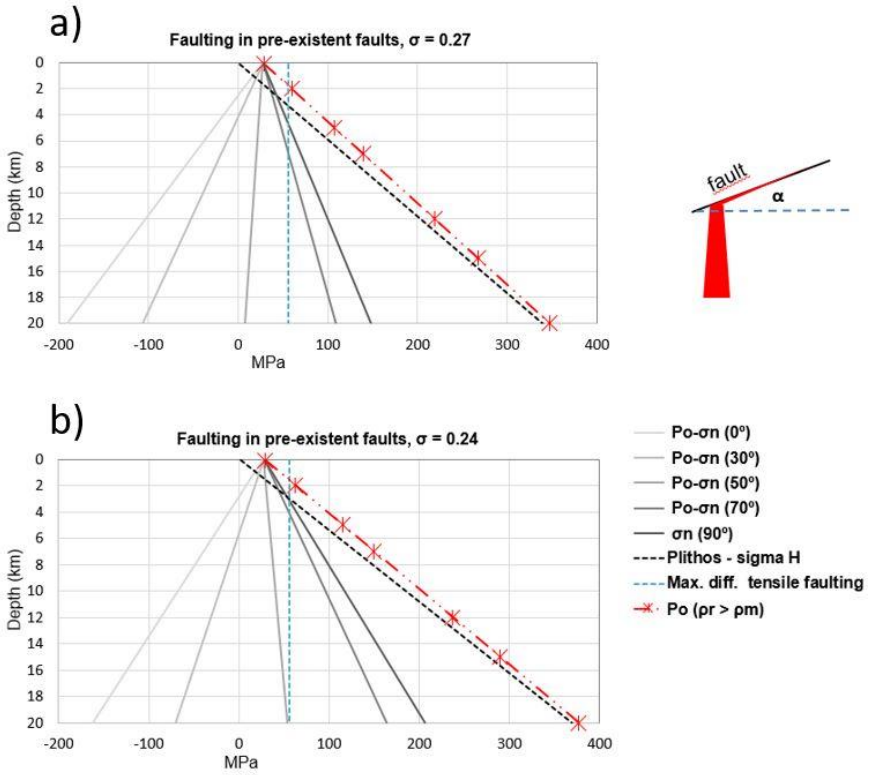

Figure 8. Magma overpressure in the fracture $P_{net} = (P - \sigma_n)$ for different dip angles, superimposing the maximum differential stress curve for the occurrence of tensile faulting (560 bar) for a) v=0.27 and b) v=0.24.

Stress modelling highlights the importance of the pre-existing faults on El Hierro. The lithosphere in the south of El Hierro could be faulted and coincide with the known low-density and gravity anomaly [*Carbó et al*., 2003; *Gorvatikov et al*., 2013]. Once the magma crossed the Moho south El Hierro, dyke stress would unclamp the pre-existing faults, thereby allowing the aperture of a magma path to the surface in a combined process of tensile and shear fracturing. During its migration, the geometry and orientation of the dyke changed to take advantage of new available fault planes (Figure 8), which gave rise to apparently aseismic migration close to the surface on 8–10 October, probably due to high-aperture tensile fracturing. This stagnation of the magma in the lower crust and the lateral propagation have been also described in previous petrological studies focusing on the olivine crystals (e.g. Longpre et al., 2014).

4.4 Conceptual model

Finally, we provide a conceptual model (Figure 9) for the unrest mechanism in which three main stages can be distinguished:

Stage 1: Magma injection overpressures the existing magma reservoir below the crust, promoting stress diffusion and hydraulic fracturing of pre-existing and new cracks in the lower crust with gas-enriched fluids. Regional fields control the migration of the stress perturbation involved in the fracturing to the south.

Stage 2: Over-pressurized magma pulses reach the crust base by migrating to below the Moho discontinuity. Increased overpressure promotes tectonic seismicity, while the reservoir increases in volume due to the tensile emplacement of additional melt material. During the reverse faulting

period (27 September–3 October) volcanic stresses were probably dominant, the source of this fracturing clearly being below the crust base. The high-velocity crust base blocked upwards dyke propagation. This stage finished with the crossing of the mantle-crust boundary in a faulted crust region south El Hierro.

Stage 3. On 3–8 October, an increase in the transport of magmatic fluids in fractures led to greater fracturing of the lower crust in a positive feedback system. Dyke propagation caused a fall in the magma pressure below the crust and the increase in the stress in the crust. The positive stress transfer in the crust could have triggered seismicity along a pre-existent fault on 3–8 October. An increasing volcanic stress balance with the regional stress field enabled the propagating dykes to use and maintain open the network of pre-existing faults from the crust base to the surface. In the upward migration, the magma starts by using vertical pre-existing faults and opens closer to the surface pre-existing faults of any dip angle, thereby promoting during the final kilometres horizontal (lateral E-W oriented) migration that reached the surface far from the area in which the previous seismicity had been located.

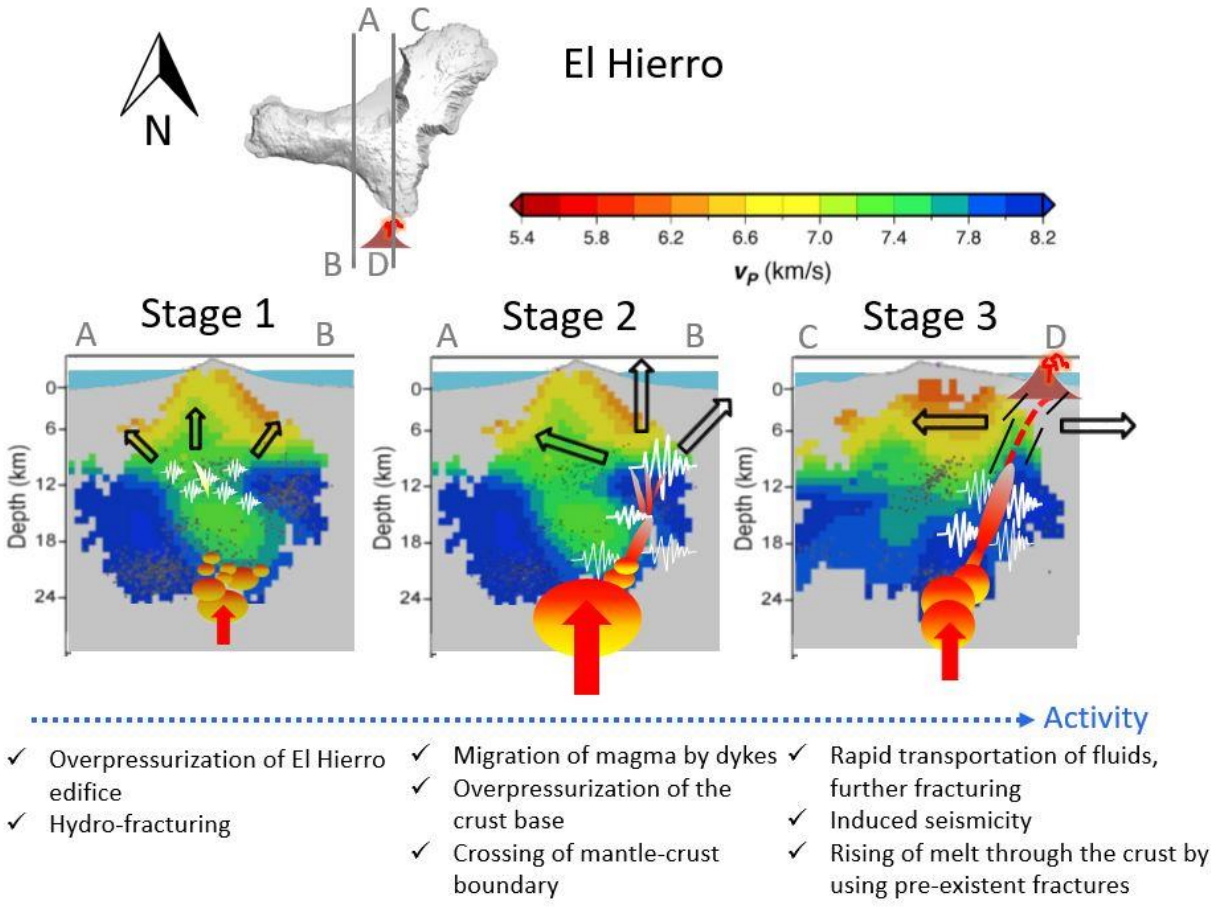

Figure 9. Conceptual model for the El Hierro volcanic unrest mechanism. Stage 1 (19 July–27 September), Stage 2 (27 September–3 October), Stage 3 (3–10 October). Vertical cross-sections drawn over a modified version of the P-wave tomography results [*Martí et al*., 2017].

5. Conclusions

Despite the fact that data used was limited, that the methods applied were merely an approximation of the physics involved in an eruptive event, and that the results include numerous uncertainties rather than simple solutions, the consistence provided by comparable results allows us to hypothesize how and why the eruption on El Hierro took place. Additionally, compared to previous studies that have employed some of the techniques used in this work (e.g. *b*-value analyses, Mogi's point source modelling), we have been able to provide a complete calculation of the whole evolution of the seismic strain and the Coulomb modelling of the stress field changes. In a similar way, no *Vp/Vs* temporal evolution study or E_S/E_P characterization of the tensile/shear fracturing, or error analyses of the deformation Mogi's modelled sources, has ever been performed using the dataset from El Hierro. Some of the evidence found is novel (e.g. occurrence of high-magnitude triggered seismicity, hydro-fracturing by gas-enriched fluids, evidence of the crossing of the mantle/crust boundary), as is the interpretation of the overall evidence in light of the detailed knowledge of the structure of El Hierro.

It is also worth noting that when the seismic activity included in a seismic catalogue does not include very low-magnitude seismicity (tensile fracturing), or when its performance is dependent on the seismic rate, only a very approximate (in the best of cases) path along which the magma is rising or accumulating can be drawn. High-magnitude activity can be partially related to the opening of the pre-existing network of fractures of the volcano edifice and some of the high magnitude events are caused by stress triggering. Likewise, it is essential to have a dense GPS network for precise modelling of the magma intrusion and the changes in its geometry as it crosses the lithosphere. Otherwise, it is only possible to derive simple and probably biased models. Therefore, we stress the crucial importance of setting up a high-quality (i.e. dense, low-noise, well-distributed) network of instruments and developing new tools for comprehensive monitoring of volcanic activity and the correct interpretation of the observational data acquired.

Annex

1. Seismic b-value and Vp/Vs ratio temporal evolution

The Gutenberg-Richter (G-R) distribution power law states that,

$$log_{10}n(M) = a - bM \quad (1),$$

where *n(M)* is the cumulative number of earthquakes of magnitude larger than *M*, *a* represents the earthquake productivity, and *b* describes their size distribution [*Gutenberg and Richter*, 1944].
The *Vp/Vs* ratio can be estimated by using a modified Wadati analysis [*Wadati*, 1933; *Jo and Hong*, 2013]:

$$\frac{Vp}{Vs} - 1 = \frac{(Ts-Tp)}{Tp} \, (2),$$

where T_P and T_S are the observer P- and S-waves phase readings.
From *Vp/Vs*, the Poisson's ratio ν (the ratio of transverse contraction strain to longitudinal extension strain in the direction of stretching force) can be calculated using:

$$\nu = \frac{1}{2}\left[1 - \frac{1}{(Vp/Vs)^2 - 1}\right] \quad (3)$$

2. Seismic strain

Kostrov's [1974] theorem states that the average seismic strain tensor can be defined by

$$\varepsilon_{ij} = \frac{1}{2\mu V}\sum_{n=1}^{N} M_{ij}^{n} \, (4),$$

where M_{ij}^{n} is the component *ij* of the seismic moment tensor M_n of the earthquake *nth* that occurred in the crustal volume *V*, (that contains the active faults), whose average elastic shear modulus is μ. If the moment tensor solution is not available, the approximation of *Frohlich and Apperson* [1992] can be applied, which calculates the contribution of the scalar seismic moment of each individual earthquake, *Mo*, by

$$|\varepsilon| = \frac{1}{2\mu V} C_S \sum_{n=1}^{N} M_o^n \quad (5),$$

where C_S is the seismic consistency and has a value $C_S \leq 1$. ε represents the amount of final permanent deformation accommodated within the considered crustal volume. If we compute ε for the seismicity occurred over a period of time, Δt, we can refer to the result as $\dot{\varepsilon} = \varepsilon/\Delta t$, the average seismic strain rate. We can compute the average strain between a range of magnitudes Mw_1 and Mw_2 by

$$\int_{M_{W1}}^{M_{W2}} \frac{d|\varepsilon|}{dM_W} = \int_{M_{W1}}^{M_{W2}} \frac{C_S}{2V\mu} n(M_W) M_0 dM_W \, (6).$$

This equation allows us to compute the contribution of the located seismic events from the completeness moment magnitude $Mw_1 = Mw_C$ to the maximum moment magnitude of the catalogue $Mw_2 = Mw_{max}$. The ratio of the integration of (6) for adjacent magnitude intervals is

$$\frac{|\varepsilon|_{M_{W0}-M_{W1}}}{|\varepsilon|_{M_{W1}-M_{W2}}} = \frac{10^{(1.5-b)M_{W1}} - 10^{(1.5-b)M_{w0}}}{10^{(1.5-b)M_{W2}} - 10^{(1.5-b)M_{W1}}} \quad (7).$$

This equation allows us to compute the contribution of the non-located earthquakes, from an *a priori* minimum moment magnitude $Mw_0 = Mw_{min}$ to $Mw_1 = Mw_C$.

3. RSAM analysis

The RSAM analysis [*Endo and Murray*, 1991] is defined by

$$RSAM = \frac{\sum_{i=1}^{n} \left| A_i - \bar{A} \right|}{n} \quad (8),$$

where A_i, is the signal amplitude corrected by the instrument response and the geometric and anaelastic attenuation occurred from the hypocentre to the station; $\bar{A}$ is the mean amplitude in the calculation window and n is the number of samples in the window.

The RSAM analysis is an approximated method for computing the continuous scalar seismic moment, *Mo*, and allows us to study the fracturing mechanism associated with the magmatic activity in the case of continuous or overlapping seismic signals. This approximation is more rewarding when the magnitude of the earthquakes decreases – thereby hindering their detection and location – during dense earthquake swarms, or when the magnitude of completeness is high. Following the description of the source radiation function of *Aki and Richards* [2002], *Mo* can be estimated from the far-field seismic P- and S-waves displacement recording, u (x,t). In a homogeneous whole space

$$u(x,t) = \frac{R^{P,S}}{4\pi\rho V^3 r} \dot{Mo}\left(t - \frac{r}{V}\right) \quad (9)$$

$$Mo = \frac{4\pi\rho V^3 r \int_{t_1}^{t_2} u(t)}{R^{P,S}} \quad (10),$$

where ρ is the rock density, V is the P- or S-wave velocity, r is the source–receiver distance, Mo the seismic moment rate, and $R^{P,S}$ is the P- and S- wave radiation patterns. If no focal mechanism solution is available, the average radiation pattern correction, 0.44 for P-waves and 0.60 for S-waves, can be used [*Boore and Boatwright*, 1984]. The approximated mean scalar seismic moment, *Mo*, can then be estimated from (9) and (10) in the (*n* samples) *t1-t2* window using the equation

$$nRSAM = \int_{t_1}^{t_2} u(t) \quad (11).$$

4. Coulomb stress calculations

The Coulomb failure criterion hypothesises that failure is promoted when the Coulomb stress change is positive

$$\Delta\sigma_f = \Delta\tau_s + \mu' * \Delta\sigma_n \quad (12),$$

where $\Delta\sigma_f$ is the change in failure stress on the receiver fault, $\Delta\tau_s$ is the change in shear stress (positive when sheared in the direction of fault slip), $\Delta\sigma_n$ is the change in normal stress (positive if the fault is unclamped), and μ is the effective coefficient of friction on the fault. The strain and the shear and normal components of the Coulomb stress change can be calculated in an elastic half-space in specific faults (receiver fault planes) or on a 3D grid [*Okada*, 1992; *Lin et al*., 2004; *Toda et al*., 2005].

5. Failure criteria and magma pressure on a propagating dyke

The 2D Mohr-Coulomb failure criteria states that new tensile opening will occur along fractures oriented within 22.5º from σ_1 (greater stress component) if the differential stress$(\sigma_1 - \sigma_3) < 2\sqrt{2}S_0$, where σ_3 is the smallest stress component and S_0 the rock cohesion. If both conditions are fulfilled the rock will fail in tensile mode or if not, in a shear or hybrid mode. For a typical rock cohesion of S_0=200 bar, the maximum differential stress for the occurrence of tensile faulting is ~560 bar, although this value can be much smaller if there are pre-existing fractures with significantly smaller cohesion [*Fischer and Guest*, 2011].

In a bi-axial modelling [*Zang and Stephansson*, 2010] σ_1 is vertical and equals σ_V (lithostatic load) and σ_3 is horizontal. In a first approximation σ_V =250 bars/km, while the horizontal or lateral stress is proportional to the vertical load depending on the material properties of the lithosphere [e.g. *Zang and Stephansson*, 2010; *Cañón Tapia*, 2013]

$$\sigma_H = k^* \sigma_v = (\nu / (1-\nu))^* \sigma_v \quad (13),$$

with *v*, the Poisson's ratio. This increasing stress is appropriate for describing the brittle oceanic lithosphere in general form, characterized by a single strength maximum. The normal stress along a fault, σ_n, for different fault dip angles, α, is defined by the equation $\sigma_n = \sigma_V cos^2\alpha + \sigma_H sin^2\alpha$. When a dyke approximates to a pre-existing fault, the magma will open a pre-existing fault that was closed by a normal stress, if the magma pressure $P_o \geq \sigma_n$. The overpressure in the new fracture $P_{net} = (P_o - \sigma_n)$ will be equal to the tensile rock strength, which in the laboratory assumes values from 10 to 200 bar for intact rock and <<10 bar if there are pre-existing fractures [*Fischer and Guest*, 2011]. The magma overpressure in a dyke, P_0, can be calculated using the equation [e.g. *Gudmundsson*, 2012; *Martí et al*., 2016]

$$P_0 = p_e + (\rho_r - \rho_m)gh + \sigma_d \quad (14),$$

where p_e is the excess pressure in the magma reservoir, σ_d the differential stress at the level of the dyke $(\sigma_d = \sigma_V - \sigma_H)$, h the height of dyke above chamber, ρ_r and ρ_m the rock and magma densities and g the gravity acceleration.

Acknowledgments

This research was partially supported by the Instituto Geográfico Nacional (IGN) and the Spanish MINECO project CGL2014-58821-C2-1-R. We would like to thank wholeheartedly all our colleagues from IGN who participated in the monitoring of the volcanic crisis on El Hierro and who furnished the observational data used in this study. We are also grateful for the valuable suggestions made by Victor Villasante (IGN), Adelina Geyer and Antonio Villaseñor (CSIC) that substantially improved this paper. The English text was reviewed and corrected by Michael Lockwood.

References

Aki, K. (1965), Maximum likelihood estimate of b in the formula logN=a−bM and its confidence level, Bul. Earthq. Res. Inst., 43, 237–239.

Aki, K., and P.G. Richards (1980), Quantitative Seismology: Theory and Methods, Freeman and Co., San Francisco, Vol. 1, 557 pp.

Albert, H., Costa, F. and Martí, J (2016), Years to weeks of seismic unrest and magmatic intrusions precede monogenetic eruptions, Geology, 44(3), 211-214.

Battaglia, M., P.F. Cervelli, and J.R. Murray (2013), dMODELS: A MATLAB software package for modeling crustal deformation near active faults and volcanic centers., J. Volcanol. Geotherm. Res., 254, 1–4.

Battaglia, J., V. Ferrazzini, T. Staudacher, K. Aki, J.L. Cheminée (2005), Pre-eruptive migration of earthquakes at the Piton de la Fournaise volcano (Réunion Island), Geophysical Journal, Volume 161, Issue 2, pp. 549-558.

Becerril, L., I. Galindo, A. Gudmundsson, J.M. Morales (2013), Depth of origin of magma in eruptions, Sci. Reports. (Nature Publishing), 3, 2762, doi: 10.1038/srep02762.

Bell, A.F., and C.R.J. Kilburn (2011), Precursors to dyke-fed eruptions at basaltic volcanoes: Insights from patterns of volcano-tectonic seismicity at Kilauea volcano, Hawaii. Bull. Volcanol., doi:10.1007/s00445-011-0519-3

Benito-Saz, M.A., M.M. Parks, F. Sigmundsson, A. Hooper, L. García-Cañada (2017), Repeated magmatic intrusions at El Hierro Island following the 2011–2012 submarine eruption, J. Volcanol. Geotherm. Res., doi: 10.1016/j.jvolgeores.2017.01.020.

Boore, D.M., and J. Boatwright (1984), Average body-wave radiation coefficients, Bull. Seism. Soc. Am., 74, 1615-1621.

Bridges, D.L, and S. Gao (2006), Spatial variation of seismic b-values beneath Makushin Volcano, Unalaska Island, Alaska, Earth Planet Sci. Lett., 245, 408–415.

Brune, J. (1970), Tectonic stress and the spectra of seismic shear waves from earthquakes, J. Volcanol. Geotherm. Res., 75, 4997-5009, http://dx.doi.org/10.1029/JB075i026p04997.

Caudron, C., B. Taisne, Y. Kugaenko, V. Saltykov (2015), Magma migration at the onset of the 2012–13 Tolbachik eruption revealed by Seismic Amplitude Ratio Analysis, J .Volcanol. Geotherm. Res., 307, 1 60-67, ISSN 0377-0273, http://doi.org/10.1016/j.jvolgeores.2015.09.010.

Carbó, A., A. Muñoz-Martín, P. Llanes, J. Alvarez, and EEZ Working Group, (2003), Gravity analysis offshore the Canary Islands from a systematic survey, Marine Geophys. Res., 24, 113–127.

Carracedo, J.C., F.J. Pérez, E. Ancochea, J. Meco, F. Hernán, C.R. Cubas, R. Casillas, E. Rodriguez and A. Ahijado (2002), Cenozoic volcanism II: The Canary Islands, In: The Geology of Spain, Ed. Gibbons, W. and Moreno, T., Geological Society of London, 439-472.

Cañón Tapia, E. (2013). Analytical models of magma chamber stability: An abridged critical review of key concepts, J. Volcanol. Geotherm. Res., 249, 174-196. http://doi.org/10.1016/j.jvolgeores.2012.10.003.

Chiarabba, C., and M. Moretti (2006), An insight into the unrest phenomena at the Campi Flegrei caldera from Vp and Vp/Vs tomography, Terra Nova, 18: 373–379, doi:10.1111/j.1365-3121.2006.00701.x

Chouet, B.A., and R.S. Matoza (2013), A multi-decadal view of seismic methods for detecting precursors of magma movement and eruption, J. Volcanol. Geotherm. Res., 252, 108-175, http://doi.org/10.1016/j.jvolgeores.2012.11.013.

Dahm, T., S, Hainzl, and T, Fischer (2010), Bidirectional and unidirectional fracture growth during hydrofracturing: Role of driving stress gradients. J. Geophys. Res., 115, B12322. doi:10.1029/2009JB006817.

Dach, R., S. Lutz, P. Walser, P. Fridez (Eds) (2015), Bernese GNSS Software Version 5.2. User manual, Astronomical Institute, Universtiy of Bern, Bern Open Publishing, doi: 10.7892/boris.72297; ISBN: 978-3-906813-05-9.

Del Fresno, C., I. Domínguez Cerdeña, S. Cesca, and E. Buforn (2015), The 8 Octover 2011 Earthquake at El Hierro (Mw 4.0): Focal Mechanisms of the Mainshock and Its Foreshocks, Bull. Seism. Soc. Am., 105 (1), 330-340, doi:10.1785/0120140151.

Del Fresno, C., I. Domínguez Cerdeña, E. Buforn, and C. López (2012), Source Time Function (STF) of the earthquake of the 8th October 2011 at El Hierro (Canary Islands), 7ª Asamblea Hispano-Portuguesa de Geodesia y Geofísica. San Sebastian 2012. ISBN 978-84-941323-1-5, 820 pp.

Del Fresno, C. (2016), Determinación de la Fuente Sísmica a Distancias Regionales: Aplicación a la serie de El Hierro 2011, PhD Thesis. Universidad Complutense de Madrid (Spain), 228pp.

Díaz-Moreno, A., J.M. Ibáñez, S. DeAngelis, A. García-Yeguas, J. Prudencio, J. Morales, T. Tuvè, and L. García (2015), Seismic hydraulic fracture migration originated by successive deep magma pulses: The 2011–2013 seismic series associated to the volcanic activity of El Hierro Island, J. Geophys Res. Solid Earth, 120, 7749–7770, doi:10.1002/2015JB012249.

Domínguez Cerdeña I., C. del Fresno, and A. Gomis Moreno (2014), Seismicity patterns prior to the 2011 El Hierro Eruption, Bull. Seism. Soc. Am. 104, Vol 1, doi: 10.1785/0120130200.

Dvorkin, J., G. Mavko, and A. Nur (1999), Overpressure detection from compressional-and shear-wave data, Geophys. Res. Lett., 26, 3417–3420.

Efron, B., and R. Tibshirani (1986), Bootstrap Methods for Standard Errors, Confidence Intervals, and Other Measures of Statistical Accuracy, Statist. Sci., 1, 1, 54-75, doi:10.1214/ss/1177013815. http://projecteuclid.org/euclid.ss/1177013815.

Endo, E.T., and T. Murray (1991), Real-time seismic amplitude measurement (RSAM): A volcano monitoring tool. Bulletin of Volcanology, v. 53, p. 533-545.

Fischer, T., and A. Guest (2011), Shear and tensile earthquakes caused by fluid injection, Geophys. Res. Lett., 38. L05 307, doi:10.1029/2010GL045447.

Frohlich, C., and K.D. Apperson (1992), Earthquake focal mechanisms, moment tensors, and the consistency of seismic activity near plate boundaries, Tectonics, 11(2), 279–296. doi:10.1029/91TC02888.

García-Yeguas, A., J.M. Ibáñez, I. Koulakov, A. Jakovlev, M.C. Romero-Ruis, J. Prudencia (2014), Seismic tomography model reveals mantle magma sources of recent volcanic activity at El Hierro Island (Canary Islands, Spain), Geophys. J. Int., 199, 3, 1739-1750, doi: 10.1093/gji/ggu339.

Geyer, A., J. Martí, and A. Villaseñor (2016), First-order estimate of the Canary Islands plate-scale stress field: Implications for volcanic hazard assessment, Tectonophysics, 679: 125-139, http://dx.doi.org/10.1016/j.tecto.2016.04.010.

González, P.J., S.V. Samsonov, S. Pepe, K.F. Tiampo, P. Tizzani, F. Casu, J. Fernández, A.G. Camacho, and E. Sansosti (2013), Magma storage and migration associated with the 2011–2012 El Hierro eruption: Implications for crustal magmatic systems at oceanic island volcanoes, J. Geophys. Res. Solid Earth, 118, 4361–4377, doi:10.1002/jgrb.50289.

Gorbatikov, A.V., F.G. Montesinos, J. Arnoso, M.Y. Stepanova, M. Benavent and A.A. Tsukanov (2013), New features in the subsurface structure model of El Hierro Island (Canaries) from low-frequency microseismic sounding: An insight into the 2011 seismo-volcanic crisis, Surv. Geophys., 3 4 (4), 463–489, doi:10.1007/s10712-013-9240-4.

Green, R.G., T. Greenfield, R.S. White (2015), Triggered earthquakes suppressed by an evolving stress shadow from a propagating dyke, Nat. Geosci., 8 (8), pp. 629–632, http://dx.doi.org/10.1038/ngeo2491

Gudmundsson, A. (2012), Magma chambers: Formation, local stresses, excess pressures, and compartments, J. Volcanol. Geotherm. Res., v. 237–238, 19–41, doi: 10 .1016 /j .jvolgeores .2012 .05 .015.

Gutenberg, B., and C.F. Richter (1944), Frequency of the earthquakes in California, Bull.. Seism Soc. A., 34, 185-188.

Hanks, T.C., and H. Kanamori (1979), A moment magnitude scale, J. Geophys. Res., 84, 2348-2350, doi:10.1029/JB084iB05p02348.

Heimisson, E.R., P. Einarsson, F. Sigmundsson, and B. Brandsdottir (2015), Kilometer scale Kaiser-effect identified in Krafla volcano, Iceland, Geophys. Res. Lett., 42, doi:10.1002/2015GL065680.

Hill, D.P., J.O. Langbein, and S. Prejean (2003). Relations between seismicity and deformation during unrest in Long Valley Caldera, California, from 1995 through 1999. J Volcanol Geotherm Res, 127 (2003) 175-193.

Hong TK., Houng SE and Jo E (2014), Temporal changes of medium properties during explosive volcanic eruption. Geophys Res Lett, 41, 1944–1950, doi:10.1002/2014GL059408.

Jackson J and McKenzie D (1988), The relationship between plate motions and seismic moment tensors, and the rates of active deformation in the Mediterranean and Middle East, Geophys J Int, 93, 45-73 .

Jo, E., and T.K. Hong (2013),VP/VS ratios in the upper crust of the southern Korean Peninsula and their correlations with seismic and geophysical properties, J. of Asian Earth Sciences, 66, 204-214.

Johnson, J.H., and M.P. Poland (2013), Seismic detection of increased degassing prior to Kīlauea's 2008 summit explosion, Nature Communications, 4, article 1668, doi:10.1038/ncomms2703.

Klügel, A., Longpré, M-A., García-Cañada, L., Stix, J., (2015),Deep intrusions, lateral magma transport and related uplift at ocean island volcanoes, Earth and Planetary Science Letters, 431,140-149, ISSN 0012-821X, https://doi.org/10.1016/j.epsl.2015.09.031.

Knopoff, L. (1971), Attenuation, in Mantle and Core. Planetary Physics, edited by J Coulomb, and M Caputo, pp. 146–156, Elsevier, New York.

Koulakov, I., et al., (2012), Rapid changes in magma storage beneath the Klyuchevskoy group of volcanoes inferred from time-dependent seismic tomography, J. Volcanol. Geotherm. Res., http://dx.doi.org/10.1016/j.jvolgeores.2012.10.014.

Kostrov V (1974), Seismic moment and energy of earthquakes, and seismic flow of rock, Izv Acad Sci USSR Phys Solid Earth, 1, 23-44.

Larson, K.M., M. Poland, and A. Miklius (2010), Volcano monitoring using GPS: Developing data analysis strategies based on the June 2007 Kīlauea Volcano intrusion and eruption, J. Geophys. Res., 115, B07406, doi:10.1029/2009JB007022.

Lin, J., and R.S. Stein (2004), Stress triggering in thrust and subduction earthquakes, and stress interaction between the southern San Andreas and nearby thrust and strike-slip faults, J. Geophys. Res., 109, B02303, doi:10.1029/2003JB002607.

Lin, G., and P.M. Shearer (2009), Evidence for water-filled cracks in earthquake source regions, Geophys. Res. Lett., 36, L17315, doi:10.1029/2009GL039098.

Longpré, M. A., Klügel, A., Diehl, A., & Stix, J. (2014). Mixing in mantle magma reservoirs prior to and during the 2011–2012 eruption at El Hierro, Canary Islands. Geology, 42(4), 315-318.

López, C., M.J. Blanco, R. Abella, B. Brenes, V.M. Cabrera-Rodríguez, B. Casas, I. Domínguez-Cerdeña, A. Felpeto, M. Fernández de Villalta, C. del Fresno, M.J. García-Arias, L. García-Cañada, A. Gomis-Moreno, E. González-Alonso, J. Guzmán-Pérez, I. Iribarren, R. López-Díaz, N. Luengo-Oroz, S. Meletlidis, M. Moreno, D. Moure, J. Pereda de Pablo, C. Rodero, E. Romero, S. Sainz-Maza, M.A. Sentre-Domingo, P.A. Torres, P. Trigo, V. Villasante-Marcos (2012), Monitoring the volcanic unrest of El Hierro (Canary Islands) before the onset of the 2011–2012 submarine eruption, Geophys. Res. Lett., 39 LI3303, doi:10.1029/2012GL051846.

López, C., J. Martí, R. Abella, and M. Tárraga (2014), Applying fractal dimensions and energy-budget analysis to characterize fracturing processes during magma migration and eruption: 2011-2012 El Hierro (Canary Islands) submarine eruption. Surv. in Geophys., DOI : 10.1007/s10712-014-9290-2.

Llanes, M.P. (2006), Estructura de la Litosfera en el Entorno de las Islas Canarias a partir del Análisis Gravimétrico e Isostático: Implicaciones Geodinámicas, Doctoral Thesis, U. Complutense de Madrid, Spain, 1-189.

Maccaferri, F., M. Bonafede, and E. Rivalta (2011), A quantitative study of the mechanisms governing dike propagation, dyke arrest and sill formation. J. Volcanol. Geotherm. Res., 208, 39 –50.

Martí, J., V. Pinel, C. López, A. Geyer, R. Abella, M. Tárraga, M.J. Blanco, A. Castro, C. Rodríguez (2013), Causes and mechanisms of the 2011–2012 El Hierro (Canary Islands) submarine eruption, J. Geophys. Res. Solid Earth, 118,1-17, doi:10.1002/jgrb.50087.

Marti, J., C. López, S. Bartolini, L. Becerril and A. Geyer (2016), Stress controls of monogenetic volcanism: a review, Frontiers in Earth Science, 4(106), doi: 10.3389/feart.2016.00106.

Martí, J., A. Villaseñor, A. Geyer, C. López, and A. Tryggvason (2017), Stress barriers controlling lateral migration of magma revealed by seismic tomography, Scientific Reports, 7, 40757, doi: 10.1038/srep40757.

Masterlark, T. (2007), Magma intrusion and deformation predictions: Sensitivities to the Mogi assumptions, J. Geophys. Res., 112, B06419, doi:10.1029/2006JB004860.

Maxwell, S.C., C.K. Waltman, N.R. Warpinski, M.J. Mayerhofer, and N. Boroumand (2006), Imaging seismic deformation induced by hydraulic fracture complexity, SPE paper 102801.

Meletlidis, S., A. Di Roberto, I. Domínguez Cerdeña, M. Pompilio, L. García-Cañada, A. Bertagnini, M.A. Benito-Saz, P. Del Carlo, S. Sainz-Maza Aparicio (2015), New insight into the 2011-2012 unrest and eruption of El Hierro Island (Canary Islands) based on integrated geophysical, geodetical and petrological data. Annals of Geophysics, Vol 58, No5, DOI: 10.4401/ag-6754.

McNutt, S. (2005), Volcanic seismology, Annu. Rev. Earth Planet Sci., 32, 461–491.

Miller, S.A., C. Collettini, L. Chiaraluce, M. Cocco, M.R. Barchi, and B. Kaus (2004), Aftershocks driven by a high pressure CO2 source at depth. Nature, 427, 724–727.

Mogi, K. (1958), Relations between the eruptions of various volcanoes and the deformations of the ground surface around them. Bull. Earthquake Res. Inst. Univ. Tokyo, 36, 99–134.

Montesinos, F.G., J. Arnoso, M. Benavent, and R. Vieira (2006), The crustal structure of El Hierro (Canary Islands) from 3-D gravity inversion, J. Volcanol. Geotherm. Res., 150 (1–3), 283-299, doi:10.1016/j.jvolgeores.2005.07.018.

Murru, M., R. Console, G. Falcone, C. Montuori, and T. Sgroi (2007), Spatial mapping of the b-value at Mount Etna, Italy, using earthquake data recorded from 1999 to 2005, J. Geophys. Res., 112, B12303, doi:10.1029/2006JB004791.

Núñez, A. (2017), Simulación de escenarios sísmicos mediante un Sistema de Información Geográfica para la Península Ibérica, las Islas Baleares y las Islas Canarias, considerando el efecto de sitio y las dimensiones y características de la fuente sísmica, Doctoral Tesis, Universidad Politécnica de Madrid, 455.

Okada, Y. (1992), Internal deformation due to shear and tensile faults in a half-space, Bull. Seismol. Soc. Am., 82 (2), 1018–1040.

Patanè, D., G. Barberi, O. Cocina, P. De Gori, and C. Chiarabba (2006), Time resolved seismic tomography detects magma intrusions at Mount Etna, Science, 313, 821–823, doi:10.1126/science.1127724.

Phillipson, G., R. Sobradelo, and J. Gottsmann (2013), Global volcanic unrest in the 21st century: An analysis of the first decade, J. Volcanol. Geotherm. Res., 264, 183-196, ISSN 0377-0273. http://doi.org/10.1016/j.jvolgeores.2013.08.004.

Pinel, V., and C. Jaupart (2004), Magma storage and horizontal dyke injection beneath a volcanic edifice, Earth and Planet Sci. Lett., 221, 245 –262.

Roman D.C. and P. Heron (2007), Effect of regional tectonic setting on local fault response to episodes of volcanic activity, Geophys. Res. Lett., 34, L13310, doi:10.1029/2007GL030222.

Roman, D.C., Rodgers, M., Geirsson, H., LaFemina, P.C., V. Tenorio (2016), Assessing the likelihood and magnitude of volcanic explosions based on seismic quiescence, Earth and Planetary Science Letters, 450, 20-28, https://doi.org/10.1016/j.epsl.2016.06.020.

Sainz-Maza, S., J. Arnoso, F.G. Montesinos, J. Martí (2014), Volcanic signatures in time gravity variations during the volcanic unrest on El Hierro (Canary Islands), J. Geophys. Res. Solid Earth, 119, DOI: 10.1002/2013JB010795.

Shapiro, S.A., E. Huenges, and G. Borm (1997), Estimating the crust permeability from fluid-injection-induced seismic emission at the KTB site, Geophys. J. Int., 131, F15–F18, doi:10.1111/j.1365-246X.1997.tb01215.x.

Shapiro, S.A., O.S. Krueger, C. Dinske, and C. Langenbruch (2011), Magnitudes of induced earthquakes and geometric scales of fluid stimulated rock volumes, Geophysics 76, WC55–WC63.

Sigmundsson, F., A. Hooper, S .Hreinsdottir, K.S. Vogfjod, B.G. Ofeigsson, E.R. Heimisson, S. Dumont, M. Parks, K. Spaans, G.B. Gudmundsson, and V. Drouin (2015), Segmented lateral dyke growth in a rifting event at Bardarbunga volcanic system, Iceland. Nature, 517(7533), 191-195

Stich D, Serpelloni E, Mancilla F and Morales J (2006), Kinematics of the Iberia–Maghreb plate contact from seismic moment tensors and GPS observations, Tectonophysics, 426 (3-4), 295-317, doi:10.1016/j.tecto.2006.08.004.

Sparks, R, (2003), Forecasting volcanic eruptions, Earth Planet. Lett., 2010(1-2), pp. 1–15, doi:10.1016/S0012821X(03)001249.

Stroncik, N.A., A. Klügel, and T.H. Hansteen (2009), The magmatic plumbing system beneath El Hierro (Canary Islands): constraints from phenocrysts and naturally quenched basaltic glasses in submarine rocks, Contributions to Mineralogy and Petrology 157, 593-607, doi:10.1007/s00410-008-0354-5.

Tárraga, M., J. Martí, R. Abella, R. Carniel, and C. López (2014), Volcanic tremors: good indicators of change in plumbing systems during volcanic eruptions, J. Volcanol. Geotherm. Res., Vol., 273, 33–40.

Traversa, P., V. Pinel, and J.A. Grasso (2010), Constant influx model for dike propagation: implications for magma reservoir dynamics, J. Geophys. Res., vol. 115 B1 pg. B01201, doi:10.1029/2009JB006559.

Telesca, L., M. Lovallo, J. Martì, C. López, and R. Abella (2014), Using the Fisher–Shannon method to characterize continuous seismic signal during volcanic eruptions: application to 2011–2012 El Hierro (Canary Islands) eruption, Terra Nova, 0, 1-5, DOI: 10.1111/ter.12114.

Telesca, L., M. Lovallo, J. Martì, C. López, and R. Abella (2015), Multifractal investigation of continuous seismic signal recorded at El Hierro volcano (Canary Islands) during the 2011–2012 pre- and eruptive phases, Tectonophysics, Vol 642, 71-77, DOI: 10.1016/j.tecto.2014.12.019.

Toda, S., R. Stein, and T. Sagiya (2002), Evidence from the AD 2000 Izu islands earthquake swarm that stressing rate governs seismicity, Nature, 419, 58–61.

Toda, S., R.S. Stein, K. Richards-Dinger, and S. Bozkurt (2005), Forecasting the evolution of seismicity in southern California: Animations built on earthquake stress transfer, J. Geophys. Res., v. 110, B05S16, doi:10.1029/2004JB003415.

Tregoning, P., and T.A. Herring (2006), Impact of a priori zenith hydrostatic delay errors on GPS estimates of station heights and zenith total delays, Geophys. Res. Lett., 33, L23303, doi:10.1029/2006GL027706.

Unglert, K., M.K. Savage, N. Fournier, T. Ohkura, and Y. Abe (2011), Shear wave splitting, VP/VS, and GPS during a time of enhanced activity at Aso caldera, Kyushu, J. Geophys. Res., 116, B11203, doi:10.1029/2011JB008520.

Vanorio, T., J. Virieux, P. Capuano, and G. Russo (2005), Three-dimensional seismic tomography from P wave and S wave microearthquake travel times and rock physics characterization of the Campi Flegrei Caldera, J. Geophy. Res., 110, B03201, doi:10.1029/2004JB003102

Vinciguerra, S. (2002), Damage mechanics preceding the September-October 1989 flank eruption at Mount Etna volcano inferred by seismic scaling exponents. J. Volcanol. Geotherm. Res., 113, 391–397.

Wadati, K. (1933), On the travel time of earthquake waves, II, Geophysical Magazine, 7, 101-111.

Walter, T.R., and F. Amelung (2007), Volcanic eruptions following M≥9 megathrust earthquakes: Implications for the Sumatra-Andaman volcanoes, Geology 35, 539-542, doi: 10.1130/G23429A.1.

Wassermann, J. (2012), Volcano Seismology, In: Bormann, P. (Ed.), New Manual of Seismological Observatory Practice 2 (NMSOP-2), Potsdam, Deutsches.

Watts, A.B. (1994), Crustal structure, gravity-anomalies and flexure of the lithosphere in the vicinity of the Canary-Islands. Geophys. J. Int., 119(2):648–666, doi:10.1111/j.1365-246X.1994.tb00147.x.

Watts A.B., C. Peirce, J. Collie, R. Dalwood, J.P. Canales, T.J. Henstock (1997), A seismic study of lithospheric flexure at Tenerife, Canary Islands. Earth Planet Sci. Lett., 146:431–448

Wiemer, S. (2001), A software package to analyze seismicity: ZMAP. Seism. Res. Lett., 72, 373–382.

Wiemer, S. and M. Wyss (2002), Mapping spatial variability of the frequency-magnitude distribution of earthquakes. Advances in Geophysics, 45, 259-302.

Zang, A. and O. Stephansson (2010), Stress field of the Earth's crust. Dordrecht: Springer.

APPENDIX

C

Short-term eruptive signs

López C., J. Martí, R. Abella and M. Tárraga (2014), Applying fractal dimensions and energy-budget analysis to characterize fracturing processes during magma migration and eruption: 2011-2012 El Hierro (Canary Islands) submarine eruption, Surveys in Geophysics, doi: 10.1007/s10712-014-9290-2.

Surv Geophys (2014) 35:1023–1044
DOI 10.1007/s10712-014-9290-2

Applying Fractal Dimensions and Energy-Budget Analysis to Characterize Fracturing Processes During Magma Migration and Eruption: 2011–2012 El Hierro (Canary Islands) Submarine Eruption

Carmen López · Joan Martí · Rafael Abella · Marta Tarraga

Received: 2 December 2013 / Accepted: 15 April 2014 / Published online: 15 May 2014

Abstract The impossibility of observing magma migration inside the crust obliges us to rely on geophysical data and mathematical modelling to interpret precursors and to forecast volcanic eruptions. Of the geophysical signals that may be recorded before and during an eruption, deformation and seismicity are two of the most relevant as they are directly related to its dynamic. The final phase of the unrest episode that preceded the 2011–2012 eruption on El Hierro (Canary Islands) was characterized by local and accelerated deformation and seismic energy release indicating an increasing fracturing and a migration of the magma. Application of time varying fractal analysis to the seismic data and the characterization of the seismicity pattern and the strain and the stress rates allow us to identify different stages in the source mechanism and to infer the geometry of the path used by the magma and associated fluids to reach the Earth's surface. The results obtained illustrate the relevance of such studies to understanding volcanic unrest and the causes that govern the initiation of volcanic eruptions.

Keywords Volcano unrest · Eruption forecast · Fractal analysis · Fracture mechanisms · Feeding system · El Hierro

1 Introduction

For an eruption to occur in a monogenetic volcano, a magma body must promote a network of fractures that stretch towards the surface and then develop a mechanism to exceed the

C. López (✉) · R. Abella
Observatorio Geofísico Central, Instituto Geográfico Nacional (IGN), C/Alfonso XII, 3, 28014 Madrid, Spain
e-mail: clmoreno@fomento.es

J. Martí · M. Tarraga
Group of Volcanology (GVB-CSIC), SIMGEO (UB-CSIC), Institute of Earth Sciences Jaume Almera, Lluis Solé Sabaris s/n, 08020 Barcelona, Spain

failure threshold in the crust volume (Valentine and Hirano 2010). The transport of magma from the reservoir to the surface is described as occurring through magma-filled dikes (Gudmundsson 1990, 2006; Menand and Tait 2002; Valentine and Hirano 2010; Menand 2011) and is driven by buoyancy, the surrounding local elastic stress and magma overpressure (Anderson 1951; Menand and Tait 2002; Roman 2005; Macaferri et al. 2011; Taisne et al. 2011). Pre-existing crustal fractures can also promote the propagation of dikes and influence their geometry and dynamics, as has been pointed out by, among others, Le Corvec et al. (2013). Therefore, the study of the fracturing surrounding the volcanic edifice provides a means of understanding the magma ascent mechanism (Kilburn 2003; Kilburn and Sammonds 2005).

The 2011–2012 submarine eruption on El Hierro (Canary Islands, Spain) is a clear example of a monogenetic eruption in which a batch of deep magma accumulated at a shallow depth for a certain time period before migrating laterally as a propagating sill for over 15 km and then finally erupting to the surface through a fissure that transported all of the magma (Martí et al. 2013a, b). The unrest episode that preceded this eruption lasted for 3 months, and its final phases were characterized by local and accelerated strain rates and seismic energy releases (López et al. 2012), indicating increasing fracturing and a strained focal volume from a depth of between 10 and 12 km and the surface.

This eruption had been long-awaited and, from its beginning, the curiosity of the scientific community was clear and gave rise to a quick response (Carracedo et al. 2012; Pérez-Torrado et al. 2012) even before it had ended. Subsequently, further studies have been able to use a complete set of observational data acquired by the monitoring networks and the geochemical and petrologic analysis of the erupted products (Troll et al. 2011; López et al. 2012; Sigmarsson et al. 2012; Meletlidis et al. 2012; Pérez et al. 2012; Ibáñez et al. 2012; Martí et al. 2013a, b; Prates et al. 2013; González et al. 2013; Domínguez Cerdeña et al. 2013). Together, these contributions help explain the general processes involved in this eruption. However, the triggering mechanisms of the eruption are still not known, and our goal here is to discuss them in the light of the results obtained in this study.

First of all, we review the applicability of time varying fractal and energy-budget analysis to the study of seismic series in active volcanoes that aim to determine the characteristics of fracturing processes during magma movement, and then we apply these techniques to the geophysical data recorded by the volcano monitoring networks of the Instituto Geográfico National (IGN, Spain) during the final pre-eruptive and first eruptive phases of the eruption on El Hierro (López et al. 2012). These data provide one of the most powerful approaches for studying the fracturing state of the host rock given that they register the elastic seismic wave field and the surface deformation (reversible and irreversible) associated with the magmatic system, thereby reflecting its dynamics over time. It also provides a potential tool for short- to medium-term forecast.

2 A Brief Summary of the Submarine Eruption on El Hierro

After a long period of quiescence on El Hierro, a persistent increment in seismic activity was observed on 19 July 2011. From that date onwards, volcanic unrest was linked to almost 10,000 earthquakes and more than 5 cm of vertical and horizontal surface deformations up to 10 October 2011, the day on which a submarine volcanic eruption occurring 2 km south of the island culminated this process (López et al. 2012). A comprehensive record of the seismic activity was obtained from the high-quality seismic network deployed by the IGN all over the island, composed of one three component (3CC) broadband station

(CTIG) and eight short- and medium-period (natural periods of 1 and 5 s) 3CC stations (Fig. 1). The IGN seismic catalogue for this period (www.ign.es) includes the hypocentre and size of the located events and provides insights into the available energy during the fracturing process. The three-dimensional surface deformation history was recorded by the IGN's geodetic network of four GPS stations located in the north of El Hierro, which provided daily displacements as a function of time (López et al. 2012). The subsequent, but delayed, installation of GPS stations in the south of the island near the point of the eruption was unable to record the comprehensive deformation history closer to the eruption site.

Distinct pre-eruptive phases were distinguished by significant changes in the evolution of the geophysical signals: (1) a north-to-south migration of magma at a depth of 12–15 km at the Mohorovicic discontinuity in the area (Watts 1994; Ranero et al. 1995); (2) a simultaneous surface deformation pattern that also reflected a correlated migration of the pressure source towards the south; (3) a clear acceleration in the process during the final days of unrest in the form of an increment in the released seismic energy and a sudden deflation–reinflation observed on the N–S component at all GPS stations (1–5 October 2011); and, finally, (4) the occurrence on 8 October 2011 of a 4.3 Mb (body wave magnitude) earthquake at a depth of 12 km in the same area where the seismicity was occurring which represented a point of inflection in the system behaviour (López et al. 2012; Martí et al. 2013a). On 10 October at 04:10 UTC, a clear emergent tremor signal was registered by all the seismic stations, indicating the onset of the eruptive activity, which lasted for more than 4 months (until the end of February 2012).

From the beginning of the seismic tremor signal, a number of relevant sea surface phenomena (e.g., dead fish, lava fragments and pyroclasts, stains and bubbles) associated with the initiation and development of the eruption were observed in the area around the eruption site. From the onset of the tremor signal to 12 October, many dead fish (characteristic of deep zones, Gobierno de Canarias 2011) appeared on the sea surface in an area around 2.5 nautical miles (NM) off the island's southern coast. On 12 October at about 17:00 UTC, small fragments of solid lava began to appear 2.5 NM offshore and a light-green stain, probably related to a massive escape of volcanic gases, was observed on the surface 2 NM from the coast. On 15 October at about 11.30 h UTC, an abundant steamy lava emission in an intensely discoloured area of sea was observed, thus proving that a submarine eruption was occurring 2 km (1.1 NM) off the village of La Restinga at a depth of 365 m (27°37.18′N: 17°59.58′W) (Salvamar Adhara Vessel's Navigation Journal, Spanish Government Maritime Rescue, personal communication 2011; Meletlidis et al. 2012).

3 Fractal Dimension and Energy-Budget Analysis in Fracturing Processes

During an intrusive process, a wide variety of seismic signals are originated by the transport of magma and related hydrothermal fluids and their interaction, including fracturing, with solid rock, showing differences in their source spectra (e.g., Chouet and Matoza 2013). Low-frequency events and tremors are associated with the movement and resulting deformation of pressurized fluids such as gas and magma in a confined space. High-frequency events, named volcano tectonic (VT) can be produced by brittle shear or tensile failure on faults, or by the shear failure of magma in the conduit (Chouet and Matoza 2013). Thus, source characterization of volcanic signals during unrest could be an efficient way of studying the dynamics of an intrusive process. What follows in this section

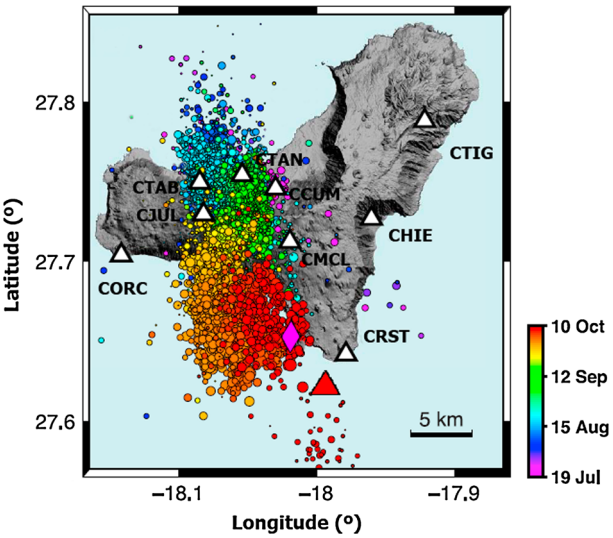

Fig. 1 Location of El Hierro and of the epicentres of the seismic events (*circles*) recorded during the unrest episode that preceded the 2011–2012 submarine eruption (*colour* ranging from 19 July to the beginning of the tremor signal on 10 October 2011). Seismic stations are represented by *white triangles*. The *pink diamond* shows the location of the 4.3 Mb event registered on 8 October 2011. The final location of the volcano vent is represented by a *red triangle* (modified from Fig. 2; López et al. 2012)

summarizes some of the most relevant tools for this purpose, from the fractal dimension (FD) analysis to other classical approaches.

Since Mandelbrot (1967) introduced the concept of fractals and the term FD to determine the length of the west coast of Great Britain, fractals and self-organized criticality have been widely used to study the level of complexity of many geological and geophysical phenomena (e.g., Turcotte 1997). Mathematically, a fractal follows the relation:

$$N_i = \frac{C}{r_i^D} \tag{1}$$

where N_i is the number of objects with a characteristic linear dimension r_i, C is a constant of proportionality, and D is the FD.

If the FD is an integer, it is equivalent to the Euclidean dimension. The Euclidian dimension of a point is zero, of a line segment one, of a square two and of a cube three (e.g., Turcotte 1997).

Time-varying fractal analysis complements the traditional Fourier analysis in the study of the complexity of waveform sample signals and shows that this technique can also be applied to observational phenomena that present self-similarity across a characteristic timescale (Higuchi 1988). This author shows that a curve with a single power-law spectrum is self-similar and the index, α, of the power spectral density (PSD) has a power-law spectrum dependence on frequency:

$$P(f) \sim f^{-\alpha}, \tag{2}$$

that is simply related to the FD D by the equation $D = (5 - \alpha)/2$ (for a self-affine fractal $1 < D < 2$). Higuchi (1988) presents a stable numerical computation algorithm for the

estimation of D using a low number of timed sequential data. Higuchi's algorithm generates multiple time series from N equi-spaced samples $(x(i),\ i = 1, \ldots, N)$ that creates a new time series x_k^m as follows:

$$x_k^m;\ x(m),\ x(m+k),\ x(m+2k), \ldots,\ x\left(m + \left[\frac{N-m}{k}\right].k\right) \quad (m = 1, 2, \ldots, k), \tag{3}$$

with m and k integers and $[a]$ denoting the integer part of a.

For each time series, the absolute differences between each two successive data points are summed to calculate the vertical length of the signal with the scale size k as follows:

$$L_{\mathrm{m}}(k) = \left\{ \left(\sum_{i=1}^{[(N-m)/k]} |x(m+ik) - x(m+(i-1)k)| \right) \frac{N-1}{\left[\frac{N-m}{k}\right].k} \right\} \tag{4}$$

The length of the series segment $L(k)$ is the mean of the $L_{\mathrm{m}}(k)$ values,

$$L(k) = \frac{\sum_{m=1}^{k} L_m(k)}{k}, \quad \text{form} = 1, \ldots, k. \tag{5}$$

If $L(k)$ is proportional to k^{-D}, then the signal is fractal-like and has the FD D.

Fractal distributions have been identified in natural phenomena, and an extensive literature exists in the fields of seismology and volcanology. The Earth's crust and the seismicity produced by tectonic stresses have been modelled as a critical self-organized process, and FD analysis has been applied to the distributions of fractures and earthquake epicentres, as well as to seismic-recurrence time studies (e.g., Chen et al. 1991; Crampin 1994; Leary and Abercrombie 1994; Barriere and Turcotte 1994; Bonnet et al. 2001; Saichev and Sornette 2007). Focusing on volcano seismicity, spatial and temporal FD studies of the seismicity and the fracture dynamics associated with eruptive episodes that analyse the variations in their FDs as a response to changes in the stress conditions have been conducted on Mt. Etna (Vinciguerra et al. 2001; Vinciguerra 2002), Mt. Vesuvius (Luongo et al. 1996) and Mt. St. Helens (Caruso et al. 2006). Fractal analysis of continuous seismic tremor recordings has correlated the evolution of temporal FDs with the complexity of the source mechanism. Konstantinou (2002) determined the fractal upper bounds of the seismic tremor attractor dimension using the continuous seismograms traces of the 1996 Vatnajokull eruption. Maryanto et al. (2011) analysed the Semeru volcano harmonic tremor seismograms that related higher FDs with the explosion and its gradual decrease during the recording of the harmonic tremor.

Given that the FD reflects the spectral dependence of time series, it offers a useful tool for the characterization of the seismic sources (e.g., VT and tremor) recorded during an eruptive process due to their source spectral model patterns.

VT amplitude seismic source spectra can be modelled in the far field following a simple circular finite-fault fracture, using the source model proposed by Brune (1970):

$$A(f) = \frac{\Omega_0}{\left(1 + \left(\frac{f}{f_c}\right)^2\right)} \tag{6}$$

where Ω_0 is the low-frequency spectral level, f is the frequency and f_c is the corner frequency of the seismic wave. For $f < f_c$, the spectra is flat (f^{-0}). For $f > f_c$, f^{-2} marks the high-frequency fall-off rate (on a log–log plot) in the spectra. Other more complex seismic

fault models give equivalent results for the seismic source spectra (Aki 1967; Brune 1970; Hanks 1979; Walter and Brune 1993; Walter et al. 2013).

Some mathematical expressions for the tremor amplitude source spectra can also be found in the literature. Ripepe and Gordeev (1999) modelled the tremor source in the far field as pressure variations induced by the growth of magma–gas bubbles under forced coalescence, expressing the source spectra in the frequency domain as:

$$A(f) = P_{\mathrm{h}} \frac{2w^2}{b(b^{-2} + w^2)^2} \tag{7}$$

where $w = 2\,\pi f$, P_{h} is the maximum pressure change induced in the magma–gas medium by gas bubble forced coalescence and b is a constant dependent on the relaxation time. For high- and low-frequency ranges, Ripepe and Gordeev (1999) modelled spectra amplitude decays as $\propto f^{\pm 2}$, the maxima amplitude corresponding to a corner frequency, f_{c}, which reflects the different magma parameters and bubble growth rate. This asymptotic behaviour of the ground displacement spectra has been found for the seismic tremors recorded from volcanoes with different types of magmatism (Ripepe and Gordeev 1999). Chouet (1985) proposed the excitation of a buried magmatic pipe as a seismic source model for the volcanic tremor. The synthetic spectral ground-motion displacement signature also has asymptotic roll-offs for high frequencies with a frequency slope $\propto f^{-(1.33;1.67)}$ on the logarithmic scale. Similarly, higher-degree frequency decays for the amplitude tremor source, proportional to f^{-3}, can be found in the model proposed by Garces and McNutt (1997) for a gas–magma mixture triggering explosive sources inside magma conduits due to sudden changes in the confining pressure. Horton et al. (2008) analysed temporal frequency slope differences in seismic source spectra recorded during the Mt. St. Helens volcanic activity episode (2004–2006) and related them to the eruption dynamics, thereby correlating the gradual decrease in the high-frequency slope with the magma's approach to the surface. In Fig. 2, we show the good agreement of both a VT event recorded in the area during the studied period and 1990s of the volcanic tremor spectra with predicted VT and tremor source models (Eqs. 6, 7), showing the applicability of source spectra models approximations.

The study of the temporal evolution of seismicity provides valuable information about the fracturing and deformation processes. Segall (2013) investigated how variations in seismicity under changing stress can be used to integrate deformation and VT seismicity in the spatial–temporal evolution of dike geometry under excess magma pressure, suggesting that in some cases dike propagation has been detected from minutes to hours prior to eruptions. For this purpose, he performed a joint analysis of the seismicity rate, $R = \mathrm{d}N/\mathrm{d}t$, where N is the number of earthquakes, and the stress change associated with dike intrusion was calculated using the seismicity rate theory of Dieterich (1994), which establishes

$$R = \frac{\mathrm{d}N}{\mathrm{d}t} = \frac{r}{\gamma \dot{\tau}_{\mathrm{r}}}, \quad \frac{\mathrm{d}\gamma}{\mathrm{d}t} = \frac{1}{a\sigma}\left(1 - \gamma \frac{\mathrm{d}s}{\mathrm{d}t}\right) \tag{8}$$

where r is the background seismicity rate at the stressing rate, $\dot{\tau}_{\mathrm{r}}$, σ is the normal stress acting on the fault, a is a frictional constitutive parameter, and s is the Coulomb stress. γ can be approximated to the inverse of the stressing rate prior to dike propagation (Segall 2013), $\gamma_0 = \frac{1}{\dot{\tau}_{\mathrm{r}}}$, and so, qualitatively, we can relate transient changes in the seismicity rate to changes in the stress field. Segall (2013) studied the case histories of St. Helens (1980), Pinatubo (1991), Soufriere Hills Volcano (1997) and Hekla (2000) and suggests that this

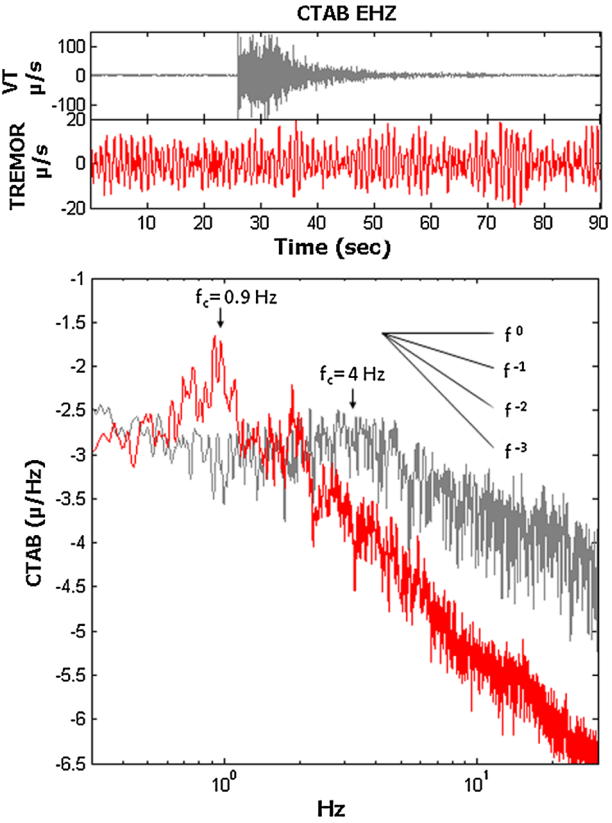

Fig. 2 Example of a typical VT event (7 October 2011, 23:52 UTC, 3.1 Mb) recorded in the volcano area during the studied time period in grey and of 90 s of the volcanic tremor registered on 11 October 2011, at 12:00 UTC in *red*, both recorded at the CTAB station. Vertical component traces have been corrected for the instrument response. Amplitude spectra curves of both signals are shown in the lower plot. Corresponding VT and tremor corner frequencies are $f_c = 4$ Hz and $f_c = 0.9$, showing high-frequency decay f^{-n} with $n \approx 2$ for VT and $2 \leq n \leq 3$ for tremor

approach could improve the resolution of existing methods and, perhaps, even real-time forecasts. Nevertheless, this theory does not address the magnitude of the earthquakes, only their occurrence.

Another important parameter is the seismic energy when it is used as a measurement of the elastic energy release during fracturing, which reflects the permanent, strain-only measurement of the deformation. The geodetic surface deformation measures both elastic (internal reversible deformation) and permanent deformation (seismic as well as aseismic), and so it is to be expected that the seismic strain (co-seismic displacement) will represent a lower limit of the geodetic strain and the geodetic strain, the upper bound (Jenny et al. 2004, Caporali et al. 2011). The minimum strain energy involved in the process approximates to the seismic wave energy under Orowan's (1960) condition, which assumes a complete stress drop (effective stress equal to stress drop) in the area (Kanamori 1977). Whether the earthquake's stress drop is complete or partial is unknown, but the condition has been verified experimentally for several earthquakes (Kanamori 1977).

We used the seismicity rate as an estimation of the local stress changes and the seismic energy per unit of the fault area to calculate the minimum bound of the strain field variation.

Finally, in order to study possible facts that could determine why a crack grows or stops growing during a dike intrusion, we can compute the critical strain energy release rate following the theories established by Irwin (1957) and Orowan (1948), who suggested that catastrophic fractures occur when the strain energy is released at a high enough rate. A modified Griffith (1921) equation establishes that the energy needed for crack growth in a brittle material is as follows (e.g., Anderson 1991; Roylance 2011):

$$\sigma_{\mathrm{f}}\sqrt{a} = \sqrt{\frac{\mathrm{E\ G}}{\pi}} \tag{9}$$

where G is the critical strain energy rate, E is Young's modulus, a the smallest length that initiated the crack growth, and σ_{f} the stress at fracture.

4 Application to the 2011–2012 El Hierro Eruption

The studied period (6–15 October 2011) included the occurrence of the final and most energetic swarms of VT events previous to the onset of the eruption, the appearance of the tremor signal on 10 October (04:10 UTC) and the observation of the first eruptive products (e.g., dead fish, stains, lava fragments) on the sea surface. In some cases, the time period was extended to 3 October in order to gain a broader view of the evolution of the signal.

Time varying fractal analysis, energy estimations rates, spectral time series and fracturing budget-balance analysis were applied to the continuous seismic data and to the seismic catalogue for the study period, and were correlated with the temporal and spatial patterns of the located seismicity and the appearance on the sea surface of different eruption indicators. Joint analysis provided information about a possible mechanism and the geometry of the fracturing process during the magma ascent and further opening of the eruptive vent.

IGN located seismicity was carefully reviewed addressing the task of completing the located event catalogue with detected events, heretofore not included, in order to estimate the true seismic release that reflects the history of the process dynamics. For this purpose, we reviewed all the continuous seismic waveforms and manually chose the arrival time and ground-motion maximum amplitude of those VT events registered by at least five stations, which were identified by their waveform as belonging to the same local families. This procedure increased the number of events detected on El Hierro from 677 to 6,343 (a more than 800 % increase). Each detected event magnitude was computed by correcting for attenuation and spreading for distance considering the mean location of the events located at closer time. Finally, the accumulated seismic energy (equal to the permanent strain energy) and seismic rate $\mathrm{d}N/\mathrm{d}t$ over the entire VT catalogue could be estimated.

Fractal dimension (FD) time evolution was estimated using the Higuchi (1988) algorithm (Eq. 4) on the vertical component of the seismic stations. Only one station (CHIE) of the seismic network was discarded due to amplitude clipping caused by its low acquisition dynamic range. Seismic data were pre-processed in order to remove bad-quality data segments, and the ground-motion was retrieved correcting by the corresponding instrument response. The following input parameters, $K_{\max} = 5$; window size, $N = 12{,}000$ samples (2 min at 100 sps, no window overlap) were used in (Eq. 4) and the angular coefficient of

the linear regression of the graph $\log(L(k))$ versus $\log(1/k)$ provided the FD, where log is the natural logarithm. Different input parameters were tested with similar performances, selecting those that were most appropriate for characterizing the persistent behaviour of both transient (VT) and continuous tremor signals in the linear fall-off segment of the source spectra.

Figure 3 shows the complete $\log(L(k))$,$\log(1/k)$ space for the time period using a k range from 1 to 50 every 2 min with no overlapping segment of continuous CTAB vertical seismic station data, which shows the stability of the slopes corresponding to $\log(1/k)$ for $k = 1,\ldots,5$ and its time variations supporting the applicability of the FD technique for describing the irregularity of the seismic time series in the high frequencies. Figure 4 shows the temporal variations of FD ($k = 1,\ldots,5$) and similar shapes for the different stations. Up to 8 October, plots suggest that there were cyclic variations with a dominant value of FD ≈ 1.5 during the most intensive seismic swarms. On 10 October, a decrease to a shorter dimension began, which reached minimum values of ≈ 1 in almost all stations by the end of 11 October.

FD analysis was complemented with spectrogram analysis for source characterization. Figure 5 shows a 5-min, non-overlapping, Hanning-tapered, ground-motion spectrogram (instrument response corrected) on the vertical component at the CTAB and CRST (the closest to the eruption site) seismic stations and their time traces. The spectrogram is represented with a semi-logarithmic frequency axis from 0.1 to 50 Hz, and the amplitude and spectrogram colour scales are the same for both stations. The successive VT swarm episodes show energy in a high-frequency band up to 25 Hz, while the tremor energy is concentrated in a 0.3–5 Hz band (in the nearest CRST station, it reached almost 15 Hz during the first 3 days). No clear harmonic resonant peaks can be seen in the tremor. The daily pattern of the high-frequency micro-seismicity can be observed in the central part of the day throughout the whole period; below 0.3 Hz, typical oceanic micro-seismic noise is recorded at both stations.

5 Results

The temporal evolution of the seismicity is shown in Fig. 6. The distribution of the accurate revised hypocentral locations (486 events with rms $\leq$0.3 s and horizontal location error $\sigma \leq 3$ km) is shown in Fig. 6a. Three different periods can be distinguished. (1) From 6 October to the occurrence of the 4.3 Mb event on 8 October at 20:34 UTC (Fig. 6b), the 360 located events reveal a NW–SE lateral migration (6-km long) and suggest a slight vertical migration from a depth of 14–10 km, with a mean depth of 12 km. (2) From the 4.3 Mb event to the beginning of the tremor signal on 10 October, 04:10 UTC (Fig. 6c), the seismicity decreased drastically and only 126 events were located in this time period, all with smaller assigned magnitudes. The first shallow event (at a depth of 3.5 km) occurred only 23 min after the main 4.3 Mb event and was located to the south of the hitherto seismic source area. From then on, the hypocentral location of seismic events alternated between the 'deep' seismic source area (75 events in total) and the new 'shallow' seismic source area (89 events in total with depths $\leq$4 km). (3) From the tremor onset to the end of 15 October (Fig. 6d), 12 events were located, all of them in the 'deep' seismic source area.

For the calculation of the seismic strain rate, we summed the seismic moment using the modified Kostrov summation equation (Kostrov and Das 1988):

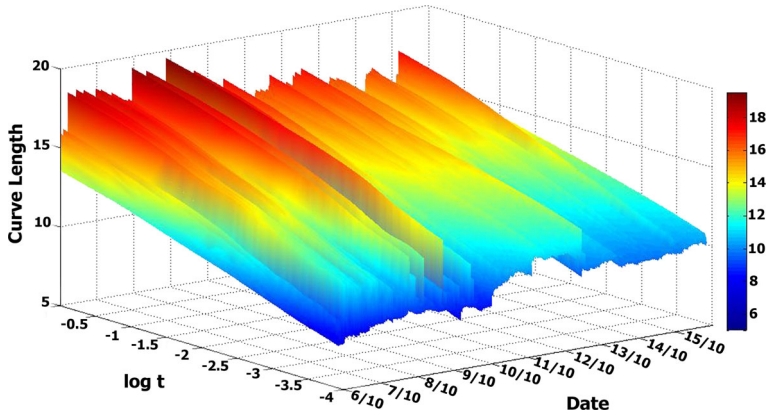

Fig. 3 Entire curve length $L(k)$ (*u.a.* arbitrary units) space for 2 min of non-overlapping moving window with k ranging from 1 to 50 on CTAB vertical seismic station data. Traces show the slope stability of the corresponding curves in the *red* area of the graph, for $k = 1,\ldots,5$, (from $0,\ldots, -1.6$ in the log t, horizontal axis). Corresponding frequency upper-bound variations ranged from 10 to 50 Hz (with 100 Hz sampling for the time series)

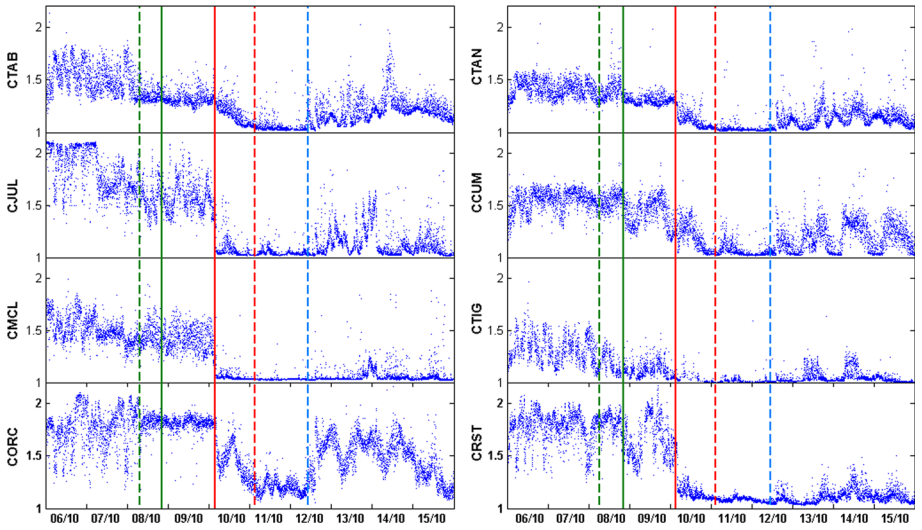

Fig. 4 Temporal variations of FD ($k = 1,\ldots,5$) at the different stations. Until 8 October, plots suggest cyclic variations with a dominant value of DF ≈ 1.5 during the most intensive seismic swarms. On 10 October, FD started to fall to a shorter dimension, reaching minimum values of ≈ 1 at almost all stations by the end of 11 October. The 4.3 Mb event and the *onset* of the seismic tremor are indicated on the graph with full *green* and *red vertical lines*, respectively. The *dashed green vertical line* indicates the beginning of the reduction in the seismic rate (*Phase III*). The *dashed red vertical line* indicates the beginning of the fall in FD shorter values (Phase VI). The *dashed blue vertical line* indicates the onset of the appearance of *light-green discoloured* sea water stained by volcanic gases, which was observed about two nautical miles off the coast

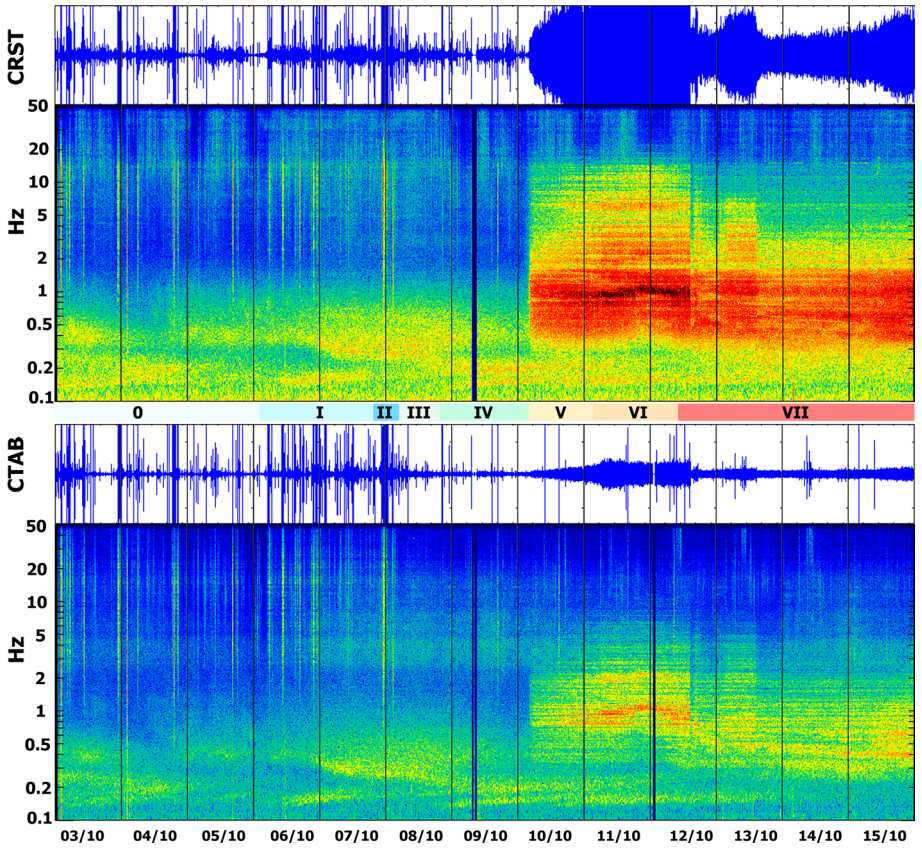

Fig. 5 Ground-motion spectrogram of the vertical component of the CTAB and CRST stations, computed on a 5-min, non-overlapping, Hanning-tapered moving window (instrument response corrected), and their time traces (amplitude and spectrogram *colour* scales are the same for both stations). The spectrogram is represented on a semi-logarithmic frequency axis plot from 0.1 to 50 Hz. *Colour* bands labelled *0*, *I*, *II*….*VII* indicate different phases (see text for details)

$$\frac{\mathrm{d}\varepsilon}{\mathrm{d}t} = \frac{1}{2\mu V \Delta t} \sum M_0 \tag{10}$$

where μ is the shear modulus, Δt is the time span for the seismic period studied, M_0 is the scalar seismic moment of each event, and V is the corresponding seismogenetic volume. In practice, V is defined as the sum of the product of the area involved in each event fracture and the hypocentral depth of each event (Caporali et al. 2011). This approach is appropriate in our case given the characteristic clustering of the seismicity, as can be seen in Fig. 6. Seismic moment (M_0) and seismic energy (E_s) were derived from the Mb magnitude using the relationships reported by Chen and Chen (1989): $M_0 = 10^{1.5*\mathrm{Mb}+9}$ (N.m) and Choy and Boatwright (1995): $E_S = 1.6 * M_0 * 10^{-5}$ (N.m). The seismic rupture area was calculated using the relationships derived by Wells and Coppersmith (1994): area $= 10^{0.9\ \mathrm{Mb}-3.42}(\mathrm{km}^2)$.

Figure 7 shows the activity time evolution in terms of energy expenditure, differentiating some phases based on the evolution of both seismic rate and seismic strain.

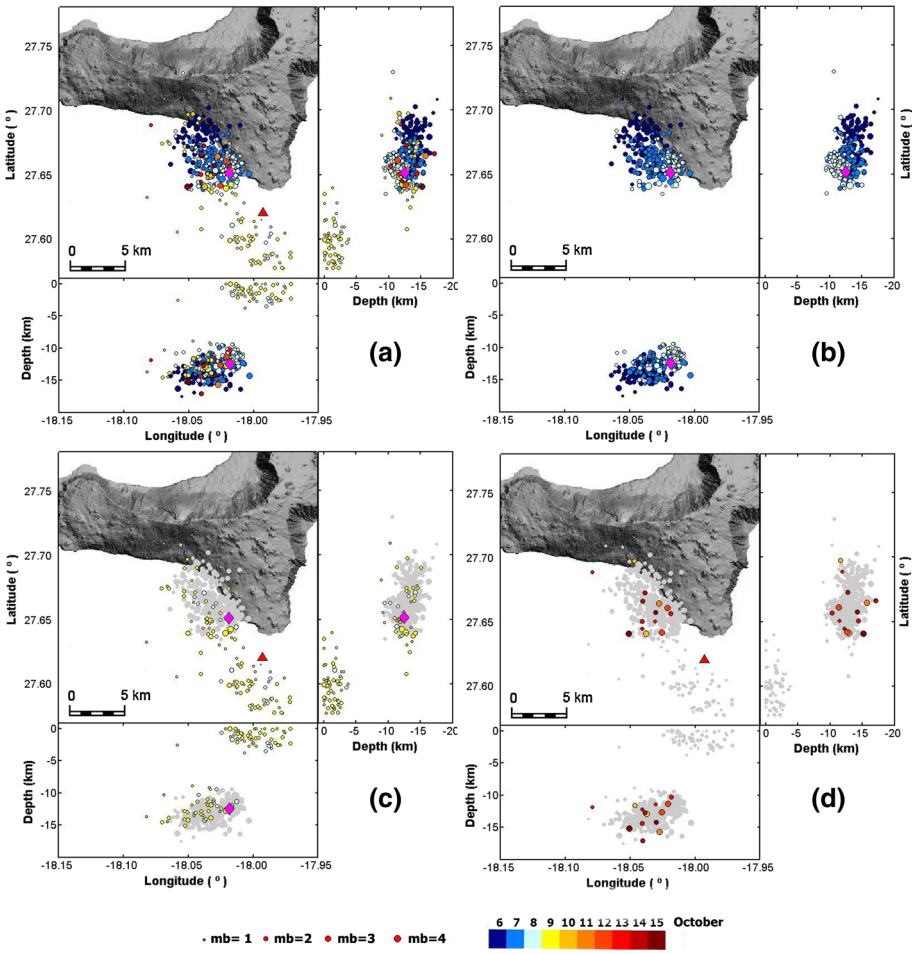

Fig. 6 **a** Revised accurate hypocentral 498 locations (with rms $\leq$ 0.3 s and horizontal location error $\sigma \leq 3$ km) and their projections in the *XZ* and *YZ* planes. **b** The 360 events located from 6 October to the occurrence of the 4.3 Mb event on 8 October at 20:34 UTC, with a NW–SE lateral migration (6-km long). **c** The 126 located events occurring from after the 4.3 Mb event to the beginning of the tremor signal on 10 October at 04:10 UTC. The seismic locations show two seismogenic areas, one a 'deep' area and the other the new 'shallow'-source area at depths of $\leq$4 km. **d** The 12 events located from after the tremor *onset* up to the end of 15 October, all in the 'deep' seismic source area. *Source of data*: IGN catalogue (www.ign.es)

(1) Phase 0: considered to represent previous activity. (2) Phase I: from 6 October, 03:00 UTC (approximately) to 7 October, 21:00 UTC (approximately), which includes swarms of events whose hypocentres moved NW–SE in a lateral and almost horizontal direction. (3) Phase II: up to 8 October, 05:30 UTC (approximately), which includes the final and strongest swarm that coincided with an upwards depth trend from 13 to 10 km. (4) Phase III: up to 8 October, 20:34 UTC (duration approximately 15 h), which includes the relative quiescence in the seismic activity before the 4.3 Mb event. (5) Phase IV: from the 4.3 Mb event on 8 October to the beginning of the volcanic tremor on 10 October, which includes the double-source seismicity. (6) Phases V, VI and VII, including the different tremor

signal behaviour and the appearance of different surface manifestations of the eruptive activity.

Figure 7a shows the time evolutions (in black) of the Mb detections and (in purple) of depth locations (magnitudes range from 1 to 4.3 Mb, with an average magnitude value below 2 Mb). Plots show the increase in seismic activity in the populated swarms during Phases I and II, which suggests that there was a periodic occurrence every 6–8 h. The depth locations plot shows a slight trend for the hypocentres to move towards the surface; 15 km mean depth on 3 October, 14 km mean depth on 6 October, 14–10 km mean depth during the final strong swarm occurring in the final hours of 7 October and the first hours of 8 October. During Phase IV, the events seem to concentrate closer to the beginning and to the end of the phase, with locations alternating between the 'deep' and the 'shallow' seismic source areas. In the first shallow swarms, the mean depth was 2 km, while in the second and final shallow swarm, the mean depth was slightly less, around 1 km. During Phases V, VI and VII, events were only observed in the 'deep' seismic source area. Figure 7b shows the 5-min detection of the seismic rate (in black) and its accumulated value (in red). The accumulated slopes of the seismic rate show different phases of the local stress field and crescent strengthening, from Phase 0 to Phase II. Figure 7c shows the seismic strain (in red) and its corresponding strain energy (in black) (or energy release under the Orowan condition). A higher contribution of the 'shallow' seismicity to the local deformation is remarkable despite its lower seismic rate. The phenomenon involved in Phase II was the most energetically expensive of the whole period and produced the maximum deformation rate, even greater than the 4.3 Mb event. During Phases I, II and III (65 h approximately), 0.82×10^{11} J and 0.76×10^{-4} strain (1.2 μ strain/h) of deformation were released in the area. In Phase IV, the corresponding values were 0.34×10^{11} J and 0.2×10^{-4} strain of deformation. Figure 7d shows the corresponding effective pressure, σ_f, at the seismic fracture surface as the minimum energy needed to initiate a catastrophic fracture through the crust towards the surface (Eq. 8). For the characteristic critical strain energy rate for the area, G, we have used the rate that was accumulated during Phases I, II and III. It is highlighted from 4 to 10 MPa on a grey background. There are two critical situations where σ_f reached its lowest value, in Phase II (6 MPa) and during the 4.3 Mb event (5 MPa). Crust state parameters were calculated using the standard value of Poisson's ratio for the crust $\sigma = 0.25$ and $\mu = 40$ GPa (Watts 1994; Watts et al. 1997).

Figure 8 shows the amplitude spectra of a 90-s window from the CTAB vertical station (instrument response corrected) of the tremor signal on 10, 11 and 15 October. Each of these signals is representative of the tremor in Phases V, VI and VII.

6 Discussion

Data analysis, integrating FD and energy-budget temporal evolution, has allowed us to distinguish several temporal stages in the preparation and initiation of the eruption. Each stage was characterized by different mechanical constraints deriving from a particular rock–fluid interaction.

6.1 Up to 6 October (Phase 0 in Fig. 7)

Accumulated seismicity rate and seismic energy released followed a quite linear behaviour. Epicentres were located to the west of the subsequent seismic swarm, and the horizontal deformation experienced a fairly complete episode of elastic recovery at the end of this

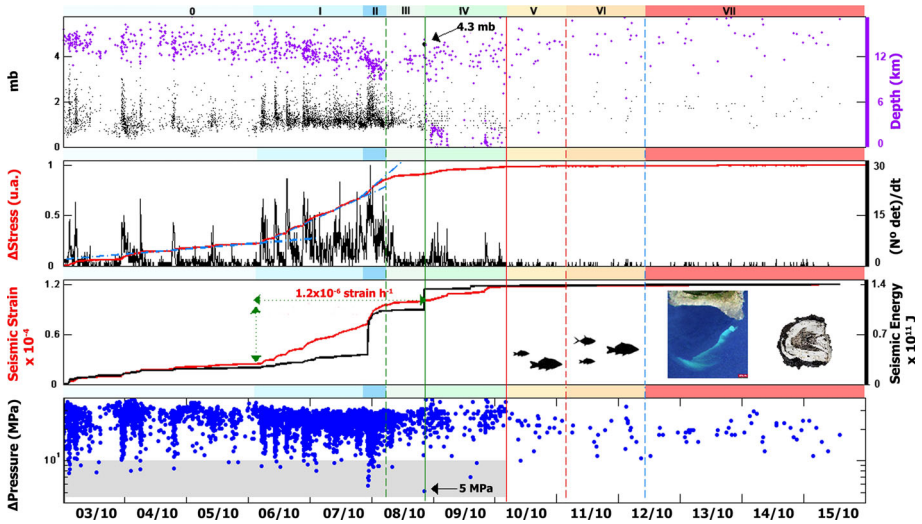

Fig. 7 *Colour* bands labelled *0*, *I*, *II*….*VII* indicate different phases (see text for details). *Green, red* and *blue full* and *dashed vertical lines* have the same significance as in Fig. 4. **a** Detection magnitude (*in black*) and location-depth time evolution (*in purple*) of seismic events. **b** Detection rate (*in black*) and its accumulated value (*in red*). **c** Seismic strain (*in red*) and its corresponding strain energy (*in black*) (or energy release under the Orowan's condition). **d** Effective pressure, σ_f, at the seismic fracture surface as the minimum energy needed to initiate a catastrophic fracture through the crust towards the surface (Eq. 9)

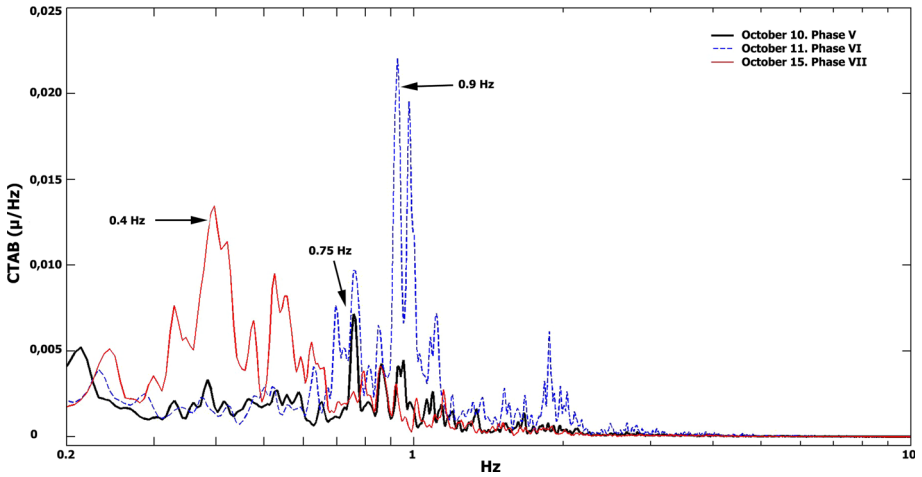

Fig. 8 Amplitude spectra of a 90-s window at the CTAB vertical station (instrument response corrected) of the tremor signal on 10, 11 and 15 October. Each of these signals is representative of the tremors in *Phases V*, *VI* and *VII*

stage (López et al. 2012). Fluid-crack intrusions are usually characterized by deflation–inflation sequences in the magma source and by associated subsidence-uplift cycles above, as well as by the lateral migration of earthquake swarms, as the magma moves from its source and into the dike (Moore and Krivoy 1964; Brandsdóttir et al. 1997; Einarsson

1991; Rubin et al. 1998; Toda et al. 2002). Therefore, this stage could suggest a propensity for the formation of a fluid crack and then dike migration at the end of this process.

6.2 6–8 October (Phases I and II in Fig. 7)

This stage started with a sudden strong increase in the seismicity rate and in the seismic energy released. Two sub-stages can be distinguished. (A) A quasi-horizontal 14–12 km magma propagation under the local Moho discontinuity up to 7 October (Phase I in Fig. 7); (B) Magma migration towards the surface from 12 to 10 km, possibly crossing the Moho discontinuity located at a depth of 12–15 km (Watts 1994; Ranero et al. 1995) on 8 October (Phase II in Fig. 7). The seismic strain reflected a permanent deformation accumulation, with a maximum rate of 1.4×10^{-6} strain h^{-1}, the greatest throughout the whole process. The increase in the seismicity rate and the migration of the epicentres were interpreted as the lateral propagation of a magma intrusion, and the changes observed in this stage could reflect differences in the host rock and/or changes in the geometry of the intrusion (see Traversa and Grasso 2009; Segall 2013).

FD analysis (Fig. 4) reflects the effects of cyclic seismic swarms; higher FD values would correspond to seismically quiet periods in which uncorrelated background seismic noise dominated, which agrees well with previous analyses of similar seismic patterns (see Boschetti et al. 1996; Tosi et al. 1999; Padhy 2004). Dominant seismicity approaches the lower FD ≈ 1.5.

According to the observational data presented here, we conclude that at the end of this stage, the over-pressurization of the system reached a critical point due to magma accumulation in the south (regardless of whether it was under or in the lower crust). This idea is also supported by the observation of high levels and a gradual increase in the H_2S flux recorded at a station located on the coastline of the Mar de Las Calmas (close to the seismic location area) prior to the onset of the eruption (Pérez et al. 2012).

6.3 October (Phase III in Fig. 7)

On this day, the seismic rate, seismic strain and released seismic energy fell drastically. The seismic strain reflected a smaller but persistent permanent deformation with a maximum rate of 0.3×10^{-6} strain h^{-1}, which was maintained until the appearance of the tremor signal. The analysis of the lava fragments collected on the sea surface near the vent area (Troll et al. 2011; Sigmarsson et al. 2012; Meletlidis et al. 2012; Martí et al. 2013b) suggests that local and rapid crustal assimilation occurred at the base of the volcanic edifice when the first magma passed through that zone. The products of that crustal assimilation episode appeared after only a few hours in the form of lava fragments with a black vesicular outer crust with bulk basanite composition, surrounding a centre with a grey-white pumiceous xenolithic core (xenopumices). Despite the different interpretations that have been proposed to explain the exact nature of these xenopumices (Troll et al. 2011; Meletlidis et al. 2012; Sigmarsson et al. 2012), all authors coincide in the fact that the assimilation of pre-existing rocks, located either at the sedimentary basement of the volcanic edifice or inside it, had occurred. Even so, the decrease in the registered seismicity and in the strain rate indicate that an important change in the intrusion conditions occurred, which is probably reflected in this magmatic assimilation episode.

6.4 8–10 October (Phase IV in Fig. 7)

This stage started with the 4.3 Mb event. We believe that this event could have surpassed the strain rate threshold necessary to initiate a catastrophic fracture and thus opened a path through the crust to the surface. The essential condition was that the fault area was affected by an effective overpressure of at least of 5 MPa, as is shown in Fig. 7d. The occurrence of the seismic event altered the shear and normal stresses and generated high local stress and local strain magnification, which increased the tendency for brittle fracturing. The 'deep' and 'shallow' seismicity (Fig. 6c) could represent the depths of the bottom and top edges of the strained volume. FD analysis (Fig. 4) suggests the predominance of seismic activity in the signal despite the scarcity of events. The possibility exists that the persistent lower magnitude seismicity was recorded because the event signals were obscured below the background seismic noise level of the recording stations. Cornet (1992) suggested that earthquakes generated by the tensile propagation of a dike tip are likely to be too small in magnitude to be identified by standard seismic networks.

6.5 From 10 October Onwards (Phase V, VI and VII in Fig. 7)

This stage started with the onset of a seismic tremor on 10 October at 04:10 UTC, which we interpret as corresponding to the start of the eruptive activity phase. Right from its beginning, the tremor signal underwent important changes in its amplitude and frequency, an indication of the complexity of the phenomenon that is also reflected in the lack of identifiable persistent frequencies of source resonance. Based on the FD, spectral analysis and surface manifestations of the eruptive activity, we have identified the following different phases at the start of the eruption:

6.6 10 October (04:10)–11 October (06:00): (Phase V in Fig. 7)

The tremor signal progressively grew from its onset until 11 October at about 6:00 UTC, with an energetic high-frequency release [0.3–15] Hz, as shown in data from the CRST station given in Fig. 5. The tremor spectrum (Fig. 8) shows a maximum frequency of 0.75 Hz (Fig. 5). FD analysis (Fig. 4) shows a continuous decrease to shorter dimensions, reaching minimum values of ≈ 1 in almost all stations by the end of this phase. During this phase, the only indirect evidence of an ongoing eruption process was the appearance on the sea surface of many dead fish characteristic of deep zones. Increasing tremor amplitudes have commonly been observed on other volcanoes and are thought to occur when ascending magma massively vesiculates due to decompression or when it interacts with external water (groundwater or surface water) (McNutt 1996; Patanè et al. 2008). Based on bathymetric evidence of the deposition of juvenile material on the seafloor during the first days of the eruption, Martí et al. (2013a) suggest that the eruption site migrated north for almost 3 km along a surface fracture of the southern rift, from a depth of 1,000–300 m. This migration was halted by the intersection with a NE–SW-oriented normal regional fault, which facilitated the establishment of a central conduit and a vent, giving rise to the construction of a volcanic cone. We suggest that, during this phase, the tremor signal was mostly caused by gas-rich fluids exsolved from the ascending magma in the final 1–4 km before the surface, which escaped massively through a complex feeding system as it changed its geometry to the smaller dimension of a central conduit.

6.7 October (06:00)–12 October (14:30) (Phase VI in Fig. 7)

The volcanic tremor reached its maximum energy on a broad frequency band rich in high frequencies, with an upper spectral bound of 15 Hz (Fig. 5) at the CRST station (Phase VI in Fig. 7). The tremor-dominant amplitude corresponded to 0.9 Hz (Fig. 8), higher than that of the previous phase. The spectra shape shows sharp narrow peaks. The simplified Chouet (1985) organ-pipe conduit model explains these effects as due to the resonance of low viscosity fluids. Morrissey and Chouet (1997) explain the high-frequency tremor associated with pressurized gas flow through a narrow constricted path. FD analysis (Fig. 4) shows stable values of FD $\approx$ 1 at almost all stations, suggesting that the minimum dimension conduit geometry was maintained. We propose that the flow of low viscosity fluids (i.e. water and CO_2) in constrained conduit geometry is a plausible source mechanism for the volcanic tremor in this phase.

6.8 October 14:30 h and Thereafter (Phase VII in Fig. 7)

This phase started on October 12, at around 14:30 UTC, with a sudden decrease in the tremor amplitude recorded at all stations and a shifting of the frequency band to smaller values (Fig. 5). The appearance of clear eruptive signals on the sea surface (stained water and small pieces of fragmented lava) provided a good indication of the explosive activity occurring at the submarine vent. FD (Fig. 4) started to fluctuate in 24-h, Earth-tide-like cycle. The dominant frequency of the tremor was lower than during the previous phases and reached 0.4 Hz (Fig. 8) on 15 October, the day on which abundant emission of xenopumitic fragments was observed. We interpret this low value as an indication of a higher-viscosity magma resonance.

7 Conclusions

The detailed analysis of the observational data recorded on El Hierro allows us to identify different stages in the eruptive dynamics and offers a possible mechanism, including the triggering of the final phase of the unrest and the geometry of the fracturing process during the magma ascent and further opening of the eruptive vent. We conclude that, on 6 October, the new magma intrusion propagated laterally along the Moho discontinuity for over 6 km. On 7 October around 21:00 h UTC, an upwards migration started, possibly breaching the discontinuity at a depth of 12–10 km, released the maximum amount of seismic energy, reaching its maximum strain rate and thereby suggesting the structural barrier. The decrease in the registered seismicity and in the strain rate on 8 October could indicate that an important change in the intrusion conditions occurred, which is probably reflected in this magmatic assimilation episode. Further eruptive development seems to have been controlled by crust heterogeneities and its rheology. The occurrence of the 4.3 magnitude event on 8 October at 20:00 UTC could potentially have led to the propagation of a fairly aseismic fracture from the hypocentre (located at a depth of 12 km) through the crust towards the surface due to the intrusion of volatile, over-saturated magma with an effective overpressure of at least 5 MPa. Decompression during the ascent caused the exsolution of volatiles which preceded the ascent of the magma during the final kilometres to the surface, and thus provided the overpressure necessary at the fracture tip. The first geophysical signals of the onset of the eruption were registered on 10 October and were mostly linked to the extrusion of the magmatic gases through a feeding system that

changed in geometry from a fracture plane to a smaller dimension, presumably in the form of a conduit as was established on 12 October. Henceforth, the recorded data and the surface eruptive products suggest that the magma emission stabilized and was massive from 12 October onwards, thereby initiating the most important phase in the construction of a volcanic edifice that lasted until the end of February 2012. This mechanism is relevant not only to the understanding of the causes governing the initiation of the eruption on El Hierro but also to the understanding of volcanic unrest in general and the forecasting of the initiation of volcanic eruptions.

Additionally, we can highlight some more general considerations. Time-varying FD analysis provides valuable information for the characterization of different seismic volcanic sources and the geometry of a radiated seismic wave field. This analysis could be valuable in real-time volcano monitoring activity. Knowledge of stress and strain states and their rates in the crust have proved essential for the monitoring and understanding of pre-eruptive processes during episodes of unrest. A precise knowledge of magma rheology and the structure and mechanics of the host rock is necessary for a proper interpretation of the observational data. The characteristics of the system (magma + host rock structure) and, consequently, of the forces acting upon it may change during the course of the process and may delay, accelerate or halt the onset of the eruption. The interpretation of the observational data in isolation can be misleading and be misunderstood if the state of the crust is not previously known—or at least taken into account as an important conditioner. Stress and strain rates can be characteristic for an area and their thresholds can be considered to be a potential tool in short-term forecasts in conjunction with other forecasting methods; we believe that the implementation of real-time analysis procedures that reflect a more comprehensive stress and strain states occurring in the crust and its continuous short- and long-term changes; this will provide us with an excellent tool for the correct identification and interpretation of eruption precursors.

Acknowledgments This research was partially funded by IGN CGL2011-16144-E grant from Spanish Ministry of Economy and Competitiveness and European Commission VUELCO (FT7 Theme: ENV.2011.1.3.3-1; Grant 282759). We would like to thank wholeheartedly all our colleagues from IGN who participated in the monitoring of the volcanic crisis on El Hierro and who made the existence of the observational data used in this study possible. We are also grateful for the valuable suggestions from Alicia Felpeto (IGN), Maria Jose Blanco (IGN), Victor Villasante (IGN) and Alvaro Marquez (URJC) that substantially improved this paper. The English text was reviewed and corrected by Michael Lockwood.

References

Aki K (1967) Scaling law of seismic spectrum. J Geophys Res 72:1212–1231. doi:10.1029/JZ072i004p01217

Anderson EM (1951) The dynamics of faulting, vol 2. Oliver & Boyd, Edinburgh, p 206

Anderson TL (1991) Fracture mechanics: fundamentals and applications. CRC Press, Boca Raton

Barriere B, Turcotte DL (1994). Seismicity and self-organized criticality. Phys Rev E 49:1151–1160. doi:10.1103/PhysRevE.49.1151

Bonnet E, Bour O, Odling N, Davy P, Main I, Cowie P, Berkowitz B (2001) Scaling of fractures systems in geological media. Rev Geophys 39(3):347–383. doi:10.1029/1999RG000074

Boschetti F, Dentith MD, List RD (1996) A fractal-based algorithm for detecting first arrivals on seismic traces. Geophysics 61:1095–1102. doi:10.1190/1.1444030

Brandsdóttir B, Menke W, Einarsson P, White RS, Staples RK (1997) Faeroe-iceland ridge experiment: 2. Crustal structure of the Kafla central volcano. J Geophys Res 102:7867–7886. doi:10.1029/96JB03799

Brune JN (1970) Tectonic stress and the spectra of seismic shear waves. J Geophys Res 75:4997–5009. doi:10.1029/JB075i026p04997

Caporali A, Barba S, Carafa MMC, Devoti R, Pietrantonio G, Riguzzi F (2011) Static stress drop as determined from geodetic strain rates and statistical seismicity. J Geophys Res 116:B02410. doi:10.1029/2010JB007671

Carracedo JC, Pérez Torrado F, Rodríguez González A, Soler V, Fernández Turiel JL, Troll VR, Wiesmaier S (2012) The 2011 submarine volcanic eruption in El Hierro (Canary Islands). Geol Today 28(2):53–58. doi:10.1111/j.1365-2451.2012.00827.x

Caruso F, Vinciguerra S, Latora V, Rapisarda A, Malone S (2006) Multifractal analysis of mount St. Helens seismicity as a tool for identifying eruptive activity. Fractals 14:179–186. doi:10.1142/S0218348X06003180

Chen P, Chen H (1989) Scaling law and its applications to earthquake statistical relations. Tectonophysics 166:53–72. doi:10.1016/0040-1951(89)90205-9

Chen K, Bak P, Obukhov SP (1991) Self-organized criticality in a crack-propagation model of earthquakes. Phys Rev A 43(2):625–630. doi:10.1103/PhysRevA.43.625

Chouet B (1985) Excitation of a buried magmatic pipe: a seismic source model for volcanic tremor. J Geophys Res 90:1881–1893. doi:10.1029/JB090iB02p01881

Chouet BA, Matoza RS (2013) A multi-decadal view of seismic methods for detecting precursors of magma movement and eruption. J Volcanol Geotherm Res 252:108–175. doi:10.1016/j.jvolgeores.2012.11.013

Choy GL, Boatwright JL (1995) Global patterns of radiated seismic energy and apparent stress. J Geophys Res 100:18205–18228. doi:10.1029/95JB01969

Cornet FH (1992). Fracture processes induced by forced fluid percolation. In: Gasparini P, Scarpa R, Aki K (eds) Volcanic seismology, IAVCEI proceeding, volcanology, vol 3. Springer, Berlin, pp 407–431

Crampin S (1994) The fracture criticality of crustal rock. Geophys J Int 118:428–438. doi:10.1111/j.1365-246X.1994.tb03974.x

Dieterich JH (1994) A constitutive law for rate of earthquake production and its application to earthquake clustering. J Geophys Res 99:2601–2618. doi:10.1029/93JB02581

Domínguez Cerdeña I, del Fresno C, Gomis A (2013) Seismicity patterns prior to the 2011 El Hierro eruption. Bull Seismol Soc Am 1:104. doi:10.1785/0120130200

Einarsson P (1991) The Krafla rifting episode 1975–1989. In: Gardarsson A, Einarsson Á (eds) Náttúra Myvatns, (The Nature of Lake Myvatn), pp. 97–139, Icelandic Nat. Sci. Soc., Reykjavik

Garces MA, McNutt SR (1997) Theory of the airborne sound field generated in a resonant magma conduit. J Volcanol Geotherm Res 78(3–4):155–178. doi:10.1016/S0377-0273(97)00018-8

Gobierno de Canarias (2011). Recomendaciones para el consumo de pescado en zonas afectadas por la erupción volcánica. Resultados de la necropsia. 01-11-2011. Consejería de Economía, Hacienda y Seguridad. http://www.gobiernodecanarias.org/dgse/sismo_hierro.html

González PJ, Samsonov SV, Pepe S, Tiampo KF, Tizzani P, Casu F, Fernández J, Camacho AG, Sansosti E (2013) Magma storage and migration associated with the 2011–2012 El Hierro eruption: implications for crustal magmatic systems at oceanic island volcanoes. J Geophys Res Solid Earth 118:4361–4377. doi:10.1002/jgrb.50289

Griffith AA (1921) The phenomena of rupture and flow in solids. Philos Trans R Soc Lond A 221:163–198. doi:10.1098/rsta.1921.0006

Gudmundsson A (1990) Emplacement of dikes, sills and crustal magma chambers at divergent plate boundaries. Tectonophysics 176:257–275. doi:10.1016/0040-1951(90)90073-H

Gudmundsson A (2006) How local stresses control magma-chamber ruptures, dyke injections, and eruptions in composite volcanoes. Earth Sci Rev 79:1–31. doi:10.1016/j.earscirev.2006.06.006

Hanks TC (1979) b values and $\omega^{-\gamma}$ seismic source models: Implications for tectonic stress variations along active crustal fault zones and the estimation of high-frequency strong ground motion. J Geophys Res 84(B5):2235–2242. doi:10.1029/JB084iB05p02235

Higuchi T (1988) Approach to an irregular time series on the basis of the fractal theory. Physica D Nonlinear Phenom 31(2):277–283. doi:10.1016/0167-2789(88)90081-4

Horton SP, Norris R, Moran S (2008) Broadband characteristics of earthquakes recorded during a dome-building eruption at Mount St. Helens, Washington, between October 2004 and May 2005. In: Sherrod SR, Scott WE, Stauffer PH (eds) A volcano rekindled: the first year of renewed eruptions at Mount St. Helens, 2004–2006: U.S. Geological Survey, Professional Paper, chapter 5

Ibáñez JM, De Angelis S, Díaz-Moreno A, Hernández P, Alguacil G, Posadas A, Pérez N (2012) Insights into the 2011–2012 submarine eruption off the coast of El Hierro (Canary Islands, Spain) from statistical analyses of earthquake activity. Geophys J Int 191(2):659–670. doi:10.1111/j.1365-246X.2012.05629.x

Irwin G (1957) Analysis of stresses and strains near the end of a crack traversing a plate. J Appl Mech 24:361–364

Jenny S, Goes S, Giardini D, Kahle H-G (2004) Earthquake recurrence parameters from seismic and geodetic strain rates in the eastern Mediterranean. Geophys J Int 157:1331–1347. doi:10.1111/j.1365-246X.2004.02261.x

Kanamori H (1977) The energy release in great earthquake. J Geophys Res 82(20):2981–2987. doi:10.1029/JB082i020p02981

Kilburn CRJ (2003) Multiscale fracturing as a key to forecasting volcanic eruptions. J Volcanol Geotherm Res 125(3–4):271–289. doi:10.1016/S0377-0273(03)00117-3

Kilburn CRJ, Sammonds PR (2005) Maximum warning times for an imminent volcanic eruptions. Geophys Res Lett 32:L24313. doi:10.1029/2005GL024184

Konstantinou KI (2002) Deterministic nonlinear source processes of volcanic tremor signals accompanying the 1996 Vatnajokull eruption, central Iceland. Geophys J Int 148(3):663–675. doi:10.1046/j.1365-246X.2002.01608.x

Kostrov BV, Das S (1988) Principles of earthquake source mechanics. Cambridge monographs on mechanics and applied mathematics. Cambridge University Press, Cambridge, p 286

Le Corvec N, Menand T, Lindsay J (2013) Interaction of ascending magma with pre-existing crustal fractures in monogenetic basaltic volcanism: an experimental approach. J Geophys Res Solid Earth 118:968–984. doi:10.1002/jgrb.50142

Leary PC, Abercrombie RE (1994) Fractal fracture scattering origin of S-wave coda: spectral evidence from recordings at 2.5 km. Geophys Res Lett 21(16):1683–1686. doi:10.1029/94GL01575

López C, Blanco MJ, Abella R, Brenes B, Cabrera-Rodríguez VM, Casas B, Domínguez-Cerdeña I, Felpeto A, Fernández de Villalta M, del Fresno C, García-Arias MJ, García-Cañada L, Gomis-Moreno A, González-Alonso E, Guzmán-Pérez J, Iribarren I, López-Díaz R, Luengo-Oroz N, Meletlidis S, Moreno M, Moure D, Pereda de Pablo J, Rodero C, Romero E, Sainz-Maza S, Sentre-Domingo MA, Torres PA, Trigo P, Villasante-Marcos V (2012). Monitoring the volcanic unrest of El Hierro (Canary Islands) before the onset of the 2011–2012 submarine eruption. Geophys Res Lett 39:LI3303. doi:10.1029/2012GL051846

Luongo G, Mazzarella A, Palumbo A (1996) A fractal approach to clustering of the 1983–1984 seismicity in the Campi Flegrei Caldera, southern Italy. Fractals 9:29. doi:10.1142/S0218348X96000054

Macaferri F, Bonafede M, Rivalta E (2011) A quantitative study of the mechanisms governing dike propagation, dike arrest and sill formation. J Volcanol Geotherm Res 208(1–2):39–50. doi:10.1016/j.jvolgeores.2011.09.001

Mandelbrot BB (1967) How long is the coast of Britain? Statistical self-similarity and fractional dimension. Science 156:636–638. doi:10.1126/science.156.3775.636

Martí J, Pinel V, López C, Geyer A, Abella R, Tárraga M, Blanco MJ, Castro A, Rodríguez C (2013a) Causes and mechanisms of the 2011–2012 El Hierro (Canary Islands) submarine eruption. J Geophys Res Solid Earth 118:823–839. doi:10.1002/jgrb.50087

Martí J, Castro A, Rodríguez C, Costa F, Carrasquilla S, Pedreira R, Bolos X (2013b) Correlation of Magma Evolution and Geophysical Monitoring during the 2011–2012 El Hierro (Canary Islands) Submarine Eruption. J Petrol 54(7):1349–1373. doi:10.1093/petrology/egt014

Maryanto S, Santosa RDR, Mulyana I, Hendrasto M (2011) Fractal and chaos properties of explosion earthquakes followed by harmonic tremor at Semeru Volcano, East Java, Indonesia. Int J Sci Eng Res 2(7). ISSN:2229-5518

McNutt SR (1996) Seismic monitoring of volcanoes: a review of the state-of-the-art and recent trends. In: Scarpa R, Tilling R (eds) Monitoring and mitigation of volcanic hazards, chapter 3. Springer, Berlin, pp 99–146

Meletlidis S, Di Roberto A, Pompilio M, Bertagnini A, Iribarren I, Felpeto A, Torres PA, D'Oriano C (2012) Xenopumices from the 2011–2012 submarine eruption of El Hierro (Canary Islands, Spain): constraints on the plumbing system and magma ascent. Geophys Res Lett 39:L17302. doi:10.1029/2012GL052675

Menand T (2011) Physical controls and depth of emplacement of igneous bodies: a review. Tectonophysics 500(1–4):11–19. doi:10.1016/j.tecto.2009.10.016

Menand T, Tait SR (2002) The propagation of a buoyant liquid-filled fissure from a source under constant pressure: an experimental approach. J Geophys Res 107(B11). doi:10.1029/2001JB000589

Moore JG, Krivoy HL (1964) The 1962 flank eruption of Kilauea Volcano and structure of the east rift zone. J Geophys Res 69(10):2033–2045. doi:10.1029/JZ069i010p02033

Morrissey MM, Chouet BA (1997) A numerical investigation of choked flow dynamics and its application to the triggering mechanism of long-period events at Redoubt Volcano, Alaska. J Geophys Res 102(B4):7965–7983. doi:10.1029/97JB00023

Orowan E (1948) Fracture and strength of solids. Rep Prog Phys XII:185–232

Orowan, E. (1960). Mechanism of seismic faulting. In: Griggs D, Handin J (eds) Rock deformation. Geol. Soc. Amer. Memoir 79, 323–345

Padhy S (2004) Rescaled range fractal analysis of a seismogram for identification of signals from an earthquake. Curr Sci Assoc 87(5):637–641. ISSN:0011-3891

Patanè D, Di Grazia G, Cannata A, Montalto P, Boschi E (2008) Shallow magma pathway geometry at Mt. Etna volcano. Geochem Geophys Geosyst 9(12):Q12021. doi:10.1029/2008GC002131

Pérez NM, Padilla G, Padrón E, Hernández PA, Melián G, Barrancos J, Dionis S, Nolasco D, Rodríguez F, Calvo D, Hernández I (2012) Precursory diffuse CO_2 and H_2S emission signatures of the 2011–2012 El Hierro submarine eruption, Canary Islands. Geophys Res Lett 39:L16311. doi:10.1029/2012GL052410

Pérez-Torrado FJ, Carracedo JC, Rodríguez-Gonzalez A, Soler V, Troll VR, Wiesmaier S (2012) La erupción submarina de La Restinga en la isla de El Hierro, Canarias: Octubre 2011-Marzo 2012. Estud Geol 68(1):5–27. doi:10.3989/egeol.40918.179

Prates G, García A, Fernández-Ros A, Marrero JM, Ortiz R, Berrocoso M (2013) Enhancement of sub-daily positioning solutions for surface deformation survillance at El Hierro volcano (Canary Islands, Spain) Bull Volcanol 75(6):1–9

Ranero CR, Torne M, Banda E (1995) Gravity and multichannel seismic reflection constraints on the lithospheric structure of the Canary Swell. Mar Geophys Res 17(6):519–534. doi:10.1007/BF01204342

Ripepe M, Gordeev E (1999) Gas bubble dynamics model for shallow volcanic tremor at Stromboli. J Geophys Res 104(B5):10639–10654. doi:10.1029/98JB02734

Roman DC (2005) Numerical models of volcanotectonic earthquake triggering on non-ideally oriented faults. Geophys Res Lett 32(2):L02304. doi:10.1029/2004gl021549

Roylance D (2011). Introduction to fracture mechanics. Department of materials science and engineering. Massachusetts Institute of Technology, Cambridge, MA, 02139. http://ocw.mit.edu/courses/materials-science-and-engineering/3-11-mechanics-of-materials-fall-1999/modules/frac.pdf

Rubin A, Gillard D, Got J (1998) A reinterpretation of seismicity associated with the January 1983 dike intrusion at Kilauea volcano, Hawaii. J Geophys Res 103:10,003–10015. doi:10.1029/97JB03513

Saichev A, Sornette D (2007) Theory of earthquake recurrence times. J Geophys Res 112:B04313. doi:10.1029/2006JB004536

Segall P (2013). Volcano deformation and eruption forecasting. In: Pyle DM, Mathier TA, Biggs J (eds) Remote sensing of volcanoes and modelling. Geological Society, London, Special Publications, 380, First published online March 20, 2013, doi:10.1144/SP380.4

Sigmarsson O, Laporte D, Martí J, Devouard B, Cluzel N (2012) Mafic intrusion remobilising silicic magma under El Hierro, Canary Islands. Geophys Res Abstr 14:EGU2012-12251

Taisne B, Tait S, Jaupart C (2011) Conditions for the arrest of a vertical propagating dyke. Bull Volcanol 73(2):191–204

Toda S, Stein RS, Sagiya T (2002) Evidence from the AD 2000Izu islands earthquake swarm that stressing rate governs seismicity. Nature 419:58–61. doi:10.1038/nature00997

Tosi P, Barba S, Rubeis VD, Luccio FD (1999) Seismic signal detection by fractal dimension analysis. Bull Seismol Soc Am 89:970–977

Traversa P, Grasso J-R (2009) Brittle creep damage as the seismic signature of dyke propagations within basaltic volcanoes. Bull Seismol Soc Am 99(3):2035–2043. doi:10.1785/0120080275

Troll VR, Klügel A, Longpré MA, Burchardt S, Deegan FM, Carracedo JC, Wiesmaier S, Kueppers U, Dahren B, Blythe LS, Hansteen T, Freda C, Budd DA, Jolis EM, Jonsson E, Meade F, Berg S, Mancini L, Polacci M (2011) Floating sandstones off El Hierro (Canary Islands, Spain): the peculiar case of the October 2011 eruption. Solid Earth Discuss 3:975–999. doi:10.5194/sed-3-975-2011

Turcotte DL (1997) Fractals and chaos in geology and geophysics, vol 2. Cambridge University Press, Cambridge, p 416

Valentine GA, Hirano N (2010) Mechanisms of low-flux intraplate volcanic fields—Basin and Range (North America) and Northwest Pacific Ocean. Geology 38:55–58. doi:10.1130/G30427.1

Vinciguerra S. (2002). Damage mechanics preceding the September-October 1989 flank eruption at Mt. Etna volcano inferred by seismic scaling exponents. J. Volcanol. Geotherm. Res. 113, 391-397, http://dx.doi.org/10.1016/S0377-0273(01)00274-8

Vinciguerra S, Gresta S, Barbano MS, Distefano G (2001). The two behaviours of Mt. Etna Volcano before and after a large intrusive episode: evidences from b value and fractal dimension of seismicity. Geophys Res Lett 28. doi:10.1029/2000GL012434

Walter WR, Brune JN (1993) Spectra of seismic radiation from a tensile crack. J Geophys Res Solid Earth 98(B3):4449–4459. doi:10.1029/92JB02414

Walter WR, Mayeda K, Gok R, Hofstetter A (2013). The scaling of seismic energy with moment: simple models compared with observations. In: Abercrombie R, McGarr A, Di Toro G, Kanamori H (eds)

Earthquakes: radiated energy and the physics of faulting, American Geophysical Union, Washington, DC. doi:10.1029/170GM05

Watts AB (1994) Crustal structure, gravity-anomalies and flexure of the lithosphere in the vicinity of the Canary-Islands. Geophys J Int 119(2):648–666. doi:10.1111/j.1365-246X.1994.tb00147.x

Watts AB, Peirce C, Collier J, Dalwood R, Canales J-P, Henstock TJ (1997) A seismic study of lithospheric flexure at Tenerife, Canary Islands. Earth Planet Sci Lett 146:431–448

Wells DL, Coppersmith KJ (1994) New empirical relationships among magnitude, rupture length, rupture width, rupture area, and surface displacement. Bull Seismol Soc Am 84(4):974–1002